



COMPUTER MODELLING
AND
NEW TECHNOLOGIES

2015
VOLUME 19 NO 1

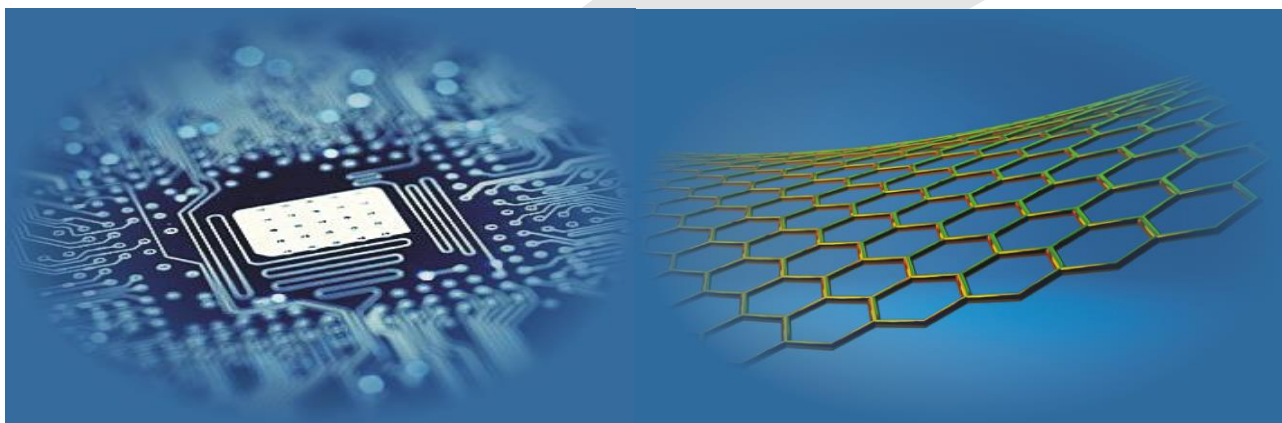
ISSN 1407-5806 ISSN 1407-5814 on-line

Latvian Transport Development and Education Association

Computer Modelling and New Technologies

2015 Volume 19 No 1

ISSN 1407-5806, ISSN 1407-5814 (*On-line: www.cmnt.lv*)



Riga – 2015

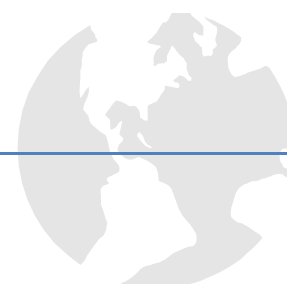
EDITORIAL BOARD

Prof. Igor Kabashkin	Chairman of the Board , <i>Transport & Telecommunication Institute, Latvia</i>
Prof. Yuri Shunin	Editor-in-Chief , <i>Information Systems Management Institute, Latvia</i>
Prof. Adolfas Baublys	<i>Vilnius Gediminas Technical University, Lithuania</i>
Prof. Stefano Bellucci	<i>Frascati National Laboratories – National Institute of Nuclear Physics, Italy</i>
Dr. Brent Bowen	<i>Embry-Riddle Aeronautical University, United States of America</i>
Prof. Olgierd Dumbrajs	<i>University of Latvia, Solid State Physics Institute, Latvia</i>
Prof. Pavel D'yachkov	<i>Kurnakov Institute for General and Inorganic Chemistry, Russian Academy of Sciences, Russian Federation</i>
Prof. Dietmar Fink	<i>University of Mexico, United Mexican States</i>
Prof. Alytis Gruodis	<i>Vilnius University, Lithuania</i>
Prof. Arnold Kiv	<i>Ben-Gurion University of the Negev, Israel</i>
Prof. Vladimir Litovchenko	<i>V. Lashkaryov Institute of Semiconductor Physics of National Academy of Science of Ukraine, Ukraine</i>
Prof. Sergey Maksimenko	<i>Institute for Nuclear Problem, Belarus State University, Belarus</i>
Prof. Ravil Muhamedyev	<i>International IT University, Kazakhstan</i>
Prof. Eva Rysiakiewicz-Pasek	<i>Institute of Physics, Wroclaw University of Technology, Poland</i>
Prof. Michael Schenk	<i>Fraunhofer Institute for Factory Operation and Automation IFF, Germany</i>
Prof. Kurt Schwartz	<i>Gesellschaft für Schwerionenforschung mbH, Darmstadt, Germany</i>
Contributing Editor	Prof. Victor Gopeyenko, <i>Information Systems Management Institute, Latvia</i>
Literary Editor	Prof. Tamara Lobanova-Shunina, <i>Riga Technical University, Latvia</i>
Technical Editor , secretary of Editorial Board	MSc Comp Nataly Burluckaya, <i>Information Systems Management Institute, Latvia</i>

Journal topics:	Publisher	Supporting Organizations
<ul style="list-style-type: none"> mathematical and computer modelling computer and information technologies natural and engineering sciences operation research and decision making nanoscience and nanotechnologies innovative education 	Latvian Transport Development and Education Association	Latvian Academy of Sciences Latvian Operations Research Society Transport and Telecommunication Institute, Latvia Fraunhofer Institute for Factory Operation and Automation IFF, Germany International IT University, Kazakhstan

Articles should be submitted in **English**. All articles are reviewed.

EDITORIAL CORRESPONDENCE	COMPUTER MODELLING AND NEW TECHNOLOGIES, 2015, Vol. 19, No.1 ISSN 1407-5806, ISSN 1407-5814 (on-line: www.cmnt.lv)
Latvian Transport Development and Education Association 68 Graudu, office C105, LV-1058 Riga, Latvia Phone: (+371) 29411640 E-mail: yu_shunin@inbox.lv http://www.cmnt.lv	Scientific and research journal The journal is being published since 1996 The papers published in Journal 'Computer Modelling and New Technologies' are included in: INSPEC , www.theiet.org/resources/inspec/ VINITI , http://www2.viniti.ru/ CAS Database http://www.cas.org/ EI Compindex



Editors' Remarks

An Legend of Truth*by Rudyard Kipling*

Once on a time, the ancient legends tell,
Truth, rising from the bottom of her well,
Looked on the world, but, hearing how it lied,
Returned to her seclusion horrified.

There she abode, so conscious of her worth,
Not even Pilate's Question called her forth,
Nor Galileo, kneeling to deny
The Laws that hold our Planet 'neath the sky.

Meantime, her kindlier sister, whom men call
Fiction, did all her work and more than all,
With so much zeal, devotion, tact, and care,
That no one noticed Truth was elsewhere.

Then came a War when, bombed and gassed and mined,
Truth rose once more, perforce, to meet mankind,
And through the dust and glare and wreck of things,
Beheld a phantom on unbalanced wings,
Reeling and groping, dazed, dishevelled, dumb,
But semaphoring direr deeds to come.

Truth hailed and bade her stand; the quavering shade
Clung to her knees and babbled, "Sister, aid!
I am--I was--thy Deputy, and men
Besought me for my useful tongue or pen
To gloss their gentle deeds, and I complied,
And they, and thy demands, were satisfied.

But this--" she pointed o'er the blistered plain,
Where men as Gods and devils wrought amain--
"This is beyond me! Take thy work again."

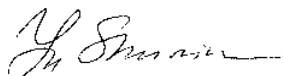
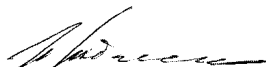
Tablets and pen transferred, she fled afar,
And Truth assumed the record of the War...
She saw, she heard, she read, she tried to tell
Facts beyond precedent and parallel--
Unfit to hint or breathe, much less to write,
But happening every minute, day and night.
She called for proof. It came. The dossiers grew.
She marked them, first, "Return. This can't be true."
Then, underneath the cold official word:
"This is not really half of what occurred."

She faced herself at last, the story runs,
And telegraphed her sister: "Come at once.
Facts out of hand. Unable overtake
Without your aid. Come back for Truth's own sake!
Co-equal rank and powers if you agree.
They need us both, but you far more than me!"

Rudyard Kipling (1865-1936)*

This 19th volume No.1 consists of four topical parts, namely, **Part A: Nanoscience and Nanotechnology**, **Part B: Operation Research: Modelling and Simulation**. These parts have a particular page numbering. References should include the symbols belonging to the part of the journal issue (A and B) and the pages of the paper quoted. (e.g.: ... **19(1A) 77-89**) We are planning to expand CMNT topics within the scope of its scientific interests.

Our journal policy is directed to fundamental and applied scientific researches, innovative technologies and industry, which is the fundamentals of the full-scale multi-disciplinary modelling and simulation. This edition is the continuation of our publishing activities. We hope our journal will be of interest for research community and professionals. We are open for collaboration both in the research field and publishing. We hope that the journal's contributors will consider collaboration with the Editorial Board as useful and constructive.

EDITORS

Yuri Shunin

Igor Kabashkin

* **Joseph Rudyard Kipling** (30 December 1865 – 18 January 1936) was an English short-story writer, poet, and novelist. He is chiefly remembered for his tales and poems of British soldiers in India and his tales for children. He was born in Bombay, in the Bombay Presidency of British India, and was taken by his family to England when he was five years old. Kipling is best known for his works of fiction, including *The Jungle Book* (a collection of stories, which includes and his poems, including "Mandalay" (1890), "Gunga Din" (1890), "The Gods of the Copybook Headings" (1919), "The White Man's Burden" (1899), and "If—" (1910). He is regarded as a major "innovator in the art of the short story"; his children's books are enduring classics of children's literature; and his best works are said to exhibit "a versatile and luminous narrative gift".



Content A

PART A Nanoscience and Nanotechnology		
Stefano Bellucci	Guest editor preface for the issue dedicated to the INFN-LNF conference on nanoscience and nanotechnology	7
A Maffucci, G Miano	A general frame for modeling the electrical propagation along graphene nanoribbons, carbon nanotubes and metal nanowires	8
S V Boroznin, E V Boroznina, I V Zaporotskova, O A Davletova, N P Polikarpova	Research into boron-carbon nanotube modified by alkaline metal atoms	15
I V Zaporotskova, A A Krutoyarov, N P Polikarpova	Adsorption of polyethylene, polypropylene, polyvinyl chloride monomer units on the single-walled carbon nanotube surface	19
I V Zaporotskova, R V Shinkarev	Superfine drug-eluting polyvinylpyrrolidone based coating for biliary stents	23
M D'Acunto, A Cricenti, M Luce, S Dinarelli	Theory of near-field detection of core-gold nanoshells inside biosystems	29
Yu Shunin, S Bellucci, Yu Zhukovskii, V Gopeyenko, N Burlutskaya, T Lobanova-Shunina	Nanocarbon electromagnetics in CNT-, GNR- and aerogel-based nanodevices: models and simulations	35
Authors' Index		43
Cumulative Index		44





Guest editor preface for the issue dedicated to the INFN-LNF conference on nanoscience and nanotechnology



Stefano Bellucci

Istituto Nazionale di Fisica Nucleare

Laboratori Nazionali di Frascati

Via E. Fermi 40, 00044 Frascati, Italy

bellucci@lnf.infn.it

The NEXT Nanotechnology group at the Laboratori Nazionali di Frascati (LNF) of INFN (the Italian Institute for Nuclear Physics) organizes since 2000 a series of international meetings in the area of nanoscience, a fast growing research field which has attracted increasing attention since many years, especially for many promising nanotechnological applications. The conferences in 2013 and 2014 held under the patronage of INFN, with the generous sponsorship by Flamar, Gambetti Vacuum Technology and Related Solutions, Ionvac Process, at LNF (see <http://www.lnf.infn.it/conference/nn2013/>, <http://www.lnf.infn.it/conference/nn2014/>), consisted of a number of tutorial/keynote lectures, as well as research talks presenting frontier nanoscience research developments and innovative nanotechnologies in the areas of biology, medicine, aerospace, optoelectronics, energy, materials and characterizations, low-dimensional nanostructures and devices.

Such yearly meetings took place earlier within the Nanotubes & Nanostructures (N&N) School and Workshop series, including a conference in Cagliari in 2000 and conferences in Frascati from 2001–2004.

More recently, the focus has shifted from the study of nanomaterials to the, by now, mature field of nanoscience and the corresponding innovative technologies in the most promising fields of application, hence yielding the Nanoscience & Nanotechnology (N&N) series.

Selected, refereed research papers, based on conference original presentations and follow-up discussions, are published in this special issue of CMNT in the division *Nanoscience and Nanotechnology*.

Dr. Stefano Bellucci,

PhD, First Researcher
Frascati National Laboratory (LNF)
National Institute of Nuclear Physics (INFN)
Via Enrico Fermi, 40 - 00044 Frascati (RM), Italy
Phone: +3906 94032883, +3906 94032888, +3906 94038222
Fax: +3906 94032427, +3906 94032688

A general frame for modeling the electrical propagation along graphene nanoribbons, carbon nanotubes and metal nanowires

A Maffucci^{1*}, G Miano²

¹*DIEI, University of Cassino and Southern Lazio, via G. Di Biasio 43, 03043 Cassino, Italy/INFN-LNF, Via E. Fermi 40, 00044, Frascati, Italy*

²*DIETI, University of Naples "Federico II", via Claudio 21, 80125, Naples, Italy*

*Corresponding author's e-mail: maffucci@unicas.it

Received 6 October 2014, www.cmnt.lv

Abstract

A general frame is proposed to model the propagation of electrical signals along nano-interconnects, either made by carbon nanotubes, graphene nanoribbons or metal nanowires. In the typical operating conditions of the next generations of integrated circuits, the electro-dynamics of the nano-interconnects may be conveniently described by means of a semi-classical transport model, based on the modified Boltzmann transport equation. From this model we derive here a generalized non-local dispersive Ohm's law, which can be regarded as the constitutive equation for the material. From the knowledge of the conduction and valence subbands, it is possible to define an equivalent number of conducting channels, which affects the circuit parameters of such interconnects. The study of the dispersion introduced by the generalized Ohm's law gives a clear explanation to the different propagation properties of nano-interconnects made by carbon materials and conventional metals.

Keywords: Carbon Nanotubes, Graphene nanoribbons, Metal nanowires, Nano-interconnects, Transmission lines

1 Introduction

Conventional materials so far used for microelectronics are not suitable for many nanoelectronics applications, because their performance does not meet the needed electrical, thermal and mechanical requirements. Therefore, a strong innovation is required, which may come either from the use of conventional materials with new structural arrangements, or by the use of innovative materials. Due to their outstanding physical properties, two possible allotropes of carbon are candidates to replace conventional materials in future nanoelectronics: the *graphene* (a graphite layer) and the *carbon nanotube* (a rolled-up version of graphene). Both materials exhibit low electrical resistivity, high thermal conductivity, high current carrying capability, besides other excellent mechanical properties [1, 2].

This is the main reason why, in the recent years, many efforts of the scientific community were devoted to the so-called *carbon electronics* [3, 4]. The fabrication of bundles of carbon nanotubes (CNTs) has reached satisfactory levels in terms of density, direction control, CMOS compatibility and contact resistance [5]. As for the graphene nanoribbons (GNRs), excellent results have been obtained for good quality large-scale fabrication [6]. The first real world applications became a reality, and so graphene and carbon nanotubes are now considered major candidates to become the silicon of the 21st century [7, 12]. The first examples of successful use of carbon-based nano-interconnects in IC technology have recently been demonstrated. The works [13] and [14] present high frequency CMOS oscillators integrating CNT or GNR interconnects, whereas [15] shows the first example of a computer with PMOS transistors entirely made by CNTs. Carbon of graphene interconnects are also successfully integrated into innovative organic transistors for the flexible plastic electronics [16]. As already pointed out, conventional materials are expected to fail in meeting

the performance requested to nano-interconnects enabling the transmission of clock, data and power in future nanoelectronics. From the electrical point of view, the main limitations expected when scaling down the conventional copper conductors to nanoscale dimensions come from the increasing electrical resistivity and insufficient current carrying capability [17].

An alternative solution to the use of new materials may come from the use of conventional materials, with new arrangements at nanoscale. An example is given by the metallic nanowires (NWs) which are made by metal atoms arranged in 1-D structures instead of the conventional 3D crystalline counterparts. Nanowires exhibit typical cross section sizes of the order of the material mean free path (some nanometers), and aspect ratios of 1000 or more. Conducting and semiconducting nanowires are proposed for nano-device applications [18], for molecular electronics [19], and in particular for interconnect applications [20].

A common feature for nanowires, carbon nanotubes and graphene nanoribbons is that the characteristic dimensions of transverse section are negligible compared to the longitudinal length. In other words, they can be regarded as one-dimensional (1-D) materials, for which the electrical conduction is characterized by two quantum-confined directions and one unconfined one. Based on this common feature, this paper shows how it is possible to derive a general frame to model the electrical propagation along nano-interconnects made by such materials.

The increasing interest in nano-interconnects leads to the quest for more and more accurate and reliable models, able to include all the quantum effects arising at nanoscale. This topic has been given a large attention by the recent literature, which presented several modeling approaches, like phenomenological [21] and semi-classical ones [22]. Based on such models, many papers predicted that carbon materials could outperform copper for IC on-chip interconnects and

vias [23-26].

In the typical working conditions of nano-interconnects, namely, frequency up to THz and low bias conditions, such nano-structures do not exhibit tunneling transport. Thus, the electrostatics may be studied by using a semi-classical description of the electron transport. This leads to the derivation of a constitutive relation between the electrical field and the density of the current in the form of a generalization of the classical Ohm's law, introducing non-local interactions and dispersion. By coupling such a relation to Maxwell equations, it is possible to derive a generalized transmission line model for such nano-interconnects. This approach has been adopted for modeling isolated metallic CNTs in [27], CNTs with arbitrary radius and chirality [28], multi-walled CNTs [29], and GNRs [30]. The semi-classical model gives results consistent with those provided by an alternative hydrodynamic model [31].

Here the formulation is extended to include nanowires of conventional metals, and a general expression is given for the constitutive relation of any nano-interconnect made by such 1D materials, Section 2. A key figure of the model is given by the effective number of conducting channels, which affects directly the parameters of the equivalent circuit models for the nano-interconnects, such as the conductance or the inductance. Section 2 presents a detailed discussion on the comparison between 1D structures made by CNT or GNRs and those made by conventional materials.

In Section 3 the propagation properties are investigated and the effects of the dispersion and quantum phenomena are discussed, referring to the phase velocity and the attenuation constant.

2 Generalized Ohm's law for 1D nano-conductors

The reference problem is depicted in Fig.1: a nano-interconnect is considered, made by a signal conductor above a perfect conducting ground (the presence of a dielectric is omitted). In the circular arrangement, the signal conductor is made by a single-wall CNT or by a conventional NW, whereas in the microstrip-like configuration the signal trace is made by a GNR. The starting point for the analysis of the electromagnetic behavior of such a structure is an accurate description of the electrostatic behavior, aimed at deriving a constitutive relation between the density of electrical current and the electrical field.

At macroscopic scale, which means for dimensions of hundreds of nanometers and greater, conventional conductors are studied by means of the classical electron transport model where the charges are treated as atoms in gas, which undergo random thermal motion with an average thermal velocity and a direct motion, characterized by the drift velocity. This approach leads to the classical Ohm's law, that reads in frequency domain:

$$J_z(z, \omega) = \sigma_c(\omega) E_z(z, \omega), \quad (1)$$

where $\sigma_c(\omega)$ is the Drude conductivity

$$\sigma_c(\omega) = \frac{\sigma_0}{1 + i\omega/\nu}, \quad (2)$$

being ν the collision frequency and σ_0 the DC value. In (1) and (2) we considered the simplified case where the

macroscopic motion is aligned along the conductor axis z .

On the opposite, at the molecular or atomic scale a quantum mechanical description is needed, since the transport is characterized by the wave-like behavior of electrons, where tunneling is possible. The Schrödinger equation is the basis for modeling the electrostatics: a Schrödinger/Maxwell model would take rigorously into account the quantum nature of the transport, but would easily lead to unaffordable numerical problems when increasing the number of carriers.

The cross-section sizes of the 1-D structures of our interest are typically large enough (at least 1 nm in the quantum confined directions) to have local crystal structures and to allow using a third approach, the *semi-classical transport model*. The electrons are classical particles but the movement takes place in a spatially periodic potential, where they move between two collisions according to the Boltzmann transport equation. Electrons behave like particles, unable to tunnel through barriers. In the collision events, the electrons can scatter inelastically, and so the kinetic energy of an incident particle is not conserved.

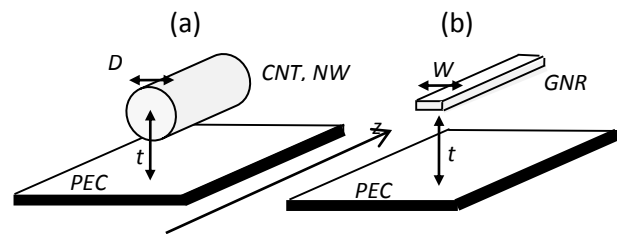


FIGURE 1 Reference geometry for the nano-interconnect: signal conductor made by (a) CNT or NW; (b) a GNR

2.1 TRANSPORT EQUATION

In any of the 1-D materials considered here, the electrons are quantum confined laterally and thus occupy quantized energy levels, instead of the traditional continuum of energy levels or bands that can be found in bulk materials. Along the longitudinal axis, the lattice exhibits translational symmetry and is long enough that the set of the possible values of the longitudinal wave-number k may be assumed to be almost continuous. The procedure presented here starts from the knowledge of the energy subbands for such materials: as pointed out before, they are quantized, so may be labeled by a band index μ and a wave vector $\mathbf{k} = k\mathbf{u}$, where \mathbf{u} is the unit vector oriented along the material lattice.

The subbands for CNTs and GNRs may be found by using the so-called *tight-binding approximation*, as shown in [32-34], whereas for metal nanowires it is possible to resort to calculations made by first principles [35].

Figure 2 shows some typical distributions of energy bands as functions of the wavenumber, for copper nanowire, metallic GNRs, and metallic CNTs.

Let us consider operating frequencies up to some THz, so that:

1. the cross section typical dimension (D or W , see Fig.1) is electrically small;
2. the transverse currents may be neglected;
3. only intraband transitions are considered, whereas interband ones are not allowed.

In these conditions, the longitudinal transport may be studied by considering the carrier transport for each of the n

subbands, either the conduction (+) and the valence (-) ones.

Let us indicate with $f_{\mu}^{(\pm)}$ the distribution function associated to the generic μ -th subband $E_{\mu}^{(\pm)}$: the carrier velocity is given by:

$$v_{\mu}^{(\pm)}(k) = \frac{dE_{\mu}^{(\pm)}}{d(\hbar k)}, \quad (3)$$

being \hbar the Planck constant. The transport may be modeled by the semi-classic Boltzmann equations [28, 29]:

$$\frac{\partial f_{\mu}^{(\pm)}}{\partial t} + v_{\mu}^{(\pm)} \frac{\partial f_{\mu}^{(\pm)}}{\partial z} + \frac{e}{\hbar} E_z \frac{\partial f_{\mu}^{(\pm)}}{\partial k} = -v (f_{\mu}^{(\pm)} - f_{0,\mu}^{(\pm)}), \quad (4)$$

where e is the electron charge, E_z is the longitudinal component of the electric field at the interconnect surface, whereas $\nu = v_F / l_{mfp}$ is the collision frequency, being l_{mfp} the mean free path and v_F the Fermi velocity.

The distribution function at equilibrium may be expressed as:

$$f_{0,\mu}^{(\pm)}(k) = F[E_{\mu}^{(\pm)}(k)] / X, \quad (5)$$

where $F[E]$ is the Dirac-Fermi distribution function

$$F[E] = \frac{1}{e^{E/k_B T} + 1}, \quad (6)$$

and

$$X = \begin{cases} D & \text{for CNT} \\ \pi W & \text{for GNR} \\ \pi(D/2)^2 & \text{for NW} \end{cases}, \quad (7)$$

being k_B the Boltzmann constant and T the absolute temperature. Note that the parameter X in (7) is a length for CNTs and GNRs, and an area for the nanowire. The reason for this difference resides in the fact that the density of electrical current J_z is given in A/m for CNTs and GNRs and in A/m² for solid NWs, as shown later.

2.2 GENERALIZED OHM'S LAW

Let us consider time-harmonic electric field $E_z(z,t) = \text{Re}\{\hat{E}_z \exp[i(\omega t - \beta z)]\}$ and current density $J_z(z,t) = \text{Re}\{\hat{J}_z \exp[i(\omega t - \beta z)]\}$, where β is the axial wavenumber.

In the low bias limit, namely for voltage values $V < k_B T / e$, we can assume small perturbations around the equilibrium:

$$f_{\mu}^{(\pm)}(k) = f_{0,\mu}^{(\pm)}(k) + \delta f_{\mu}^{(\pm)}(k, \beta, \omega) \quad (8)$$

and solve in the wave-number and frequency domain a linearized version of the transport equation (4), obtaining the first order term of (9):

$$\delta f_{1,\mu}^{(\pm)}(k) = \frac{1}{\hbar} \frac{df_{01,\mu}^{(\pm)}}{dk} \frac{e \hat{E}_z}{\omega - v_{\mu}^{(\pm)} - i\nu}. \quad (9)$$

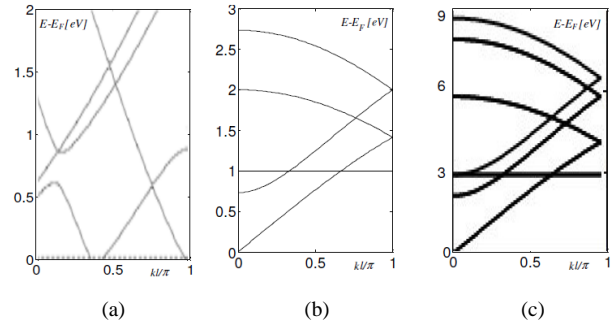


FIGURE 2 Energy band structure versus the normalized wavenumber $k' = kl / \pi$, for (a) copper NW, (b) metallic GNR, and (c) metallic CNT

Following the stream of what done in [30], the current density \hat{J}_z is expressed as:

$$\hat{J}_z(\beta, \omega) = \sum_{\mu=1}^N \int_{-\pi/l}^{+\pi/l} [e v_{\mu}^{(-)}(k) \delta f_{1,\mu}^{(-)}(k, \beta, \omega) + e v_{\mu}^{(+)}(k) \delta f_{1,\mu}^{(+)}(k, \beta, \omega)] dk. \quad (10)$$

The first term in the integral gives the contribution from to the valence bands, while the second term that from the conduction bands. In case of symmetry, the sum may be limited to the conduction subbands only, as done in [28] for CNTs and in [30] for GNRs.

By combining (9) and (10) we get:

$$\hat{J}_z(\beta, \omega) = \hat{\sigma}_{zz}(\beta, \omega) \hat{E}_z(\beta, \omega) s, \quad (11)$$

where the longitudinal conductivity in the wavenumber domain is given by the sum of all the contributions of the subbands:

$$\hat{\sigma}_{zz}(\beta, \omega) = \sum_{\mu=1}^N \hat{\sigma}_{\mu}, \quad (12)$$

$$\hat{\sigma}_{\mu} = i \frac{e^2}{\hbar} \int_{-\pi/l}^{+\pi/l} \left[\frac{v_{\mu}^{(-)}(k)}{\omega - v_{\mu}^{(-)}(k)\beta - i\nu} \frac{df_{0,\mu}^{(-)}}{dk} + \frac{v_{\mu}^{(+)}(k)}{\omega - v_{\mu}^{(+)}(k)\beta - i\nu} \frac{df_{0,\mu}^{(+)}}{dk} \right] dk. \quad (13)$$

The quantities $\hat{\sigma}_{\mu}$ are not, in general, of the same order of magnitude: only some of the subbands give a significant contribution to the conduction, those for which the energy gap with respect to the Fermi level E_F is such that $|E_{\mu} - E_F| \leq 5k_B T$. To catch in a simple way the main features of the dependence of $\hat{\sigma}_{zz}(\beta, \omega)$ on the wavenumber β and frequency ω , we assume that v_{μ} is approximately constant for all the subbands near the Fermi level, and hence:

$$\hat{\sigma}_{zz}(\beta, \omega) \cong -i \frac{2e^2 v_F}{\pi X \hbar} \frac{1}{\omega - i\nu} M \left[1 + \alpha \left(\frac{v_F \beta}{\omega - i\nu} \right)^2 \right] \quad (14)$$

and thus, from (14) and (11), we finally obtain the *generalized Ohm's law*

$$\left[1 - \psi(\omega) \beta^2 \right] \hat{J}_z(\beta, \omega) = \frac{\sigma_0}{1 + i\omega / \nu} \hat{E}_z(\beta, \omega). \quad (15)$$

In (14) and (15) we have introduced:

$$\psi(\omega) = \frac{\alpha(\omega)v_F^2}{v^2(1+i\omega/v)^2}, \quad \sigma_0 = \frac{2v_F M}{vR_0 X}, \quad (16)$$

being $R_0 = 12.9 \text{ k}\Omega$ the *quantum resistance*, and

$$M = \frac{\hbar}{v_F} \sum_{\mu=1}^N \int_0^{\pi/l} \left[v_{\mu}^{(+)} \left(-\frac{dF}{dE_{\mu}^{(+)}} \right) + v_{\mu}^{(-)} \left(-\frac{dF}{dE_{\mu}^{(-)}} \right) \right] dk. \quad (17)$$

Finally, the function $\alpha(\omega)$ is equal to 1 for CNTs [12], whereas for GNR it is

$$\alpha = \frac{\hbar}{Mv_F^3} \sum_{\mu=0}^{n-1} \int_0^{\pi/l} \left[v_{\mu}^{(+)} \left(-\frac{dF}{dE_{\mu}^{(+)}} \right) + v_{\mu}^{(-)} \left(-\frac{dF}{dE_{\mu}^{(-)}} \right) \right] dk \quad (18)$$

and for solid nanowires [36]:

$$\alpha(\omega) = \frac{1}{3} \frac{1+1.8i\omega/v}{1+i\omega/v}. \quad (19)$$

The interpretation of the generalized Ohm's law (14) is discussed in the next Section. Here we observe that the quantity M in (17) is the *equivalent number of conducting channels*, a measure of the number of subbands that effectively contribute to the electric conduction, i.e. those that cross or are closer to the Fermi level. In general, this number may be expressed as

$$M = \xi X N_{DOS}, \quad (20)$$

where ξ is a material constant, X is defined in (7) and N_{DOS} is the total number of available states, which are related to the density of states. A detailed discussion on the behavior of such number M for CNTs and GNRs may be found in [28, 30, 37, 38], where it is clearly shown how such a quantity strongly depends on the chirality, size and temperature of such carbon nanostructures. Here we compare the number of channels for metallic CNTs, GNRs and Cu nanowires, assuming $T = 300 \text{ K}$, with varying dimensions. The results shown in Table 1 highlights the strong difference between conventional materials and carbon-based ones: as the cross section dimension increases, the number of subbands contributing to the conduction exhibits a limited increase for CNTs and GNRs, whereas for conventional metals such a number experience a steep increase. In other words, for CNTs and GNRs the energy levels may be assumed to be quantized for transverse dimensions up to some hundreds of nm, whereas for nanowires of conventional metals this phenomenon only happens for dimensions of the order of tens of nm or lower.

TABLE 1 Number of conducting channels for metallic NW, GNR and CNT at 300 K

	1 nm	10 nm	50 nm	100 nm
CNT	2.00	2.12	5.04	9.93
GNR	1.00	1.07	1.57	3.13
NW	3.12	11.75	220.98	874.82

3 Propagation properties of nano-interconnects

In this Section we investigate the generalized Ohm's law (14) and its impact in the properties of the electrical propagation

along the nano-interconnects of Figure 1.

3.1 GENERALIZED TRANSMISSION LINE MODEL

By using the charge conservation law, Eq. (16) may be rewritten in frequency domain as follows:

$$I(z, \omega) - i\omega\psi(\omega) \frac{\partial I(z, \omega)}{\partial z} = \frac{\sigma_0 X}{1+i\omega/v} E_z(z, \omega), \quad (21)$$

where the second term in the l.h.s introduces a spatial and frequency dispersion, whereas the coefficient of the electric field introduces a frequency dispersion.

By coupling (21) to the Maxwell equations, in the low bias condition and for operating frequencies up to the order of THz, it is possible to derive a simple transmission line model for the nano-interconnects schemes in Figure 1. The details of such a derivation are given in [28-30]. The final expressions for the a transmission line per-unit-length resistance, inductance and capacitance are given by:

$$R_{TL} = \frac{vL_k}{\Theta(\omega)}, \quad L_{TL} = \frac{L_k + L_m}{\Theta(\omega)}, \quad C_{TL} = C_e, \quad (22)$$

where L_m and C_e are the p.u.l. magnetic inductance and electrostatic capacitance, and

$$L_k = \frac{1}{v\sigma_0 X}, \quad \Theta(\omega) = 1 + \frac{C_e}{C_q} \frac{\alpha}{1-i\omega/v}, \quad C_q = \frac{v_F^2}{L_k}. \quad (23)$$

The p.u.l. *kinetic inductance* L_k takes into account the effects of the mass inertia of the conduction electrons, whereas the p.u.l. *quantum capacitance* C_q is related to the effects due to the quantum pressure arising from the zero-point energy of such electrons.

The parameters of the TL model (24) generalize those given for the classical TL model, which can be viewed as the limit of (24) when the effects of the kinetic inductance and the quantum capacitance are negligible. Let us for instance consider the simple interconnect of Figure 1a, assuming the signal trace to be made by bulk copper, with a radius of 100 nm and distance to the ground of 400 nm. For such dimensions and assuming room temperature, the number of conducting channel is $M \approx 3.1 \cdot 10^5$, which provides the bulk copper DC conductivity of $\sigma_0 \approx 6 \cdot 10^7 \text{ S/m}$ and leads to the p.u.l. parameters reported in Table 2. Given these values, it is easy to show that $\Theta \approx 1$ and $L_k \ll L_m$, and so the expressions in (24) reduce to the classical ones:

$$R_{TL} = \frac{1}{\sigma_0 X}, \quad L_{TL} = L_m, \quad C_{TL} = C_e. \quad (24)$$

This means that the quantum, kinetic and dispersive effects introduced in (22) are experienced only for smaller sizes, when the density of states and consequently the number of conducting channels M drops down dramatically, as discussed in Section 2.

TABLE 2 P.u.l. parameters for the line in Figure 1a, made by bulk copper

L_m [nH/mm]	L_k [nH/mm]	C_e [fF/mm]	C_q [fF/mm]
0.42	0.01	26.7	$3 \cdot 10^7$

3.2 PROPAGATION PROPERTIES

The propagation properties of the nano-interconnects in Figure 1 may be investigated starting from the TL p.u.l. parameters (24) and deriving the longitudinal propagation wavenumber, defined as:

$$k_{TL}(\omega) = \alpha_{TL}(\omega) + i\beta_{TL}(\omega) = \sqrt{(R_T + i\omega L_T)i\omega C_T}, \quad (25)$$

In particular, it is useful to study the normalized phase velocity $\beta_{TL}(\omega)$, i.e. the phase velocity compared to the value obtained if the line were made by ideal perfect conductor, $k_0 = i\omega\sqrt{L_m C_e}$. The real part $\alpha_{TL}(\omega)$ in (25), instead, is the attenuation constant, and gives a measure of the damping and dispersion of the signal introduced by the losses.

Let us consider two case-studies: the first refers to an on-chip local level interconnect at the 14 nm node [17], for which we assume, according to Fig.1, $D=W=14$ nm, $t=2D$ and a dielectric constant of the embedding medium $\epsilon_r=2.2$. Let us consider room temperature and let us assume the signal conductor of Fig.1 to be made by a metallic single-wall CNT, a metallic GNR and a copper NW. The second case study refers to the same arrangements and conditions, but with $D=W=1$ nm.

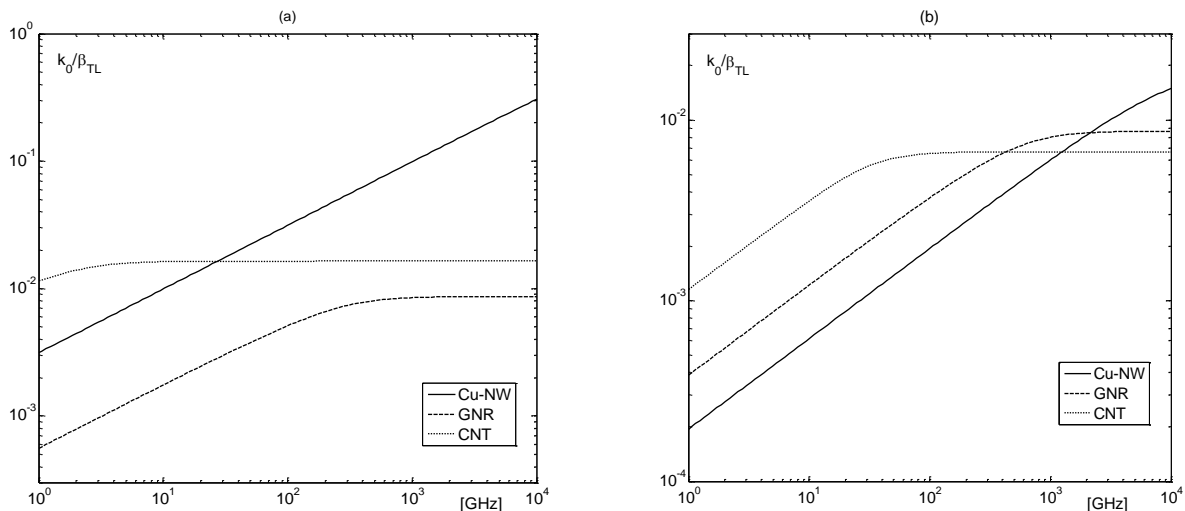


FIGURE 3 Dispersion in the normalized phase velocity for an on-chip interconnect of width of: (a) 14 nm; (b) 1 nm

5 Conclusions

A general frame has been derived to study the propagation of electrical signals along nano-interconnects made by 1D materials, in low bias conditions and for frequencies up to THz. A semi-classical model for the electrodynamics allows writing a generalized Ohm's law to describe the relation between the density of current and the electric field.

The propagation properties of such interconnects have been investigated, showing that the dispersion phenomena affect in different way the carbon-based interconnects and those made by conventional metals, arranged in nanowires. A crucial role is played by the different behavior of the number of conducting channels, which exhibits a strong

dependence on the quantization in the transverse direction. Such an effect is observed in graphene and carbon nanotubes with transverse sizes up to hundreds nanometers, whereas the nanowires exhibits a low number of conducting channels only up to some tens of nanometers.

As a consequence, the propagation velocity for carbon-based interconnects is 1-2 order of magnitude smaller than the ideal one, whereas that of nanowires of conventional materials is close to the ideal one, unless for transverse dimensions smaller than 10 nanometers. This provides a physical explanation of a well-known result for the carbon nanotubes and graphene nanoribbons.

Figure 3 shows the normalized phase velocity $k_0/\beta_{TL}(\omega)$, for the two case-studies. The different dispersion introduced by the generalized Ohm's law, leads to saturation in different frequency ranges. In all cases, the carbon line velocity saturates to a value that is two orders of magnitude smaller than the ideal velocity. This is a well-known consequence of the role played by the kinetic inductance [21-31]. For case-study 1 the copper line is not evidently affected by the quantum effects, and so its phase velocity exhibits a behavior similar to bulk copper, with saturation close to the ideal velocity.

In case-study 2, the copper line behaves like the carbon ones, exhibiting the same slowing down of velocity. The reason for this behavior is given in Table 1, from which it is clear that copper nanowires start to experience the effect of the transverse quantum confinement only for dimensions below 10 nanometers.

Figure 4 shows the dispersion for the attenuation constant $\alpha_{TL}(\omega)$, i.e. the frequency behavior of the losses. The attenuation introduced by CNTs is lower than the other two realizations and is almost constant over the considered frequency range. As expected, the attenuation introduced by the copper NW is increasing with frequency increasing, and is generally lower than the one introduced by GNRs for 14 nm, whereas for 1 nm the performance of Cu-NW is the worst one.

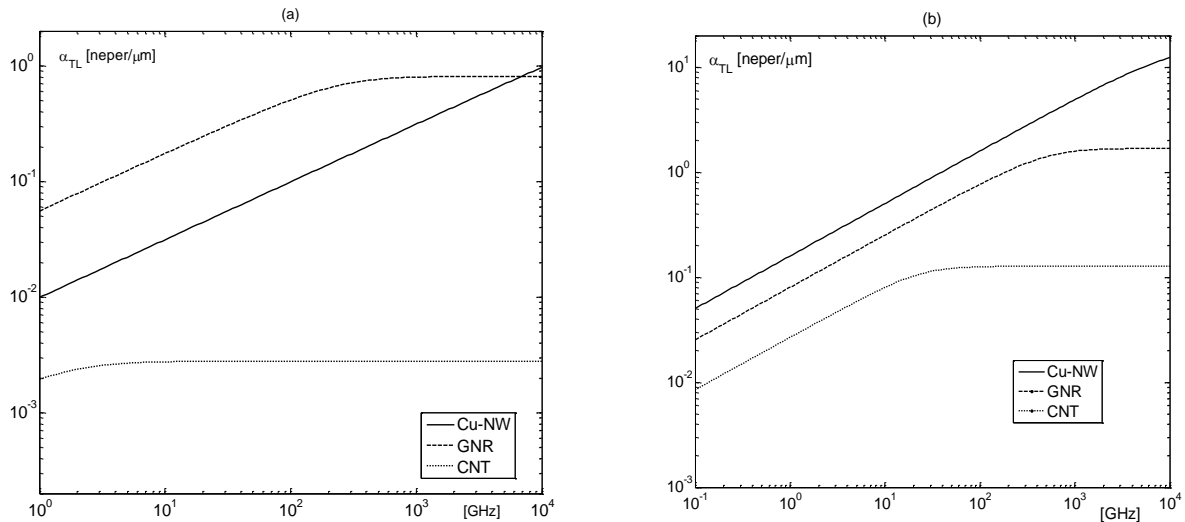




FIGURE 4 Dispersion in the attenuation constant for an on-chip interconnect of width of: (a) 14 nm; (b) 1 nm

As for the attenuation, the carbon interconnects exhibit a saturation phenomena, which means that in a subrange of the investigated frequency range this attenuation is constant. This is more evident in carbon nanotubes, for which the

attenuation values are also the best. Also in this case, moving from 14 nm to 1 nm, the copper nanowire exhibits a strong degradation of its performance.

References

- [1] Saito R, Dresselhaus G., Dresselhaus M S 2004 *Physical Properties of Carbon Nanotubes* Imperial College Press: Singapore
- [2] Castro Neto A H, Guinea F, Peres N M R, Novoselov K S, K. Geim A K 2009 *Reviews of Modern Physics* **81** 109
- [3] Avouris P, Chen Z, Perebeinos V 2007 *Nature Nanotech.* **2** 605
- [4] Van Noorden R 2006 *Nature* **442** 228
- [5] Li Y, Zhang X B, Tao X Y, Xu J M, Huang W Z, Luo J H, Luo Z Q, Li T, Liu F, Bao Y, Geise H J 2005 *Carbon* **43** 295
- [6] Li X, Cai W, An J, Kim S, Nah J, Yang D, Piner R, Velamakanni A, Jung I, Tutuc E, Banerjee S K, Colombo L, and Ruoff R S 2009 *Science* **324** 1312
- [7] Zhou Y, Sreekala S, Ajayan P M, Nayak S K 2008 *J. Phys. Cond. Matter* **20** 095209
- [8] Geim A K 2009 *Science* **324** 1530
- [9] Naeemi A, Meindl J D 2008 *IEEE Trans. Electron Devices* **55** 2574
- [10] Maffucci A, Miano G, Villone F 2008 *IEEE Trans. on Advanced Packaging* **31** 692
- [11] Li H, Xu C, Srivastava N, Banerjee K 2009 *IEEE Trans. on Electron Devices* **56** 1799
- [12] Cui J-P, Zhao W-S, Yin W-Y, Hu J 2012 *IEEE Trans. on Electromagnetic Compatibility* **54** 126.
- [13] Close G F, Yasuda S, Paul B, Fujita S, Philip Wong H-S 2009 *Nano Letters* **8** 706
- [14] Chen X, Akinwande D, Lee K-J, Close G F, Yasuda S, Paul B C, Fujita S, Kong J, Philip Wong H-S 2010 *IEEE Trans. Electr. Devices* **57** 3137
- [15] Shulaker M M, Hills G, Patil N, Wei H, Chen H-Y, Philip Wong H-S, Mitra S 2013 *Natur* **501** 526
- [16] Valitova I, Amato M, Mahvash F, Cantele G, Maffucci A, Santato C, Martel R, Ciccoira F 2013 *Nanoscale* **5** 4638
- [17] International Technology Roadmap for Semiconductors 2011 <http://public.itrs.net>.
- [18] Tseng G Y, Ellenbogen J C 2001 *Science* **294** 1293
- [19] Joachim C, Gimzewski J K, Aviram A 2000 *Nature* **408** 541
- [20] Morris J E 2008 *Nanopackaging: Nanotechnologies and electronics packaging* Springer: New-York, USA
- [21] Burke P J 2002 *IEEE Trans. Nanotechnology* **1** 129
- [22] Salahuddin S, Lundstrom M, Datta S 2005 *IEEE Trans. Electron. Devices* **52** 1734
- [23] Xu C, Li H, Banerjee K 2009 *IEEE Trans. Electron Devices* **56** 1567.
- [24] Zhao W-S, Yin W-Y, Guo Y-X 2012 *IEEE Trans. on Electromagnetic Compatibility* **54** 149
- [25] Maffucci A, Miano G 2013 *IEEE Trans. Components, Packaging and Manufacturing Technology* **3** 1926.
- [26] Naeemi A and Meindl J D 2009 *IEEE Trans. Electron Dev.* **56** 1822
- [27] Maffucci A, Miano G, Villone F 2009 *IEEE Trans. Nanotechnology* **8** 345
- [28] Miano G, Forestiere C, Maffucci A, Maksimenko S A, Slepian G Y 2011 *IEEE Transactions on Nanotechnology* **10** 135
- [29] Forestiere C, Maffucci A, Maksimenko S A, Miano G., Slepian G Y 2012 *IEEE Transactions on Nanotechnology* **11** 554
- [30] Maffucci A, Miano G 2013 *Nanoscience and Nanotechnology Letters* **5** 1207
- [31] Forestiere C, Maffucci A, Miano G 2010 *Journal of Nanophotonics* **4** 041695
- [32] Zheng H, Wang Z F, Luo T, Shi Q W, Chen J 2007 *Physical Review B* **75** 165414
- [33] Moradinab M, Nematian H, Pourfath M, Fatipour M, Kosina H 2012 *Journal of Applied Physics* **111** 074318
- [34] Wakabayashi K, Sasaki K, Nakanishi T, Enoki T. 2010 *Sci. Technol. Adv. Mater.* **11** 054504
- [35] Zhou Y, Sreekala S, Ajayan P M, Nayak S K, 2008 *J. Phys. Cond. Matter* **20** 095209
- [36] Hanson G W 2011 *IEEE Trans. Microwave Theory and Tech.* **59** 9
- [37] Forestiere C, Maffucci A, Miano G 2011 *IEEE Transactions on Nanotechnology* **10** 1221.
- [38] Maffucci A, Miano G 2013 *IEEE Trans. Nanotechnology* **12** 817

Authors	
	<p>Antonio Maffucci</p> <p>Current position: Associate Professor University studies: M.Sc. Electronic Engineering, PhD in Electrical Engineering Scientific interest: electromagnetic modeling, electromagnetic compatibility, computational electromagnetism and nanotechnology Publications: about 160 papers in international journals and conference proceedings, 1 book: "Transmission Lines and Lumped Circuits", 2001, Academic: New York. Experience: University of Naples Federico II (Italy); JET – Culham (UK)</p>
	<p>Giovanni Miano</p> <p>Current position: Full professor University studies: M.Sc. Electronic Engineering, Ph.D. Electrical Engineering Scientific interest: ferromagnetic materials, nonlinear dielectrics, plasmas, electrodynamics of continuum media, nanotechnology and modeling of lumped and distributed circuits. Publication: about 200 papers in international journals and conference proceedings, 1 book: "Transmission Lines and Lumped Circuits", 2001, Academic: New York. Experience: University of Naples Federico II (Italy); GSI, Darmstadt (Germany); University of Maryland (USA).</p>

Research into boron-carbon nanotube modified by alkaline metal atoms

**S V Boroznin*, E V Boroznina, I V Zaporotskova,
O A Davletova, N P Polikarpova**

Volgograd State University, Volgograd 400062, str. Bogdanova, 32

*Corresponding author's e-mail: sboroznin@mail.ru

Received 10 October 2014, www.cmnt.lv

Abstract

All articles *must* contain an abstract. The abstract follows the addresses and should give readers concise information about the content of the article and indicate the main results obtained and conclusions drawn. As the abstract is not part of the text it should be complete in itself; no table numbers, figure numbers, references or displayed mathematical expressions should be included. It should be suitable for direct inclusion in abstracting services and should not normally exceed 200 words. The abstract should generally be restricted to a single paragraph. These pages provide you with instructions on how to use this word template to prepare your paper according to the required layout and style for CM&NT papers.

Keywords: boron-carbon nanotubes, ionic-built covalent-cyclic cluster model, quantum chemical calculations, adsorption, metal superlattice.

1 Introduction

The discovery of carbon NTs in the early nineties was followed by intensive investigation into their electronic structure and energy spectrum parameters as well as physical and chemical properties. Along with studying of nanotube properties researchers started searching for ways to modify NTs and fabricate structures having new mechanical, electronic and other properties. Due to high surface activity, nanotubes can be used as basis for fabricating various types of composites. In particular, it was found that introduction of metal atoms between the tubulene layers leads to the formation of nanotube based composite structures such as hollow alternating metallic supercells, nanotube conductors in semi-conducting coating, etc., that possess new conducting, magnetic and electrical properties [1].

However, apart from carbon nanotubes, current research focuses on theoretical and experimental investigation of non-carbon nanotubes, namely recently discovered boron-carbon nanotubes of BC₃ type. Research conducted into the electron structure and energy characteristics of this class of non-carbon structures showed that boron-carbon nanotubes (BCNTs) as well as carbon nanotubes of “zigzag” type represent a class of narrow gap semiconductors [2-6] whereas the study of BCNTs surface activity revealed that they display better adsorption properties in respect to certain elements that CNTs [7-12]. That is why one of the most interesting aspects of BCNTs study is research into the interaction mechanism of alkaline metal atoms with the BCNT external surface.

The present paper presents calculations of alkaline metal atoms (AM) (Li, Na, K) adsorption on the boron-carbon BC₃ nanotubes (6, 0) type external surface with the view of exploring a possibility to fabricate boron-carbon nanotube based metal-phase composites.

As geometrical models of the studied tubulenes we selected clusters containing six hexagon boron-carbon cycles located on the tube perimeter and four elementary layers

located along the tube axis. Since a nanotube is an infinite structure hydrogen pseudo atoms were used to complete loose chemical bonds on the nanotube edge. A model of a covalent cyclic cluster built in via ionic bonding in the framework of the semi-empirical quantum chemical MNDO calculation procedure was applied [1]. Two possible positions of carbon and boron atoms in respect to a lithium atom on the tube external surface in BC₃-tubulenes clusters are shown in Figure 1.

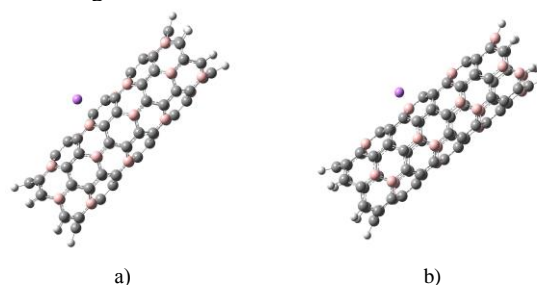


FIGURE 1 BC₃ nanotube (6,0) with an adsorbed lithium atom on the nanotube surface: a) type A of C and B atoms positions; b) type B of C and B atoms position

In order to eliminate the influence of boundary effects, we modelled the process so that adsorbed atoms (Li, K, Na) bound either to a carbon or boron atom located approximately in the middle of the boron-carbon nanotube cluster. The adsorption process for alkaline metal atoms was modeled in increments of 0,1 Å in the direction of the perpendicular to the tube axis passing through the boron or carbon atom on which the adsorption takes place. The geometrical parameters of the system were optimized in quantum-chemical calculations. As a result of calculations we obtained the potential energy curves of these processes. Analysis shows that all the curves for the nanotubes reveal the presence of energy minimum that enabled us to conclude that atoms adsorbed on the BC₃ tubulene external surface formed stable

adsorption complexes (Figures 2–5). Adsorption energy values were calculated as the difference between the total energy value of non-interacting adsorbent model of a corresponding atom and a related adsorption complex, formula (1):

$$E_{ad} = E_{ad.c.} - (E_{tub} + E_{H, Cl, O, F}). \quad (1)$$

Adsorption energy values E_{ad} for Li, K, Na atoms and corresponding adsorption distances R_{ad} are shown in Table 1.

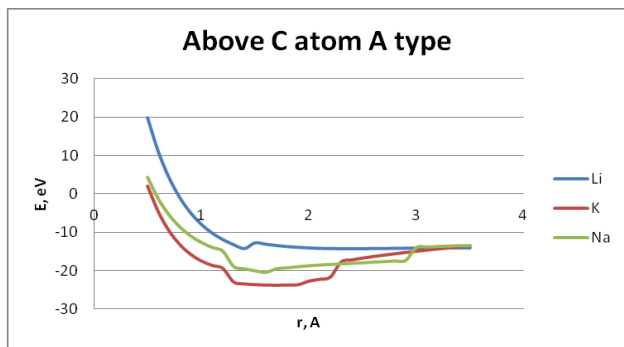


FIGURE 2 The energy curve of the alkaline metal atoms adsorption process on the boron-carbon nanotube A type (6, 0) external surface (C atom)

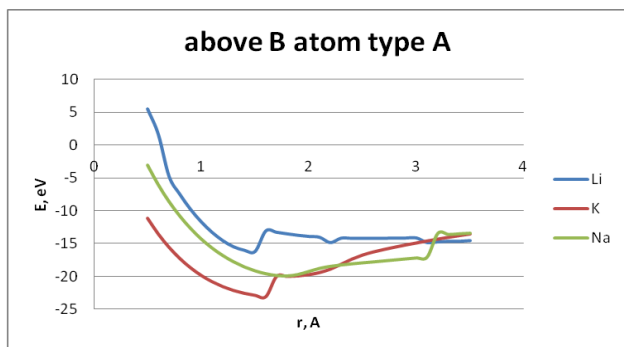


FIGURE 3 The potential energy curve of the alkaline metal atoms adsorption process on the boron-carbon nanotube A type (6, 0) external surface (B atom)

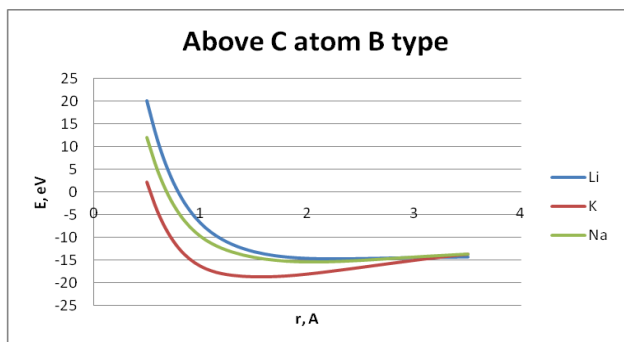


FIGURE 4 The potential energy curve of the alkaline metal atoms adsorption process on the boron-carbon nanotube B type (6, 0) external surface (C atom)

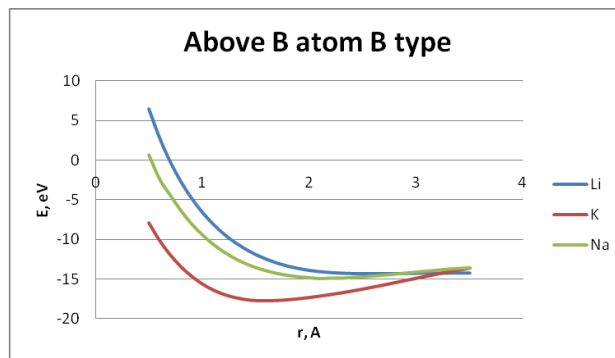


FIGURE 5 The potential energy curve of the alkaline metal atoms adsorption [process on the boron-carbon nanotube B type (6, 0) external surface (B atom)]

TABLE 1 The adsorption energies E_{ad} for Li, K, Na atoms and corresponding adsorption distances R_{ad} . Letters C and B denote an approximation to boron and carbon atoms, respectively

	Li		K		Na	
	C	B	C	B	C	B
Type A						
E_{ad}, eV	14,21	15,97	23,73	23,13	20,33	19,94
$R_{ad}, \text{Å}$	1,4	1,4	1,7	1,6	1,6	1,8
Type B						
E_{ad}, eV	14,63	14,28	18,7	17,77	15,4	14,98
$R_{ad}, \text{Å}$	2,3	2,6	1,6	1,6	2,1	2,1

The charge distribution over the metal atoms indicates that electron transfer to boron and carbon atoms located on the nanotube external surface takes place, which increases the number of majority charge carriers in tubulenes; as a result BC_3 nanotubes, which we had previously classified as narrow-gap semiconductor, begin to take on metallic properties (the occurrence of surface conductivity is attributed to electrons from metal atoms).

2 Regular binding of alkaline metal atoms to the BC_3 nanotubes (6,0) type B surface

On performing calculations of single alkaline metal atoms adsorption on the boron-carbon nanotube external surface that has shown that interaction between metal atoms and BC_3 tubulenes is possible, it seemed interesting to study the possibility of alkaline metal atoms regular binding (modification) to this type of tubulene to find out whether metal-phase boron-carbon based composites can be fabricated. We chose BC_3 nanotubes (6,0) type B that interact with alkaline metal atoms located over carbon or boron atoms on the BC_3 tubulene external surface as shown in Figure 6. In the selected positions the distance between metal atoms is taken to be 4.2 Å. It is known that lattice parameters for alkaline metals are 3.5 Å (for Li) and 4.2 Å (for Na) [13], that is, they are in good agreement with the values we obtained for interatomic distances Li-Li, Na-Na or K - K. Thus, alkaline metal atoms that bind to the external nanotube surface can be considered one-dimensional metallic cells (further called a superlattice on boron-carbon nanotube external surface), and the distances between the atoms can be called superlattice constants.

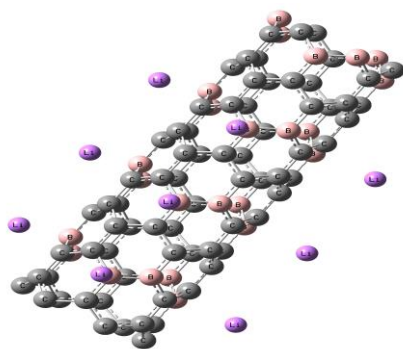
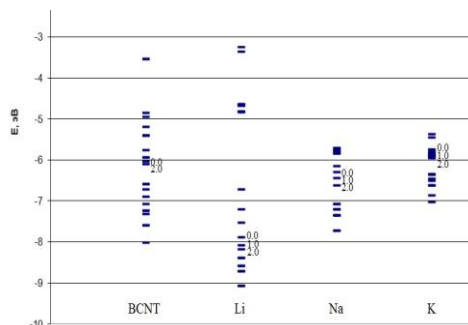


FIGURE 6 Extended elementary cell (6, 0) modified by Li atom

To study the electron energy structure of the described nanosystems a BC_3 - type (6,0) tubulene cluster consisting of ninety-six nanotube atoms and nine alkaline metal atoms located above the tubulene surface and forming superlattices either of rectangular or rhombic type was selected. Calculations were performed by applying the procedure described in the previous section. Bond length between the boron and carbon atoms were taken to be equal to 1.44 Å, and the distance between the metal atoms and tubulene surface atoms corresponded to the values obtained in the study of single Li, K, Na adsorption. Calculations allowed us to build one-electron spectra of the nanocomposites under study and then compare the values with the ones obtained for the energy spectrum of pure - BC_3 tubulene (Figure 7). The values of the bandgap ΔE_g are seen in Table 2. Figure 7 shows that the band gap structure in boron-carbon nanotubes modified by Li atoms when compared to pure BC_3 tubulenes does not change within a predetermined degree of accuracy. In BC_3 tubulenes modified by K atoms the band gap value approaches zero that reveals the presence of metallic conductivity. Nanotubes modified by Na atoms have a slight increase in the band gap, but, nevertheless, the structure can be classified as a narrow-gap semiconductor. Analysis of the charge reveals that likewise in the case of single atom adsorption electron density is transferred from alkaline metal atoms on the BC_3 tubulene surface atoms (Table 2).

References

- [1] Zaporotskova IV 2009 Carbon and un-carbon nanomaterials and composite structures on their base: structure and electronic properties Volgograd: Volgograd State University Publishing 490 p
- [2] Liu X M, Gutiérrez H R, Eklund P C 2010 Electrical properties and far infrared optical conductivity of boron-doped single-walled carbon nanotube films *J Phys: Cond Matter* **22** 334223
- [3] Debnarayan J, Sun C-L, Chen L-C, Chen K-H 2013 Effect of chemical doping of boron and nitrogen on the electronic, optical, and electrochemical properties of carbon nanotubes *Progress in Materials Science* **58** 565-635
- [4] Ayala P, Reppert J, Grobosch M, Knupfer M, Pichler T, Rao A M 2010 Evidence for substitutional boron in doped single-walled carbon nanotubes *Appl Phys Lett* **96** 183110-3
- [5] Panchakarla L S, Govindaraj A, Rao C N R 2010 Boron-and nitrogen-doped carbon nanotubes and graphene *Inorg Chim Acta* **363** 4163-74
- [6] Zaporotskova I V, Boroznin S V, Perevalova E V, Polikarpov D I, 2012 Electronic structure and characteristics of certain types of boron containing nanotubes *Vestnik VolGU: ser 10 Innovatsionnaya deyatel'nost* **6** 81-6
- [7] Boroznin S V, Boroznina E V, Zaporotskova I V, Polikarpov D I 2013 Adsorption of atomic hydrogen on the surface of the boron-carbon nanotubes *Russian Journal of General Chemistry* **83**(3) 1580-5
- [8] Boroznin S V, Zaporotskova I V, Boroznin S V 2012 Investigation of oxidation in boron-containing nanotubes *Nanoscience and Nanotechnology Letters* **4** 1096-9
- [9] Boroznin S V, Boroznina E V, Zaporotskova I V, Polikarpov D I, Polikarpova N P 2013 Hydrogenation of boron-carbon nanotubes *Nanoscience and Nanotechnology Letters* **5** 1-6
- [10] Boroznin S V, Boroznina E V, Zaporotskova I V, Polikarpov D I 2013 About hydrogen adsorption on the boron-carbon nanotube surface *Journal of General Chemistry* **83**(8) 1351-6
- [11] Boroznin S V, Boroznina E V, Zaporotskova I V, Polikarpov D I, Krutoyarov A A 2013 Vacancy transport properties in boron-carbon BC_3 nanotubes *Physics of wave processes and radio systems* **16**(2) 14-8
- [12] Perevalova E V, Zaporotskova I V, Zaporotskova N P 2011 Boron Nanotubes: Sorption Properties and Proton Conductivity *Nanoscience and Nanotechnology Letters* **3**(6) 1-6
- [13] Penkalya T M 1972 Essay about crystal chemistry Leningrad: Chemistry 496 p (in Russian)

FIGURE 7 One-electron energy spectra of BC_3 -tubulenes (6, 0)TABLE 2 Energy characteristics of modified boron-carbon tubulenes type B (6, 0); Q - charges on alkaline metal atoms; ΔE_g – bandgap (eV)

	Q	ΔE_g , eV
BCNT		0,14
BCNT +9Li	0,96	0,2
BCNT +9K	0,96	0,01
BCNT +9Na	0,92	0,15

3 Conclusions

Calculations reveal that surface modification of boron-carbon nanotubes with alkaline metal atoms (Li, K, Na) leads to metallization of the tube external surface. The optimum adsorption distance was found and adsorption energy values were calculated. It can be assumed that a regular adsorption process on the external nanotube surface will cause the "metal - metal" transition. It means that by introducing, for example, metal atoms between the layers of multi-walled tubulenes alternating hollow metal superlattices can be fabricated as well as other nanotube based composite structures having novel conductive, magnetic and electrical properties. Surface modification of boron-carbon nanotubes with metal atoms does not change their conductivity, but leads to the formation of free charge carriers on the tube surface, thereby ensuring the emergence of transition "narrow-gap semiconductor – metal" in the obtained metal-phase boron-carbon nanotube based composites.

Authors	
	<p>Sergei Boroznin , 08.03.1987, Volgograd, Russian Federation</p> <p>Current position, grades: associate professor, PhD, Institute of priority technologies Volgograd State University University studies: Volgograd State University Scientific interest: nanotechnology, nanostructures and atomic clusters, boron-carbon nonmaterial, solid state physics Publications: 52 published scientific works, including 7 in journals included in the database Scopus Main: [1] Zaporotskova I V, Boroznin S V, Boroznina E V, Plikarpova N P 2014 Boron-carbon Nanotube Modification Using Alkaline Metal Atoms <i>Journal of nano- and electronic physics</i> 6(3) 03006-1 – 03006-2. [2] Boroznin S V, Zaporotskova I V, Polikarpov D I, Boroznina E V 2013 Adsorption of atomic hydrogen on the surface of the boron-carbon nanotubes <i>Russian Journal of General Chemistry</i> 83(3) 1580-5 [3] Boroznin S V, Zaporotskova I V, Boroznina E V, Polikarpov D I, Polikarpova N P 2013 Hydrogenation of boron-carbon nanotubes <i>Nanoscience and Nanotechnology Letters</i> 5(11) 1195-1200 Experience: The holder of a scholarship of the President of the Russian Federation, Head of the grant of the Volga, participation in the grant of the Ministry of Education "study of the structure, physico-chemical and dynamical properties of nanostructures", defended PhD thesis on "boron nanotubular structures: the structural features and properties (2013)</p>
	<p>Irina Zaporotskova , 12.11.1963, Melitopol, Ukraine</p> <p>Current position, grades: professor, Doctor of Physical and Mathematical Sciences University studies: Volgograd State University, Molecular physics, Solid State Physics Scientific interest: nanotechnology, boron-carbon nonmaterial, nanocomposites. Publications: 326 publications Recent main: [1] Zaporotskova I V, Boroznin S V, Boroznina E V, Polikarpov D I 2013 Vacancy Transport Properties in Boron–Carbon BC3 nanotubes <i>Nanoscience and Nanotechnology Letters</i> 5 (11) 1164-8 [2] Zaporotskova I V, Polikarpova N P, Ermakova T A, Polikarpov D I 2013 Carbon Nanotubes, New Material for Purification of Water–Ethanol Mixtures from Isomers of Propanol <i>Russian Journal of General Chemistry</i> 83(8) 1601–6 [3] Zaporotskova I V, Anikeev N A, Kojitov L V, Davletova O A, Popkova A V 2014 Theoretical Studies of the Structure of the Metal-carbon Composites on the Base of Acryle-nitrile Nanopolimer <i>Journal of nano- and electronic physics</i> 6(3) 03035-1 - 03035-3 Experience: since 2008 - the managing editor of the journal "Bulletin of the Volga. Series 10: Innovation activities; since 2007 - the head of Research and Education Center VoISU "Nanomaterials and Nanotechnologies", repeatedly participated in conferences, symposiums, forums and academic seminars of national and international level.</p>
	<p>Evgenia Boroznina, 01.11.1980, Volgograd, Russian Federation</p> <p>Current position, grades: associate professor, PhD University studies: Volgograd State University, Atomic physics Scientific interest: nanotechnology, boron nanomaterial, nanotubes. Publications: 50 Main: [1] Zaporotskova I V, Boroznin S V, Boroznina E V, Polikarpova N P 2014 Boron-carbon Nanotube Modification Using Alkaline Metal Atoms <i>Journal of nano- and electronic physics</i> 6(3) 03006-1 – 03006-2 [2] Zaporotskova I V, Boroznin S, Boroznina E, Zaporotskov P A, Davletova O A 2014 Migration processes on the surface of carbon nanotubes with substitute boron atoms <i>Nanosystems: physics, chemistry, mathematics</i> 5(1) 107-12 [3] Boroznin S V, Zaporotskova I V, Polikarpov D I, Boroznina E V 2013 Adsorption of atomic hydrogen on the surface of the boron-carbon nanotubes <i>Russian Journal of General Chemistry</i> 83(3) 1580-6 Experience: In 2012, defended his thesis on "Nanotubular form boron: features the electron energy structure and conducting properties." Boroznina Eugene participated in the grant of the Ministry of Education "study of the structure, physico-chemical and dynamical properties of nanostructures."</p>
	<p>Olessya Davletova, 19.12.1981, Buzinovka, Volgograd region, Russian Federation</p> <p>Current position, grades: associate professor, PhD University studies: Volgograd State University, Computer modeling of nanostructures Scientific interest: nanotechnology, pyrolyzed poliakrilonitril, quantum-chemistry calculations. Publications: [1] Zaporotskova I V, Anikeev N A, Kojitov L V, Davletova O A, Popkova A V 2014 Theoretical Studies of the Structure of the Metal-carbon Composites on the Base of Acryle-nitrile Nanopolimer <i>Journal of nano- and electronic physics</i> 6(3) 03035-1 - 03035-3 [2] Zaporotskova I V, Boroznin S, Boroznina E, Zaporotskov P A, Davletova O A 2014 Migration processes on the surface of carbon nanotubes with substitute boron atoms <i>Nanosystems: physics, chemistry, mathematics</i> 5(1) 107-12 [3] Zaporotskova I V, Kravchenko A A, Ermakova T A, Davletova O A, Zaporotskova I V, Korchagina T K, Popov U V, Kalmikova G A 2014 The semi-empirical research of the adsorption of biologically active molecules on the outer surface of carbon nanotubes <i>Nanosystems: physics, chemistry, mathematics</i> 5(1) 98-100 Experience: She defended her thesis on "The structure and electronic properties of the pyrolyzed polyacrylonitrile." (2010), has scientific journal articles from the list of HAC and included in the Scopus database, is the deputy director of the Institute of priority technologies Volgograd State University in social work.</p>
	<p>Natalia Polikarpova, 11.03.1989, Volgograd, Russian Federation</p> <p>Current position, grades: associate professor, PhD University studies: Volgograd State University, Spectroscopy Scientific interest: nanotechnology, sensor activity of nanostructures, quantum-chemistry calculations. Publications: 47 Main: [1] Zaporotskova I V, Boroznin S V, Boroznina E V, Plikarpova N P 2014 Boron-carbon Nanotube Modification Using Alkaline Metal Atoms <i>Journal of nano- and electronic physics</i> 6(3) 03006-1 – 03006-2. [2] Polikarpova N P, Vilkeeva D E, Polikarpov D I, Zaporotskova I V 2014 Sensor properties of carboxyl-modifies carbon nanotubes <i>Nanosystems: physics, chemistry, mathematics</i> 5(1) 101-6 [3] Polikarpova N. P., Vil'keeva D. E., Zaporotskova I V 2013 Sensor Activity of Carbon Nanotubes with a Boundary Functional Group <i>Nanoscience and Nanotechnology Letters</i> 5(11) 1169-73 Experience: Has 47 scientific publications, including 4 articles in journals included in the Scopus database. In defended her thesis on "SENSORY PROPERTIES OF SEMICONDUCTOR Nanotubular SYSTEM "(2013), takes part in the grant of Ministry of Education 'Study of the structure, physical, chemical and dynamical properties of nanostructures'</p>

Adsorption of polyethylene, polypropylene, polyvinyl chloride monomer units on the single-walled carbon nanotube surface

I V Zaporotskova*, A A Krutoyarov, N P Polikarpova

Volgograd State University, Volgograd 400062, Universitetskii prospect, 100

*Corresponding author's e-mail: irinazaporotskova@gmail.com

Received 10 October 2014, www.cmnt.lv

Abstract

The paper presents the results of research into the interaction mechanism between single-walled carbon nanotubes and most common polymers that results in the formation of stable polymer based nanotube reinforced composites. Nanotubes used as reinforcement provide strong as well as plastic polymer based nanocomposites that have a promising field of commercial application. The main characteristics of the interaction process between the nanotube (6, 6) and monomers of the polymers under study are defined. Calculations are performed by applying DFT method and B3LYP functional.

Keywords: carbon nanotubes, polyethylene, polypropylene, polyvinyl chloride, adsorptive interactions, polymer based nanocomposites, reinforcement, density functional theory method

1 Introduction

One of the most important fields in polymer technology offering promising results is the development of polymer based nanocomposites that are produced by modifying the polymer matrix structure with various nanoparticles (carbon nanotubes, fullerenes [1-5]). It is reported that these nano-sized fillers change the polymer matrix structure and have the potential to enhance its operational and other properties [6]. Of the various nanofillers used to modify polymer matrices, carbon nanotubes have attracted great interest recently as structural reinforcements because of their unique properties. Reports show that composites filled with carbon nanotubes (CNTs) displayed an increase in strain before breakdown as compared to the original pure polymer (for epoxy based composites the effect is described in [7], for phenylon [8]). Small amounts of CNTs (0.1-2 %) added to the polymer structure increase both the elastic modulus and tensile strength of the polymer manifold [9, 10]. Simultaneously, thermal and electrical conductivity of the composite showed a considerable increase. The paper [10] reported the fabrication of a polymer composite composed of a large number of vertically arranged multi-walled carbon nanotubes where the space between the layers was filled with polydimethylsiloxane. Research showed that a cyclic load on the polymer did not cause mechanical fatigue and led to the composite hardening.

The major drawback of polymer composites is a gradual decrease in elasticity with an increasing amount of filler content, all polymer composites modified with CNTs show a significant elasticity enhancement, and this effect is important for practical application. However, the interaction mechanism between polymers and carbon nanotubes contributing to improvements in plasticity, elasticity and hardening of nanocomposites has not been studied so far.

In this paper, we present the study of the interaction mechanism between single-walled carbon nanotubes and the most common polymers - polyethylene, polypropylene and polyvinyl chloride. Taking into consideration the atomic and electronic structure of CNTs that is characterized by the presence of non-zero curvature of the surface that results in non-orthogonality of σ and π - bonds, we believe it is possible to implement adsorption of polymers on the nanotube surface. This process will lead to the formation of stable polymer-based composites reinforced with CNTs having enhanced strength and plasticity.

We performed quantum-chemical calculations of the interaction process between polyethylene, polypropylene and PVC monomers and single-walled carbon nanotubes of «arm-chair» type (n, n) that have cylindrical symmetry. Calculations were performed by using the density functional method (DFT) and B3LYP functional [11].

2 Study of polyethylene adsorption mechanism on the single-walled nanotube surface (6,6)

The possibility for the monomer ethylene $\text{CH}_2=\text{CH}_2$ to bind to the single-walled carbon nanotube (6, 6) external surface was investigated. Molecular clusters (MC) containing six hexagon cycles on the tube perimeter and four elementary layers along the tube axis were selected as a geometric model of the tubulene. Since a nanotube is an infinite structure hydrogen pseudo atoms were used to complete loose chemical bonds on the nanotube edge. The interaction model between tubulene (6, 6) and ethylene monomer is shown in Figure 1. The interaction takes place via one of the possible adsorption centers of ethylene: a – the monomer hydrogen atom when as a result of interaction C – H bond is formed; b – the monomer carbon atom when as a result of interaction C – C bond is formed. To avoid the boundary effects the position for the adsorbed monomer was chosen approximately in the middle of the nanotube cluster.

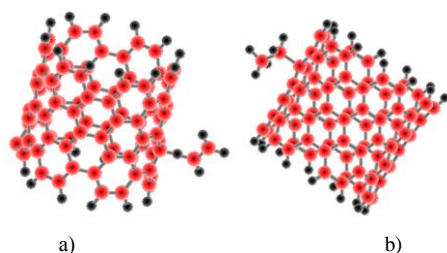


FIGURE 1 The interaction model between the ethylene monomer and carbon nanotube (6, 6): a) adsorption via the H centre of ethylene with C – H bond formation; b) adsorption via the C centre of ethylene with C – C bond formation

The adsorption process for the *polyethylene* molecule on the selected atom on the nanotube external surface was modeled in increments of 0,01 Å. Optimization of the system geometry was performed incrementally and as a result the potential energy curves of the adsorption process were calculated (Figure 2).

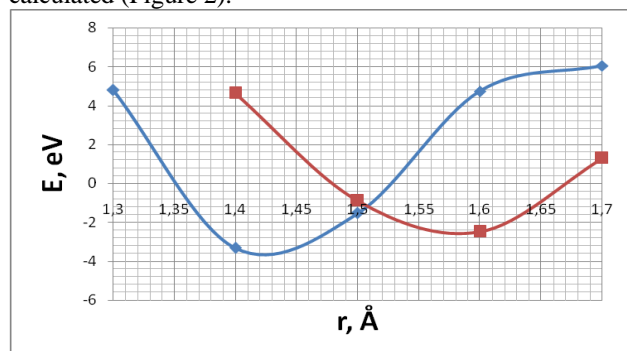


FIGURE 2 The energy curves of the ethylene molecule adsorption process on the nanotube external surface via the H adsorption center of ethylene with the C – H bond formation (the blue line) and via the center C adsorption center of ethylene with C – C bond formation (the red line)

Analysis of the adsorption complex geometry optimization results found that the cylindrical symmetry of the tube is broken due to an increase in length of the C – C bond in the carbon hexagon when the ethylene molecule is adsorbed on the C atom. An average elongation is 5 % of the original C – C bond length that is equal to 1,4 Å. Values of interaction energies were calculated as the difference between the total energy of the non-interacting adsorbent (in this case, the carbon nanotube plus ethylene monomer) and the one of the adsorption complex: $E_{ad} = E_{ad.c.} - (E_{tub} + E_{eth})$.

Analysis of the results showed that the interaction process is implemented, which is illustrated by the presence of a minimum on the energy curves (Fig. 2). Basic parameters for variants (a) and (b) of the adsorption interaction are shown in Table 1.

TABLE 1 The main characteristics of the interaction process between carbon nanotube (6, 6) and polyethylene, polypropylene and polyvinyl chloride monomers for different variants: a - via hydrogen atom of the monomer with C – H bond formation, b - via a carbon atom of the monomer with C – C bond formation; r_{ad} – adsorption distance, E_{ad} – adsorption energy.

Interaction variants	a, C-H bond		b, C-C bond	
	r_{ad} , Å	E_{ad} , eV	r_{ad} , Å	E_{ad} , eV
Polyethylene	1,42	-3,83	1,59	-2,48
Polypropylene	1,8	-6,64	1,5	-5,43
Polyvinyl chloride	2,5	-8,41	2,1	-1,98

Thus, calculations revealed that for both variants of interaction (a – C – H bond, b – C – C bond) adsorption is possible. Meanwhile, it was found that energetically more favorable interaction with the carbon nanotube takes place via the hydrogen atom adsorption center with C – H bond formation (the adsorption energy value in this case is larger than in the case of (b), $\Delta E = 1,35$ eV). The fact that chemical interaction takes place at a sufficiently small distance proves that there is a strong bond between CNT and polyethylene fragment. Thus, it can be assumed that CNTs can form the so-called reinforcement for polyethylene polymer matrix that provides strength of the polymer composite.

3 Study of polypropylene monomer adsorption mechanism on the single-walled nanotube surface (6,6)

The possibility of monomer $CH_2=CH-CH_3$ polypropylene- CH_3 to bind to the external surface of single-walled carbon nanotube (6, 6) was investigated. The interaction model was similar to the one described in the previous section for CNTs and ethylene monomer. Interaction is carried out through one of the propylene molecule adsorption centers: a – hydrogen atom of the monomer, b - a carbon atom of the monomer (Figure 3).

As a result of incremental calculations the energy curves of the adsorption process for the two variants of the interaction process were built, that are shown in Fig. 4. Each of the curves has a minimum which indicates the presence of adsorption interaction systems. It is obvious that interaction via a hydrogen atom of propylene is energetically more favorable. The curve analysis for the variant where adsorption takes place via C atom of the propylene molecule revealed that the curve has two minima.

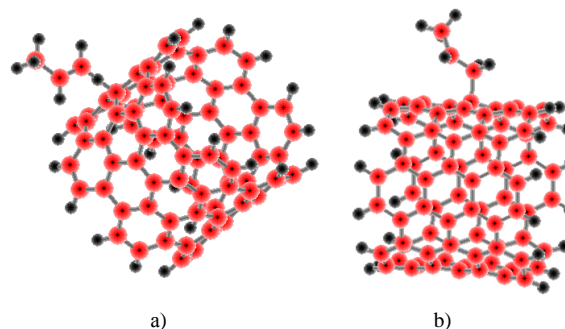


FIGURE 3 The interaction model between propylene monomer and carbon nanotube (6, 6): a) adsorption via H center of ethylene with C – H bond formation; b) adsorption via C center of ethylene with C – C bond formation

It means that in order to reach a second minimum at a distance of 1,52 Å, the propylene molecule has to overcome a small potential barrier height of 2.8 eV. The second minimum is energetically more favourable ($E_{ad(II)} = -5,8$ eV), that is why this state of the adsorption complex is more stable as compared to the one that is formed when the propylene molecule is located at a distance of 1,89 Å, where $E_{ad(I)} = -1,2$ eV. The main parameters of the process are given in Table 1.

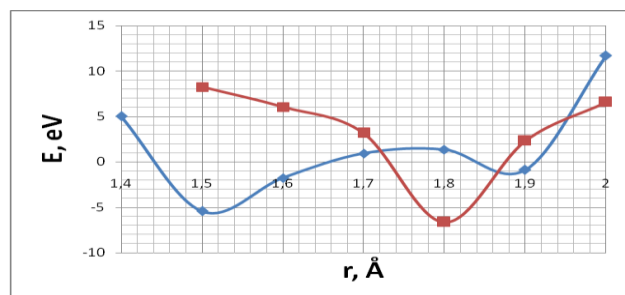


FIGURE 4 The energy curves of the propylene molecule adsorption on the external surface of the nanotube via the H adsorption center H of propylene with C–C bond formation (the blue line) and via the C center of ethylene with the C–H bond formation (the red line)

Thus, the results of the study proved the possibility of adsorption interaction between carbon nanotube and polypropylene monomer. This allows us to assume that the reinforcement of the polymer matrix with small diameter carbon nanotubes will provide useful properties of polymer composites promising for practical application.

4 The adsorption mechanism of polyvinyl chloride monomer on the single-walled nanotube surface (6,6)

Further, the possibility for polyvinyl monomer - CH₂-CH-Cl- to bind to the external surface of single-walled carbon nanotube (6, 6) was investigated. As in previous cases, molecular clusters containing six hexahydric carbon cycles (hexagons) around the tube perimeter and four elementary layers along the tube axis were selected to serve as a geometric model of the tubulene. The cluster boundaries were completed by pseudo hydrogen atoms. The interaction was modeled via one of the adsorption centers of polyvinyl chloride (PVC) monomer: A – the hydrogen atom of the monomer, b - the carbon atom of the monomer. To eliminate the boundary effects the position of the adsorbed monomer was taken to be in the middle of the nanotube cluster.

The adsorption process of PVC monomer on the carbon nanotube external surface was modeled in increments of 0,01 Å and accompanied by full optimization of the geometrical structure of the interacting systems. The calculations of the energy curves constructed for the interaction process are shown in Fig. 5. The presence of minimum on the curves indicates adsorption interaction of the systems. It was found that energetically more favorable type of interaction takes place via a hydrogen atom of PVC monomer. However, in contrast to the previously considered cases where chemical interaction between CNTs and polyethylene and polypropylene monomers was observed, long adsorption distances for the PVC monomer and CNTs interaction reveal that

References

- [1] Saito R, Dresselhaus M S, Dresselhaus G 2009 *Physical properties of carbon nanotubes* Imperial London: College Press 251p
- [2] Harris P J F 1999 *Carbon nanotubes and related structures. New Materials for the Twenty-first Century* New York: Cambridge University Press 336 p
- [3] Zaporotzkova I V 2009 *Carbon and non-carbon nanomaterials and composite structures on its base: morphology and electron properties* Volgograd: Volgograd University Press 456 p
- [4] Dresselhaus M S, Dresselhaus G, Avouris P 2000 *Carbon nanotubes:*

physical adsorption is implemented, which indicates a weaker interaction between the carbon nanotube and polyvinyl chloride matrix. In this case, the most active monomer center is a hydrogen atom.

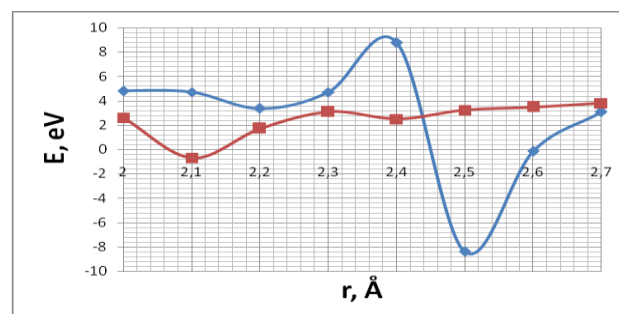


FIGURE 5 The energy curves of the interaction process between monomer polyvinyl chloride ethylene and the external surface of the nanotubes via H adsorption center of the monomer with C–H bond formation (the blue line) and via C adsorption center of the monomer with C–C bond formation (the red line)

Analysis of single-electron spectra for all the considered interaction types found that the main contribution to the valence band of the obtained composite polymer systems is made by s- and p-orbitals of carbon atoms and s-orbital of the hydrogen atom of the selected polymers. For PVC monomer based composite s- and p-orbitals of the chlorine atom also contribute to the valence band. The conductivity band is formed by 2p atomic orbitals of carbon nanotubes in all the cases under study.

5 Conclusions

The studies of interactions between carbon nanotubes of small diameter and monomers of most common polymers of polyethylene, polypropylene and polyvinyl chloride showed that adsorption on the active centers of the monomers (C and H atoms) is possible. It was found that for all the selected polymers the interaction of the carbon nanotube and the polymer molecule via a hydrogen atom that is followed by a C-H bond formation is energetically more favorable. The calculations revealed that for interactions of the CNT and the monomers of polyethylene and polypropylene chemical interaction is realized providing a strong bond between the nanotube and polymer matrix. In contrast, “CNT – PVC” complex revealed the emergence of a weaker (in terms of energy) physical adsorption. It is concluded that CNTs may form the so-called reinforced frame of the polyethylene and polypropylene polymer matrix that provides the strength of the obtained polymer composite, which is very valuable for practical application.

synthesis, structure, properties, and application Berlin: Springer-Verlag 464 p

- [5] D'yachkov P N 2010 *Electron properties and application of carbon nanotube*, Moscow : BINOM 488 p
- [6] Wang C, Guo Z-X, Fu S, Wu W, Zhu D 2004 *Polymers containing fullerene or carbon nanotube structures* *Prog. Polym. Sci.* **29** 1079–141
- [7] Khabashesku V N, Barrera E V, Lobo M R F 2007 *Current Research on Nanotechnology* **1**(2) 165-82
- [8] Janovskij Ju G, Kozlov G V, Burja A I, Lipatov Ju S *Fizicheskaja*

mezomehanika 10(6) 63-7

- [9] Coleman J N, Khan U, Blau W J, Gun'ko Y K 2006 Small but strong: A review of the mechanical properties of carbon nanotube-polymer composites *Carbon* 44(9) 1624-52
- [10] Carey J B, PrabirPatra K, Ci Lijie, Glaura Silva G., and Pulickel Ajayan

M 2011 Observation of Dynamic Strain Hardening in Polymer Nanocomposites *ACS Nano* 5(4) 2715-22

- [11] Koch W, Holthausen M 2002 *A Chemist's Guide to Density Functional Theory* Weinheim: Wiley-VCH. 19 p

Authors	
	<p>Irina Zaporotzkova, 12.11.1963, Melitopol, Ukraine</p> <p>Current position, grades: professor, Doctor of Physical and Mathematical Sciences University studies: Volgograd State University, Molecular physics, Solid State Physics Scientific interest: nanotechnology, boron-carbon nonmaterial, nanocomposites. Publications: 326 publications Recent main: [1] Zaporotzkova I V, Boroznin S V, Boroznina E V, Polikarpov D I 2013 Vacancy Transport Properties in Boron-Carbon BC3 nanotubes <i>Nanoscience and Nanotechnology Letters</i> 5 (11) 1164-8 [2] Zaporotzkova I V, Polikarpova N P, Ermakova T A, Polikarpov D I 2013 Carbon Nanotubes, New Material for Purification of Water-Ethanol Mixtures from Isomers of Propanol <i>Russian Journal of General Chemistry</i> 83(8) 1601-6 [3] Zaporotzkova I V, Anikeev N A, Kojitov L V, Davletova O A, Popkova A V 2014 Theoretical Studies of the Structure of the Metal-carbon Composites on the Base of Acryle-nitrile Nanopolimer <i>Journal of nano- and electronic physics</i> 6(3) 03035-1 - 03035-3 Experience: since 2008 - the managing editor of the journal "Bulletin of the Volga. Series 10: Innovation activities; since 2007 - the head of Research and Education Center VolSU "Nanomaterials and Nanotechnologies", repeatedly participated in conferences, symposiums, forums and academic seminars of national and international level.</p>
	<p>Aleksej Krutoyarov, 31.03.1986</p> <p>Current position, grades: assistant of professor University studies: Volgograd State University, Department of Physics and Telecommunications. Molecular physics practice Scientific interest: nanotechnology, sensor activity of nanostructures, quantum-chemistry calculations. Publications: 20 Main: [1] Krutoyarov A A, Zaporotzkova I V 2013 About adsorption of polyethylene monomer unit on the single-walled carbon nanotube surface <i>Nanoscience & nanotechnology</i> 2013 14th International Workshop on Nanotechnology, 30 September – 4 October 2013 Frascati National Laboratories INFN <i>Book of abstract</i> 82 [2] Krutoyarov A A, Elbakyn L S, Zaporotzkova I V 2013 About adsorption of the polyethylene monomer unit on the single-walled carbon nanotube surface <i>International Conference Advanced carbon Nanostructures ACNS'2013</i> July 01-05 2013 St-Petersburg Russia <i>Book of Abstracts</i> 2.17 [3] Krutoyarov A, Elbakyan L, Zaporotzkova I V 2013 About adsorption of the polyethylene monomer unit on the single-walled carbon nanotubes surface <i>European Polymer Congress EPF 2013 Pisa (Italy)</i> 16 – 21 June 2013 <i>Book of Abstracts</i> 3-6 Experience: graduated in 2008, the Department of Physics and Telecommunications Volgograd State University with a degree in radio physics and electronics, in 2009 entered the correspondence department graduate of Volgograd State University, majoring in 01.04.17 - the chemical physics, combustion and explosion physics of extreme states of matter. Since 2012 he has been working as an assistant of the department of forensic and physical materials. In 2011/2012, participated in the implementation of the grant for young scientists of the Volga. He has more than 20 scientific publications. In 2009 he was awarded a first degree at the National Youth Exhibition-contest of applied research, inventions and innovations for the project "The technology of composite materials based on carbon nanotubes."</p>
	<p>Natalia Polikarpova, 11.03.1989, Volgograd, Russian Federation</p> <p>Current position, grades: associate professor, PhD University studies: Volgograd State University, Spectroscopy Scientific interest: nanotechnology, sensor activity of nanostructures, quantum-chemistry calculations. Publications: 47 Main: [1] Zaporotzkova I V, Boroznin S V, Boroznina E V, Polikarpova N P 2014 Boron-carbon Nanotube Modification Using Alkaline Metal Atoms <i>Journal of nano- and electronic physics</i> 6(3) 03006-1 – 03006-2. [2] Polikarpova N P, Vilkeeva D E, Polikarpov D I, Zaporotzkova I V 2014 Sensor properties of carboxyl-modifies carbon nanotubes <i>Nanosystems: physics, chemistry, mathematics</i> 5(1) 101-6 [3] Polikarpova N. P., Vil'keeva D. E., Zaporotzkova I V 2013 Sensor Activity of Carbon Nanotubes with a Boundary Functional Group <i>Nanoscience and Nanotechnology Letters</i> 5(11) 1169-73 Experience: Has 47 scientific publications, including 4 articles in journals included in the Scopus database. In defended her thesis on "SENSORY PROPERTIES OF SEMICONDUCTOR Nanotubular SYSTEM "(2013), takes part in the grant of Ministry of Education 'Study of the structure, physical, chemical and dynamical properties of nanostructures'</p>

Superfine drug-eluting polyvinylpyrrolidone based coating for biliary stents

I V Zaporotskova*, R V Shinkarev

Volgograd State University, Volgograd, 400062, Universitetskii prospect, 100

*Corresponding author's e-mail: irinazaporotskova@gmail.com

Received 15 October 2014, www.cmnt.lv

Abstract

The paper describes a chemical method for the fabrication of superfine polyvinylpyrrolidone based coating for doxorubicin-eluting polymer biliary stents. The optimal conditions for the fabrication were defined and the effectiveness of the coating when exposed to bile in static conditions was proved. The study found that the obtained drug-eluting coating reduces the process of bile crystallization on the sample polymer stent surface. The mechanism of "PVP- doxorubicin" stable adsorption complex formation was studied using quantum - chemical method DFT. A number of positions of doxorubicin molecule in respect to polyvinylpyrrolidone fragment were analyzed, and the basic characteristics of adsorption processes were defined. It was found that energetically more favorable interaction occurs via the doxorubicin molecule oxy group.

Keywords: biliary stents, N-vinylpyrrolidone, polyvidone, doxorubicin, crystallization process, adsorption, semi-empirical scheme DFT.

1 Introduction

Stenting as a method for treating narrow or weak arteries by placing inside metallic tubes was first implemented about fifty years ago [1, 2]. Currently, as many as four hundred types of stents made of various materials are applied in medicine. They differ from one another in length, design and surface coating that comes in contact with bodily fluids [3, 4]. Apart from being intensively used in the treatment of coronary heart disease, stents are universally required to recover natural passages in the body such as the biliary tract and ureter. For this particular purpose, stents made of plastic (polyethylene, PVC) are used [5]. These so-called biliary stents counteract disease-induced flow restrictions caused by stones or malignant tumors or help to ensure the passage of stones or drainage after surgery or injury [6-8]. However, the efficiency of stents can seriously decline in case infection sets in or salts build up on the stent surface [9]. To eliminate the possible negative effects an effective coating is required that when applied on the stent surface will ensure high concentration of bactericidal medication, prevent the buildup of salts and stones and provide systemic treating effects while the stent releases drug into the body [10-12]. At present, drug-eluting stents are considered to be a most important tool of treatment. When combined with modern medical therapy they enable to quickly, efficiently and safely eliminate disease-induced symptoms. That is why a demand for a broader range of possible drug carriers that prolong drug release and possess additional antibacterial properties increases and the development of new simple and inexpensive methods to apply coating on the surface of polymer stents seems to be vital.

In this paper we describe a new method to prepare thin film coating that is based on a well-known antioxidant polymeric substance N- vinylpyrrolidone made from the monomer polyvinylpyrrolidone (PVP or polyvidone) [13-16]. As a drug to saturate the polymeric coating applied on the biliary stent surface we chose doxorubicin [17, 18]. As drug carrier

we chose PVP because it has a number of valuable characteristics, namely non-toxicity, solubility in most organic solvents and water, good adhesive properties and high tendency to form compounds [19].

We have designed a technique that can be used to apply drug-releasing thin film coating on biliary stents. The experimental results are reinforced by theoretical quantum-chemical calculations for the interaction processes between the coating components (PVP and doxorubicin). The theoretical data turned out to be in good agreement with the obtained experimental results.

2 Experimental studies of possibility for application of superfine drug coating on the biliary stent surface

A biliary stent represents a polymer sample in the shape of a flexible cylinder made from polyurethane. For application of drug coating on the biliary stent surface an aqueous solution was prepared, which is a complex of drug and polymer that acts as a carrier for the drug substance. The solution of «PVP + doxorubicin» was applied on the biliary stent surface by chemical means and formed the expected drug coating. Polyvidone (PVP) can be described as a mixture of linear amorphous polymers with varying degrees of viscosity. PVP is a yellow-white or white hygroscopic powder with a faint characteristic odor, it becomes soft at a temperature of 140° –160° C. The substance is soluble in water, alcohol, concentrated and diluted mineral acids, aromatic hydrocarbons. The polyvidone (C₆H₉NO)_n macromolecule structure is shown in Figure 1.

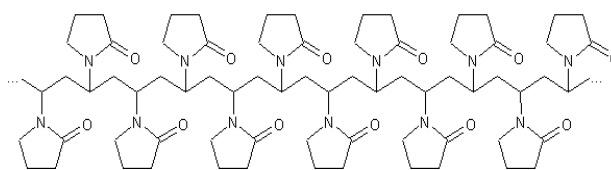


FIGURE 1 Polyvidone macromolecule structure

The choice of polyvidone as substance carrier was determined by the following reasons. The electronic nature of the PVP functional groups (fragments of the macromolecule) provides this polymer with a number of unique features that ensure its wide application in industry and medicine. It is characterized by high absorption capacity and tendency to form compounds. This property of polyvidone to bind to many substances (low molecular compounds) including drugs, dyes, etc., is used in medical practice to prolong the effect of drugs and remove disease-causing toxins from the body of humans and animals [13-16]. Polyvidone does not display any effect on the body, since it cannot be split by enzymes and it passes unchanged through the kidneys [15]. When binding to substances of protein origin including toxins, products of tissue decomposition, products of bacterial origin, PVP forms compounds that can easily pass through the kidneys. But for polyvidone these organic compounds would have accumulated in the body. Polyvidone based compounds help to normalize permeability of cell membranes and restore electrolyte composition. As a result, the liver and kidneys regain their normal functions, enzymatic processes as well as protein synthesis restore, etc. [16].

Doxorubicin (gross formula $C_{27}H_{29}NO_{11}$) (Figure 2) is a crystalline or amorphous orange-red or red powder. The substance solves well in water, aqueous acids, acetone, butanol, chloroform. Doxorubicin is used as a chemotherapy drug in the treatment of certain cancers [17].

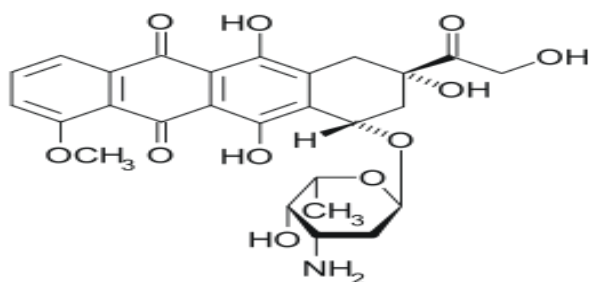
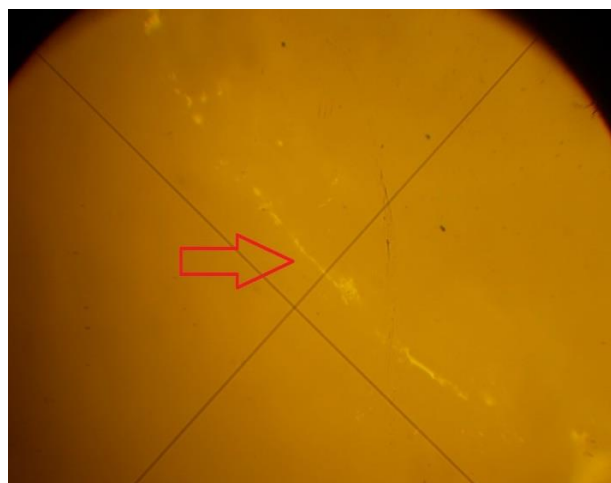


FIGURE 2 Doxorubicin formula

The application of drug coating on the polyurethane stent surface was performed as follows. Firstly, 50% aqueous polyvidone solution was prepared. Full dissolution of the required concentration of PVP in water required 24 hours. The obtained solution had a yellow color and sufficient viscosity that allowed it to mount well on the polyurethane sample surface. We also prepared another solution of the same polyvidone concentration, but this time we added doxorubicin into the solution in an amount of 8.5 % of the total volume. On thorough mixing and complete dissolving of the substances in water we obtained a bright orange color solution. Further, we degreased a biliary stent surface by placing it in a solvent (acetone) for 30 minutes and then chemically applied coating by placing the stent in each of the prepared solutions. The dwell time of the stent in the solution was 24 hours. After being dried, the coated samples were examined under an optical microscope with magnification 100 x. Analysis of the images (Figure 3) allowed us to determine the coating thickness, which turned out to be equal to 0.03 mm.



a)



b)

FIGURE 3 Fragments of the polymer stent with drug coating: a) 50%-PVP solution, b) 50%-PVP solution + 8,5% doxorubicin; (magnification x100)

The next stage of the experiment was to test the effectiveness of the obtained biliary stent drug coating by exposure to bile. According to the fundamental research by K. Juniper that studied the bile elements it was found that the main ones that play a decisive role in the crystallization process, are cholesterol (CH), calcium carbonate (CC), calcium bilirubinate (BC) crystals, or a combination of them [20-22]. The study of bile by using polarized light microscopy showed that it can undergo a multi stage crystallization process. Homogeneous micellar solution is an evenly spread dark field. In polarized light the crystals form optical shapes – textures that have various shapes depending on the phase and type of crystal [17]. Taking into consideration these data, we conducted an experiment to test possibility to reduce the intensity of bile crystallization on the biliary stent surface by means of “PVP + doxorubicin” complex coating application.

The experiment was conducted in three stages. First, the clean polymer stent was placed in a vessel filled with bile for 24 hours and after being removed from the bile the sample was immediately examined in polarized light by microscope MIKMED -5. The images captured show that in polarized

light crystals are well observable whereas other (non-crystalline) elements are not visible, which eliminates errors in the identification of the observed objects. The obtained photographs of the sample are presented in Figure 4. Crystallization began about 4-5 minutes later after the sample had been removed from the bile. Further, we studied bile crystallization process on the stent with PVP based coating. It was found that crystallization process started six-seven minutes later after the stent had been removed from the vessel with bile. Finally, a study of the bile crystallization process on the stent surface coated with "PVP + Doxorubicin" complex was conducted. The sample stent coated with drug under study was placed in a vessel with bile for 24 hours, then removed and immediately studied under a microscope. The obtained pictures are shown in Figure 5. The process of crystallization began in 18-20 minutes after we had removed the sample from the bile. That is, the time interval until the onset of crystallization increased approximately 3-fold. The observation showed that the crystals on the surface of the drug-eluting stent were substantially smaller in size.

Then, we estimated the size of crystallization area at magnification 100 x that took place 5 minutes later after the stents under study had been removed from the vessel with

bile and compared the one in all the three cases: 1) on the surface of the clean stent, 2) on the stent surface with PVP based coating, 3) on the stent surface with "PVP + doxorubicin" complex coating. The observations showed that the surface of the clean stent in the time interval of 5 minutes was found to be 100 % covered in crystals. In the case with PVP based coated stent as much as 80 % of the surface area was estimated to be crystallized whereas the stent coated with «PVP + doxorubicin» complex displayed no signs of crystallization process.

Thus, we empirically tested that application of coating on the biliary stent is possible by chemical method when certain conditions are observed. In the course of this experiment, we found optimal proportions of polyvidone, water and doxorubicin volumes to produce the most stable coating. The effectiveness of coating was tested under exposure to bile, and it was found that the empirically obtained coating reduces bile crystallization processes on the sample surface. Resistance of the coating that provides uniform dissolution of doxorubicin and enables its prolonged effect due to which long-term presence of the drug in the body is possible was tested. This prolonged action is much more effective as compared to a doxorubicin injection on the daily basis.

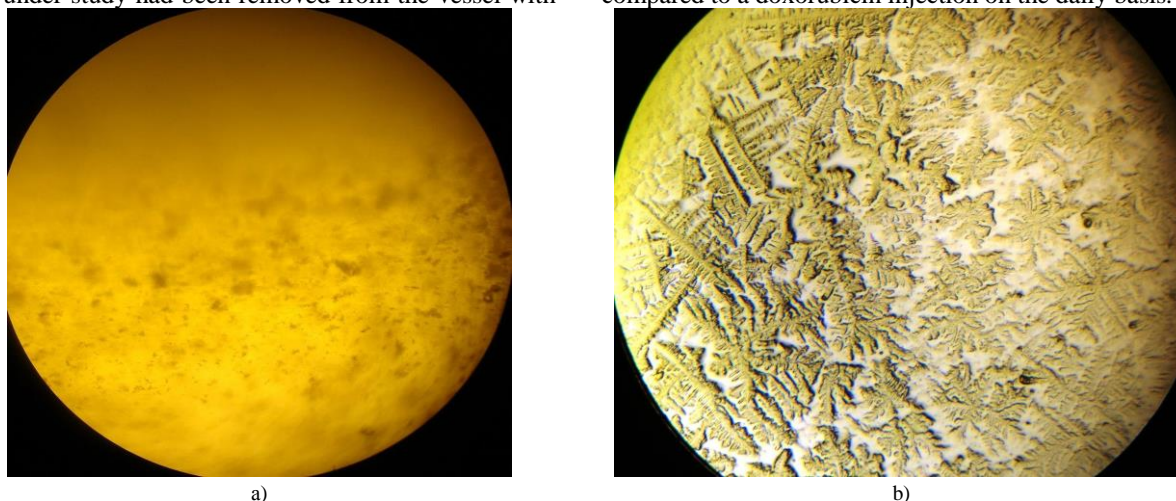


FIGURE 4 A fragment of the clean stent before the onset of bile crystallization process on its surface (a) and a fragment of the stent five minutes later it had been removed from the bile (b)

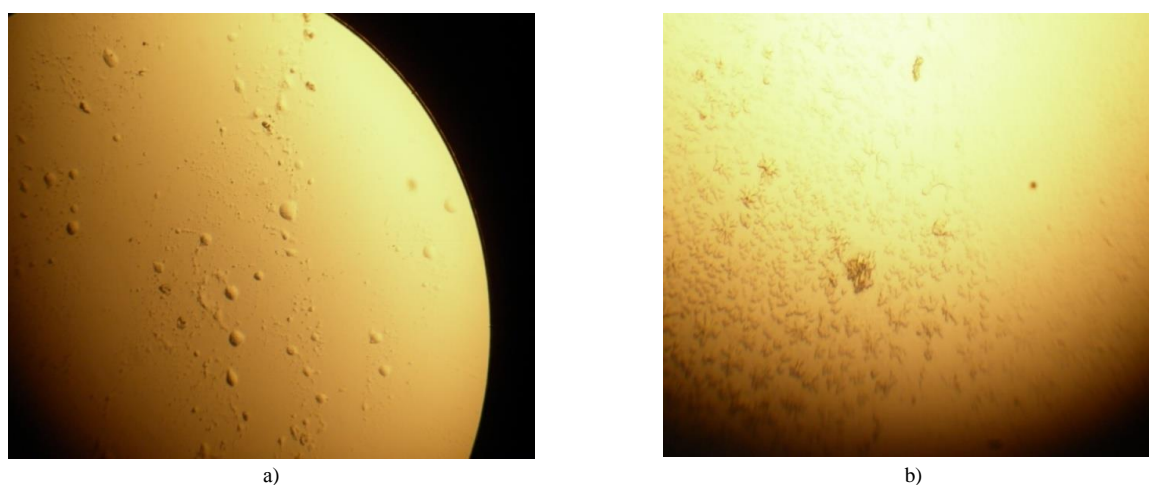


FIGURE 5 A fragment of the stent coated with "PVP + Doxorubicin" complex before the onset of bile crystallization process on its surface (a) and a fragment of the stent five minutes later (b)

3 Quantum chemical study of the interaction between PVP macro- molecules and doxorubicin molecules

We studied the interaction mechanism between polyvidone and doxorubicin and performed calculations of the interaction process in the framework of quantum-chemical method DFT (density functional theory) using B3LYP functional [23]. To describe the polymer PVP a molecular cluster consisting of three monomers N-vinylpyrrolidone was modeled.

It is known that one of the most important properties of PVP is the ability to form stable complexes with phenolic compounds due to the formation of a hydrogen bond between the functional group of polyvidone $>N-C=O$ and the oxy group of polyphenol molecule. In the structure of doxorubicin molecule five oxy groups can be identified. Taking this fact into consideration, we selected hydrogen atoms belonging to these groups as possible active adsorption centers. In Figure 6 they are numbered 1 – 5.

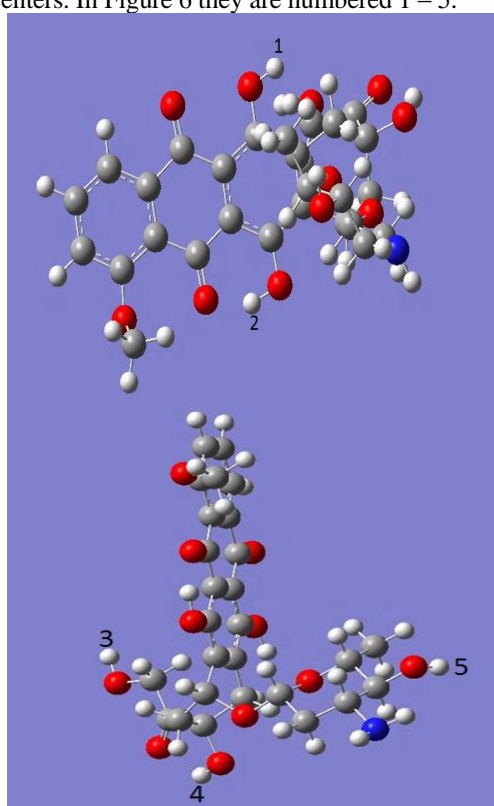
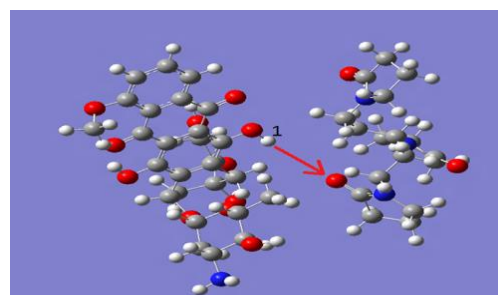


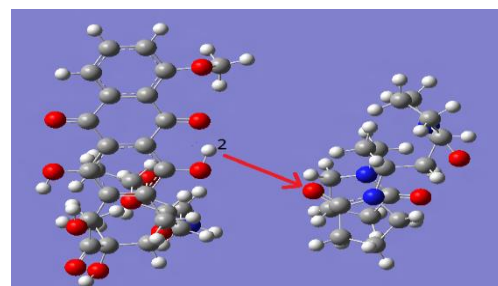
FIGURE 6 Possible adsorption centres of a doxorubicin molecule

We considered several positions of a doxorubicin molecule in respect to the fragment of PVP shown in Figure 7. As the figure shows interaction takes place at the doxorubicin active centre – the hydrogen atom of the oxy groups: a) adsorption center 1; b) adsorption center 2; c) adsorption center 3; d) adsorption center 4; e) adsorption center 5.

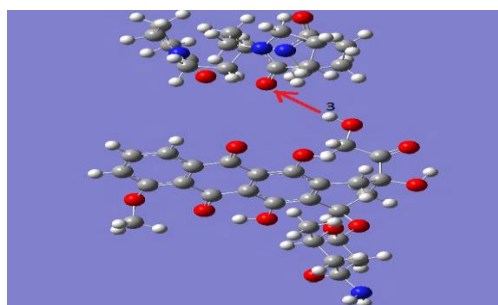
The adsorption process was modeled in increments of 0.1 \AA of doxorubicin molecule to a fragment of Polyvidone macromolecule. The calculations allowed us to construct energy curves of these processes (Figure 8). The chart analysis showed that each of the three curves (variants 1, 4, 5) has an energy minimum that indicates the case of adsorption. The rest of the positions studied (namely, variants 2 and 3) correspond to the unstable state of the system since the minimum is located in the range of positive energies.



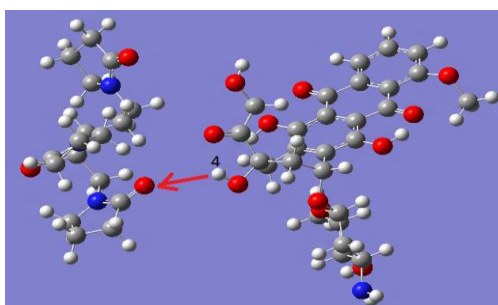
a)



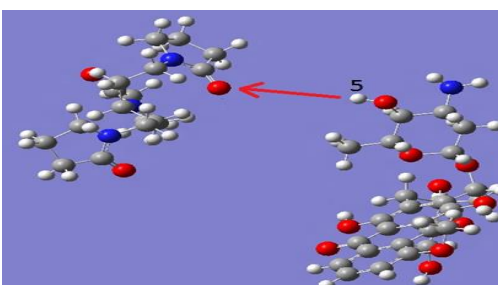
b)



c)



d)



e)

FIGURE 7 The process of doxorubicin molecule approaching an O atom of the PVP molecule; interaction takes place via the active centre of doxorubicin – H atom of the oxy group: a) adsorption center 1; b) adsorption center 2; c) adsorption center 3; d) adsorption center 4; e) adsorption centre 5

The curves show that energetically more favorable interaction is observed in variant 5 (Table 2, Figure 10) where adsorption energy $E_{ads} = -0.57$ eV, which corresponds to theoretically obtained values of hydrogen bond energy and indicates the formation of the most stable structure. The main characteristics of doxorubicin and PVP interaction process are shown in Table 1.

The obtained values of the main characteristics of the interaction determine the possibility of fairly easy desorption of doxorubicin from PVP and its gradual release into the body thus providing a long-term medical effect.

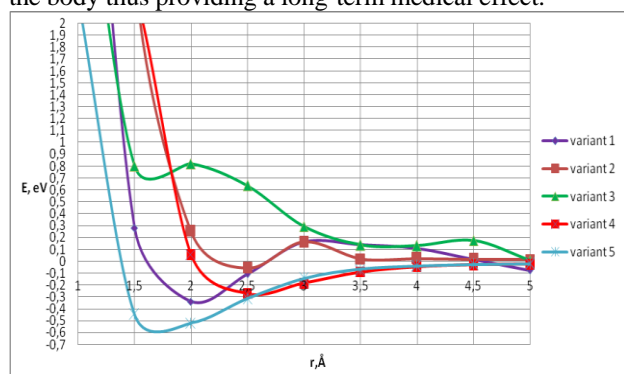


FIGURE 8 The dependence of doxorubicin and polyvidone macromolecules interaction energy values on a distance

TABLE 1 The main characteristics of PVP and doxorubicin interaction process for different positions: r_{ads} , Å – adsorption distance, E_{ads} , eV – adsorption energy

Variants	r_{ads} , Å	E_{ads} , eV
1	2.1	-0.34
2	-	-
3	-	-
4	2.6	-0.28
5	1.7	-0.57



4 Conclusions

We proposed a method for preparing drug-eluting coating for polymeric stent surface, namely, we experimentally found optimal proportions of polyvidone, water and doxorubicin volumes to produce the most sustainable coating, and we tested the coating efficiency under exposure to bile in static conditions. We found that the obtained coating reduces the process of bile crystallization on the sample surface.

We proposed and studied theoretically a plausible stable adsorption complex “PVP doxorubicin” formation mechanism that can be used as effective coating enabling prolonged release of drug into the body. We analyzed a number of positions of doxorubicin molecule with respect to polyvidone in the interaction process and calculated the main characteristics of adsorption processes. We found that energetically more favorable variant is the one where interaction takes place via the oxy group in a doxorubicin molecule. The obtained values of distance and adsorption energy indicate the possibility of a gradual release of doxorubicin into the body when it desorbs from PVP.

References

- [1] Kalesan B, Pilgrim T, Heinimann K et al 2012 Comparison of drug-eluting stents with bare metal stents in patients with ST-segment elevation myocardial infarction *European Heart Journal* **33**(8) 977–87
- [2] Cook S, Eshtehardi P, Kalesan B 2012 Impact of incomplete stent apposition on long-term clinical outcome after drug-eluting stent implantation *European Heart Journal* **33**(11) 1334–43
- [3] Stone G W, Moses J W, Ellis S G et al 2007 Safety and efficacy of sirolimus and paclitaxel-eluting coronary stents *N. Engl. J. Med.* **356** 998–1008
- [4] Patel M R, Holmes D R Jr 2008 Next-Generation Drug-Eluting Stents: A Spirited Step Forward or More of the Same *JAMA* **299**(16) 1952–3
- [5] *Varianty biliarnyh stentov* [Types of biliary stents] URL: <http://amberlife.com.ua>
- [6] Il'chenko A A 2004 *Zhelchnokamennaja bolezn'* [Cholelithiasis] Moscow: Anaharsis [Anacharsis] 199 p
- [7] Kulikovskij V F, Soloshenko A V, Jarosh A L et al 2013 *Biliarnyj stent s almazopodobnym uglerodnym pokrytiem* [Diamond-like carbon coated biliary stent] *Jendoskopicheskaja hirurgija* [Endoscopic surgery] **19**(3) 16–20
- [8] Zabolotnyj V T, Kolmakov A G, Sevost'janov M A, et al 2013 *Sovershenstvovanie medicinskih izdelij dlja jendovaskuljarnyh operacij* [Improvement of medical devices for endovascular operations] Moscow: Integral (3) 42–5
- [9] *Vmeshatel'stva na zhelchevyvodjashhih putjah* [Biliary tract invasions] URL: <http://www.rusmedserv.com/radiology/biliary-interventions/>
- [10] Cai X B, Zhang W X, Wan X J et al 2014 The effect of a novel drug-eluting plastic stent on biliary stone dissolution in an ex vivo bile perfusion model *Gastrointestinal Endoscopy* **49**(1) 156–62
- [11] Lee Dong Ki 2009 Drug-eluting stent in malignant biliary obstruction *Journal of Hepato-Biliary-Pancreatic Surgery* **16**(5) 628–30
- [12] Windecker S, Juni P 2009 The Drug-Eluting Stent Saga *Circulation* **119**(5) 53–56
- [13] Kirsh Yu E 1998 *Poli-N-vinilpirrolidon i drugiye poli-N-vinilamidy* [Poly-N-vinylpyrrolidone and other poly-N-vinylamides] – Moscow: Nauka 252 p (in Russian)
- [14] Sidel'kovskaja F P 1970 *Himija N-vinilpirrolidona i ego polimerov* [Chemical properties of vinylpyrrolidone and its polymers] – Moscow: Nauka 160 p
- [15] *N-vinilpirrolidon* 2014 *Bol'shaja jenciklopedija nefti i gaza* [Encyclopedia of Oil and Gas] URL: <http://www.ngpedia.ru/id658762p1.html>
- [16] *Polivinilpirrolidon* 2014 *Farmmedhim* URL: <http://fmchem.ru/catalog/115>
- [17] *Doksorubicin* 2014 *Reestr lekarstvennyh sredstv* [The register of drugs] <http://www.reles.ru/cat/drugs/Doxorubicin/>
- [18] D'yachkov E P, D'yachkov P N, Zhdanov R I 2011 Vzaimodejstvie odnostennnyh nanotrubok s doksorubicinom i poliehtilenglikolem po dannym metoda molekulyarnogo dokinga [Interaction of single-walled nanotubes with doxorubicin and polyethylene glycol from data of molecular docking method] *Doklady Akademii Nauk* [Academy of Sciences reports] **437**(4) 1–3
- [19] Gao Y, Jiang P, Liu D F et al 2004 Evidence for the monolayer assembly of poly(vinylpyrrolidone) on the surfaces of silver nanowires *J. Phys. Chem. B* **108**(34) 12877–881
- [20] Juniper K, Burson N 1954 Peculiar crystals occurring in bile and associated with biliary tract disease *Clin. Res. Proc.* **2** 153–41
- [21] Juniper K, Burson E N 1957 Biliary tract studies. The significance of biliary crystals *Gastroenterology* **32** 175–211
- [22] Juniper K, Woolf W E 1956 Biliary tract studies. X-ray diffraction analysis of gallstones, correlation with occurrence of microspheroliths in bile *Am. J. Med.* **20** 385–591
- [23] Koch W A 2002 *Chemist's Guide to Density Functional Theory* eds W Koch and M Holthausen Weinheim: Wiley-VCH, 19–28

Authors	
	<p>Irina Zaporotskova, 12.11.1963, Melitopol, Ukraine</p> <p>Current position, grades: professor, Doctor of Physical and Mathematical Sciences University studies: Volgograd State University, Molecular physics, Solid State Physics Scientific interest: nanotechnology, boron-carbon nonmaterial, nanocomposites. Publications: 326 publications Recent main: [1] Zaporotskova I V, Boroznin S V, Boroznina E V, Polikarpov D I 2013 Vacancy Transport Properties in Boron–Carbon BC3 nanotubes <i>Nanoscience and Nanotechnology Letters</i> 5 (11) 1164-8 [2] Zaporotskova I V, Polikarpova N P, Ermakova T A, Polikarpov D I 2013 Carbon Nanotubes, New Material for Purification of Water–Ethanol Mixtures from Isomers of Propanol <i>Russian Journal of General Chemistry</i> 83(8) 1601–6 [3] Zaporotskova I V, Anikeev N A, Kojitov L V, Davletova O A, Popkova A V 2014 Theoretical Studies of the Structure of the Metal-carbon Composites on the Base of Acryle-nitrile Nanopolimer <i>Journal of nano- and electronic physics</i> 6(3) 03035-1 - 03035-3 Experience: since 2008 - the managing editor of the journal "Bulletin of the Volga. Series 10: Innovation activities"; since 2007 - the head of Research and Education Center VolSU "Nanomaterials and Nanotechnologies", repeatedly participated in conferences, symposiums, forums and academic seminars of national and international level.</p>
	<p>Roman Shinkarev, 05.06.90, Kamyshin, Russia</p> <p>Current position, grades: Assistant, postgraduate student University studies: Volgograd State University 2013, Nanotechnology Scientific interest: X-ray analysis, nanotechnologies in medicine, computer modeling of nanosystems. Publications: [1] Zaporotskova I V, Shinkarev R V 2014 The superfine covering on base of polyvinylpyrrolidone for MEDICAL stents 5 <i>International Conference on NANO-structures Self-Assembly (NanoSEA 2014)</i> France Marseille 7 – 11 June 2014 <i>Book of abstract</i> 202 [2] Zaporotskova I V, Shinkarev R V 2013 The new medicinal superfine covering on base of polyvinilpirrolidone for biliary stents <i>Nanoscience & nanotechnology</i> 2013 14th International Workshop on Nanotechnology, 30 September – 4 October 2013 Frascati National Laboratories INFN <i>Book of abstract</i> 83-5 Experience: Currently - postgraduate student on "Condensed Matter Physics", several publications in Russian and foreign journals, won regional competition of innovative projects "UMNIK-2014"(2014)</p>

Theory of near-field detection of core-gold nanoshells inside biosystems

M D'Acunto^{1, 2, 3*}, A Cricenti¹, M Luce¹, S Dinarelli¹

¹Istituto di Struttura della Materia, Consiglio Nazionale delle Ricerche, ISM-CNR, via Fosso del cavaliere, 100, I-00133, Roma, Italy

²Istituto di Scienza e Tecnologie dell'Informazione, Consiglio Nazionale delle Ricerche, ISTI-CNR, via Moruzzi 1, I-56124, Pisa, Italy

³NanoICT laboratory, Area della Ricerca CNR, Pisa, Italy

*Corresponding author: mario.dacunto@ism.cnr.it

Received 1 March 2015, www.cmmt.lv

Abstract

Metal nanoshells composed by a dielectric core with a thin gold layer are stimulating growing interests due to the unique optical, electric and magnetic properties exhibited by the local field enhancement near the metal – dielectric core interface due to strong local plasmon resonance and the high tunability of such resonance as a function of shape and core-material. These unique characteristics have found promising applications in a wide range of areas, such as biosensing, optical communication and medicine. In this paper, we developed a theoretical and numerical simulation based on a near-field approach to study the possibility to identify nanoshells inside mouse cells. Taking advantage from the characteristic near-infrared transparency window of many biological systems, i.e. the low light absorption coefficient of biological systems between 750-1100nm, we show the possibility to identify and detect 100-150nm diameter gold nanoshells inside the animal cells.

Keywords: Gold nanoshells, Mie theory, SNOM, animal cells, Near-infrared

1 Introduction. General requirements for sensing activity in biosystems

With recent advances in material synthesis and fabrication, metal nanoparticles have received considerable attention over the last decade [1-2]. Metallic nanoparticles when excited with an electromagnetic field, produce an intense absorption normally recognized as due to the collective oscillation of plasmon electrons on the particle surface. The resonance frequency is highly dependent on particle size, shape, material, and environment medium. Within the class of metallic nanoparticles, metal nanoshells stimulated the highest interest due to their remarkable optical properties [3-4]. Metal nanoshells are a type of nanoparticle composed of a non-metallic core and a metallic coating. Analogously to metal colloids, they show selective absorption peaks at specific wavelengths due to surface plasmon resonance. In addition, unlike bare metal colloids, the wavelengths, at which such resonance occurs can be tuned by changing the core radius or coating thickness or particle shape. Due to such relevant properties, metal nanoshell particles find one main application in medicine, where it is supposed that nanoshells with absorption peaks in the near-infrared can be attached to cancerous tumors and hence excited by a laser for heating them up and so killing the tumors cells [5-6]. The optical properties of such nanoshells in the near infrared (NIR) range is particularly important when they are used in biological systems because a certain range of wavelengths (700–1000nm), also called as *tissue transparency window*, is of special interest for in-depth cell investigations, thus making the NIR spectral range most convenient for a tailored instrumentation to look beneath the limits of visible outreach [7]. Even though NIR photons can travel farther than their shorter wavelength due to longer free path in the

matter, they become elastically scattered which makes direct microscopy impossible beyond the depth of several hundred microns. However, thanks to the higher transmittance rate, this spectral range allows for a number of image reconstruction techniques to re-build the original or close to original picture out of backscattered and dispersed non-ballistic photons.

In this paper we developed a theoretical and numerical simulation based on the near-field Mie theory to study the possibility to identify nanoshells inside animal cells. Taking advantage from the characteristic near-infrared transparency window of many biological systems, i.e. the low light absorption coefficient of biological systems between 750-1100nm, we were able to identify the 100-150nm diameter gold nanoshells inside the animal cells.

2 Far-to-near field quantitative Mie theory

In a system composed by a biological component like a cell and a population of metal nanoshell, the calculations of near field optical response must be reported accurately. The far-field response of a single nanoparticle with a diameter falling in the range 50-200nm can be calculated using the Mie theory [8]. Nevertheless, the near-field response require a supplemental work, stimulated recently by the rapid development in various fields, such as high spatial resolution of SNOM, single-molecule spectroscopy by surface-enhanced Raman scattering, nanodevices based on surface-plasmon photonic forces and quantum-optical processes in photonic crystals [9-12]. In all such fields, the calculation of the near field on ensembles of nanoparticles is a fundamental theoretical challenge. When the nanoparticles can be simplified to spheres, the analytical solution to the light scattering can

be obtained by extending the Mie theory. In a far-field treatment, one can consider at once to obtain a super-matrix, the so called T-matrix. T-matrix works well for far-field calculations of extinction-scattering-absorption spectra. However, for calculations of near field, this method fails due to irregular nanoparticles shape or induces mistakes due to nanoparticles aggregates of more than two particles. Because the entanglement of particles increases the size of the scattering matrix tremendous making difficult to manage accurate calculations with T-matrix. Another treatment is based on orders of scattering, which consist of a sum of simple scattering events from single particles in which the boundary conditions are considered in each scattering event. The core-shell particle is schematically described in figure 1(a) and the experimental system to detect a nanoshell inside a volume of dielectric constant ϵ_3 (in our case, the animal cell dielectric constant).

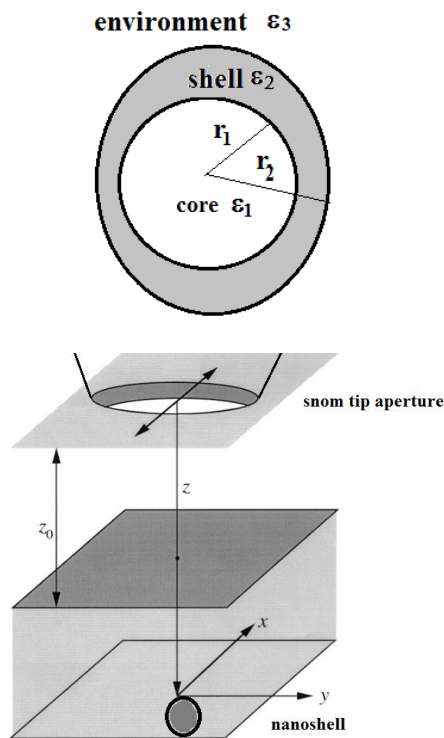


FIGURE 1 (upper) Schematic sketch of a nanoshell. The dielectric core of radius r_1 and the dielectric constant ϵ_1 forms the core region. The core is coated with a gold shell layer of thickness r_2-r_1 and the dielectric function ϵ_2 and the shell forms the region 2. Finally, an embedding medium of dielectric constant ϵ_3 forms the third region, usually named the environment, in our paper, the environment is the air or the cell. (lower) The schematic sketch of the spatial dimensions of a SNOM aperture system. Note that the dimension of the SNOM aperture (normally 50nm diameter) is not in scale with the nanoshell dimension taken in consideration in this paper (100-150nm diameter).

For a satisfactory identification of nanoshells inside a biosystem using a NIR transparency window, we need to develop a near field treatment of gold nanoshell. Following the approach of Stratton, we solve the Maxwell's equations for incident fields as time-harmonic, with an $\exp(-i\omega t)$ dependence so that a vector basis function formalism can be used [13-15]. In a linear, isotropic medium, with no external sources and no divergence of the electric field, the general

diffraction equation takes on the form of the vector Helmholtz equation

$$\nabla \times \nabla \times \mathbf{E} - \omega^2 \mu \epsilon \mathbf{E} = 0 \quad (1)$$

where ω is the angular frequency and ϵ is the dielectric function and μ the magnetic permeability. This equation describes the propagation of scalar waves in a medium. Introducing a scalar generating function ψ , eq. 1 can be written as

$$\nabla^2 \psi(\mathbf{r}, t) + k^2 \psi(\mathbf{r}, t) = 0 \quad (2)$$

The e.m. fields of the incident wave, scattered wave, and the wave inside the particle can in general, be written as a series expansion of the spherical harmonics basis vectors (\mathbf{M} , \mathbf{N} , \mathbf{L}) [13-15]. \mathbf{M} , \mathbf{N} , and \mathbf{L} can be constructed as follows

$$\mathbf{M} = \nabla \times (\mathbf{c}\psi), \quad \mathbf{N} = (\nabla \times \mathbf{M}) / k, \quad \mathbf{L} = \nabla \psi \quad (3)$$

where \mathbf{c} is an arbitrarily constant vector and $k^2 = \omega^2 \epsilon \mu$ is the wave-number of the electromagnetic wave. Due to the required orthogonality and completeness of such basis, we can write the electric or magnetic field as a series of the spherical vector basis functions

$$\mathbf{E} = \sum_{mn} \{ a_{mn} \mathbf{M}_{mn} + b_{mn} \mathbf{N}_{mn} + c_{mn} \mathbf{L}_{mn} \} \quad (4)$$

The field is completely defined by the coefficients (a_{mn} , b_{mn} , c_{mn}), and if the divergence is assumed to be zero, the coefficients c_{mn} can be considered zero, so that the contribution to the field is given only by \mathbf{M} and \mathbf{N} .

For light scattering from a nanoshell, the electromagnetic fields must satisfy Maxwell's boundary conditions at each layer boundary of the interfaces sketched in figure 1. At the interface between penetrable materials such as dielectrics and metals with finite conductivity, the tangent components of the electromagnetic fields are continuous, i.e. the fields are subject to the boundary conditions:

$$\hat{\mathbf{n}}(s) \times \mathbf{E}_{s^-} = \hat{\mathbf{n}}(s) \times \mathbf{E}_{s^+} \quad \text{and}$$

$\hat{\mathbf{n}}(s) \times \mathbf{H}_{s^-} = \hat{\mathbf{n}}(s) \times \mathbf{H}_{s^+}$, where s is a point on the surface and s^- and s^+ are the points just inside or out the sphere, respectively.

For a spherical nanoshell with the plane wave incident field defined in equation 2, the electric fields can be expressed as a series of the vector harmonics in the 3 regions as

$$\mathbf{E}_1 = \sum_{n=1}^{\infty} \left\{ a_{\pm 1n}^{(1)j} \mathbf{M}_{\pm 1n}^{(1)j} + b_{\pm 1n}^{(1)j} \mathbf{N}_{\pm 1n}^{(1)j} \right\}, \quad (5a)$$

$$\mathbf{E}_2 = \sum_{n=1}^{\infty} \left\{ a_{\pm 1n}^{(2)j} \mathbf{M}_{\pm 1n}^{(2)j} + b_{\pm 1n}^{(2)j} \mathbf{N}_{\pm 1n}^{(2)j} + a_{\pm 1n}^{(2)b} \mathbf{M}_{\pm 1n}^{(2)b} + b_{\pm 1n}^{(2)b} \mathbf{N}_{\pm 1n}^{(2)b} \right\}, \quad (5b)$$

$$\mathbf{E}_3 = \sum_{n=1}^{\infty} \left\{ a_{\pm 1n}^{(3)b} \mathbf{M}_{\pm 1n}^{(3)b} + b_{\pm 1n}^{(3)b} \mathbf{N}_{\pm 1n}^{(3)b} \right\}. \quad (5c)$$

and analogous expressions are obtained for the magnetic fields $\mathbf{H}_i = -i \sqrt{\epsilon_i / \mu_i} \mathbf{E}_i$. In the eqs. (5), the superscripts represent the regions and the types of the scattering coefficients. The region that includes the core (region 1) has only radial contributions from the spherical Bessel functions (denoted by the superscript j), while regions that are not bounded as the environment (region 3) contain only the Hankel functions of the first kind (h). Finally, region 2 containing the gold shell presents contributions from both types of functions. Indeed, it should be noted that the scalar Helmholtz equation presents solutions that in spherical-polar coordinates are as follows

$$\psi_{nm}(r, \theta, \varphi) \cong z_n(kr) P_n^m(\cos \theta) e^{im\varphi}, \quad (6)$$

where $z_n(kr)$ denotes either the spherical Bessel functions $j_n(kr)$ or the spherical Hankel functions of the first kind, $h_n(kr)$, and the $P_n^m(\cos \theta)$ are the associated Legendre functions. It should be pointed out that the Bessel functions are regular at the origin, whereas the spherical Hankel functions diverge at the near the origin. As a consequence, a region including the core can only present spherical Bessel functions in its expression for the field. While, in contrast, a region not including the origin, as the shell, should have contributions from both such functions. Solving the eqs. (5) for the electric field and the corresponding expression for the magnetic fields we can obtain the fields everywhere. All

$$a_n = \frac{\psi_n(y) [\psi_n'(m_2 y) - A_n \chi_n'(m_2 y)] - m_2 \psi_n'(y) [\psi_n(m_2 y) - A_n \chi_n(m_2 y)]}{\xi_n(y) [\psi_n'(m_2 y) - A_n \chi_n'(m_2 y)] - m_2 \xi_n'(y) [\psi_n(m_2 y) - A_n \chi_n(m_2 y)]}, \quad (8a)$$

$$b_n = \frac{m_2 \psi_n(y) [\psi_n'(m_2 y) - B_n \chi_n'(m_2 y)] - \psi_n'(y) [\psi_n(m_2 y) - B_n \chi_n(m_2 y)]}{m_2 \xi_n(y) [\psi_n'(m_2 y) - B_n \chi_n'(m_2 y)] - \xi_n'(y) [\psi_n(m_2 y) - B_n \chi_n(m_2 y)]}, \quad (8b)$$

$$\text{with } A_n = \frac{m_2 \psi_n(m_2 y) \psi_n'(m_2 x) - m_1 \psi_n'(m_2 x) \psi_n(m_1 x)}{m_2 \chi_n(m_2 x) \psi_n'(m_1 x) - m_1 \chi_n'(m_2 x) \psi_n(m_1 x)}$$

$$\text{and } B_n = \frac{m_2 \psi_n(m_1 x) \psi_n'(m_2 x) - m_1 \psi_n'(m_2 x) \psi_n(m_1 x)}{m_2 \chi_n(m_2 x) \psi_n'(m_1 x) - m_1 \chi_n'(m_1 x) \psi_n(m_2 x)},$$

where $x = kr_1 = 2\pi N r_1 / \lambda$ and $y = kr_2 = 2\pi N r_2 / \lambda$ are the size parameters of the core and the shell respectively, and m_1 and m_2 is the relative refractive index of the core and the shell to that of environment medium. ψ_n , χ_n and ξ_n are the Riccati-Bessel functions, and the primes indicate differentiation with respect to the argument [17]. If the limit of small particles is taken in consideration, the Riccati-Bessel functions can be expanded in power series, and while the denominator of b_n will never vanish for any n , the denominator of a_n will vanish as $x \rightarrow 0$, and $y \rightarrow 0$, $m_2 = i(n+1/n)^{1/2}$, with $n=1, 2, \dots$. For example for a dipole $m_2 = i\sqrt{2}$, that requires a negative refractive index, condition satisfied by a metallic particles. The presence of the core provides a shift that depends on $f = (r_1/r_2)^3$, i.e. the volume fraction of the core and the total volume, and the dielectric constant of both core and shell. We simulated red-shifts for several core materials, such as SiO₂, TiO₂ and BaTiO₃, for nanoshell particles with diameters falling in the range 100-150nm (with core-shell ratio of 75%), the most relevant shift

the numerical results were obtained writing a specific code based on Matlab® language and using the boundary element method (BEM) [16].

The far-field scattering properties, absorption and extinction cross-sections emerging from the nanoshell can be determined determining the coefficients a and b in eq. (5). In terms of such coefficients, and analogously to the standard Mie theory [8], we obtain

$$\sigma_{sca} = \frac{2\pi}{k^2} \sum_{n=1}^{\infty} (2n+1) \left(|a_{1n}^{(3)h}|^2 + |b_{1n}^{(3)h}|^2 \right), \quad (7a)$$

$$\sigma_{ext} = -\frac{2\pi}{k^2} \sum_{n=1}^{\infty} (2n+1) \text{Im} \left(a_{1n}^{(3)h} + b_{1n}^{(3)h} \right), \quad (7b)$$

$$\sigma_{abs} = \sigma_{ext} - \sigma_{sca}. \quad (7c)$$

In Mie theory the electric and magnetic fields are expressed as infinite sums over the vector spherical harmonics, eqs. (5a-c), and the harmonics for the scattered fields are weighted by the coefficients a_n and b_n , eqs. (7a-c). The vector spherical harmonics represent normal modes of the nanoshell, with the two modes for each n corresponding to transverse magnetic and transverse electric modes, where there is no radial electric and magnetic fields respectively. For the case of a nanoshell of core radius r_1 and total radius r_2 , the coefficients a and b are given as follows [8, 15]:

towards NIR was observed for the BaTiO₃ core based nanoshells, [16]. Second harmonic generation for a BaTiO₃ core gold nanoshell has been recently described in [18]

In far-field conditions, the scattering contributions generally dominate with the respect the absorption contributions, making very difficult to detect nanoshells. In the local near field around the nanoshell, the absorption efficiency can be enhanced by the coupling with the plasmon oscillations. The Mie theory developed and utilized for the far field quantification of the plasmon-e.m. coupling can be used for the near field case as a limiting case.

3 Numerical simulation of the optical response of gold nanoshells as observed using an aperture SNOM

Near-field enhancement due to plasmonic coupling of the nanoshell with external e.m. field should produces measurable effects, particularly, when the evanescent wave is not absorbed by the biological system. In practice, if nanoshells are located just under a short depth inside the biological system we could collect signals identifying absorbing objects with the dimensions of the nanoshell particles. To confirm such prevision, we have simulated the optical signal detected by an aperture SNOM operating in air in collection mode with different illumination wavelengths ranging from visible to near infrared. The samples

used for the experimental testing are animal cells, interacting with gold nanoshells with dielectric core (SiO_2 , BaTiO_3). Preparation of cell samples are described elsewhere [19], while the interest in using BaTiO_3 as the dielectric core of the sample is due essentially to the relevant shift towards near infrared shown by nanoshells with 100nm and 20nm dimension for core and shell respectively [16].

The SNOM is considered to be used in reflection mode measurements with aperture tips of nearly 50nm diameter. The extinction signal of cell samples has been detected in reflection acquisition mode: the sample can be illuminated

on top by an external source, laser, with different wavelengths λ , ($\lambda=488\text{nm}$, 632nm , 780nm , 980nm were used), an optical fiber was used for the detection of the reflected signals. If the nanoshell is located just under the cell cytoskeleton, and the evanescent signal produced by the nanoshell is not absorbed by the cell due to the transparency window, then it should be possible to locate the nanoshell inside the cell, see figure 2, where the (a) image corresponds to the topography of a cell recorded with a SNOM system. Fig. 2 (b) represents the line-trace along the white line in (a) (full line) together with the contour simulation (dashed line) and the nanoparticles distribution (small circles).

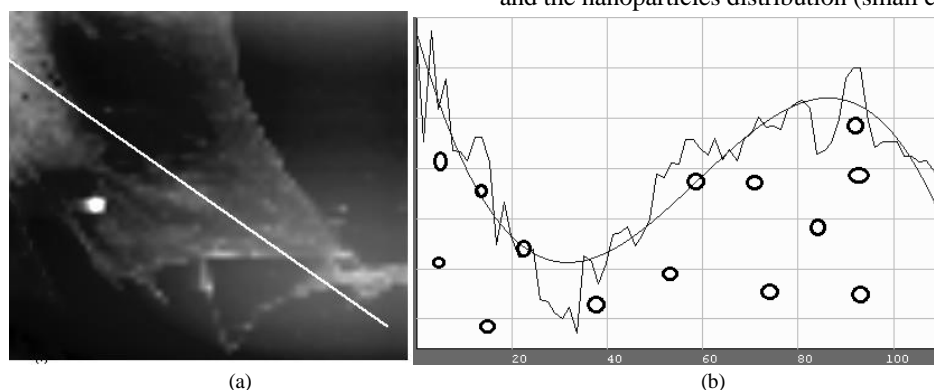


FIGURE 2 (a) Topographic image of a cell recorded with a SNOM, and (b) schematic sketch of the distribution of nanoshells (back circles) inside a cell

In figure 3, we report the results of a Finite Difference Time Domain (FDTD) simulation of a single nanoshell obtained simulating a SNOM operating in collection mode with a 780nm wavelength laser light with nanoshell dis-

persed inside an animal cell (for instance, we have considered dielectric constant of the h9c2 mouse type cell, [20]). The fields simulated and the Poynting vector are calculated along the z-direction, with the origin fixed at the SNOM aperture.

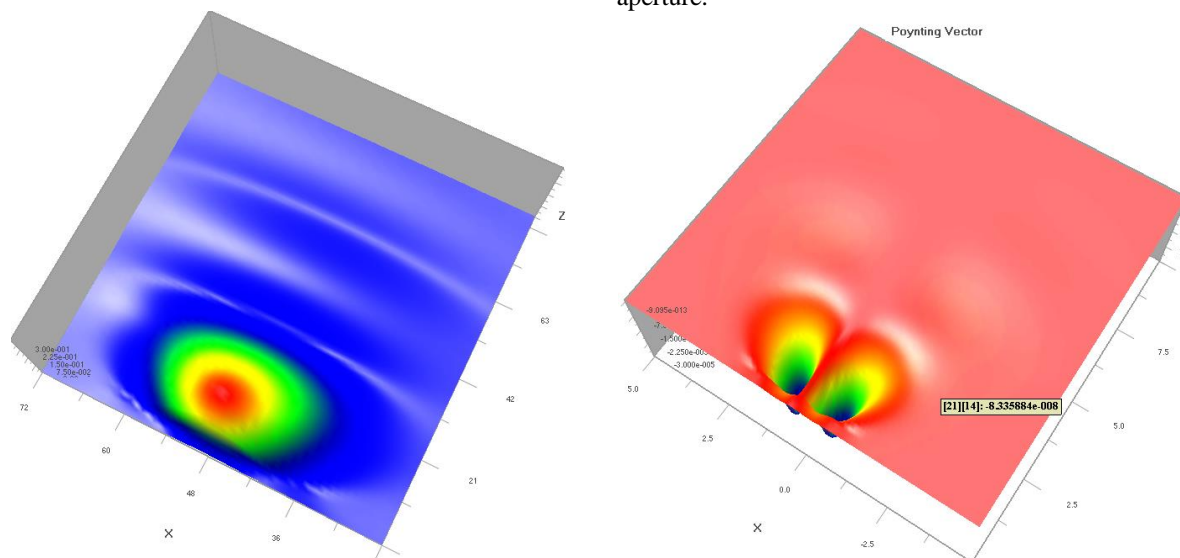


FIGURE 3 (upper) FDTD simulation of a gold nanoshell recorded with the SNOM operating in collection mode. The gold nanoshell can be represented as point-like absorption sources due to near-field enhancement due to plasmonic coupling of the nanoshell with external e.m. (a) E_z component of the extinction fields due to confined plasmonic nanoshelle behavior; (lower) correspondent Poynting vector

The gold nanoshells as observed by a SNOM in reflection mode are denoted by *point-like absorption sources*. Point-like absorption source presents dimension very close to nanoparticle falling in the range 120-150nm diameters, so that the identification of such points with the gold nanoparticles is immediate. The isolated point-like

sources can be immediately identified as the core-shell nanoparticles. The electric field distribution along the z-direction of a particle located at \mathbf{a} and collected at the SNOM tip aperture, as represented in figure 3(a), is approximately given by the expression [21]:

$$E_z(\mathbf{r}, t) \equiv E_0(\mathbf{p} \cdot \mathbf{n})(\mathbf{n} \cdot \mathbf{e}_a) \frac{\cos(kr_a - \omega t)}{\sqrt{r_a}} \exp(-r_a/l), \quad (9)$$

where \mathbf{E}_0 and \mathbf{p} are the electric field amplitude and the polarization direction of the illuminating light, respectively; $r_a = |\mathbf{r}_a| = |\mathbf{r} - \mathbf{a}|$ is the magnitude of the separation vector with $\mathbf{e}_a = \mathbf{r}_a/r_a$ being the unit vector. The terms $\mathbf{p} \cdot \mathbf{n}$ and $\mathbf{n} \cdot \mathbf{e}_a$ describe the role of the polarization on the efficiency of near field plasmon-e.m. coupled excitation, being \mathbf{n} the normal vector to the probe (recognized as the maximum dipole radiation) and the cosine angular distribution of the radiation, respectively. The two factors k and l represent the propagation constant and the length of the nanoparticles plasmonic field, respectively. The detected SNOM signal is formed by the complex light scattering processes between the tip and the sample, mixing different field components. Thus, electromagnetic field collected near the probe cannot be simply linked to a specific component of the unperturbed electromagnetic field distribution.

To exhibit the relative absorption and scattering ability of the nanoshells, the cross sections for absorption and scattering can be defined as $\sigma_{abs} = W_{abs}/I_{inc}$ and $\sigma_{scat} = W_{scat}/I_{inc}$ respectively, while the efficiencies are defined as $Q_{abs} = \sigma_{abs}/A$ and $Q_{scat} = \sigma_{scat}/A$, for the absorption and the scattering processes, respectively. Here, $I_{inc} = (1/2)\epsilon_0 c E^2$ represents the intensity of the incident wave, $A = \pi r^2$ is the particle cross-section projected onto a plane perpendicular to the incident wave, and r is the total radius on the nanosphere. Finally, the absorption and scattering energy $W_{abs/scat}$ are defined respectively as

$$W_{abs} = \frac{1}{2} \text{Re} \left[\iint \left(\mathbf{E}_{tot} \times \mathbf{H}_{tot}^* \right) \cdot \mathbf{n} ds \right] \text{ and}$$

$$W_{scat} = \frac{1}{2} \text{Re} \left[\iint \left(\mathbf{E}_{scat} \times \mathbf{H}_{scat}^* \right) \cdot \mathbf{n} ds \right]. \quad (10)$$

In far field, we can insert the components fields as given by the eqs. 5a and 5b, inside eqs (10), and integrating on all a solid angle; on the contrary, in near field, if we consider a finite dimension of tip aperture, we have that scattered and absorbed intensities are proportional to the solid angle.

In addition, if we consider a near field solution of electric and magnetic fields and the field enhancement in z -direction in proximity of the SNOM probe tip, under some specific condition we can observe intense enhanced absorption, The E_z components under the SNOM tip could be about 10 times larger if compared to the in-plane components, so, it is

References

- [1] Kelly K L, Coronado E, Zhao L L, G C Schatz G C 2003 *J. Phys. Chem. B* **107** 668
- [2] Myroshnychenko V, Rodríguez-Fernández J, Pastoriza-Santos I, Funston A M, Novo C, Mulvaney P, Liz-Marzán L M, García de Abajo F J 2008 *Chem. Soc. Rev.* **37** 1792
- [3] Jackson J B, Westcott S L, Hirsch L R, West J L, Halas N J, 2003 *Appl. Phys. Lett.* **82** 257
- [4] Hirsch L R, Gobin A M, Lowery A R, Tam F, Drezek R A, Halas N J, West J L 2006 *Ann. Biomed. Eng.* **34** 15
- [5] Lin A W H, Halas N J, Drezek R A 2005 *J. Biomed Opt.* **10** 064301
- [6] Liu C, Mi C C 2008 *IEEE Transactions of Nanobioscience* **7** 206

reasonable to suppose that when the probe signal displays a point-like absorption peaks, this can be identified with a nanoshell [22]. This is because the field enhancement caused by the local surface plasmon resonance mainly focuses on the metal-dielectric interface (and decays exponentially) is not absorbed by the biological tissue due to the transparency window. In figure 4, we have calculated the absorption (continue line) and the scattering coefficients (dashed line) for a nanoshell with a varying gold layer in the range 0-100nm, with a BaTiO₃ core dimension fixed at 100nm. Our nanoparticles should have a nominal gold layer of 20-40nm, i.e., in the region where the absorption is significantly higher with respect to scattering mechanisms.

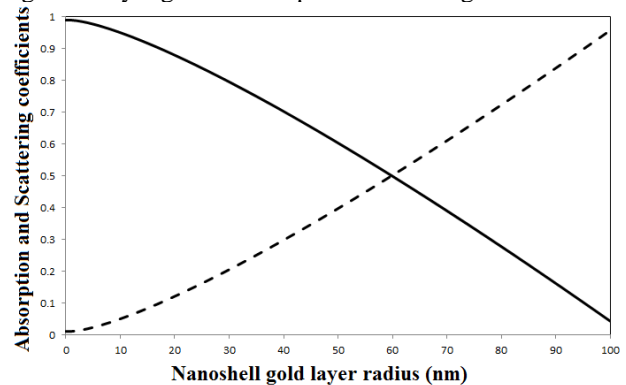


FIGURE 4 Absorption and scattering efficiency coefficients as a function of gold nanoshell layer dimension. The BaTiO₃ core was fixed at 100nm

Finally, one open problem is represented by the optical response of gold nanoparticles clusters that could present the enlarged absorption regions. The interpretation of nanoshell cluster signals that could be source of controversial interpretation require supplementary theoretical and numerical tools [23].

5 Conclusions





In this paper, a theoretical and numerical approach has been developed to support the possibility to use an aperture SNOM (aperture nearly 50nm diameter) to identify 100-150nm diameter gold nanoshells inside animal cells. The results confirm that SNOM is able to identify nanoshells located inside the upper cell layers.

Acknowledgments

The authors would like to acknowledge the contribution of the COST Action MP1302 Nanospectroscopy.

- [7] König K 2000 *J. Microscopy* **200** 83
- [8] Mie G 1908 *Ann. Phys. (Leipzig)* **25** 377
- [9] Zavelani-Rossi M, Celebrano M, Biagioni P, D. Polli D, Finazzi M, Duò L, Cerullo G, Labardi M, Allegrini M, Grand J, Adam P M 2008 *Applied Physics Letters* **92** 093119
- [10] Fan P, Chettair U K, Cao L, Afshinmanesh F, Engheta N, Brongersma M L 2012 *Nature Photonics* **6** 380
- [11] Feng J, Siu V C, Roelke A, Metha V, Rhieu S Y, Palmore G T R, Pacifici D 2012 *Nano Letters* **12** 602
- [12] Chen Y F, Serey X, Sarkar R, Chen P, Erickson D 2012 *Nano Letters* **12** 1633

- [13] Stratton J A 1941 *Electromagnetic Theory* McGraw-Hill:New York
- [14] Sarkar D, Halas N J 1997 *Physical Review E* **56** 1102
- [15] Le D SURE Project, Spectroscopic Characterization of Silica-Gold Nanoshells, available at <http://www.cmmmp.ucl.ac.uk/~mdl/cam/Mie/nanoshells.pdf>
- [16] D'Acunto M, Moroni D, Salvetti O 2012 *Advances in Optical Technologies*
- [17] Gradshteyn I S, Ryzhik I M 2007 *Table of Integrals, Series and Products* Seventh Edition, A. Jeffrey and D. Zwillinger eds.
- [18] Farrokh Takin E, Ciofani G, Puleo G, de Vito G, Filippeschi C, Mazzolai B, Piazza V, Mattoli V 2013 *International Journal of Nanomedicine* **8** 2319
- [19] Cricenti A, Marocchi V, Generosi R, Luce M, Perfetti P, Vobornik D, Margaritondo G, Talley D, Thielen P, Sanghera J S, Aggarwal I D, Miller J K, Tolk N H, Piston D W 2004 *Journal of Alloys and Compounds* **362** 21
- [20] Stacey M W, Sabuncu A C, Beskok A 2015 *Biochim. Biophys. Acta* **1840**(1-12)
- [21] Dvorák P, Neuman T, Brínek L, Šamoril T, Kalousek R, Dub P, Varga P, Šíkola T 2013 *NanoLetters* **13** 2558
- [22] Nedyalkov N N, Dikovska A, Dimitrov I, Nikov R, Atanasov P A, Toshkova R A, Gardeva E G, Yossifova L S, Alexandrova M T 2012 *Quantum Electronics* **42** 1123
- [23] Girard C 2005 *Report on Progress of Physics* **68** 1883

Authors	
	<p>Antonio Cricenti, 28/05/1959, Monterosso Calabro (I)</p> <p>Current position, grades: Research Director, National Research Council University studies: PhD in Physics Scientific interest: Surface Physics, Semiconductors, Biological cells Publications: 220 international peer reviewed publications Experience: Ultra-high-vacuum, scanning probe microscopy, clean semiconductor surfaces, biological material</p>
	<p>Mario D'Acunto, 20/08/1966, Minturno (I)</p> <p>Current position, grades: Researcher, National Research Council University studies: PhD in Surface Mechanics Scientific interest: Surface Physics, Nanotribology, Soft matter Publications: 100 international peer reviewed publications Experience: scanning probe microscopy, friction and wear, sensors</p>
	<p>Marco Luce, 26/05/1967, Roma (I)</p> <p>Current position, grades: Electronic engineering, National Research Council University studies: Electronic degree Scientific interest: Surface Physics, Semiconductors, Biological cells Publications: 42 international peer reviewed publications Experience: Ultra-high-vacuum, scanning probe microscopy, clean semiconductor surfaces, biological material</p>
	<p>Simone Dinarelli, 26/05/1984, Roma (I)</p> <p>Current position, grades: post-doc of the Institute of Structure of Matter, National Research Council, Rome University studies: PhD in biochemistry, University of Rome "La Sapienza" Scientific interest: He is a specialist in the field of SNOM and AFM in material science and biology.</p>

Nanocarbon electromagnetics in CNT-, GNR- and aerogel-based nanodevices: models and simulations

**Yu Shunin^{1, 2}, S Bellucci², Yu Zhukovskii¹,
V Gopeyenko³, N Burlutskaya³, T Lobanova-Shunina⁴**

¹ Institute of Solid State Physics, University of Latvia, Kengaraga Str. 8, LV-1063 Riga, Latvia

² INFN-Laboratori Nazionali di Frascati, Via Enrico Fermi 40, I-00044, Frascati-Rome, Italy

³ ISMA University, 1 Lomonosov, Bld 6, LV-1019, Riga, Latvia

⁴ Riga Technical University, Aviation Institute, 1 Lomonosov, Bld V, LV-1019, Riga, Latvia

Corresponding author's e-mail: yu_shunin@inbox.lv

Received 15 September 2014, www.cmmt.lv

Abstract

Electromagnetic properties of nanocarbon systems are essential for the creation of various nanoelectronic devices. Our major attention is focused on CNTs, graphene nanostructures (*e.g.*, GNR and GNF), graphene-based aerogels (GBA) and CNT-based aerogels (CNTBA) as the basis for high-speed nanoelectronics and prospective nanosensors. Special attention is paid to fundamental properties of CNTs, GNRs and various CNT-Me, GNR-Me, CNT-graphene interconnects. Nanosystems of 3D GBA and CNTBA are regarded as complicated systems made up of basic nanocarbon interconnected elements. Technological interest to contacts of CNTs or GNRs with other conducting elements in nanocircuits, FET-type nanodevices, GBA and CNTBA is the reason to estimate various interconnect resistances, which depend on chirality effects in the interconnects. Simulations of electromagnetic properties in interconnects have been performed to evaluate integral resistances, capacitances and impedances of various topologies (1D, 2D and 3D) in nanodevices, including their frequency properties (GHz&THz).

Keywords: CNTs - carbon nanotubes, GNR – graphene nanoribbons, CBA – Carbon Based Aerogels, Carbon Nanoporous Materials, Carbon-based nanocomposites

1 Introduction

The objective of the current study is to demonstrate the implementation of advanced simulation models to ensure a proper description of the electronic properties, electrical conductivity, electromagnetic and electromechanical phenomena of functionalized CNT- and GNR-based nanostructures of different morphologies and their interconnects for nanosensor and nanomemory systems. The developed cluster approach based on the multiple scattering theory formalism as well as effective medium approximation is used for nanosized systems modeling supported by calculations of dispersion law, electronic density of states, conductivity, *etc.* [1]. The sensitivity of the local electronic density of states to external influences (mechanical, chemical, magnetic, etc) on the fundamental electromagnetic properties of CNTs, GNRs and their metal interconnects have been analyzed from the point of view of nanosensor applications [1, 2]. We develop a set of prospective models of nanocarbon-based nanomaterials and nanodevices based on various interconnects and interfaces (see Figure 1).

Correlations between multiple external influences (mechanical, chemical, electromagnetic *etc* factors) and fundamental properties of nanocarbon materials are studied.

2 Nanodevices for effective electron transport

We have developed structural models for CNT-Me and GNR-Me junctions, based on their precise atomistic structures, which take into account the chirality effect and its influence on the interconnect resistance for Me (= Fe, Ni, Cu, Ag, Pd, Pt, Au) with the predefined CNT (or GNR) geometry. In the simplest cases, the electronic structure of CNT-Ni interconnects can be evaluated through the DOS for a C-Metal contact considered as a 'disordered alloy' [1]. In the current study, we have developed more complicated structural models of CNT-metal junctions based on a precise description of their atomistic structures. When estimating the resistance of a junction between a nanotube and a substrate, the main problem is caused by the influence of the nanotube chirality on the resistance of SW and MW CNT-Me interconnects (Me = Fe, Ni, Cu, Ag, Pd, Pt, Au), with a predefined CNT geometry [2-3].

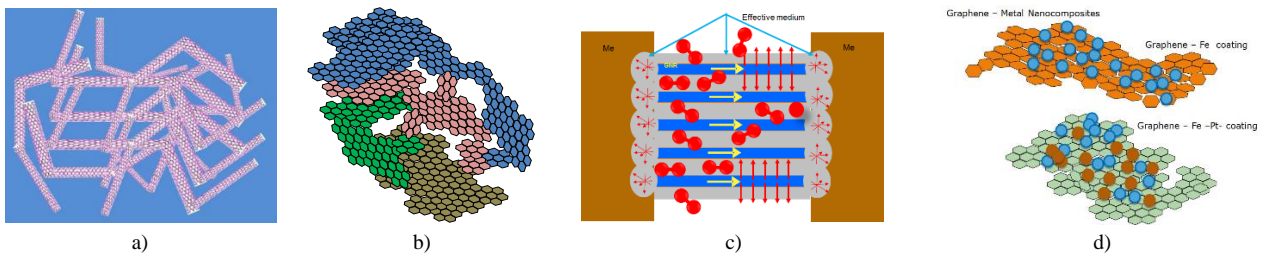


FIGURE 1 A set of simulation models: a) Structural model of CNTBA; b) Structural model of GBA; c) GNRs-based gas nanosensor device; d) Graphene-metal nanocomposites - Fe and Fe-Pt coatings.

2.1. CONDUCTIVITY AS AN IDENTIFYING TOOL OF NANOSENSOR SYSTEMS

Usually two basic electron conductivity mechanisms are considered in CNT-based structures. The ballistic mechanism is engaged in electron transport within CNTs, while the collisional mechanism is characteristic of CNT-substrate interconnects [4]. Hence the general conductivity σ_{gen} is evaluated as follows:

$$\frac{1}{\sigma_{gen}} = \frac{1}{\sigma_{coll}} + \frac{1}{\sigma_{ball}} \quad (1)$$

For pure CNTs, we clearly observe that $\sigma_{ball} \gg \sigma_{coll}$. The collisional contribution is basically connected with the specific morphology of the interconnect space. In the framework of multiple scattering theory formalism and effective medium approximation, we can evaluate both factors of conductivity. A special question for modelling is the dependence of both conductivity mechanisms on the electron free path length, which, in the case of pure CNT, is usually considered as the nanotube length.

The analysis of Kubo-Greenwood conditions in relation to CNT and GNR morphologies has been presented taking into account dc ($\omega=0$), ac ($\omega \neq 0$) regimes and the temperature factor of the electron transport.

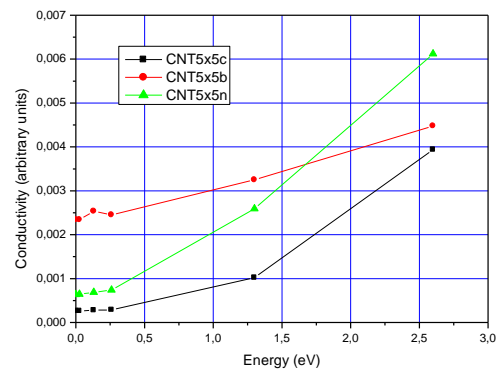
The calculations of conductivity are usually performed using Kubo-Greenwood formula [1, 2]:

$$\sigma_E(\omega) = \frac{\pi \Omega}{4\omega} [f(E) - f(E + \hbar\omega)] |D_E|^2 \rho(E) \rho(E + \hbar\omega) dE, \quad (2)$$

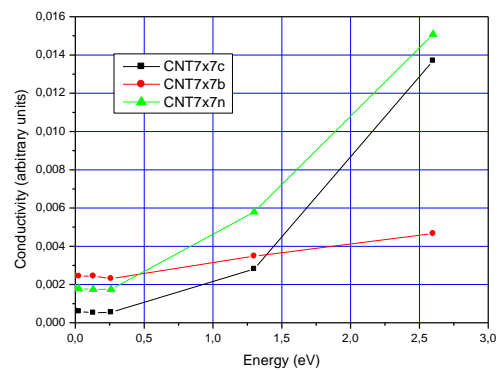
where ω is a real frequency parameter of Fourier transform for the time-dependent functions, $f(E)$ is Fermi-Dirac distribution function, $D_{E,E'} = \int_{\Omega} \Psi_{E'}^* \nabla \Psi_E d\mathbf{r}$, where

$\Psi_{E(\mathbf{K})} = A \exp(i\mathbf{K}\mathbf{r})$ and \mathbf{K} is the complex wave vector of the effective medium. The dispersion function $E(\mathbf{K})$ determines the properties of the wave function $\Psi_{E(\mathbf{K})}$ upon the isoenergy surface in \mathbf{K} -space.

However, *Kubo-Greenwood* formalism is free from this division on ballistic and collisional mechanisms and seems to be more objective. The analysis of Kubo-Greenwood's conditions in respect of CNT morphology has been presented taking into account both dc ($\omega=0$) and ac ($\omega \neq 0$) regimes as well as the temperature factor of electron transport [5, 6].



a)



b)

FIGURE 2 Conductivities of pure perfect and doped (B or N) CNTs in the limit of non-interacting defects: a) (5,5); b) (7,7)

Parametrical numerical simulations of conductivity have been carried out for zig-zag (0,m), arm-chair (m,m) and chiral (n,m) CNTs and GNRs [2] on the basis of EDOS calculations in [8], where the sensitivity of conductivity to the local electronic density of states in CNTs and GNRs with local impurities (N and B atoms) are shown (see, e.g., (5,5), (7,7) CNTs, Figures 2a, b). Similar calculations for graphene-based structures (graphene, CO-graphene, Al-doped, Al-Graphene and Al-CO-Graphene, Figure 3) and (N and B doped graphene, Figure 4).

In particular, this sensitivity implies that CNT- and graphene-based nanodevices can be potentially used as nanosensor systems, when local electronic density of states induced by external influences takes place. Similar

calculations of conductivities based on the EDOS results have been made for graphene-based materials [9,10] (see Figures 3 and 4).

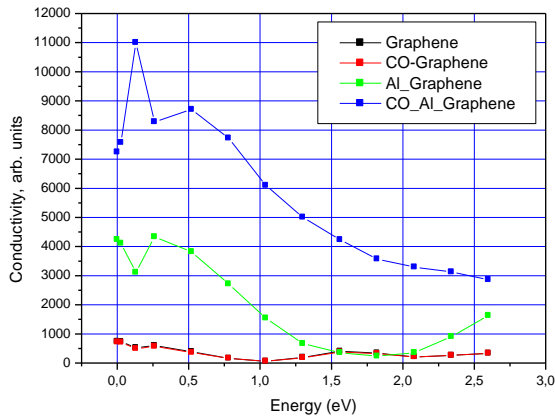


FIGURE 3 Conductivities of pure perfect and Al- doped graphene for EDOS of [9]

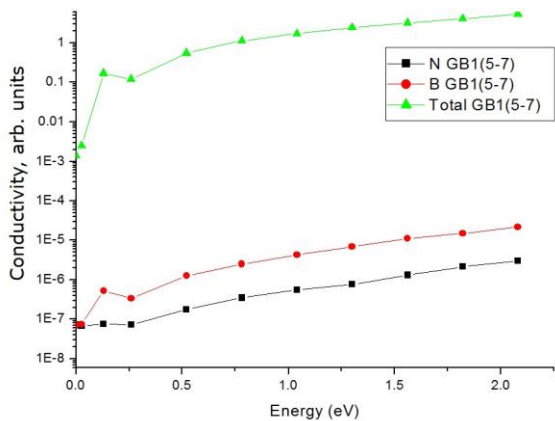


FIGURE 4 Conductivities of pure perfect and N- and B-doped graphene for EDOS of [10]

3 CNT interconnects magnetic phenomena and magnetically stimulated CNT growth in CVD processes

There is a relation between the use of magnetic catalysts and the CVD growth of CNTs determining the most commonly used materials for the CNT growth - Fe, Co and Ni. Nanoparticles of the latter catalysts are magnetically isotropic. It is possible to use magnetically anisotropic nanoparticles such as those in the alloys with a different substitutional disorder (e.g., Fe_xPt_{1-x}) to manage the CVD process with the formation of the predefined CNT chiralities. Limitations in the control after the parameters of CNTs

growth are discussed. The role of the number of effective bonds inside interconnects and the discrete character of chiral indices have been studied in relation to the expected qualities of CNT output in the CVD process. Moreover, it is a way to create effective magnetic nanomemory, where a CNT ‘forest’ provides communication with other parts in novel integrated nanodevices by means of spin waves transport.

Nanocarbon-magnetic metal interfaces open new possibilities for the creation of nanospintronic devices, e.g., nanomemory devices. The model of CNTs growth with the predefined chiralities in a magnetically managed CVD process with the use of magnetically anisotropic Fe_xPt_{1-x} nanoparticles with various substitutional disorders has been developed. The model and magnetically controlled conditions, stimulating the CNT growth in a CVD process, aim at the predictable SWCNT diameter and chirality. The perfect picture of the magnetically stimulated CVD process for CNTs growth can be presented as a CNT forest (see Figure 5). Such a system of nanotubes can also be considered as a prototype of the magnetic memory, where ferromagnetic nanoparticles serve as cells of the magnetic memory – that is, ferromagnetic contacts are controlled by spin pulses, the transport of which is provided by nanotubes.

At the same time, the growth control over chiral and non-chiral nanotubes essentially depends on stoichiometric composition of Pt-Fe nanoparticles. The beginning of the nucleation process providing the growth of nanotubes might be connected with stochastic fluctuations of the magnetic moment in a carbon atom relative to the direction of the local magnetic field in a nanoparticle.

Distribution of the fluctuation angle obeys the Gaussian law:

$$f(\theta) = \frac{1}{\sigma\sqrt{2\pi}} \cdot \exp\left(-\frac{(\theta - \theta_B)^2}{2\sigma^2}\right), \quad (3)$$

where σ^2 is the angular dispersion of thermal fluctuations of the magnetic moment angle of a carbon atom. To evaluate this dispersion, the potential energy change of the magnetic moment under the influence of the thermal energy should be evaluated: $\mu_C B(1 - \cos\theta_T) \approx k_B T_{CVD}$, where μ_C is the induced magnetic moment of a carbon atom $\mu_C = 1.25\mu_B$ (see evaluations in [65], $\mu_B = 5.788 \cdot 10^{-5} eV/T$, B is the magnetic induction of the catalyst surface, $\theta_T = \theta - \theta_B$, T_{CVD} - is the operating temperature of the CVD process, $k_B = 8,617\ 3324(78) \cdot 10^{-5} eV/K$ - is the Boltzmann constant.

Hence $2 \sin^2 \frac{\theta_T}{2} \approx \frac{k_B T_{CVD}}{\mu_C B}$. Taking into consideration one of

the main problems of the nanotubes growth control – the chirality control – it is necessary to look for the minimal fluctuation angle θ .

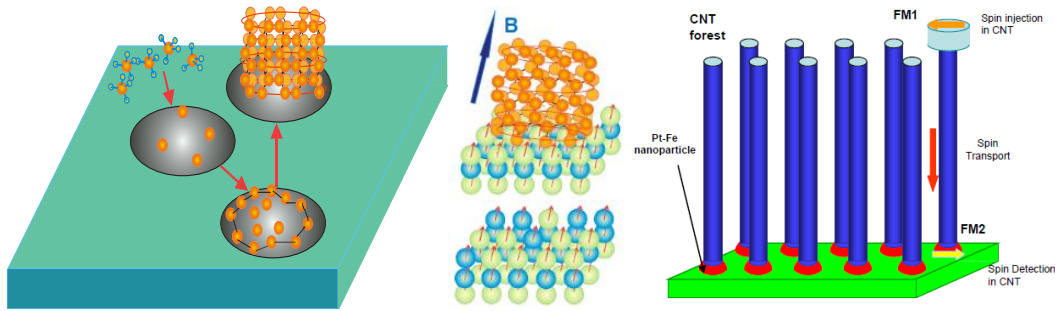


FIGURE 5 Model of CNTs growth in a magnetically controlled CVD process based on Fe-Pt nanodrops catalysts

$$\text{Then } \sigma^2 = \theta_t^2 = \frac{2k_B T_{CVD}}{\mu_C B}$$

The condition of the small fluctuation angle (e.g., $< 10^\circ$) at certain temperature of the CVD process imposes limitations on the values of the demanded magnetic induction B . Taking into account the ratio between the chirality angle and the direction of the magnetic field $\phi = \theta_B$, Figure 13 displays the predictable scattering of chiralities for nanotubes of approximately the same diameter.

We are also able to evaluate the necessary value of the magnetic field B providing the expected chirality angles scattering, e.g. $\sigma = 0.2$ (approximately 12°) leads to the B evaluation for the CVD process temperature $T_{CVD} = 700^\circ C$ as

$$B = \frac{2k_B T_{CVD}}{\sigma^2 \mu_C} \approx \frac{16755}{\sigma^2 \mu_C} \approx 57895 \approx 6 \cdot 10^4 T.$$

For small angle dispersions $\sigma^2 = \theta_t^2 = \frac{2k_B T_{CVD}}{\mu_C B}$ the high local

magnetic field on the nanoparticle surface is necessary. The result also strongly depends on the carbon atom magnetic moment μ_C [4] (see also Figure 6).

Taking into account the possible errors in diameters of the growing nanotubes, their evaluation from beneath is defined by the minimal variations in parameters of the chirality vector $\vec{c} = (n, m)$ Δn and Δm , which equal 1.

Considering the formula for calculating the diameter of CNT:

$$d = \frac{\sqrt{3}a}{\pi} \sqrt{m^2 + n^2 + mn}, \text{ where } a = 0,142 \text{ nm is the}$$

distance between the neighboring carbon atoms in the graphite plane.

The relationship between chirality indices (n and m) and the angle ϕ is presented by the ratio:

$$\sin \phi = \frac{m\sqrt{3}}{2\sqrt{m^2 + n^2 + mn}}$$

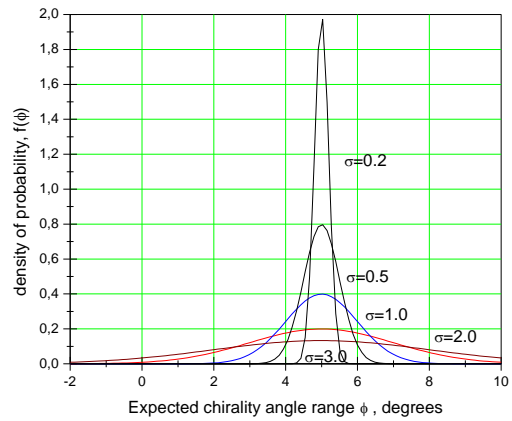


FIGURE 6 The predictable scattering of chiralities for nanotubes of approximately similar diameters

Then the minimum relative error in the diameter of CNT is possible to define as:

$$\varepsilon_d = \frac{\Delta d}{d} \approx \frac{\sqrt{5m^2 + 5n^2 + 8mn}}{2(n^2 + m^2 + mn)} \tag{4}$$

Particularly, in the case of arm-chair CNT ($m=0$)

$$\varepsilon_d \approx \frac{\sqrt{5}}{2n}, \text{ in the case of zig-zag CNT } (m=n)$$

$$\varepsilon_d \approx \frac{1}{2\sqrt{2}n} \tag{5}$$

Thus, the errors in the diameter of the growing CNTs are incorporated in discrete morphological properties. But these minimum estimates are only reinforced, given the obvious errors in the size of catalyst nanoparticles are taken into consideration.

Another possibility for the creation of magnetic memory devices is the magnetoresistance phenomenon. The giant magnetoresistance (GMR) was discovered in 1988 as a large change in resistance of magnetic Fe/Cr multilayer in the presence of an applied magnetic field [11] and tunnelling magnetoresistance (TMR) was discovered in 1975 by M. Jullière [12] in a device that consisted of two Fe films separated by Ge, namely, trilayer structures, i.e. sandwiches

of two ferromagnetic metals separated by a thin spacer layer of **normal metal** (see e.g. Figure 2) or **semiconductor**. They are called spin-valves and are used as magnetic field sensors. The resistance of the device is dependent on the relative magnetization orientation of the ferromagnets. It is R_P when the magnetizations are parallel and R_A when they are antiparallel. The GMR ratio is defined as $GMR = \frac{R_A - R_P}{R_P}$ as well as for TMR is $TMR = \frac{R_A - R_P}{R_P}$

(Moodera,1995). It was first in 1995 when room temperature TMR was discovered by Jullière [2] and caused a great interest in spintronics after GMR was discovered in

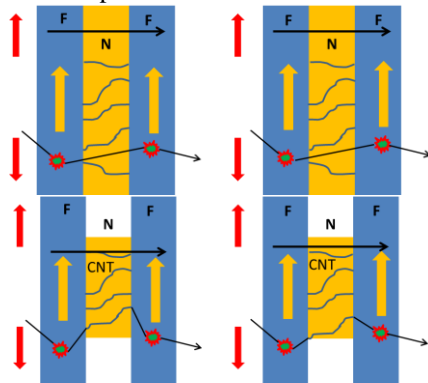


FIGURE 7a Giant magnetoresistance (GMR) device. A thin normal metal spacer (N) separates two ferromagnets (F). The current flows perpendicular to the plane of the sample. N space can be filled by introduced (or grown) CNT, e.g. – metal-like

The device shown in Figure 7 is the so-called current perpendicular to the plane (CPP, Figure 7a) geometry. The resistance of such geometry is very low and difficult to detect. For practical applications, structures with the current in the plane (CIP, Figure 7b) are used because they have higher resistance and thus higher difference with the magnetic field.

4 Nanoporous and nanocomposite material models

Nanoporous systems are considered as complicated ensembles of basic nanocarbon interconnected elements (e.g., CNTs or GNRs with possible defects and dangling boundary bonds) within the effective media type environment (Figures 1a, 1b, 1c). Interconnects are essentially local quantum objects and are evaluated in the framework of the developed cluster approach based on the multiple scattering theory formalism as well as effective medium approximation [1,2]. Particular properties of carbon-based nanoporous systems in dependence on the porosity extent, morphology and fractal dimension are practically studied to find useful correlations between their mechanical and electrical properties.

In cases when nanocarbon clusters are embedded in high resistance media (instead of vacuum) we come to the model of nanocomposite material. Now we pay attention to the model of nanocomposite materials based on carbon nanocluster suspensions (CNTs and GNRs) in dielectric polymer environments (e.g., epoxy resins) is considered as a disordered system of fragments of nanocarbon inclusions

1988 (Baibich et al [3]). Our idea is that the same effect can be reached by introducing metal or semiconductor-like CNTs into the N space. The TMR signal operates in the same way as the GMR, where R_P and R_A are the resistances of the device for parallel and antiparallel orientations respectively of the ferromagnets magnetization.

The sign and size of the interlayer exchange coupling is dependent on the thickness of the nonmagnetic spacer. The coupling can thus be ferromagnetic and antiferromagnetic dependent on the spacer thickness.

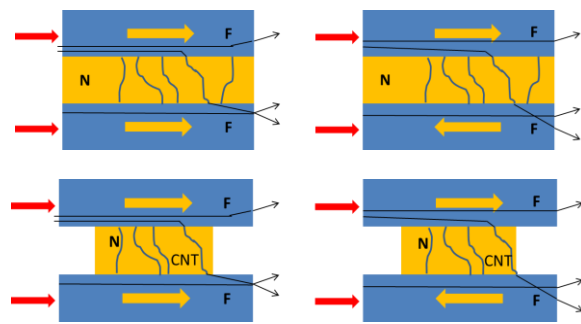


FIGURE 7b Current in Plane (CIP) spin-valve and equivalent resistor mode. Separate channels are for minority and majority spins. The electrons scatter from one F layer to the other on the way through the sandwich

with different morphology (chirality and geometry) in relation to a high electrical conductivity in a continuous dielectric environment. Presumably, the electrical conductivity of nanocomposite material will depend on the concentration of nanocarbon inclusions (in fact, carbon macromolecules). Isolated nanocarbon inclusions will provide conductivity due to the hopping conductivity mechanism through dangling bonds up to the percolation threshold, when at high concentrations (some mass %) a sustainable ballistic regime appears, which is characteristic of pure carbon systems.

Considering the *Kubo-Greenwood* relationship for small $\hbar\omega$ we can take $\rho(E) \approx const$.

A wave function ψ_a of Hamiltonian with the central symmetric potential energy for large distances is proportional to $\exp(-\alpha R)$, where $\alpha \sim a^{-1}$, a is the characteristic ‘Bohr-like’ radius. The interaction between the electronic states localized at points \mathbf{R}_i and \mathbf{R}_j describes the *overlapping integral*:

$$I = \int \psi_a^*(\mathbf{r} - \mathbf{R}_i) \psi_a(\mathbf{r} - \mathbf{R}_j) d^3 \mathbf{r} \sim \exp\left\{-\frac{|\mathbf{R}_i - \mathbf{R}_j|}{a}\right\}$$

If two states are divided by a distance R , then D can be approximated: $D = \frac{m\omega R}{\hbar} \exp(-\alpha R)(\alpha a)^{3/2}$.

If two centres are close and wave functions are in resonance: $D = \frac{m\omega R}{2\hbar} (\alpha a)^{3/2}$

Following to Mott [13] we can see:

$$\sigma(\omega) = \frac{\pi e^2}{2\hbar} \left\{ \rho(E_F) \right\}^2 (\hbar\omega)^2 a R_\omega^4,$$

where

$$R_\omega = \frac{1}{\alpha} \ln \left(\frac{2I_0}{\hbar\omega} \right),$$

when, e.g., $I_0 = e^2 \alpha \left[\frac{3}{2}(1 + \alpha R) + \frac{1}{6}(\alpha R)^2 \right]$ is the amplitu-

de of overlapping integral for hydrogen-type wave functions.

When the centers are strongly separated from each other, the overlap integral is very small, but strictly speaking, it never turns into zero.

However, in the material, which is considered an insulator, it is easy to detect very small currents due to tunneling of electrons from site to site, possible because of this overlap of the wave functions. Actually implemented mechanisms of electron hopping throughout "islands" of conductivity (nanocarbon clusters) is very complex.

However, we should accept that the probability of electron transition from the center point \mathbf{R}_i to the center point \mathbf{R}_j is proportional to the quadrat of overlapping integral: $I \sim \exp(-2|\mathbf{R}_i - \mathbf{R}_j|/a)$.

A macroscopic conductivity can be estimated as : $\sigma \sim \exp(-4\alpha R/a)$.

The constant α is evaluated as 0,70. This is approved by Monte-Carlo numerical simulations [14]. Only the most favourable ways for the electron hopping i.e. some of their share ξ should be taken into account. Evaluation of conductivity in this case is modified by:

$$\sigma(\xi) \sim \exp(-4\alpha\xi^{-1/3}R/a - \frac{1}{3}\xi W/kT).$$

The most precise averaged evaluation of the overall conductivity of the system [15], which is regulated by the

$$R_k = \sum_{j=1}^M \sum_{i=1}^N (\sigma_{\text{nano},i,j,k}^{-1} + (N_{\text{eff-in},i,j,k} \sigma_{\text{IC-in},i,j,k})^{-1} + (N_{\text{eff-out},i,j,k} \sigma_{\text{IC-out},i,j,k})^{-1}), \quad (9)$$

where M - is the number of conductivity channels, N - is the number of nanocarbon clusters in the conductivity channel, N_{eff} is the number of effective bonds of tunneling bonds, $\Sigma_D = (R_D)^{-1}$ is the conductance of dielectric medium, σ_{nano} is the conductivity nanocluster, σ_{IC} - the hopping conductivity of the *in-* and *out-type* effective bond, which for large nanocarbon inclusion concentrations create their interconnect.

hopping of electron between 'nanocarbon macromolecules', then will be: $\sigma_{\text{IC}} = \sigma_0 \exp(-\frac{4}{3} \left(\frac{4\alpha r_{\text{IC}}}{a} \right)^{3/4} \left(\frac{W_0}{kT} \right)^{1/4})$,

where r_{IC} - is the length of the tunnel 'jump' of the electron equal to the distance between 'nanocarbon' clusters, σ_0 is the normalization constant which means the conductivity of monolithic dielectric medium.

If we introduce the volume part as an indicator of the nanocarbon inclusions concentration: $\eta = \left(\frac{R_0}{R_0 + R} \right)^3$,

where R_0 is the average nanocarbon macromolecule radius, R is, as earlier, the width of potential barrier between the nearest nanoclusters which is responsible for percolation ability of the model nanocomposite. We should also diminish the hopping phenomena and percolation probability taking into account the nanocarbon macromolecule orientation within a hypothetical sphere embedded into high resistance dielectric medium.

On the basis of this definition we can obtain a contribution of potential nanocarbon interconnects to nanocomposite conductivity as follows (see also Figure 8):

$$\ln \left(\frac{\sigma_{\text{IC}}}{\sigma_0} \right) = -\frac{4}{3} \left(\frac{4\alpha}{a} R_0 (\eta^{-1/3} - 1) \right)^{3/4} \left(\frac{W}{kT} \right)^{1/4}. \quad (6)$$

Added to this is the effect of intrinsic nanocarbon cluster conductivity, which is dependent on its morphology. The electric conductivity will also depend on the spatial orientation of nanocarbon inclusions. It will be greater for the longitudinal electric field orientations and lower for the transverse ones.

Of course, any spatial orientations are technologically possible. The overall conductivity of nanocomposite material is: $\Sigma \approx \Sigma_D + \sum_{k=1} R_k^{-1}$, where

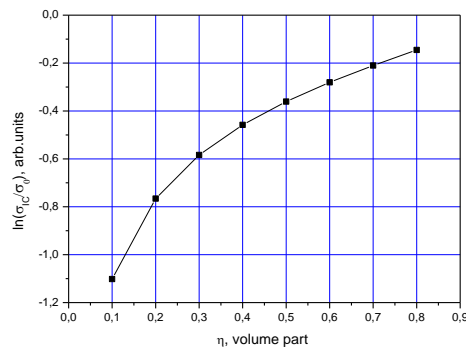


FIGURE 8 The hopping conductivity correlation via the average nanocarbon macromolecules volume part within continuous dielectric medium

A natural application of this kind of nanocomposite materials is nanosensors of pressure and temperature.

5 Instead of conclusion. CNTBA and GBA electromechanical properties



Talking about porous materials in general and, in particular, about nanocarbon-based systems such as CNTBA and GBA, we meet new complications for Solid state theory. We lose a strong dimension, regularity and continuity. In some sense, porous materials are 'pure' surfaces. We should also control the fractal dimension of porous materials as a key parameter of their morphology. A porous material in certain cases present a mixture where one component is a substance (for example – a metal) and the other - emptiness. To describe the properties of porous bodies, the percolation theory can be used.

One important difference: the system can not exist as finite metal clusters, since they cannot hang in a vacuum. Consequently, the metal component is always connected - all metals belong to the infinite cluster.

In a conventional two-component mixture two percolation transitions occur at different values of x , corresponding to the formation of an infinite cluster for each of the two components.

References

- [1] Shunin Yu N, Schwartz K K 1997 *Computer Modelling of Electronic and Atomic Processes in Solids* ed R C Tennyson and A E Kiv Dodrecht/Boston/London: Kluwer Acad. Publisher 241-257
- [2] Shunin Yu N, Zhukovskii Yu F, Burlutskaya N Yu, Gopejenko V I, Bellucci S 2012 *Nanodevices and Nanomaterials for Ecological Security, Series: Nato Science for Peace Series B - Physics and Biophysics*, ed Yu Shunin and A Kiv Hiedelberg: Springer Verlag 237-262
- [3] Shunin Yu N, Zhukovskii Yu F, Gopejenko V I, Burlutskaya N, Lobanova-Shunina T and Bellucci S 2012 *Journal of Nanophotonics* 6(1) 061706-16
- [4] Shunin Yu N, Bellucci S, Zhukovskii Yu F, Gopejenko V I, Burlutskaya N, Lobanova-Shunina T, Capobianchi A, Micciulla F 2014 *Computer Modelling & New Technologies* 18(2) 7-23
- [5] Shunin Yu N, Zhukovskii Yu F, Bellucci S, 2008 *Computer Modelling & New Technologies* 12(2) 66
- [6] Shunin Yu N, Zhukovskii Yu F, Burlutskaya N, Bellucci S 2011 *Central Eur J Phys* 9(2) 519
- [7] Shunin Yu N, Gopeyenko V I, Burlutskaya N, Lobanova-Shunina T, Bellucci S 2013 Electromagnetic properties of CNTs and GNRs based nanostructures for nanosensor systems *Proc Int Conf „Physics, Chemistry and Application of Nanostructures (Nanomeeting-2013, Minsk, Belarus)* eds V E Borisenko, S V Gaponenko, V S Gurin and C H Kam New Jersey-London-Singapore: WorldScientific 250-3
- [8] D'yachkov P N, Kutlubayev D Z, Makaev D V 2010 *Phys Rev B* 82 035426
- [9] Ao Zh, Yang J, Li S 2011 Applications of AI Modified Graphene on Gas Sensors and Hydrogen Storage *Physics and Applications of Graphene – Theory* ed S Mikhailov Rijeka-Shanghai: InTech 534 p
- [10] Brito W H, Kagimura R, Miwa R H 2012 *Phys. Rev. B* 85 035404
- [11] Baibich M N, Broto J M, Fert A, Van Dau F N, Petroff F, Eitenne P, Creuzet G, Friederich A, Chazelas 1988 *J Phys Rev Lett* 61 2472
- [12] Jullière M 1975 *Phys Lett A* 54 225
- [13] Mott N F 1970 *Phil Mag* 22 7
- [14] Seager C H, Pike G E 1974 *Phys Rev B* 10 1435
- [15] Mott N F 1968 *Rev Mod Phys* 40 677-83

Authors	
	<p>Yuri N Shunin Current position, grades: Professor and Vice-Rector on academic issues at Information Systems Management University and a leading researcher at the Institute of Solid State Physics, University of Latvia. University studies: PhD (physics and maths, solid state physics, 1982) at the Physics Institute of Latvian Academy of Sciences and Dr. Sc. Habil. (physics and maths, solid state physics, 1992) at Saint-Petersburg Physical Technical Institute (Russia). Scientific interests: His current research activities concern nanophysics, nanoelectronics, nanodevices, nanomaterials, nanotechnologies, nanorisks, nanoeducation, and nanotechnology. Publications: over 470, 1 book with Springer Experience: director of NATO ARW "Nanodevices and Nanomaterials for Ecological Security," Riga, Latvia, 2011, a visiting researcher at Gesellschaft für Schwerionenforschung mbH, Darmstadt, Germany (1995), INFN—Laboratori Nazionali di Frascati, Frascati-Roma, Italy (2010 to 2015), participation in EU FP7 Projects CATHERINE (2008 to 2011) and CACOMEL (2010 to 2014), education practitioner in Higher Education from 1975 till nowadays</p>
	<p>Stefano Bellucci Current position, grades: PhD, Professor, currently coordinates all theoretical physics activities at INFN Laboratori Nazionali di Frascati (Italy). University studies: April 1982: Laurea in Physics (Magna cum Laude), University of Rome "La Sapienza" July 1984: Master in Physics of Elementary Particles, SISSA and University of Trieste, PhD in physics of elementary particles in 1986 at SISSA, Trieste, Italy. Publications: over 400 papers in peer-reviewed journals (with $h = 40$), and more than 10 invited book chapters, the editor of ten books with Springer Scientific interests: research interests include theoretical physics, condensed matter, nanoscience and nanotechnology, nanocarbon-based composites, and biomedical applications. Experience: He worked as a visiting researcher at the Brandeis University, Waltham, MA, USA (1983 to 1985); at the M.I.T., Cambridge, MA, USA (1985 to 1986); the University of Maryland, USA (1986 to 1987); at the University of California at Davis, USA (1987 to 1988). He is an editorial board member of the Springer Lecture Notes in Nanoscale Science and Technology, as well as the editorial board member of the Global Journal of Physics Express and the Journal of Physics & Astronomy</p>

	<p>Yuri Zhukovskii Current position, grades: Dr.Chem., Head of Laboratory of Computer Modeling of Electronic Structure of Solids, Institute of Solid State Physics (University of Latvia). Publications: He is the author of over 120 regular and review papers in international scientific journals. His Hirsch index is 16. Experience: From 1977 until 1995 he was a researcher at the Institute of Inorganic Chemistry, Latvian Academy of Sciences. Since 1995 he has been a leading researcher at the Institute of Solid State Physics, University of Latvia. Within the last 20 years he has been granted several fellowships for collaboration, visiting activities and positions at seven universities and scientific centers of Canada, Finland, Germany, United Kingdom, and the United States. He has also been actively engaged in developing active collaboration with some scientific groups in Belarus, Italy, Russia, and Sweden. Simultaneously, he has been a contact person and participant in a number of collaboration projects under support of European Commission. His current research activities concern theoretical simulations on the atomic and electronic structure of crystalline solids (with 3D, 2D and 1D dimensionalities).</p>
	<p>Victor Gopeyenko Current position, grades: professor, Dr.Sc.Eng Vice-Rector on scientific issues at Information System Management University and the director of ISMU Computer Technologies Institute. University studies: Riga Civil Aviation Engineering Institute (Latvia), obtained his doctor's degree (Dr. Sc. Eng., 1987) at Riga Civil Aviation Engineering Institute (Latvia). Scientific interests: current research activities concern nanophysics, nanoelectronics, nanodevices, and nanotechnologies in the EU FP7 Project CACOMEL (2010 to 2014). His special interests concern carbon nanotubes and graphene systems applications and modeling. Publications: 80 regular papers in international scientific journals Experience: he was the member of local organizing committee of NATO ARW "Nanodevices and Nanomaterials for Ecological Security," Riga, Latvia, 2011, he is the editor-in-chief of the journal 'Information Technologies, Management and Society' and editorial board member of the journal 'Innovative Information Technologies'.</p>
	<p>Nataly Burlutskaya Current position, grades: a researcher at the Information Systems Management University and the Institute of Solid State Physics, University of Latvia University studies: Master degree in computer systems (2011) at Information Systems Management University, Riga, Latvia. Scientific interests: current research activities concern theoretical simulations of the electronic and electrical properties of carbon nanotubes and graphene nanoribbons in the EU FP7 Project CACOMEL (2010 to 2014). Publications: 30 regular papers Experience: Nataly Burlutskaya was the secretary of organizing committee of NATO ARW "Nanodevices and Nanomaterials for Ecological Security," Riga, Latvia, 2011.</p>
	<p>Tamara Lobanova-Shunina Current position, grades: Associate Professor at Riga Technical University, Aeronautics Institute, PhD, Dr.edu University studies: University of Latvia, She obtained her PhD (2009) on innovative education at South-Ukrainian National University Scientific interests: current research activities concern nanotechnologies, nanomanagement, nanoeducation, nanorisks, and nanotechnology in the EU FP7 Project CACOMEL (2010 to 2014), special interests are connected with the systemic approach to nanosystems applications. Publications: 53 regular papers Experience: She was a member of the NATO ARW Local Organizing Committee 'Nanodevices and Nanomaterials for Ecological Security', Riga, Latvia, 2011. She has been working as a visiting researcher at INFN-Laboratori Nazionali di Frascati, Frascati-Roma, Italy (2010 to 2015). She was the Head of International Business Communications Department, Director of the study programme 'International Business Communications' at Information Systems Management University (till 2013). She is the Editorial Board member of the journal 'Innovative Information Technologies'. She is the author of over 53 scientific papers in international scientific journals.</p>

Authors' index	
Bellucci Stefano	7
Boroznin S V	15
Boroznina E V	15
Cricenti A	29
D'Acunto M	29
Davletova O A	15
Dinarelli S	29
Krutoyarov A A	19
Luce M	29
Maffucci A	8
Miano G	8
N Burlutskaya	35
Polikarpova N P	15
Polikarpova N P	19
S Bellucci	35
Shinkarev R V	23
Shunin Yu	35
T Lobanova-Shunina	35
V Gopeyenko	35
Yu Zhukovskii	35
Zaporotskova I V	15, 19, 23

NANOSCIENCE AND NANOTECHNOLOGY**A general frame for modeling the electrical propagation along graphene nanoribbons, carbon nanotubes and metal nanowires**

Maffucci Antonio, Miano Giovanni

Computer Modelling & New Technologies 2015 19(1A) 8-14

A general frame is proposed to model the propagation of electrical signals along nano-interconnects, either made by carbon nanotubes, graphene nanoribbons or metal nanowires. In the typical operating conditions of the next generations of integrated circuits, the electrodynamics of the nano-interconnects may be conveniently described by means of a semi-classical transport model, based on the modified Boltzmann transport equation. From this model we derive here a generalized non-local dispersive Ohm's law, which can be regarded as the constitutive equation for the material. From the knowledge of the conduction and valence subbands, it is possible to define an equivalent number of conducting channels, which affects the circuit parameters of such interconnects. The study of the dispersion introduced by the generalized Ohm's law gives a clear explanation to the different propagation properties of nano-interconnects made by carbon materials and conventional metals.

Keywords: Carbon Nanotubes, Graphene nanoribbons, Metal nanowires, Nano-interconnects, Transmission lines

Research into boron-carbon nanotube modified by alkaline metal atoms

Boroznin S V, Boroznina E V, Zaporotskova I V, Davletova O A, Polikarpova N P

Computer Modelling & New Technologies 2015 19(1A) 15-18

All articles must contain an abstract. The abstract follows the addresses and should give readers concise information about the content of the article and indicate the main results obtained and conclusions drawn. As the abstract is not part of the text it should be complete in itself; no table numbers, figure numbers, references or displayed mathematical expressions should be included. It should be suitable for direct inclusion in abstracting services and should not normally exceed 200 words. The abstract should generally be restricted to a single paragraph. These pages provide you with instructions on how to use this word template to prepare your paper according to the required layout and style for CM&NT papers.

Keywords: boron-carbon nanotubes, ionic-built covalent-cyclic cluster model, quantum chemical calculations, adsorption, metal superlattice

Adsorption of polyethylene, polypropylene, polyvinyl chloride monomer units on the single-walled carbon nanotube surface

Zaporotskova I V, Krutoyarov A A, Polikarpova N P

Computer Modelling & New Technologies 2015 19(1A) 19-22

The paper presents the results of research into the interaction mechanism between single-walled carbon nanotubes and most common polymers that results in the formation of stable polymer based nanotube reinforced composites. Nanotubes used as reinforcement provide strong as well as plastic polymer based nanocomposites that have a promising field of commercial application. The main characteristics of the interaction process between the nanotube (6, 6) and monomers of the polymers under study are defined. Calculations are performed by applying DFT method and B3LYP functional.

Keywords: carbon nanotubes, polyethylene, polypropylene, polyvinyl chloride, adsorptive interactions, polymer based nanocomposites, reinforcement, density functional theory method

Superfine drug-eluting polyvinylpyrrolidone based coating for biliary stents

Zaporotskova I V, Shinkarev R V

Computer Modelling & New Technologies 2015 19(1A) 23-28

Conduct the analysis of available type B residual current device in the market, compare their functions and technical characteristics, research their operation principle and feature, then propose the corresponding solution. Finally, develop a prototype and conduct the test. There are three samples. They are ABB RC223 residual current release, which can be combined with the Tmax T4 four-pole circuit-breaker in the fixed or plug-in version, Socomec earth leakage relay RESYS B 475 and Bender residual current monitor RCMA470LY

Keywords: residual current device (RCD), ABB RC223, circuit-breaker

Theory of near-field detection of core-gold nanoshells inside biosystems

M D'Acunto, A Cricenti, M Luce, S Dinarelli

Computer Modelling & New Technologies 2014 19(1A) 29-34

Metal nanoshells composed by a dielectric core with a thin gold layer are stimulating growing interests due to the unique optical, electric and magnetic properties exhibited by the local field enhancement near the metal – dielectric core interface due to strong local plasmon resonance and the high tunability of such resonance as a function of shape and core-material. These

unique characteristics have found promising applications in a wide range of areas, such as biosensing, optical communication and medicine. In this paper, we developed a theoretical and numerical simulation based on a near-field approach to study the possibility to identify nanoshells inside mouse cells. Taking advantage from the characteristic near-infrared transparency window of many biological systems, i.e. the low light absorption coefficient of biological systems between 750-1100nm, we show the possibility to identify and detect 100-150nm diameter gold nanoshells inside the animal cells.

Keywords: Gold nanoshells, Mie theory, SNOM, animal cells, Near-infrared

Nanocarbon electromagnetics in CNT-, GNR- and aerogel-based nanodevices: models and simulations

Yu Shunin, S Bellucci, Yu Zhukovskii, V Gopeyenko, N Burlutskaya, T Lobanova-Shunina

COMPUTER MODELLING & NEW TECHNOLOGIES 2015 19(1A) 35-42

Electromagnetic properties of nanocarbon systems are essential for the creation of various nanoelectronic devices. Our major attention is focused on CNTs, graphene nanostructures (e.g., GNR and GNF), graphene-based aerogels (GBA) and CNT-based aerogels (CNTBA) as the basis for high-speed nanoelectronics and prospective nanosensors. Special attention is paid to fundamental properties of CNTs, GNRs and various CNT-Me, GNR-Me, CNT-graphene interconnects. Nanosystems of 3D GBA and CNTBA are regarded as complicated systems made up of basic nanocarbon interconnected elements. Technological interest to contacts of CNTs or GNRs with other conducting elements in nanocircuits, FET-type nanodevices, GBA and CNTBA is the reason to estimate various interconnect resistances, which depend on chirality effects in the interconnects. Simulations of electromagnetic properties in interconnects have been performed to evaluate integral resistances, capacitances and impedances of various topologies (1D, 2D and 3D) in nanodevices, including their frequency properties (GHz&THz).

Keywords: CNTs - carbon nanotubes, GNR – graphene nanoribbons, CBA – Carbon Based Aerogels, Carbon Nanoporous Materials, Carbon-based nanocomposites

Operation Research: Modelling and Simulation		
Zhang Huyin, Wang Jing, Xu Fang, Xu Ning, Wang Zhiyong, Zhou Xuejun, Lin Haitao, Yu Peng, Zhou Yuanyuan	An improved adaptive weighted clustering algorithm based on time interval grade in Mobile Ad Hoc networks	7
Karatun N, Khatjatouski S, Statsenko A	Calculation modelling of static constructions	15
Wang Xiaodong, Yang Jianhui	Application of the fiber image detection algorithm based on the Grey system theory and Directed graph	18
Liu Wei, Tang Cunchen, Kang Fan	Research in search engine user behaviour based on cloud computing	23
Zhu Shan hong	Worm detection and prevention based on network segmentation algorithm	29
Liu Feng, Wang Jing	Selection method of wireless communication modes in internet of vehicles	33
Cao XiaoBo, Xu ChengDong, Fan GuoChao	Study on the task scheduling problem of complicated products' design	41
Solomentsev O, Zuiev O, Zaliskyi M, Yashanov I	Diagnostics programs efficiency analysis in operation systems of radioelectronic equipment	49
Wang Chaoyou	Time series neural network systems in stock index forecasting	57
Zhu Shan hong	Study on the electrodeposited Au-Co alloy coating	62
Ma Yun, Si Hua	The micro-structure study on mechanical properties of Dredge fills	66
Zheng Jiahzu, Gao Yehemin	Method of calculating forest land surface area based on automatic boundary extraction	72
Wang Ying	Application of computer virtual reality technology in ship equipment assembly	77
Ji Fengquan, Jia Yuanyuan	Ecological architecture system based on landscape ecology	80
X B Hong, N Z Li, W W Yin, J H Feng, G X Liu	Modelling and simulation of relationship between internal cell temperature and apparent resistivity for lithium-ion battery	85
Authors' Index		92
Cumulative Index		93



An improved adaptive weighted clustering algorithm based on time interval grade in Mobile Ad Hoc networks

Huyin Zhang¹, Jing Wang^{1, 2*}, Fang Xu¹, Ning Xu¹, Zhiyong Wang¹, Xuejun Zhou², Haitao Lin², Peng Yu², Yuanyuan Zhou²

¹Computer Institute of Wuhan University, Wuhan, Hubei province, China

²Department of Information and Network Technology, Electronic Engineering School, Naval University of Engineering, Wuhan, Hubei, China

*Corresponding author's e-mail: wang_jing28@126.com

Received December 2014, www.cmnt.lv

Abstract

Mobile Ad Hoc Networks (MANETs) are self-configuring dynamic networks of mobile devices connected by wireless links without any fixed infrastructure or centralized administration. In order to achieve stable clusters, the cluster-heads (CHs) maintaining the cluster should be stable with minimum re-affiliation times and number of changes on CHs, with maximal throughput of the clustering formation and maintenance. An improved adaptive weighted clustering algorithm based on time interval grade (IATIGWCA) in MANETs is proposed. Each node can be assigned an adaptive role and set its status value through their Hello messages in the formation procedure of clusters, and an appropriate CH of a cluster is elected by the calculation the total weight which comprising four factors: degree difference, average Euclidean distance, average relative speed and consumed battery power. In the maintenance procedure of clusters, the duration of clustering maintenance is set to 2 grades which are Little Time Slot and Big Time Slot in order to improve the efficiency of clustering and decrease the times of computation of the total weight of every node. The simulation results show that the selection of numbers of CHs and numbers of clusters in the stage of the formation of clusters is an optimal solution which brings higher throughput, less re-affiliation times, less number of changes on CHs and longer residence time of cluster in IATIGWCA than LID and WCA.

Keywords: clustering, cluster-head (CH), time interval grade, clustering maintenance

1 Introduction

Mobile Ad Hoc Networks are called MANETs, comprising a great deal of mobile devices that form the wireless networks without any fixed infrastructure or centralized administration. In fact, MANETs are dynamic because of the mobility of device nodes. Every node interconnects with each other and performs as a router or a package forwarder.

With the continuous increase of the size of MANETs, flat routing schemes do not scale well in terms of performance. The routing tables and topology information become more and more tremendous. In order to enhance the low bandwidth utilization and reduce the high overhead of using routing schemes in large networks, some kind of organization structure of nodes is required, and thus grouping a number of nodes into an easily manageable set which is called "Cluster". Clustering (grouping a number of nodes into a cluster) is the most popular method to impose a hierarchical structure in MANETs. In clustering algorithm, CHs are responsible for the designation of the members of the clusters and maintenance of the topology of the network, and then selecting a suitable node in a cluster as a Cluster-Head (CH) is so important. Herein, CHs act as local coordinators and handle various network functions. The clusters are able to store minimum topology information; each CH acts as a temporary base station within its cluster and communicates with other CHs. A clustering scheme should

be adaptive to changes with minimum clustering management overhead, which is incurred by changes in the network topology. Due to the mobility of device nodes, their affiliation and disaffiliation from clusters perturb the stability of the network and the reconfiguration of CHs is unavoidable. It is a serious issue that the frequent changes of CHs adversely affect the performance of other mechanisms or protocols such as scheduling, routing and resource allocation [1].

An efficient clustering algorithm must adapt itself to frequently and unpredictable topology changes in MANETs. It must generate stable clusters as much as possible to reduce their update times, which can result in updates of other information such as routing, security and management information. Otherwise, recomputation of CHs and frequent information exchange among the participating nodes will bring high computation overhead. Therefore, a proper maintenance scheme of the process of clustering should be designed, and the overhead of electing CHs and maintenance should be least, and high frequency of re-affiliation (the process of joining a new cluster) could be decreased as much as possible.

In this paper, we propose an improved adaptive weighted clustering algorithm based on time interval grade (IATIGWCA) in MANETs to maintain stable clusters by electing a node with strong battery power as a CH to decrease the re-affiliation as much as possible, minimizing

the number of clusters, and minimizing the number of changes on CHs and maximizing the throughput for the clustering formation and maintenance.

The rest of this paper is organized as follows. In Section II, we review previous related several clustering algorithms proposed. Section III presents the proposed algorithm for MANETs. The conditions of experimental setup and simulation results of the proposed algorithm are given in Section IV. Finally, we give conclusions of this paper in Section V.

2 Related work

In order to enhance network manageability, channel efficiency and energy economy, a several classic clustering algorithms in wireless ad hoc networks have been investigated in the past. Probably the most crucial point when dealing with clustering is the criterion how to choose the CHs. The number of CHs and average number of changes on CHs strongly influences the communication overhead and latency. And some classic clustering mechanisms have been proposed, namely, Lowest-ID [2], Highest-Connectivity [3], Distributed Mobility-Adaptive Clustering Algorithm [4], Distributed Dynamic Clustering Algorithm [5], Node-Weight Clustering Algorithm [4], and Weighted Clustering Algorithm (WCA) [1]. And they are as described below.

A. Lowest-ID Clustering Algorithm (LID):

Each node is assigned a distinct ID and broadcasts the list of IDs of nodes that it can hear including its own ID periodically. A node, which only hears nodes having higher IDs than its own ID, becomes a CH. And the lowest-ID node that a node hears is its CH, unless the lowest-ID specifically gives up its role as a CH. If a node can hear two or more CHs, it is a Gateway. Then, the other nodes are ordinary nodes.

B. Highest-Connectivity Clustering Algorithm:

Each node broadcasts the list of IDs of nodes that it can hear including its own ID. If a node is elected as a CH if it is the most highly connected node of all its uncovered neighbor nodes. In case of a tie, the lowest-ID prevails. And if a node which has not elected its CH yet, is an uncovered node, otherwise it is a covered node. When a node has already elected another node as its CH, it gives up its role as a CH.

Due to resource limitations, a CH may not be able to handle a large number of nodes, and resulting in more number of changes on CHs can lead to instability of the cluster.

C. Distributed Mobility-Adaptive Clustering Algorithm (DMAC):

This algorithm determines the CHs not based on the node ID, but based on the nodes generic weights W , which is a positive real number. Ideally, the W captures the mobility and reliability of a node and characterizes the preferences on which a node is suitable as CH. An example for a mobility based metric for clustering is given in [6].

Each node determines its role as either an ordinary node or a CH on its own. Only local information is required. That is, the role of a node is determined by using its node ID and its node weight, as well as the weights of all its neighbors, and, for cases where ties occur, their node IDs. In order to allow for fast communication between two nodes, the DMAC algorithm requires every node to be connected to at least one CH. Moreover, no two CHs can be one-hop

neighbors. This is used to ensure that the CHs are well spread out in the network. A node that is added to the network starts an initialization algorithm that determines its role in the network. The decision is based on its own weight and its neighbors' weight. If the new node has a neighboring CH with a higher node weight, it decides to be an ordinary node, joins the cluster corresponding to that CH and sends a Join-message. Otherwise, it decides to become a CH itself and sends out a message of CH. This helps the neighbor nodes in getting the information about the existence and role of a new node.

D. Distributed Dynamic Clustering Algorithm (DDCA):

The (α, t) criterion of DDCA describes a probabilistic bound α on the availability of paths in the corresponding cluster over a certain time t . A new node seeking a cluster to join sends out a JoinRequest message. If it does not receive any responses, it basically builds a new cluster and becomes a CH. If the new node upon sending a JoinRequest receives one or more JoinResponse messages before its JoinTimer runs out, it decides to join the cluster with the highest (α, t) value. This value has to exceed the minimum required value (α, t) threshold, otherwise the JoinResponse is ignored. And the cluster strength, seen by a node m and given by the (α, t) value, gives the measure of the availability of a path from the node m over some initial hop node n to the CH of the corresponding cluster.

An important property of DDCA is that new nodes tend to join existing cluster. New nodes don't first of all seek to become CHs, hence the clustering algorithm is very stable. However, it is disadvantageous in this algorithm that the suitability of nodes to be a CH is not considered in the CH election process.

E. Node-Weighted Clustering Algorithm (NWC):

In this approach, each node is assigned weights based on its suitability of being a CH. A node is chosen to be a cluster head if its weight is higher than any of neighbor's weight; otherwise, it joins a neighboring cluster head. The smaller ID node id is chosen in case of a tie. Making an assumption is that the network topology does not change during the execution of the algorithm. To verify the performance of the system, the nodes were assigned weights which varied linearly with their speeds but with negative slope. Since node weights were varied in each simulation cycle, computing the cluster heads becomes very expensive.

F. Weighted Clustering Algorithm (WCA):

The Weighted Clustering Algorithm (WCA) was originally proposed by M. Chatterjee et al [1]. In order to decide how well suited a node is for being a CH and maintenance of cluster is more reasonable, four factors are taken into account. And the four factors are node degree ($V1$), distance summation to all its neighboring nodes ($V2$), mobility ($V3$) and remaining battery power ($V4$) respectively.

So, the clustering problem is converted into an optimization problem since an objective function is formed. The weight of a node is calculated as

$$W_{node} = w1 \times V1 + w2 \times V2 + w3 \times V3 + w4 \times V4$$

Keeping in view the above factors, the combined weight for each node is calculated. The node with the smallest weight is then chosen as the CH. One of the drawbacks of

this algorithm is that it uses the concept of global minima. All the nodes in the network have to know the weights of all the other nodes before starting the clustering process. This process can take a lot of time. Also, two CHs can be one-hop neighbors, which results in the clusters not necessarily being spread out in the network, and the overhead induced by WCA is very high.

3 Proposed algorithm: an improved adaptive time interval grade-based weighted clustering algorithm (IATIGWCA)

A. Objectives.

In order to design and implementing the IAIGWCA algorithm, the core objectives are underlying points:

1. The clusters of MANET should be efficient and stable, and some hello messages between CHs and cluster members are needed to maintain the routing structure and avoid congestion in the network.
2. The selection of numbers of CHs and numbers of clusters in the stage of the formation of clusters is an optimal solution which brings higher throughput versus some classic algorithms (LID and WCA) [7].
3. In the stage of the maintenance of the clusters, the CHs have to be re-elected in the specified time interval. So the re-affiliation times of the clusters should be less, and the residence time of cluster should be longer.

B. The formation procedure of clusters.

We consider that MANET is represented by an undirected graph $G = (V, E)$ where V is the set of nodes and E is the set of bi-directional communication links. In the formation phase of clusters, V is divided into a collection of subsets $\{V_1, V_2, \dots, V_n\}$, where $V = \bigcup_{i=1}^n V_i$. And every subset V_i induces a connected sub graph of G , and is called cluster set which can overlap.

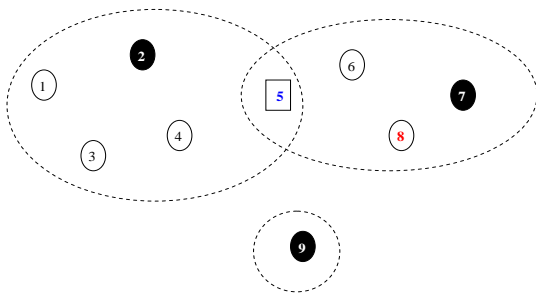


FIGURE 1 Roles assignment of nodes in different clusters

Figure 1 shows the distribution of the nodes of clusters, and the difference of roles of nodes is presented. The roles of nodes in clusters are classified four types: cluster-head (CH), gateway, ordinary member and original role. For example, node 2, 7 and 9 are CHs which are responsible for the designation of the members of the clusters and maintenance of the topology of the network. Node 5 is a gateway node which is responsible for data relaying between clusters; node 8 is a new original node which has not joined in any cluster, not liking the ordinary member nodes which are including node 1, 3, 4 and 6.

Therefore, all nodes of clusters have their roles, and the role assignment algorithm of member nodes in clustering setup is given as follows.

Algorithm 1. Role assignment of member nodes in clustering setup.

Every node can receive the Hello messages from its all 1-hop neighbors.

- 1: **IF** node u which is not a cluster-head receive a MAC_{CH}
- THEN**
- 2: Assign the status of node u to an ordinary member role, and its status value is 1.
- 3: Update the neighborhood lists of node u .
- 4: **IF** node u receive another MAC_{CH} **THEN**
- 5: Assign the status of node u to a gateway role, which node is responsible for data relaying between clusters, and its status value is 2.
- 6: Update the neighborhood lists of node u .
- 7: **END IF**
- 8: **ELSE IF** node u is a cluster-head **THEN**
- 9: Assign the status of node u to a cluster-head role, and its status value is 0.
- 10: Update the neighborhood lists of node u .
- 11: **ELSE IF** node u which is not a cluster-head does not receive a MAC_{CH} **THEN**
- 12: Assign the status of node u to an original role which has not joined in any cluster, and its status value is 3.
- 13: Update the neighborhood lists of node u .
- 14: **END IF**

In the algorithm 1, every node can receive the Hello messages from its neighbors. According to their Hello messages, the node can be assigned an adaptive role and set its status value in the procedure of clustering setup. MAC_{CH} is the physical address of cluster head in an ordinary cluster.

However, the election method of CH is most important part in the procedure of clustering setup. An improved adaptive time interval grade-based weighted clustering algorithm (IATIGWCA) is proposed.

Algorithm 2. Calculation the total weight of node u in clustering setup.

- 1: Compute the degree difference Δ_u of the node u , $\Delta_u \leftarrow |d_u - N|$, where d_u is the degree of connectivity of the node u by counting its neighbors, and N is a predefined threshold, i.e. the ideal number of nodes that a cluster-head can manage ideally.

- 2: Compute the average Euclidean distance \overline{D}_u between the node u and its all neighbors, and a predefined moving duration of node u is partitioned several intervals ($n \Delta t$), $\overline{D}_u \leftarrow$

$$\frac{\sum_{i=1}^n \sqrt{(X_u(t_i) - X_v(t_i))^2 + (Y_u(t_i) - Y_v(t_i))^2}}{\sum_{v \in \text{Neighbour}(u, n\Delta t)} n}, \text{ where } (X_u(t_i), Y_u(t_i)) \text{ is the position of the node } u \text{ at the } i\text{-th interval}$$

- 3: Compute the average relative speed \overline{V}_u , utilizing the same

$$\text{method of } \overline{D}_u, \overline{V}_u \leftarrow \frac{\sum_{j=1}^n |v_{u(t_j)} - v_{(t_j)}|}{\sum_{v \in \text{Neighbour}(u, n\Delta t)} n}$$

- 4: Compute the consumed battery power E_u of the node u

5: Calculate the total weight of the node u ,
 $W_u = w_1 \times \Delta_u + w_2 \times \overline{D}_u + w_3 \times \overline{V}_u + w_4 \times E_u$, where w_1, w_2, w_3, w_4 are the weighting factors and $w_1 + w_2 + w_3 + w_4 = 1$

6: Elect the node u which its total weight value is the minimum of the all cluster nodes as a cluster-head (dominant set)

In the algorithm 2, an adaptive CH of a cluster is elected through the calculation the total weight in clustering setup. Like WCA algorithm, four factors are taken into account, and the four factors are degree difference Δ_u , average Euclidean distance \overline{D}_u , average relative speed \overline{V}_u and consumed battery power E_u respectively. The CH has the least total weight value.

C. The maintenance procedure of clusters.

The election of CH during the formation stage of clusters may not remain the best choice for long in an emergency MANET. Due to the mobility and consumption of battery power, we have to monitor the performance of the CHs and every member node by periodically updating the relative location information *Position* and the relative speed information *Speed* as follows.

Step 1: In the maintenance procedure of clusters each node periodically broadcasts the Hello message to its neighbors, which is shown below [8].

MAC _u	MAC _{CH}	Channel	Status	Position	Speed	Priority
------------------	-------------------	---------	--------	----------	-------	----------

FIGURE 2 Format of Hello message

TABLE 1 Neighborhood main list of node u

$ID_{neighbour}$	$MAC_{neighbour}$	Channel	Status	Priority
a	xx-xx-xx-xx-xx-xx	0	0	0.65
b	xx-xx-xx-xx-xx-xx	3	1	0.48
c	xx-xx-xx-xx-xx-xx	4	1	0.34

TABLE 2 Neighborhood sub-list of node u

$ID_{neighbour}$	i	D_i	V_i
a	0	$D_0 = \sqrt{(X_a(t_0) - X_u(t_0))^2 + (Y_a(t_0) - Y_u(t_0))^2}$	$V_0 = V_a(t_0) - V_u(t_0) $
a	1	D_1	V_1
a	2	D_2	V_2
a
b	0	$D_0 = \sqrt{(X_b(t_0) - X_u(t_0))^2 + (Y_b(t_0) - Y_u(t_0))^2}$	$V_0 = V_b(t_0) - V_u(t_0) $
b	1	D_1	V_1
b	2	D_2	V_2
b

In Table 1, the parameters, such as $ID_{neighbour}$, $MAC_{neighbour}$, Channel, Status and Priority are the same meaning as the Hello message's. And in Table 2, during every Hello message cycle i , the $Position_i$ and $Speed_i$ value are saved and calculated in D_i and V_i , therein the value of i is from 0 to $N-1$.

In order to improve the efficiency of clustering and decrease the times of computation of the total weight of

MAC_u : Physical address of node u ;

MAC_{CH} : Physical address of cluster head in an ordinary cluster;

Channel: Through utilizing the different channels, data can be transmitted from node u to its neighbor nodes;

Status: Status information of node u , where value 0 means that node u is a cluster-head; value 1 indicates that u is an ordinary node in a cluster; value 2 represents that u is a gateway node which is affiliated with several clusters; value 3 means that node u has not joined any cluster and it is regarded as a new node;

Position: Relative location information of node u , including its x-coordinate and y-coordinate;

Speed: Relative speed information of node u , including its direction and value for system of coordinates;

Priority: Priority of node u in grade of Little Time Slot, through comparing the priority with its neighbor's, the node which has a least priority can become a new cluster-head.

Step 2: Each node builds up a neighborhood main list and a sub-list with the aid of the Hello messages sent by its neighbors, and the neighborhood lists are periodically updated according to the Hello messages received, and its explicit format are shown in Table 1 and Table 2.

every node, the duration of clustering maintenance is set to 2 grades which are Little Time Slot and Big Time Slot.

Phase 1: in Little Time Slot, priority of node u is calculated periodically. And then node u forwards it to its neighbor nodes. Through comparing the Priority value of node u and its neighborhood, the node x which has a least priority can be elected as a new cluster-head (dominant set), and its status value is set to 0, updating the neighborhood lists of the node x . i.e. algorithm 3 is executed.

For example, the priority of node u is 0.37, and the priorities of a, b and c are 0.65, 0.48 and 0.34 separately. Through comparison, node c has the least priority value, and it is elected as a new cluster-head.

The computation and comparison algorithm of priority of nodes in grade of Little Time Slot is proposed in algorithm 3.

Algorithm 3. Computation and comparison of priority of nodes in grade of Little Time Slot.

1: In order to improve the efficiency of clustering and decrease the times of computation of the total weight of every node, the duration of clustering maintenance is set to 2 grades which are Little Time Slot and Big Time Slot, and elect which one become a new cluster-head through comparing the priority of nodes in grade of Little Time Slot.

2: Define the priority of node u is PRI_u , $PRI_u \leftarrow \frac{\sum_{k \in Neighbour(u)} P_k \times \log(P_k)}{\log C(Neighbour(u))}$, $\alpha \times E_{remainder} + \beta \times (-H(u))$, $H(u) \leftarrow \frac{\sum_{k \in Neighbour(u)} P_k \times \log(P_k)}{\log C(Neighbour(u))}$, $P_k \leftarrow \frac{\sqrt{(X_k - X_u)^2 + (Y_k - Y_u)^2}}{\sum_{i \in Neighbour(u)} \sqrt{(X_i - X_u)^2 + (Y_i - Y_u)^2}}$, where α, β are the

priority factors and $\alpha + \beta = 1$, and $E_{remainder}$ is the remaining power of node u , and $H(u)$ is the entropy of node u , and $C(Neighbour(u))$ is the cardinality (degree) of set $Neighbour(u)$.

3: IF a new arrival node u (status value is 3) is moving into a cluster THEN

4: Compute the priority of node u PRI_u , and compare with PRI_{CH} .

5: IF $PRI_u > PRI_{CH}$ THEN

6: Elect node u as a new cluster-head (dominant set), and its status value is 0.

7: Update the neighborhood lists of node u .

8: Assign the status of old cluster-head (CH_{old}) to an ordinary member role, and its status value is 1.

9: Update the neighborhood lists of old cluster-head (CH_{old}).

10: ELSE IF $PRI_u \leq PRI_{CH}$ THEN

11: Node u join in the cluster, and the status of node u is assigned to an ordinary member role, and its status value is 1.

12: Update the neighborhood lists of node u .

13: The cluster-head (CH) continues its role.

14: END IF

15: ELSE IF the cluster has not new arrival node, or lose some member node(status value is 1 or 2) THEN

16: For each member node N_i in the $ClusterSet$ do

17: IF $PRI_{N_i} > PRI_{CH}$ THEN

18: Elect node N_i as a cluster-head of the cluster, and its status value is 0.

19: Update the neighborhood lists of node N_i .

20: Assign the status of old cluster-head (CH_{old}) to an ordinary member role, and its status value is 1.

21: Update the neighborhood lists of old cluster-head (CH_{old}).

22: END IF

23: END FOR

24: END IF

Phase 2: in Big Time Slot, total weight of node u is calculated periodically. Big Time Slot period is partitioned N times Little Time Slot period, and a Hello message can be broadcasted from a node in Little Time Slot period, and N depends on the specific network topology. During every Little Time Slot period i , the euclidean distance D_i between the node u and its all neighbors is computed,

$$D_i = \sqrt{(X_{neighbours}(t_i) - X_u(t_i))^2 + (Y_{neighbours}(t_i) - Y_u(t_i))^2}$$

and relative speed V_i between the node u and its all neighbors is computed, $V_i = |V_{neighbours}(t_i) - V_u(t_i)|$. Through executing algorithm 2, the node y which its total weight value is the minimum of the all cluster nodes is elected as a new cluster-head (dominant set), and its status value is set to 0, updating the neighborhood lists of the node y .

The re-election algorithm of cluster-head in grade of Big Time Slot is proposed in algorithm 4.

Algorithm 4. Re-election procedure of cluster-head in grade of Big Time Slot.

1: In grade of Big Time Slot, according to Algorithm 1, the total weight of every node is compared with its cluster-head (CH)'s for a predefined long duration.

2: For each node N_j in the $ClusterSet$ do

3: IF $W_{N_j} < W_{CH}$ THEN

4: Re-elect N_j as a new cluster-head (dominant set), and its status value is 0.

5: Update the neighborhood lists of node N_j .

6: Assign the status of old cluster-head (CH_{old}) to an ordinary member role, and its status value is 1.

7: Update the neighborhood lists of old cluster-head (CH_{old}).

8: ELSE IF $W_{N_j} \geq W_{CH}$ THEN

9: Don't perform the re-election and the cluster-head (CH) continues its role.

10: END IF

11: END FOR

4 Experimental setup and results

A. Simulation environment and parameters.

In order to evaluate the performances of the proposed clustering algorithm (IAGWCA), we implemented the proposed algorithm in NS2 [9]. We performed different simulation scenarios, and through the simulation to evaluate the performance metric of different classic algorithm, such as average number of clusters, average number of changes on CHs, re-affiliation times, average number of clusters, throughput and average cluster residence time. We use a commonly used mobility model such as the Random Way Point model [10] that represents a particular case of the Random Trip model [11]. In the Random Way Point model, each node chooses its direction and its speed according to a fixed time interval [12]. The move of the node is done

during a time Δt with some pauses. However, the possibility of no pause represents the Random Walk model. Other basic parameters used in our experiments are summarized in the Table 3.

TABLE 3 Simulation parameters

Parameter	Value
Number of nodes	20-120
Size of network	500m×500m
Speed of the nodes	2-15Km/h
Transmission range	30-300m
Pause Time	1 sec
Little Time Slot (Hello Interval)	4 sec
Big Time Slot	40 sec
Frequency band	5.4GHz
Size of cluster	12 nodes
Time of simulation	400 sec

According to the experimental environment, in the calculation of the algorithm 2, we can set $w_1=0.2$; $w_2=0.3$; $w_3=0.3$; $w_4=0.2$, in order to compute the appropriate total weight of each node in clustering setup.

B. Metrics and simulation results.

The following metrics serve as the ways of our performance evaluations, contrasting the Lowest-ID Clustering Algorithm (LID), Weighted Clustering Algorithm (WCA) and the proposed clustering algorithm (IAGWCA).

a. The average number of clusters:

$$\frac{\text{number of nodes}}{\text{average number of nodes in a cluster}} ;$$

b. The average number of changes on CHs:

$$\frac{\text{total number of changes on CHs}}{\text{number of CHs}} ;$$

c. The re-affiliation times: times of re-election procedure of cluster-head;

d. The throughput: data transmitting rate of all clusters;

e. The average cluster residence time:

$$\frac{\text{total stable time of all clusters}}{\text{number of clusters}} .$$

Figure 3 shows the variation of the average number of clusters with respect to the transmission range from 30m to 200m. The results are indicated for three different values of number of nodes (30 nodes, 70 nodes and 120 nodes). We observe that the average number of clusters is decreased when the transmission range increases, and the reason is that the node with a higher transmission range means it covers a larger area in wireless network.

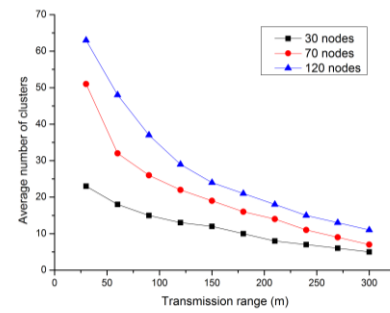


FIGURE 3 Average number of clusters versus transmission range

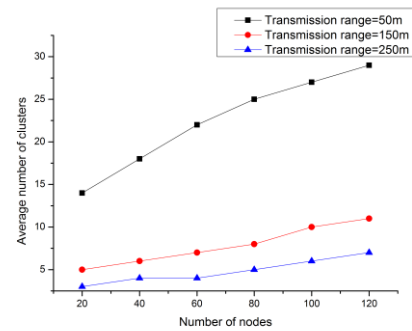


FIGURE 4 Average number of clusters versus number of nodes

Figure 4 presents the relationship between the average number of clusters and the number of nodes on the three different conditions of the transmission range (50m, 150m and 250m). As is shown in Figure 3, a bigger number of nodes can increase the average number of clusters, and the average number of clusters is less dynamic when the transmission range increases.

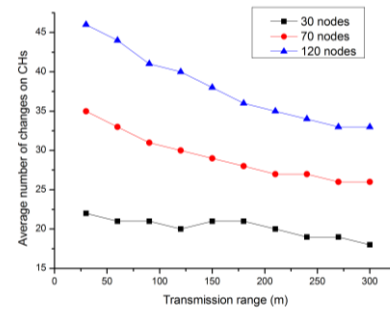


FIGURE 5 Average number of changes on CHs versus transmission range

In Figure 5, we can observe that the average number of changes on CHs decreases and the clusters, in which the nodes tend to remain in the range of their neighbors become more and more stable when the transmission range begins to be larger. And the number of nodes becomes more and more, while the influence of transmission range on average number of changes on CHs is less and less.

Figure 6 depicts that the average number of clusters increases when the maximum speed of node begins to be larger. Our proposed algorithm exhibits a lower sensitivity to the maximum speed of node than the LID and WCA. The improved resilience against node velocity fluctuations is attributed to the quantitative consideration of the average

relative node-mobility measure (speed) and the neighbourhood list of every node.

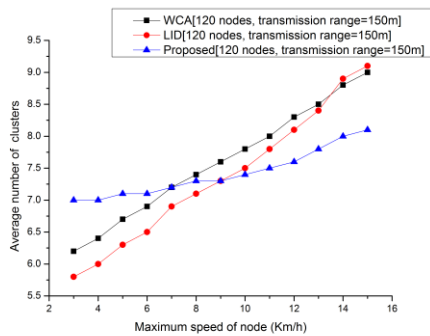


FIGURE 6 Average number of clusters versus maximum speed of node

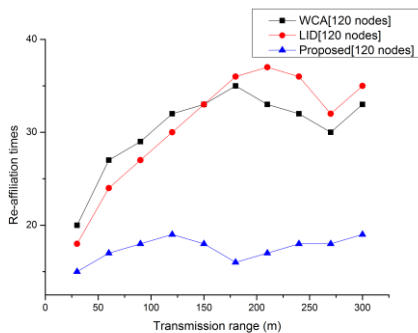


FIGURE 7 Re-affiliation times versus transmission range

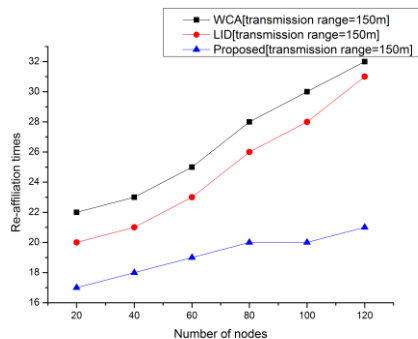


FIGURE 8 Re-affiliation times versus number of nodes

The re-affiliation times for three algorithms increases when the transmission range begins to be larger as described in Figure 7. And the times of LID and WCA are almost twice than the proposed which exhibits a lower sensitivity to the transmission range. This is due to the nodes of clusters in IAGWCA is more stable than the others. In Figure 8, we can observe the re-affiliation time is a direct proportion function of the number of nodes. The same phenomena are that the times of the proposed is lower than the others.

Figure 9 plots the throughput for three algorithms achieved in bits/second as a function of the maximum speed of node. As is shown, the proposed is found to achieve a better throughput than LID and WCA. It is clear that the maximum speed of node increases there is a reduction in the throughput of the network.

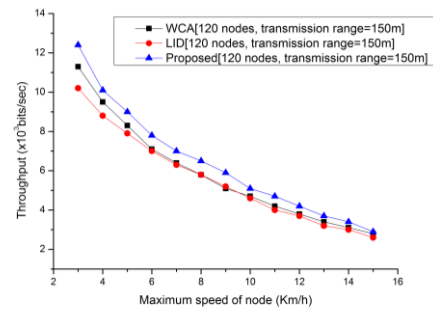


FIGURE 9 Throughput versus maximum speed of node

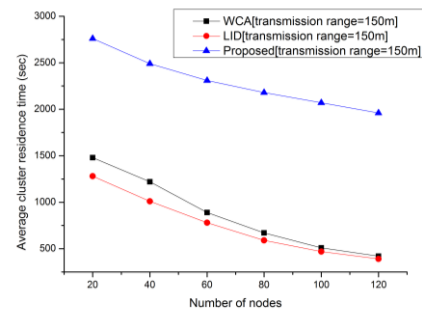


FIGURE 10 Average cluster residence time versus number of nodes

In Figure 10, the average cluster residence time for three algorithms is described versus number of nodes. It can be seen that when number of nodes increases, for three algorithms the average cluster residence time is decreased, and it confirms that the average cluster residence time of proposed is almost twice than the other two.

5 Conclusions

This paper has presented an improved adaptive weighted clustering algorithm based on time interval grade (IATIGWCA) in MANETs to maintain stable clusters. In the formation procedure of clusters, according to their Hello messages, each node can be assigned an adaptive role and set its status value. And through the calculation the total weight an appropriate CH of a cluster is elected. In the calculation the total weight, four factors are taken into account, such as degree difference, average Euclidean distance, average relative speed and consumed battery power. And in the maintenance procedure of clusters, the duration of clustering maintenance is set to 2 grades which are Little Time Slot and Big Time Slot in order to improve the efficiency of clustering and decrease the times of computation of the total weight of every node. Simulation results indicated that the selection of numbers of CHs and numbers of clusters in the stage of the formation of clusters is an optimal solution which brings higher throughput in IATIGWCA than LID and WCA. Furthermore, the re-affiliation times of the clusters and the average number of changes on CHs can be less, and the residence time of cluster should be longer in the maintenance procedure of clusters.

Acknowledgments

Wang Jing thanks for being supported by the National Natural Science Foundation of China under Grant No.

61272454 and the Specialized Research Fund for the Doctoral Program of Higher Education of China under Grant No. 20130141110022.

References

[1] Chatterjee M, Das S K, Turgut D 2002 WCA: A Weighted Clustering Algorithm for Ad hoc Networks *Clustering Computing* **5** 193-204

[2] Ephremides A, Wieselthier J E, Baker D J 1987 A Design Concept of Reliable Mobile Radio Networks with Frequency Hopping Signaling *Proceedings of the IEEE* **75**(1) 56-73

[3] Gerla M, Tsai J 1995 Multicluster, mobile, multimedia, radio network ACM-Baltzer Journal of Wireless Networks **1**(3) 255-65

[4] Basagni S 1999 Distributed Clustering for ad hoc networks In Proceedings of International Symposium on Parallel Architectures, Algorithms, and Networks (IS-PAN) Perth/Fremantle Australia 310-5

[5] McDonald A B, Znati T F 1999 A mobility-based framework for adaptive clustering in wireless ad hoc networks *IEEE Journal on Selected Areas in Communications* **17**(8) 1466-87

[6] Basu P, Khan N, Little T D C 2001 A mobility Based Metric for Clustering in Mobile Ad Hoc Networks *In Proceedings of IEEE ICDCS 2001 workshop on Wireless Networks and Mobile Computing Phoenix AZ* 412-8

[7] Rohini S, Indumathi K 2011 Consistent Cluster Maintenance Using Probability Based Adaptive Invoked Weighted Clustering Algorithm in MANETs *In Proceedings of the National Conference on Innovations in Emerging Technology-2011 Kongu Engineering College India* **17&18** 37-42



[8] Wu K, Zhong Z, Hanzo L 2010 A Cluster-head Selection and Update Algorithm for Ad Hoc Networks *In Proceedings of IEEE Globecom 2010 Miami FL* 6-10

[9] The Network Simulator-ns-2. <http://www.isi.edu/nsnam/ns/>

[10] Navidi W, Camp T 2004 Stationary distributions for the random waypoint mobility model *IEEE Transactions on Mobile Computing* **3**(1) 99-108

[11] Boudec J Y L, Vojnovic M 2005 Perfect simulation and stationarity of a class of mobility models In Proceedings of the IEEE Infocom: 24th Annual Joint Conference of the IEEE Computer and Communications Societies **4** 2743-54

[12] Lin G, Noubir G, Rajaraman R 2004 Mobility models for ad hoc network simulation In Proceedings of IEEE Infocom: Twenty-third Annual Joint Conference of the IEEE Computer and Communications Societies **1** 1433-9

Authors	
	<p>Zhang Huyin, 02.1962, Wuhan, China</p> <p>Current position, grades: professor, PhD supervisor in Computer Institute of Wuhan University in China. University studies: Computer Institute of Wuhan University, Wuhan, Hubei province, China. Scientific interest: architecture of computer and computer network. Publications: 15 papers, 6 books. Experience: 18 research projects.</p>
	<p>Wang Jing, 08.1980, Wuhan, China</p> <p>Current position, grades: PhD the fourth grade. University studies: Computer Institute of Wuhan University, Wuhan, Hubei province, China. Scientific interest: wireless network and architecture of computer. Publications: 5 papers, 3 books.</p>

Calculation modelling of static constructions

N Karatun^{1*}, S Khatjatouski², A Statsenko²

¹ISMA University, 1 Lomonosov Str., build. 6, LV-1019, Riga, Latvia

²Belarusian-Russian University, 43 Mir Avenue, Mogilev, 212000, Belarus

*Corresponding author's e-mail: nmata_li@inbox.lv

Received 18 December 2014, www.cmnt.lv

Abstract

The mathematic model of force loads calculations of static constructions in the framework of Theoretical Mechanics course is presented. The software to visualize and analyse force loads of static constructions is created.

Keywords: theoretical mechanics, informative systems of engineering analysis, visualization and analysis of static constructions, visualization of the force loading

1 Introduction

Computer-Aided Design (CAD) systems have spread widely in engineering to create solid models of real solid bodies as well as to simulate their motion and interaction. NX, Solid Edge, CATIA, SolidWorks, Inventor, Creo Elements/Pro, etc. [1, 2] are among the software products that are used for the purpose above. These CAD systems have numerous disadvantages preventing their usage for academic studies, for instance, within Theoretical Mechanics course. One of the drawbacks to utilize them for the course is CAD versatility, a wide range of interrelated tasks the software aims to support, which makes CAD to be a complex tool consuming considerable time and efforts to master. Another obstacle to use the software products above within academic curriculum is their focus on solid models meanwhile the types of the links the CADs consider differ from those accepted within conventional Theoretical Mechanics course.

CAD systems are generally licensed software products which makes them a black box for the end-user as there is no evidence of which mathematic principles they are based upon. A user can not estimate the validity of calculations without making some experiments. That is why some original customized software focused on academic course of Theoretical Mechanics might be a unique solution for the studies.

The mathematic model presented in the present paper is the foundation for this kind of software. This model is oriented at two dimensional system of active loads applied to a static construction, i.e. a body with some constraints. The aim of the research is to define indeterminate constraints as well as inertial forces. Subsequently dynamic model can be created on the basis of the model above.

2 General mathematic statement of the problem

The system of equations, equilibrium condition for a plane system of forces, can be described as follows:

$$\begin{cases} a_{11} \cdot x_1 + a_{12} \cdot x_2 + a_{13} \cdot x_3 = b_{11} \\ a_{21} \cdot x_1 + a_{22} \cdot x_2 + a_{23} \cdot x_3 = b_{21} \\ a_{31} \cdot x_1 + a_{32} \cdot x_2 + a_{33} \cdot x_3 = b_{31} \end{cases}$$

where x_1, x_2, x_3 are indeterminate constraints and inertial forces; a_{11}, a_{12} , etc are coefficients depending on a type and direction of indeterminate constraints and inertial forces (Table 1); b_{11}, b_{21}, b_{31} are the values depending on applied active forces.

We shall understand that X-axis, an axis of abscissa, is always directed horizontally to the right and Y-axis, an axis of coordinates, is directed vertically up. We shall assign the axis l for each indeterminate constraint of a force which lays on this very axis; by convention we shall align the direction of the constraint and positive direction of the axis. Correspondingly we shall assign positive direction of the moment sought to act counterclockwise for each indeterminate constraint of a force couple.

b_{11}, b_{21}, b_{31} values can be determined as follows:

$$b_{11} = - \sum X_i;$$

$$b_{21} = - \sum Y_i;$$

$$b_{31} = - \sum M_{iO},$$

where X_i - the projection of i -th active force on X-axis; Y_i - the projection of i -th active force on Y-axis; M_{iO} - the moment of i -th active force with respect to a point O .

Inertial forces depend on the type of feasible motion of the construction [3, 4]. We shall carry out the calculations taking into the account that center-of-mass velocity, i.e. point C , is equal to zero and its acceleration is different to zero. Suppose under the rotation angular velocity is equal to zero but angular acceleration ϵ might occur.

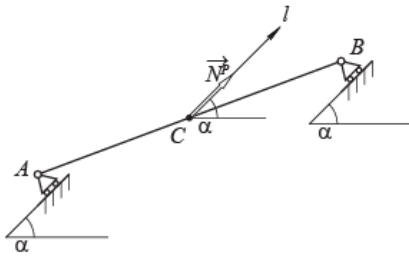


FIGURE 1 Translation motion

Resultant vector of forces \vec{N}^P applied in the point of center of mass C acts upon the construction and it is of an indeterminate value. We shall determine the direction of l axis by virtue of rotation of the normal by the angle of -90° to the support surface of A support.

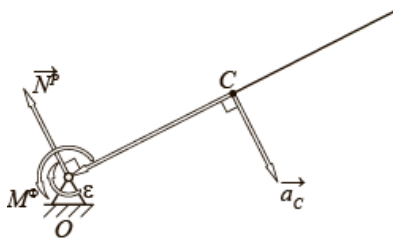


FIGURE 2 Rotation motion

The resultant moment of inertial forces M^Φ is an indeterminate value. The resultant vector of inertia forces can be determined as follows:

$$N^P = \frac{m}{I_0} \cdot CO \cdot M^\Phi,$$

where m - mass of the body; I_0 - moment of inertia with respect to the point O .

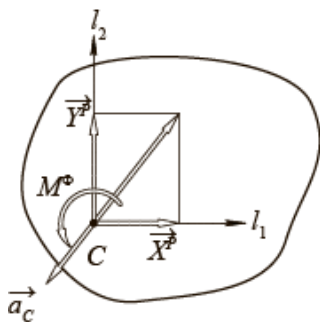


FIGURE 3 Plain motion of a free rigid body

Resultant moment of inertial forces and resultant vector of inertia forces projections onto x and y axes, i.e. X^P and Y^P values, are the indeterminate values here.

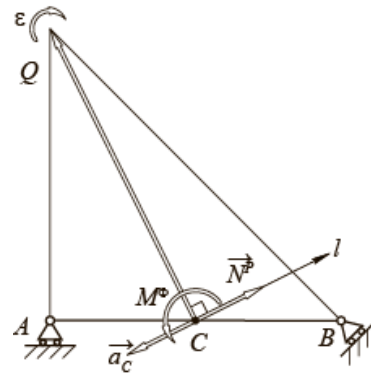


FIGURE 4 Plain motion of a free rigid body with respect of two points

The mass center has got the acceleration which aligns with the rotation acceleration. This very acceleration is perpendicular on \vec{CQ} vector which joins the mass center with an instantaneous acceleration center and it is aligned with the direction of angular acceleration ϵ . The position of the instantaneous acceleration center can be determined as the intersection of perpendiculars on the support planes of A and B supports. The moment M^Φ , which is an indeterminate one, can be used by analogy with the rotation motion to find the value of N^P :

$$N^P = \frac{m}{I_c} \cdot CQ \cdot M^\Phi,$$

where I_c is the moment of inertia with respect to the point C .

The direction of l axis which \vec{N}^P force lies along can be determined by means of rotation of the \vec{CQ} vector by the angle of -90° .

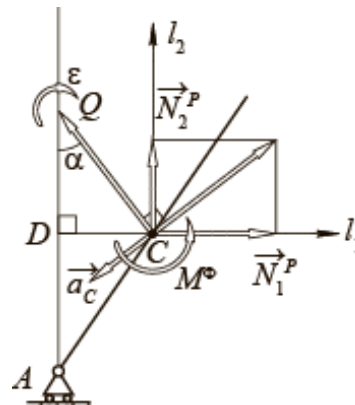


FIGURE 5 Plain motion of a rigid body with respect of one point

Moment M^Φ and force N_1^P are indeterminate ones. The axis l_1 of the latter can be determined by virtue of rotation of the normal by the angle of -90° to the support surface of A support. We shall obtain the value of force N_2^P with the help of an indeterminate moment M^Φ as below:

$$N_2^P = \frac{m}{I_c} \cdot CD \cdot M^\Phi.$$

The axis l_2 of N_2^P force is co-directional with the normal to the support surface of A support.

TABLE 1 Matrix A coefficients

N	Type of variables	Matrix A coefficients		
		a_{1i}	a_{2i}	a_{3i}
1	X, X^p	1	0	
2	Y, Y^p	0	1	$x \cdot a_{2i} - y \cdot a_{1i}$, where x and y are horizontal coordinates of the point of the force application with respect of the center where the moment is to be calculated.
3	N, N^p	$\cos\alpha$, where α is an angle between positive directions of the axes x and l .	$\sin\alpha$, where α is an angle between positive directions of the axes x and l .	
4	M^p at rotation motion of a construction	$\frac{m}{l_0} \cdot CO \cdot \cos\alpha$, where α is an angle between positive directions of the axes x and l .	$\frac{m}{l_0} \cdot CO \cdot \sin\alpha$, where α is an angle between positive directions of the axes x and l .	1
5	M^p at plain motion with respect of two points	$\frac{m}{l_c} \cdot CQ \cdot \cos\alpha$, where α is an angle between positive directions of the axes x and l .	$\frac{m}{l_c} \cdot CQ \cdot \sin\alpha$, where α is an angle between positive directions of the axes x and l .	1
6	M^p at plain motion with respect of one point	$\frac{m}{l_c} \cdot CD \cdot \cos\alpha$, where α is an angle between positive directions of the axes x and l .	$\frac{m}{l_c} \cdot CD \cdot \sin\alpha$, where α is an angle between positive directions of the axes x and l .	1

3 Conclusions

The mathematic model to determine force loads of static constructions simulating all types of their possible motions has been created on the basis of Theoretical mechanics laws.

This model can be implemented into an educational computer software product to visualize and analyse force loads of static constructions within the academic curriculum of Theoretical Mechanics course.

References

[1] Gamma E, Johnson R, Helm R, Vlassides J 1994 Design Patterns. Elements of Reusable Object-Oriented Software Addison-Wesley
 [2] Cherepashkov A A 2008 Komp'juternye tehnologii Sozdanie, vnedrenie i integracija promyshlennyh avtomatizirovannyh sistem v mashinostroenii Ucheb posob – Samara: Samar gos tehn un-t
 [3] Jablonskij A A 1986 Kurs teoreticheskoy mehaniki uchebnik M: Vyssh shk – Ch1
 [4] Ignatishhev R M 2004 Kurs teoreticheskoy mehaniki Vvedenie, statika, kinematika, dinamika Ucheb posobie Ignatishhev R M, Gromyko P N, Hatetovskij S N – Minsk: UP «Tehnoprint»

Authors	
	<p>Natalia Karatun, 14.11.1972, Mogilev, Republic of Belarus</p> <p>Current position, grades: Dozent of Department of Natural Sciences and Computer Technologies ISMA University of Applied Sciences, Msc ing, Msc comp. University studies: theory of metalcutting, CAD, programming. Scientific interest: design, CAD, programming. Publications: 10 papers.</p>
	<p>Stanislav Khatetovsky, 04.06.1974, Mogilev, Republic of Belarus</p> <p>Current position, grades: Head of chair "Metalcutting tools and instruments" of Belarusian-Russian University (Mogilev, Belarus), PhD (Engineering), associate professor. University studies: theory of metalcutting, CAD, Theory of metalcutting instruments. Scientific interest: design of gears, CAD. Publications: more than 40 papers.</p>
	<p>Andrei Statsenko, 07.09.1972, Mogilev, Republic of Belarus</p> <p>Current position, grades: Dozent of Professional Development and Retraining Institute within Belarusian-Russian University (Mogilev, Belarus), PhD (Engineering). University studies: CAD, Machine Elements, ESP. Scientific interest: CAD, IT. Publications: about 50 papers. Experience: 20 years' academic experience, 10 years corporate training expertise.</p>

Application of the fiber image detection algorithm based on the Grey system theory and Directed graph

Xiaodong Wang^{1*}, Jianhui Yang²

¹Department of Mathematics and Physics, Zhengzhou Institute of Aeronautical Industry Management, China

²School of Mathematics and Statistics, ZhouKou Normal University, Henan, China

*Corresponding author's e-mail: 2364970768@qq.com

Received 1 March 2014, www.cmmt.lv

Abstract

After doing research on fiber image with low quality and the Grey prediction model, the Grey correlation degree, directed graph and existing edge detection algorithm, this article proposed a new edge detection algorithm to obtain complete and continuous edge and to improve the defects in traditional operators profiled fiber contour extraction, such as the discontinuous edge, the false edge. This article obtains the fiber outline firstly, and then the edge detection algorithm is applied to the adhesive fibers. Thus, filling algorithm and contour tracking algorithm are used to get the fibers' outer contour. After that applying the directed graph algorithm to edge detection and the complete edge is gained after the burr is eliminated. Proven by the experimental results, the proposed edge detection algorithm can overcome the defects of the conventional edge detection algorithm, such fracture as edge, false edge, etc.

Keywords: grey correlation degree, directed graph, edge detection algorithm, directed graph

1 Introduction

In recent years, digital image processing technology which is widely used in textile industry has obtained certain achievement in the field of fiber composition detection. In the process of the digital image processing, test analysis to the microscopic images of the fiber, the way of extraction from the edge of the fiber, adhesion of the fiber separation accurately has a direct impact on fiber composition detection, is also an important part of fiber microscopic image recognition.

In 1982, the Chinese scholar, Professor Julong Deng proposed Grey system theory which is a new method researching minority and the of poor uncertainty question. In recent years, the Grey system theory received the wide attention of scholars both at home and abroad, the Grey prediction and Grey relational analysis among Grey system theory are applied to the research of edge detection, the corresponding improved algorithm is proposed, the detection has been improved effectively, but cannot meet the requirements of continuous fiber edge. Based on this, this paper proposed edge detection algorithm based on Grey system theory and the direction. This method combined the Grey forecasting model with Niblack algorithm, obtaining the edge of the fiber information for part of the fiber within the phenomenon of false edge, using area filling algorithm, direction graph algorithm and contour tracking algorithm to extract the edge of fiber completely.

Some domestic scholars attributed the problem of the image edge detection to poor information uncertainty systems, the Grey system theory is applied to the image edge detection, and has achieved certain results. Application of Grey system theory in this paper is mainly the Grey

prediction model GM (1, 1) and Grey absolute correlation degree, which is used to detect the fiber edge. Among them, the Grey prediction is based on the difference between the size of the gray gradation values of a predicted image and the actual point of the gray value to determine whether the point is an edge point; while the gray correlation is mainly based primarily on collating sequence associated with the reference sequence determine whether the point is an edge point.

2 The basic principles of Grey prediction

Through the neighborhood in one-pixel point build Grey prediction equation, and then use the Grey values of these points and the establishment of Grey prediction equations to predict this pixel Grey value, if the difference between the predicted and the actual value of the pixel Grey values is in the predetermined threshold value, the pixel is considered with its neighborhood in the same Grey value Grey on stage, which does not think the point of this pixel on the image edge; otherwise, consider this pixel and its neighborhood is not the same Grey level, which determines the pixel is an edge point of the image. This method takes full advantage of the mutation of edge point gray value.

This algorithm in this paper is mainly based on fiber Grey value and the background on the edge of the area and the characteristics of internal Grey value of relatively large differences. Its basic algorithm thought: put image in the each pixel points corresponding to gray value considered initial series of Grey forecast model, then, put image in the pixel points x and its neighborhood pixel points into original sequence, accumulate the original sequence by using data processing for a regular series of Grey modeling, again for

Grey forecast, after getting the forecast value sequence, for data reduction by that point in the actual forecast data, if the difference between forecast value and actual value is larger, which is for edge points, otherwise, for non-edge points. The main steps of the algorithm of GM (1,1) model are shown as follows:

1) Let the original sequence as

$$x^{(0)} = (x_{(1)}^{(0)}, x_{(2)}^{(0)}, \dots, x_{(n)}^{(0)})$$

2) Generates a sequence for the record

$$x^{(1)} = (x_{(1)}^{(1)}, x_{(2)}^{(1)}, \dots, x_{(n)}^{(1)})$$

among them,

$$x_{(k)}^{(1)} = \sum_{i=1}^k x_{(i)}^{(1)} \quad k = 1, 2, \dots, n.$$

3) $z^{(1)}$ is close to $x^{(1)}$ as the mean value generates a sequence

$$z^{(1)} = (z_{(2)}^{(1)}, z_{(3)}^{(1)}, \dots, z_{(n)}^{(1)})$$

among them,

$$z_{(k)}^{(1)} = 0.5x_{(k)}^{(1)} + 0.5x_{(k-1)}^{(1)}, \quad k = 2, 3, \dots, n$$

4) GM (1,1) model that is an order of one yuan gray model, which is defined as

$$x_{(k)}^{(0)} + ax_{(k)}^{(1)} = b$$

where a is a factor of development; b is the Grey action.

5) The whitening model of GM (1,1) is

$$\frac{dx^{(1)}}{dt} + ax^{(1)} = b$$

6) The albino-response of GM (1,1) is

$$\hat{x}_{(k+1)}^{(1)} = (x_{(1)}^{(0)} - \frac{b}{a})e^{-ak} + \frac{b}{a}$$

$$\hat{x}_{(k+1)}^{(0)} = \hat{x}_{(k+1)}^{(1)} - x_{(k)}^{(1)}$$

7) Under the least-squares criterion parameter

$$\begin{bmatrix} a \\ b \end{bmatrix} = (B^T B)^{-1} B^T y^n$$

among them,

$$B = \begin{bmatrix} -z_{(2)}^{(1)} & 1 \\ -z_{(3)}^{(1)} & 1 \\ \vdots & \vdots \\ -z_{(n)}^{(1)} & 1 \end{bmatrix}, \quad y^n = \begin{bmatrix} x_{(2)}^{(0)} \\ x_{(3)}^{(0)} \\ \vdots \\ x_{(n)}^{(0)} \end{bmatrix}.$$

The strong edge detection based on Grey prediction of Grey forecasting model of image edge detection studies focus on the sequence of points on the options, and options for sequence points improvements are only detects the edges more informative, does not meet the requirements of full fiber edge. Based on Grey forecast detection out of edge exists serious of fracture phenomenon, but its can accurate to find fiber edge of location, this paper has a new idea, puts Grey forecast application into fiber image of strong edge of detection, based on strength edge connection of thought, and put this strong edge and by Niblack value of the two algorithm get of weak edge for connection, then get fiber of edge information.

Based on the Grey prediction model in sequence point selection scheme and fiber image Gray scale characteristics analysis, the paper selected 12 masked sequences, and choose GM(1,1) model to model, thus get the strong edge in the fiber. The specific Grey prediction algorithm of the main steps is described below.

Let the size of an $M \times N$ image I , the Grey value of midpoint $I(i, j)$ is $g(i, j)$, $i = 1, 2, \dots, M$, $J = 1, 2, \dots, N$

1) For each pixel in the image I , in turn, use mas sequences and GM(1,1) model to calculate the gray forecast value of the center point x and constitutes the forecast image II.

2) Original I minus the predicted figure II get error images III, its gray value of each point is $\xi(i, j)$.

3) According to the error histogram of the image, the threshold value T , if $\xi(i, j) > T$, the pixel image $B(i, j) = 1$ is the binary image of strong edges, otherwise, $B(i, j) = 0$, thus, getting the binary images of edges obtained by gray forecast model.

3 Grey correlation degree

Basic principles of grey correlation degree.

According to the gray correlation analysis of the gray system theory, the size of the gray correlation reflects the reference sequence and comparative sequence similarity. According to the different features between the gray value of the image edge points and the gray value of the background area is large, it is understood that the edge and its neighboring pixel values consisting of comparison sequence associated with the reference sequence is relatively small. The calculating process of Grey absolute correlation degree is described as follows.

The calculation steps of correlation degree is as follows.

Let the reference sequence $X_0 : \{x_i(k), k = 1, 2, \dots, n\}$,

comparison sequence $X_i : \{x_i(k), k = 1, 2, \dots, n\}$.

1) Initialization:

$$Y_0 : \left\{ \frac{x_0(k)}{x_0(1)} = y_0(k), \quad Y_1 : \left\{ \frac{x_i(k)}{x_i(1)} = y_i(k) \right. \right.$$

Initialized so that all sequences comparable.

2) Calculate the correlation coefficients of each point:

$$r(y_0(k), y_i(k)) = \frac{1}{1 + |(y_0(k+1) - y_0(k) - y_i(k+1) - y_i(k))|}$$

where $k = 1, 2, \dots, n-1$.

3) Calculate the correlation degree:

$$r(x_0, x_i) = \frac{1}{n-1} \sum_{k=1}^{n-1} r(y_0(k), y_i(k))$$

4 Extract the region of interest based on grey correlation

In this paper, through the analysis and research on the Grey correlation degree, and basing on the gray value changes of background regions in fiber image is small and characteristics of gray value change of fiber internal is larger, the Grey correlation degree is applied to fiber area, namely extraction of region of interest, and realize the innovation of Grey correlation degree of application. In this paper, on the basis of predecessors' research to improve the selection of comparison sequence, were selected for eight neighbourhoods, up, down, left and right of four neighborhood pixels were composed of comparison sequences. So the selection of two comparison sequence, respectively

$$k_1 = (g_{i,j}, g_{i-1,j}, g_{i+1,j}, g_{i,j-1}, g_{i,j+1}, g_{i-1,j-1}, g_{i-1,j+1}, g_{i+1,j-1}, g_{i+1,j+1})$$

$$k_2 = (g_{i,j}, g_{i-1,j}, g_{i,j}, g_{i,j-1}, g_{i,j}, g_{i,j+1}, g_{i,j}, g_{i+1,j}, g_{i,j})$$

and let an equivalent sequence $k_0 = (1,1,1,1,1,1,1,1,1)$ as reference sequence. $g(i, j)$ as the gray-scale values of point $I(i, j)$. The algorithm steps are as follows:

1) Determine the reference sequence k_0 , and according to point $I(i, j)$ of the original image to determine the comparison sequence $k_1(i, j)$ and $k_2(i, j)$.

2) Absolute correlation $r_1(i, j)$ and $r_2(i, j)$ were calculated between k_0 and $k_1(i, j)$ with $k_2(i, j)$, take $r(i, j) = \min(r_1, r_2)$, whereby correlation diagram.

3) Threshold T is determined by the histogram of correlation chart, if $r(i, j) > T$, $I(i, j)$ is not a region of interest; otherwise, $I(i, j)$ is the region of interest and obtain a binary image of the region of interest.

5 Principles of pattern

Pattern is used on the outline of each pixel in the direction to fiber images. Using edge direction of gradient operators obtained method has been widely used, including: divide the image into small $M \times M$ window, for each pixel within the window according to the Sobel operators calculate the gradient along the horizontal and vertical direction G_x and G_y and the angle θ . If the image size is $M \times N$, the Grey value of point $I(i, j)$ in image is $g(i, j)$. Its specific calculation steps are as follows:

1) Calculation of the horizontal gradient:

$$G(i, j) = \sum_{u=i-m/2}^{i+m/2} \sum_{v=j-m/2}^{j+m/2} S_x(m, n) \cdot g(i+m, j+n)$$

among them,

$$S_x = \begin{bmatrix} -1 & 0 & 1 \\ -2 & 0 & 2 \\ -1 & 0 & 1 \end{bmatrix}$$

2) Calculation of the gradient of the vertical direction:

$$G_y(i, j) = \sum_{u=i-m/2}^{i+m/2} \sum_{v=j-m/2}^{j+m/2} S_y(m, n) \cdot g(i+m, j+n),$$

where

$$S_y = \begin{bmatrix} -1 & -2 & 1 \\ -2 & 0 & 2 \\ -1 & 2 & 1 \end{bmatrix}$$

3) Calculating the direction of the edge angle

$$\theta(i, j) = \arctan\left(\frac{G_y(i, j)}{G_x(i, j)}\right),$$

among them,

$$G(i, j) \neq 0, \quad -\frac{\pi}{2} < \theta(i, j) < \frac{\pi}{2}$$

6 Edge detection based on direction

We can find out the image edge according to the direction of graph algorithm, and carries on the increase, but the direction graph algorithm is prone to edge discontinuity and fracture phenomenon. Therefore, this ideological pattern and bound algorithm is applied to the gray prediction, gray correlation degree and Niblack value of the two algorithm to obtain fiber outer contour map strengthen, which can be used to overcome the weaknesses of pattern edge detection

algorithm, thereby detecting the outer contour of the complete fiber, while the adhesion can be well separated from the fibers, the purpose of the fiber can be accurately detected edge information.

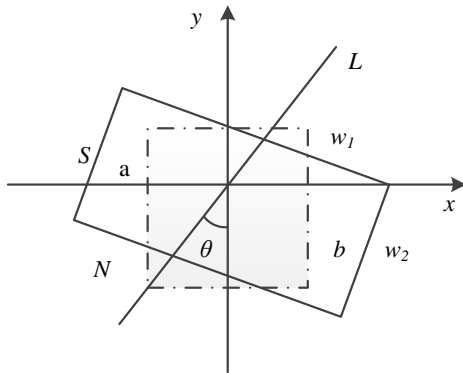


FIGURE 1 The diagram of direction graph

Because fiber edge line and profile directions are basically the same, so it can be based on edge direction of consecutive points on a line to define the outline of the current direction. Graph edges define algorithm motioned in the direction as shown in Figure 1, the image is divided into 3×3 fiber widget w_1 (shown in dashed box in Figure 1), the average direction of the inner edge points w_1 substituted approximation to the center direction of the contour direction, and assume the contour true direction is L , and the contour line L is the vertical angle θ . While setting the window defining edge $w_2 = S \times N$ (solid line rectangle in Figure 2, the selected paper size 3×5), w_1 and w_2 coincide with the center phase, S -side of the fiber parallel to the contour line L , N -sided contour line L and perpendicular to the fiber. Then, based on the image obtained by the Sobel operator for each point along the horizontal, vertical gradients G_x and G_y , and the direction angle θ . Using of Canny operator edge points obtained contour and the statistics of the number of edge points. Then according to the contour line L divided w_2 into two parts a and b , respectively, a and b values of statistical gray midpoint, and the two parts with respect to the calculation of the membership of the contour line L , and to determine the true profile by the fuzzy search in order to detect the edge of the fiber, to be separated from the effect of the adhesion area.

7 Algorithm in this paper

Based on fiber identification system to extract the full edge of the grey prediction and grey correlation degree requirements and characteristics, this paper presents a grey forecasting, grey correlation degree and direction graph based edge detection algorithm, the algorithm flow as shown in Figure 2.

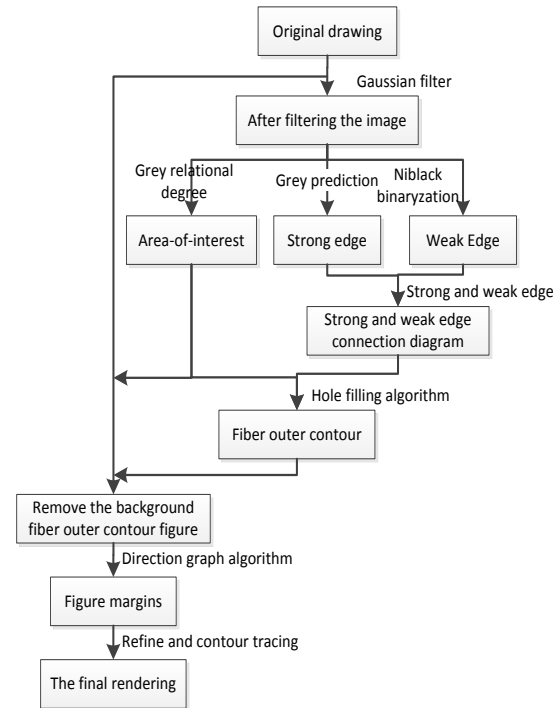


FIGURE 2 The algorithm process

This algorithm example schematic is shown in Figure 3.

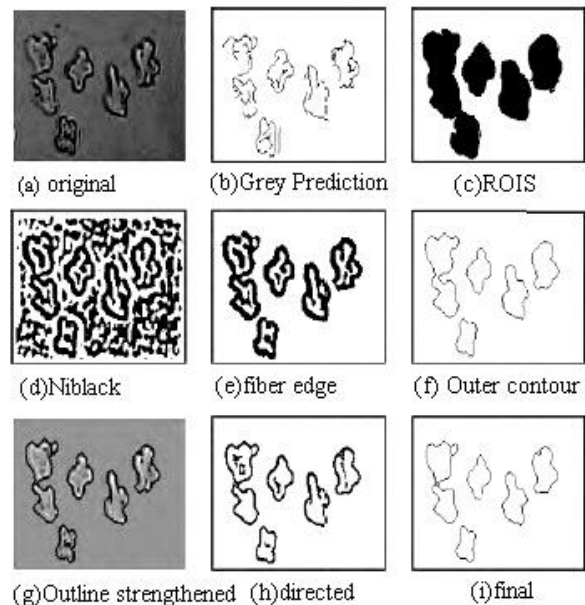


FIGURE 3 The diagram of proposed algorithm

- 1) The use of Gaussian filter pre-treatment original Figure 3a;
- 2) Using the algorithm of Grey prediction and Grey correlation degree towards the filtered images obtained in Figure 3b of the edges as shown in diagram and Figure 3c shows regions of interest;
- 3) The strong edges obtained from the gray forecast connected to the weak edge map from the Niblack value algorithm (Figure 3d), and then combined with the region of interest, the edge of the fiber are obtained as shown in Figure 3e;

4) The cavity is filled by the algorithm (for filling fiber edge map and use contour tracking algorithm, and obtained as shown in Figure 4f of the external profile;

5) For the adhesion of the fibers, the outer contours and regions of interest to get this article combined with the original, non-interested in image area fills to mean, and (4) the obtained fiber on the outer profile is added to the original image, to obtained in Figure 3g as shown in the background of the outer contour of the fibers to strengthen;

6) Using pattern-and-bound algorithm for edge detection, obtained as shown in Figure 3h are shown in the picture, and then refine and use contour model tracking algorithm for removing burrs, and obtained as shown in Figure 3i the ultimate fiber edge.

8 Experimental results and analysis

This article selects 320 fiber images as experiment objects, including the MTS form, VY type, W type, U type, cross five types of fiber image. By the algorithm in this paper and the other edge detection algorithms fiber edge detection results are shown in Figure 4. The Figure 4 shows that although these fibers original image edge is not obvious, the phenomenon such as adhesion. This algorithm can well extract fiber edge information. But the Log operator, Prewitt operator is not well detected fiber weak edge, and the fracture phenomenon is serious. Canny operator can better extract the weak edge fiber, but the phenomenon of false edges are prone to fracture; background level set algorithm for image noise pollution is not serious, which can better extract the outer contour of the fiber, but cannot apart the fibers adhesions, when noise pollution is serious. The method cannot find the outline of the fibers accurately. The proposed algorithm has better robustness, with good noise immunity, and out of the fiber edge detection both accurate and complete, but also avoiding the LOG operator, Prewitt operator, Canny operator edge algorithms are prone to false fracture edges and phenomena, but also overcoming the noise pollution level set algorithm is sensitive to defects and shortcomings cannot be separated adhesions fibers. Algorithm on adhesion of fiber can effectively detect the

References

- [1] Miao Ma, Song-yun Xie, etc 2003 The image edge detection new algorithm based on Grey system theory *Chinese journal of image and graphics: A edition* 8(10) 1136-9
- [2] Liu S, Fang Z-g, etc 2010 *The grey system theory and its application* Beijing: science press 195-210
- [3] He R, Chen J 2005 Image edge detection based on grey prediction model *Journal of northwestern polytechnical university* 23(1) 15-8
- [4] Siddiqi K, Bouix S, etc. 2010 Hamilton-Jacobi Skeletons *Computer Vision* 48(3) 215-31
- [5] Dimmit P, Phillips C, Siddiqi K 2008 Robust and Efficient Skeletal Graphs *IEEE Conf. Computer Vision and Pattern Recognition* 1417-23
- [6] Mayya N, Rajan V T 2004 Diagrams of Polygons: A Framework for Shape Representation *IEEE Conf. Computer Vision and Pattern Recognition* 638-43
- [7] Nello, Shawe-Taylor J 2003 An Introduction to Support Vector Machines and Other Kernel-based Learning Methods *Cambridge University Press* 7(12) 23-5
- [8] Deng J Basic Methods of Grey System Wuhan: Huazhong University of science and technology press
- [9] Jie Yan 2006 Image edge algorithm based on grey relational analysis and Canny operator *Computer engineering and application* (28) 68-71
- [10] Xue-lian Li 2011 Grey system theory and its application in medical image processing Harbin engineering university

adhesive part of the contour lines, achieving accurate segmentation of complex fiber image purposes.

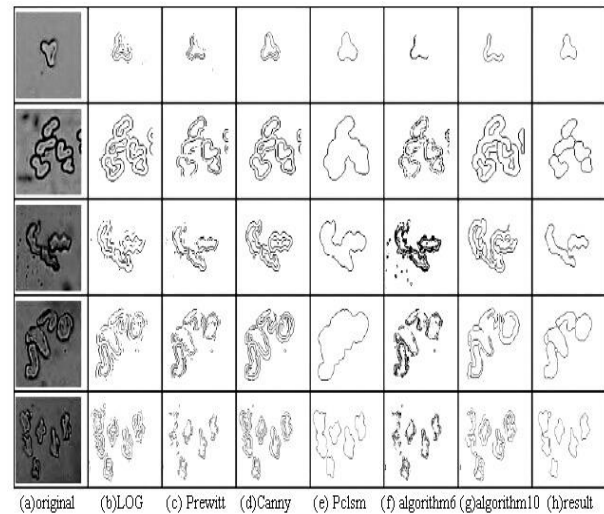


FIGURE 4 comparison with other edge detection methods

5 Conclusions

This paper is based on the situation LOG operator, Prewitt operator, Canny operator and gray prediction model and gray correlation algorithm used double edge and contour extraction fiber fracture edge of existence. This algorithm not only can extract the edge of the fiber image accurately, but also can get the edge of the adhesive fibers effectively, which provide a guarantee of the subsequent separation and identification. And the level set algorithm cannot extract the exact position of the edge and fiber adhesion defects cannot be separated, on the basis of gray system theory, the use of algorithms to detect patterns of fiber edge and using contour tracking well removing, which reach the purpose of a good prospect of noise suppression, detection of precise and continuous fibers edge. The results of this study for subsequent fibers separation provide a very good foundation.

Research in search engine user behaviour based on cloud computing

Wei Liu^{1, 2*}, Cunchen Tang¹, Fan Kang¹

¹International School of software, Wuhan University, Wuhan, Hubei, 430079, China

²Department of Information Engineering, Wuhan Business University, Wuhan, Hubei, 430056, China

*Corresponding author's e-mail: yoxiky2003@tom.com

Received 20 December 2014, www.cmmt.lv

Abstract

User behavior analysis is important for both Web information retrieval technologies and commercial search engine algorithms. With the expansion of information data, the current search engine is facing some serious problems, such as limited storage space and computing power. The paper discussed the shortcomings and technical bottlenecks of the current traditional search engine. Then, in the understanding of search engine features and technical requirement, it improved the system by means of the cloud computing architecture. With the combination of the static analysis of user behaviour and real-time monitoring, real-time acquisition of Web log and user to access the context information of the page, the paper tested the whole system performance in the laboratory environment, demonstrated the superiority of the system by analysis of experimental data.

Keywords: user behavior analysis, search engine, cloud computing, system performance

1 Introduction

At present, cloud computing is a hot spot in IT industry, almost every IT company is promoting this newly emerging business model and spending huge amounts of money researching cloud computing. With storage system becoming more cheaper, internet bandwidth higher, processing unit faster, the old assumption that moving computing and storage into the cloud is becoming true. Now there is no common interface for cloud computing, nor related standard published. IT companies are focusing on building their own "clouds" in different fields including: e-commerce, internet storage, online office, search engine, online map, etc. Among them, search engine is the forefront of these applications. Cloud Computing will play a very important role in the evolution of search engine. Up to now, most search engine company's backgrounds are not cloudy yet, there is still much work to do. It is a very good practice to research Cloudy Computing from the characteristics of search engine.

User behavior analysis has already drawn the wide attention of scholars at home and abroad. Cen Rongwei, based on 756000000 real network user behavior log on, the user search behavior in the query length, query modification rate, related search hits, the first / last click distribution and query hits distribution information, in order to optimize the search engine algorithm and the improved system cable. Wang Zhenyu, Guo Li and so on, through the HDFS MapReduce distributed file system and parallel computing model to support massive log file analysis, user click behavior, so as to enhance the search engine retrieval algorithm and the retrieval efficiency of service, freeing users from abundant disorderly search results. China Telecom Guangdong Institute's Tao Caixia, Xie Xiaojun proposed an engine analysis solutions of mobile Internet user behavior data based on cloud

computing, including the overall system architecture design, data storage and preprocessing module, user behavior data analysis model, the design of the key module. At the same time, the foreign scholars such as Joohee Kim, Chankyoun Hwang MapReduce model using cloud computing platform is proposed for IPTV user behavior analysis method of Hadoop, describes the IPTV user regional characteristics.

To sum up, at present, for the analysis of user behavior are mostly concentrate on mining WEB log, the log is the intentions of the user, the actual performance, motivation in action. However, Web log is not enough to describe the scene when the user visits a website, the user must be collected in real time on the client end operation behavior and the context information. We combine the two according to the maximum possible to reproduce the user, the real scene browsing Web pages, to extract the comprehensive of the user behavior trajectory, provide effective data support for the analysis of user behavior.

Analysis of user behavior refers to the site access to basic data, through the study on statistical analysis of the relevant data, found that the laws of the user to access the website, to allow enterprises to more detailed, clear understanding of user behavior, to find out the existing problem of business website, marketing channels, marketing environment, help enterprises to obtain high conversion page, let the enterprise marketing is more accurate, efficient, improve business conversion rate, so as to enhance the enterprise income.

2 User behavior analysis engine based on cloud computing engine architecture

In this study, "user behavior analysis engine" is defined as: according to certain strategy, respectively, to obtain user

dynamic behavior and behavior, and summarize analysis and reasoning, the system user behavior habit and characteristics.

"The scale of user behavior based on cloud computing analysis engine" for user behavior information, the use of cloud technology, storage and analysis of its efficiently find, mining user behavior, its structure as shown in Figure 1. It from the client to obtain real-time dynamic behavior of context information, asynchronous upload to the server to save; trigger server processing module pre-processing, aggregation analysis; access to Web log from the server, filtering, denoising and mining, and according to the point in time restore user history context information; at the same time, the dynamic behavior, treatment history stored in HBase database which: Static behavior analysis: mainly completes the Web log mining, and according to the time point the user to restore the historical context of user behavior, filtering, denoising, fusion operation, save the processed results and user behavior database.

Dynamic behavior analysis: based on the Markoff model, the dynamic behavior of reasoning, to collect, analysis of user behavior and characteristics.

The dynamic behavior of acquisition and preprocessing: access to information users real-time operation page from the client's behavior, and pre-processing, storing the results in HBase database. Including data cleaning, transformation, reduction, delete the useless content, check the information completeness and consistency.

User behavior information storage based on HBase: storage of user behavior information from the client and the server, the dynamic and static user behavior data, results and analysis.

The polymerization behavior of dynamic user: dynamic user behavior data filtering, integration, excluding those correct but invalid information user behavior but invalid.

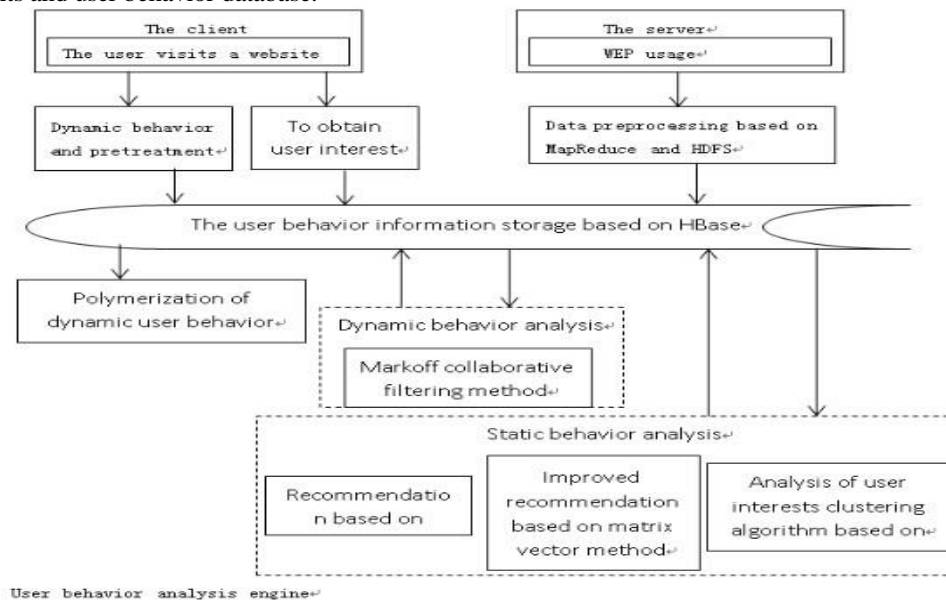


FIGURE 1 User behavior analysis engine based on cloud computing

3 The dynamic behavior of the user acquisition and preprocessing

The dynamic behavior of user refers to the user (including login and not logged in two cases. The user login, registered account user identification by acquiring ID; for users who are not logged in, record visit their website SessionID logo) occurred in accessing the page a moment of behavior, the behavior includes the occurrence time, the page (contains the page title and page URL), related to the operation and behavior subject, real-time capture them and carry on the effective analysis, has an important significance for understanding user behavior characteristics.

From the client gets information including the user dynamic behavior and context information, the context, including: behavior occurrence time; the current user ID or SessionID; the current page title; the address URL of the current page; the current user search conditions; access to the same page number; page retention time; do you want to

save the page; printed the page whether or not; whether add to favorites; copy or cut the page content and so on; the environmental context information includes: the client machine configuration, current network condition, the server working condition etc.

Because the user behavior data, acquired it, by using MapReduce model in cloud environment, including filtering, eliminate duplication, delete the useless content, check the information completeness and consistency. As the following methods used:

- 1) Data cleaning: removal of the incomplete data, delete duplicate data, delete access to pictures, delete pages of animation, the user behavior analysis of useless data [8].
- 2) Data conversion: the pages print, collection, preservation, downloaded operation, in the acquisition, will be converted into the corresponding data format in the database.
- 3) Data reduction: the user behavior data in large quantity, to standardize the data quantity, reduce the very necessary, but must maintain the integrity of the data.

4 The historical behavior mining

Analyzing the historical behavior mainly comes from on the WEB log mining, due to a surge in the number of Internet, the amount of data the WEB log and exponential growth, which makes the analysis platform of based on the single node has been unable to meet the needs of massive data analysis. Therefore, the analysis engine user behavior based on cloud platform, the cloud storage technology will be the mass of WEB log is stored in the HDFS distributed file system, and the calculation model by using MapReduce, the log file cleared, denoising, protocol, finally, on a variety of data mining algorithms are parallelized modification, in the form of services to the users with mining analysis functions, including: analysis, research, user behavior improved matrix vector association rules method based on clustering algorithm based on user interest degree of user behavior query vector space model based on cloud environment, mining results, stored in the HBase user behavior information base, in order to combine with the dynamic behavior, reasoning user interest. In order to enhance the efficiency analysis of log file.

5 Study on the vector space model of retrieval based on user behaviour

Vector space model (VSM:Vector Space Model) proposed by Salton and others in twentieth Century 70 years, it is the basic idea of each text and query contains some features independent properties reveal its content, and each feature attributes can be regarded as a dimension vector space, then the text can be expressed as a collection of these attributes, ignoring the complex relationship between paragraphs, sentences and words in the text structure. At the same time, given the feature weight vocabulary certain (weight), anti should vocabulary in the importance and the value of the contents of the file identification, this value is called the indexing vocabulary "significant value (Term Significances)" or "weight", by the lexical statistics calculate the document and to, such as: the feature words appear frequency (Term frequency, TF). Vector of each file is in fact all the document feature through a combination of computing, called "the document feature item vocabulary matrix". And then all of the document vector based on specific computing methods of similarity measure between each other.

Vector space retrieval model can be described as $I = (D, T, Q, F, R)$. Among them: $D = \{d_1, d_2, \dots, d_n\}$ as a collection of text, n text collection number; $T = \{t_1, t_2, \dots, t_n\}$ set as a feature, m feature of all. A text m feature indexing can be represented as a vector space $d_i = \{w_{i1}, w_{i2}, \dots, w_{im}\}, i = 1, 2, \dots, n$, w_{ij} is characteristic t_j for the text d_i of the weight, if the weight value w_{ij} is 0, indicating t_j that it is not appeared in d_i , $Q = \{q_1, q_2, \dots, q_m\}$ for the query set, a query q_r can be represented by vectors $q_r = \{q_{r1}, q_{r2}, \dots, q_{rm}\}$, q_{rj} is a characteristic to t_j the query

q_r weights, if the weight value q_r is 0, indicating that t_j is not appeared in q_r .

Further definition: frequency tf_{ij} : t_j is the feature for text d_i appear in the frequency.

Inverse document frequency word idf_i (inverse document frequency): the word in the quantitative distribution of document collection, the calculation $\log(N/n_k + 0.5)$ is usually, where N is the total number of document centralized, n represents a number of documents containing K , called the document frequency of the term.

The normalization factor: in order to reduce the inhibitory effect of high frequency characteristics of individual word on other low-frequency feature words, the standardization of components.

Based on the above three factors to term weighting Equation (1):

$$w_{ik} = \frac{tf_{ik} \log(N/n_k + 0.5)}{\sqrt{\sum_{k=1}^n (tf_{ik})^2 \times [\log(N/n_k + 0.5)]^2}} \quad (1)$$

The similarity between the text and the query can be used to measure the distance between two vectors. There are many kinds of calculating method of similarity, commonly used methods of inner product, Dice coefficient, Jaccard coefficient and cosine coefficient, usually uses the cosine coefficient method, namely the cosine of the angle between two vectors to represent the similarity between the text and the query $Sim(d_i, q_j)$, see Equation (2). Cosine similarity calculation method is a normalization, the angle between the two vectors of the smaller, the greater the degree of correlation between documents, correspondence \cos is higher. Two vector included angle cosine is equivalent to their standard vector inner product unit length, it reflects the similarity term component two vector of relative distribution.

$$Sim(d_i, q_j) = \cos \theta = \frac{\sum_{k=1}^n w_{ik} \times w_{jk}}{\sqrt{(\sum_{k=1}^n w_{ik}^2) \times (\sum_{k=1}^n w_{jk}^2)}} \quad (2)$$

6 Algorithm design

Input: user access to key words each time the user query log in.

Output: the similarity with the query keywords vector existing values in the database is not paper and similarity of 0, and according to the similarity value from big to small order.

1) Extracted from each Webpage keywords as the feature word, and these feature words and keywords query every time the user binding, rearrangement and according to a lexicographic order, combined together to form a standard feature set of words;

For example, there are Webpage document set (NDoc1, NDoc2, NDoc3, NDoc4), all the feature words together for (W1, W2, W3, W4, W5, W6), and when the query words (WQ1, WQ2), where $wq1 = W4$, the standard set of words

as features (W1, W2, W3, W4, W5, W6, WQ2), Webpage document feature item vocabulary matrix in Table 1.

TABLE 1 Webpage document vector space model

	W1	W2	W3	W4	W5	W6	WQ2
Q1	0	0	0	0	0	0	1
NDoc1	14	21	33	0	0	0	0
NDoc2	0	11	15	0	0	22	0
NDoc3	8	0	0	14	15	17	0
NDoc4	0	8	9	12	0	15	0

2) t_j is calculated for each term tf_{ij} appears in the Webpage text d_i frequency; calculation of $\log(N/n_k + 0.5)$ words formula of inverse document frequency idf_i . Then the formula with weight (3.1) to calculate the weight of each feature words each Webpage of document vectors, forming the Webpage document vector in a vector space.

3) To calculate the similarity of each document vector and the query vector Webpage between the cosine coefficient methods, see Equation (2). The interception of similarity values greater than 0.2000 articles, and from high to low return results.

Association rule mining is used to find correlation between the attributes of databases. Association rules is the initial motive of shopping basket analysis problem, the goal is to find the different commodities of association rules mining in transaction database, the relationship between the useful knowledge description data item value. These knowledge characterizes customer buying behavior and mode, use these rules, can effectively guide the scientific arrangement and design business purchase goods shelves. The form of association rule is a rule is, "to buy milk and bread customers, 90% of people bought butter", namely "(milk, bread) → butter" issue.

Let be the $I = \{i_1, i_2, \dots, i_m\}$ set of items. A related task data D is a collection of database transactions, where each transaction is a set of $T \subseteq I$, so. Each transaction is an identifier, called TID. Let A be a set of transaction, $A \subseteq T$ T contains A if and only if. Association rules are shaped implication $A \Rightarrow B$, such as one $A \subset I, B \subset I$, and $A \cap B = \emptyset$. Rule $A \Rightarrow B$ D in the transaction set, with the support of S , where s is the D transaction contains the percentage of $A \cup B$, namely $P(A, B)$. Rule $A \Rightarrow B$ $D C$ has confidence in the transaction set, where C is contained in the $D A$ transaction also includes a percentage of B , namely $P(B|A)$.

$$Support(A \Rightarrow B) = P(A \cup B) \tag{3}$$

$$Confidence(A \Rightarrow B) = P(B | A) \tag{4}$$

The support and confidence are two important concept description of association rules, the former for statistical measure of the importance of association rules in the data, said the rules which is used to measure frequency; credible degree of association rules, said the strength of the rules. In general, only the support and confidence of association rules

are high may be only the interesting rules, useful. Association rules mining is mainly realized by the two steps:

Step 1, according to the minimum support degree to find the database in D all the frequent item sets.

Step 2, according to the frequent item sets and minimum confidence generated Association rules.

Task one step is to quickly and efficiently find all frequent item sets in D , is the central problem of the association rule mining algorithm of association rules mining, is a measure of the standard; step two, relatively easy to achieve, so now all association rules mining algorithm is designed for the first step forward.

7 The matrix vector association rules algorithm

Definition 1: Boolean matrix: transaction set on the database and project sets a Boolean matrix representation. The specific method for each transaction set in a row, item sets are arranged according to a column. The transaction said row vector, the project said column vector respectively, if the first I project in the j transaction, then matrix line j , the I column value is 1, or 0, Boolean matrix called the matrix for the database.

Definition 2: Vector inner product: for any two n dimensional vector $\alpha = \{x_1, x_2, \dots, x_n\}$, $\beta = \{y_1, y_2, \dots, y_n\}$, $\langle \alpha, \beta \rangle = \sum_{i=1}^n x_i y_i$ is defined as the inner product of α and β .

Lemma 1: Any k of item in the set C_{k-1} is a superset of C_k .

Lemma 2: Frequent item sets corresponding to the n dimensional row vector 2 transaction database in D lemma and Boolean matrix R in each row vector inner product results do not exceed the number of frequent item sets containing project.

Definition 3: Column vector counting: counting is the column vector sum of a column element. Similarly, a row vector count is the sum of a line element.

Lemma 3: If the Boolean matrix a column vector count is less than the minimum support count, then delete this column. (Transaction compression).

Lemma 4: In a k -frequent item sets, if the Boolean matrix a row vector count less than k , then delete (Project compression).

Definition 4: Calculation γ_i method: R in a tuple vector α_i ($i=1, 2, \dots, M$, and the line scanning $a \neq 1$), $\langle \alpha_i, \alpha_j \rangle = \langle \alpha_i, \alpha_i \rangle$ the number of calculated $\gamma_i, j=1, 2, \dots, M$ and $j \neq i$.

8 Algorithm design

Input: All the dynamic behavior of the user to query the URL user input information.

Output: Recommended URL possible next set.

1) For cleaning and pretreatment of all the dynamic behavior of the user context information, see Table 2, picking out each record in the User ID, Danymic Behavior

Time, Search URL, Page-Stay Time, Save-Page, Print-Page, Favorites field.

2) To establish the matrix of Markov model is selected to identify each user: User-ID. According to the users to search the record time, sorting out the user's Search URL front to back Mark off sequence, with the users to search the record all Search URL matrix row and column, statistics of the users in each of the current Search URL to the other Search URL jump number, ratio of the number of the users and the total number of jumps as state the transfer matrix in the position value. In order to establish the Mark off state of each user transfer matrix. Among them, each gear position matrix is set to User-ID_Search URL, each column head position is set to Search URL, matrix stored in the Hbase table in user Shift Matrix.

3) Mark-off state transition matrix weighted: select Page-Stay Time (page retention time, in seconds) as the state transfer of additional weight matrix an element value calculation of one of the conditions, if Page-Stay Time (0,30), in the corresponding matrix elements *1, if Page-Stay Time (30,60), in the matrix corresponding to the element value * (1+1/20), if Page-Stay Time (60.), in the matrix corresponding to the element value * (1+2/20); one

additional value selection of Save-Page, Print-Page, Favorites as the state transition matrix elements corresponding value calculation, as long as one parameter value is 1, the corresponding matrix element values * (1+2/20).

4) The similarity calculation method based on the cosine factor: interest model parameters in Table 3, the interest in the registered information in the U keyword user selected as vector u, the similarity between the user employs cosine score vector measurement, cosine value is greater, the higher the similarity between users. Set (U,V) that similarity

$$\text{of } sim(u, v) = \cos(u, v) = \frac{u \cdot v}{|u| |v|} \text{ user } u \text{ and user } v.$$

5) Results: recommended for querying URL user input, transfer URL possible matrix find next in the current user owned by the state, is greater than a certain threshold (e.g. 0.1000) probability values that are consistent with the conditions recommended values. In addition, choose the maximal similarity of N users in the input current query URL in the transition matrix of the user's requirements to meet the threshold of a probability value as the recommended URL reasonable set.

TABLE 2 Parameters of dynamic behavior

Table name	Danymic Behavior_T		Dynamic behavior description table dynamic behavior description table		
Explain	This table to record the dynamic behavior description, representing the dynamic behavior by the following parameters, behavior analysis				
Primary key	Danymic Behavior Time				
The field name	Data type	Whether can be empty	The field description	Default value	Remarks
Danymic Behavior Time	Date time	No	The time of their occurrence		PK
User ID	Var char(10)	No	The current user ID		
Page Title	Text	No	The current page title		
Search URL	Text		Search URL for the current user	Null	
Page-Stay Time	Int		The current user search conditions corresponding to the URL Page retention time	0	Represents a user from entering into the page to the current trigger time duration of stay
Save Page	Char(1)		Do you want to save the page	0	0 not preserved, 1 saves
Print Page	Char(1)		Whether the print page	0	0 means no print, 1 said the print
Favorites	Char(1)		Whether to add to Favorites	0	0 do not add, add 1 representation
Copy Or CutContent	Text		Copy or cut the page content		

TABLE 3 Interest model parameters

Table name	Favorites Model_T		Interest degree model table		
Explain	This table records the user interest model description (each for a period of time, six months or a year, must put the backup data)				
Primary key	User ID				
The field name	Data type	Whether can be empty	The field description	Default value	Remarks
User ID	Var char(10)	Whether or not	Online user ID		Matching with the online user ID type
Favorite Field	Text		The user's domain of interest		
UserField	Text		User field		
Deduction	Text		User current interest keywords		

9 Application examples

Using the above research results, relying on the research project, the analysis engine system user behavior based on cloud computing is a design and development.

The analysis engine platform running on the Ubuntu12.10 user behavior, the software mainly includes: jdk-1.7.0_11, Jena-2.6.4, Myeclipse-8.0, Hive-0.10.0, HBase-0.94.4,

Hadoop-1.0.4, Tomcat-6.0, Jquery-1.6, Spring-3.0, Struts2-2.2.1, the browser is above IE8.0. The context aware behavior analysis as an example, system operation is as follows.

The system calculates the Mark off matrix intermediate important, as shown in Figure 2.

Select a user's current URL, system using Markov model and collaborative filtering, given URL probably next, as shown in Figure 3, Figure 4.

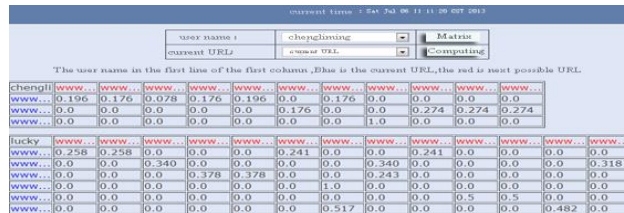


FIGURE 2 Markoff matrix

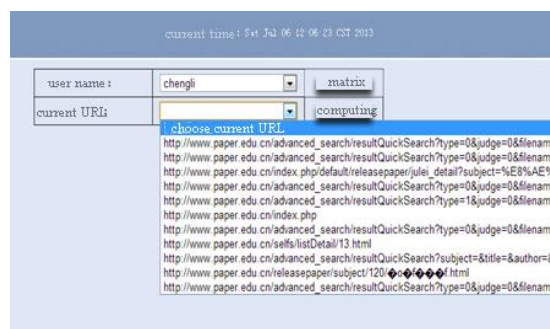


FIGURE 3 To select the current URL

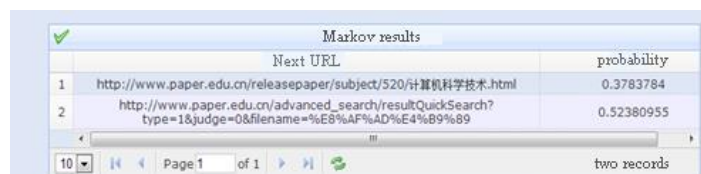


FIGURE 4 Markoff results

10 Research and prospect

In order to improve the retrieval system query processing ability, we have proposed user behavior analysis engine based on the use of cloud environment in which MapReduce parallel computing model, HBase cloud storage capacity, and uses the relevant data mining algorithms, static analysis, dynamic monitoring of user behavior characteristics and synthesis reasoning are used behavior.

That can efficiently push their interested information and provide the basis for the site structure adjustment for the user.

To sum up, this work is currently only integrating three cloud platf 7gvvborn of the data mining model, looking for more scene data mining model, integrated with the cloud platform. Making the system more universal, is the next step of work to do.

Acknowledgments

The National Natural Science Foundation of China (U1204609), the Education Department of Henan Province Science and Technology Key Project (14A510011), the Youth Science Foundation of Henan Normal University (2012QK21).

References

- [1] Voas J, Zhang J 2009 Cloud Computing: New Wine or Just a New Bottle 11(2) 15-7
- [2] Youseff L, Butriero M, Da Silva D 2008 Toward a Unified Ontology of Cloud Computing Grid Computing Environments Workshop.GCE'08 12-16 Nov 1-10
- [3] Grossman R L 2009 The Case for Cloud Computing IT Professional 11(2) 23-7
- [4] Mika P, Tununarello G 2008 Web Semantics in the Clouds Intelligent Systems IEEE 23 82-7
- [5] Hewitt C 2008 ORGs for Sealable, Robust, Privacy-Friendly Client Cloud Computing Internet Computing IEEE 12 96-9
- [6] Jepson T C 2004 The basics of reliable distributed storage networks IT Professional 6(3) 18-24
- [7] SVD M W, Do T, O'Brien GW, Krishna V, Varadhan S 1993 BENDPACKC (Version 1.0) User, 5 Guide University of Tennessee
- [8] Foster I, Yong Zhao, Raicu I, Lu S 2008 Cloud Computing and Grid Computing 360-Degree Compared Grid Computing Environments Workshop GCE 1-10

Worm detection and prevention based on network segmentation algorithm

Shanhong Zhu*

School of Computer and Information Engineering, Xinxiang University, Henan, China

International School of Software, Wuhan University, Wuhan, China

**Corresponding author's e-mail: 14878670@qq.com*

Received 1 March 2014, www.cmmt.lv

Abstract

Due to large space demanding and time-consuming, as the Internet is large and complex, the detection and prevention of the worm has many engineering constraints factors, the classic graph theory algorithms cannot suitable for solving some problems in the large-scale network. Sub-graphs of vertices have a higher density of edges within them while a lower density of edges between sub-graphs. To solve large-scale network analysis, the method of using DFS network segmentation algorithm based on network topology was proposed by analyzing the study of graph depth-first search (Depth First Search, referred to as DFS) segmentation algorithm, and thus obtain a description of the network connectivity of undirected connected graph $G(V, E)$. this provide a strong theoretical support for fast access network backbone node. The result of experiments shows that the proposed method is effective.

Keywords: worm detection, sub-graphs, DFS, network segmentation algorithm

1 Introduction

Social networks worms (hereinafter called "social network worm ") is use of social engineering to entice users to click various ways to spread a worm, it has the characteristics of hidden, long life cycle and difficult to eradicate, and so on. it is difficult to spread through released patches and other technical means for effective control, and so the potential hazard is more serious. At the same time, the actual environment network administrators and network user lack of security awareness, so it provide a breeding ground for social network worm propagation and survival. With the rapid development of the growing number of Internet users and various forms of virtual social network, spread through the network user's social network worm has become one of the major threats to network security risks.

In response to the threat of worms, as well as potential large-scale network anomalies, there is a big shortage in methods and strategies used by people currently. These methods, some still in the theoretical stage, such as benign worms; others due to too much impact of engineering factors is not practical, and practical application is still far, such as auto repair vulnerabilities. Endless variety of worms, and once a major outbreak, it caused huge losses. The traditional host-based protection, including virus prevention technology and virus firewall technology, can only be the point guard; and LAN-based worms isolation, the same cannot cope with the large-scale network worm outbreaks.

In this paper, we apply the method of using DFS network segmentation algorithm based on network topology by analyzing the study of graph depth-first search (Depth First Search, referred to as DFS) segmentation algorithm, and thus obtain a description of the network connectivity of undirected connected graph $G(V, E)$. this provide a strong theoretical support for fast access network backbone node.

2 Effect of network size on worm propagation

Since the Internet itself is an open and complex giant system with multi-variable, the size of the dynamic change constantly, but taking into account the worm outbreak time is short, and in general the target node number is relatively large, in a certain period of time the number of N can be regarded as a constant. Social networks, social networks derived from social networks, it starts form the email, BBS, instant messaging and P2P content sharing promoted the development of social networks, with the application of WEB2.0 technology, the appearance of online social networking sites further enrich the social network in the form of Internet. Mainstream social networks of currently existing including: e-mail network, P2P content sharing network, instant chat network and online social network sites and so on. In order to define the scope of the study and social network worms and other types of Internet worm phase difference, the social network worms is defined as: social network worm is a section of malicious programs which does not depend on the specific vulnerabilities, Take advantage of social engineering techniques to deceive Internet users click to execute and infect computer systems. Worms spread through social networks released immune system patches and other technical means, only by way of enhanced user safety awareness to prevent it.

2.1 WORM PROPAGATION STAGE

Worm propagation process can be divided into of the three stages of slow start, fast propagation and slow end as shown in Figure 1.

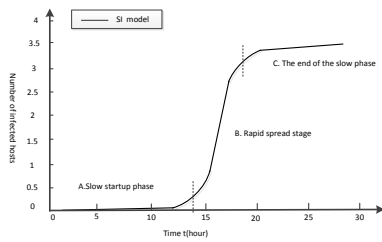


FIGURE 1 Propagation phases

As can be seen from the figure, if the worm is in fast propagation and slow end stage, large-scale worm propagation will lead to network congestion, and result in a decline in the performance of network routers, and worms have caused enormous damage, thus inhibiting study in this paper is the first stage in the spread of the worm, which would be truly effective in inhibiting the spread of worms.

2.2 NETWORK SIZE AND WORMS COVERAGE

For random scanning of worm propagation, assuming a slow start in each phase of the network nodes, such as the probability of being susceptible to infection, the worm's infection rate β is constant interference, regardless of network performance and other factors.

Then for random scanning, the infection rate can be defined as:

$$\beta = kN \tag{1}$$

Among them, k is a constant, determined by the scan efficiency and success rate and frequency. At time t network, the number of the susceptible host is $s(t)$, the number of the infected host is $I(t)$, then the classical SI models:

$$\frac{dI_t}{dt} = \beta(k) \frac{S(t)I(t)}{N} \tag{2}$$

In this way, combined with (1) and (2), set the initial number of infected nodes $I(0)=I_0$, then:

$$\frac{dI_t}{dt} = KN I_t (N - I_t) \tag{3}$$

Due to the slow starts of the worm stage, $N - I_t \approx N$, so you can approximate that the solution of Equation (3) is:

$$I_t = I_0 e^{KN^2 t} \tag{4}$$

By Equation (1) can be seen, rates of random scanning directly depends on the size of the network, so as to affect the speed of the worm's spread. If the network of n nodes, and I nodes infected with worms, now defines I/N as the worms cover p , then $p=I/N$. Substituted into Equation (2), you can get worms cover Equation for:

$$\frac{dP_t}{dt} = KN^2 P_t (1 - P_t) \tag{5}$$

Worm cover Equation (5) reflects the impact of network worm propagation.

2.3 THE SIMULATION RESULTS

On the basis of random scanning and SI model, the analysis of worm propagation is not affected by other means of communication network, segmentation of worm inhibitory effect. If $K=2^{-64}$, $I(0)=10$ unchanged, the spread of the worm was simulated under the different network scale: a) worms spread throughout the IPV4 address space, the network size $N=2^{32}$; b) the size of the network $N=2^{32}/3$; c) the size of the network $N=2^{32}/10$. The simulation results are shown in Figure 2.

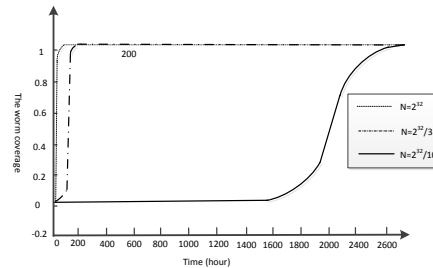


FIGURE 2 Worm coverage and network scale simulation diagram

As can be seen from the figure, the number of infected nodes and infected nodes in the percentage of the entire network, when the network is small, the spread of the worm has been a much longer time before they start to rise significantly.

3 DFS partition algorithm thought and realization of graphs

Based on the detection of worms, it should divide the network to reduce the scale of the network, detect and isolate the worms on the demarcation of the border, only in this way can effectively curb the worm in large-scale network wandering and impact, curb the spread of worms.

Method of providing or using the Internet as measured by network management institutions at all levels [8-10], it is possible to obtain a more accurate network topology information and data. Through the analysis of network topology, you can get a description of the network connection undirected connected graph $G(V, E)$.

Definitions 3.1. The collection V and E consists of Graph G , by denoted $G(V, E)$. Where: V is the set of vertices, E is a finite set of vertices in V , generally, the graph G , the vertex set and edge set denoted by $V(G)$ and $E(G)$. $E(G)$ can be the empty set, if $E(G)$ is empty, then the G graph only vertices and no edges.

The basic idea of DFS algorithm of the graph is:

Assume that the initial state is the graph of all vertices not been accessed, for a vertex V_i from the figure, the access to this vertex, followed by V_i from the neighbors have not been accessed in a depth-first traversal until all of the figure and there is a path V_i vertices are visited until; this case, if there are vertex graph is not accessible, the vertices of the alternative access is not the starting point and the process repeats until all graph vertices have been visited so far.

Known figure $G(V, E)$, when each edge of the figure search, according to the following steps:

1) When $E(G)$ of all sides without fully search, either take a vertex $v_i \in V(G)$, to v_i and to mark the stack.

2) When search v_i points associated with the edge, if the other side to mark the endpoint is not present, then the other end to make [as v_i , give signs, and stack, sub (2)], otherwise transfer (3).

3) When all the search associated with v_i edge is completed (V_i when that does not exist in order to search for the endpoint and without side), then v_i exit point from the top of the stack, the stack is not empty, as if to let [v_i removed after the top element as v_i , turn (2)], otherwise transfer (4).

4) If the stack is empty, but there are still signs of the vertices not given, take any of the vertices as v_i , turn (2), if all the vertices have signs, the algorithm ends.

Definitions 3.2. When graph $G(V, E)$ carried DFS search, the first vertex is called the root vertex first began; searching from the point the v along (v, w) side, nodes v called the father points w (using father (w) indicates the father of the node w), w called son node of v ; when the w has no sign, (v, w) side called branches, when w has sign, (V, w) is called the back side edge.

Definition 3.3. TREE, BACK. TREE is defined as the set of branches side, BACK is defined as the set of back edges.

Definitions 3.4. Mark (v). Mark(v)=0 means that v point has not been searched, mark(v)=1 means that v point has been searched.

Definitions 3.5 Num(v). Num(v) represents DFS number of point v , that is, point v in the search process to be accessed in the order. If the edge(v_i, v_j) is the branch side, there $num(v_i) < num(v_j)$; if (v_i, v_j) is back, with $num(v_i) > num(v_j)$.

DFS algorithm steps are as follows:

1) TREE $\leftarrow \emptyset$, BACK $\leftarrow \emptyset$, $i \leftarrow 1$,
 $v \in V(G)$ for

[father (v) $\leftarrow 0$, mark (v) $\leftarrow 0$];

2) Choose one point r optionally satisfies the condition mark (r) = 0, for

[$v \leftarrow r$, mark (v) $\leftarrow 1$, num (v) $\leftarrow i$];

3) If all edges associated with v points have signs, then turn (5); otherwise choose one side not sign (v, w) switch (4);

4) to (v, w) side with direction from v to w , and give the sign* to show through checking;

If the mark(w)=0, then for

[$i \leftarrow i+1$, num (w) $\leftarrow i$, TREE \leftarrow TREE \cup $\{(v, w)\}$, mark (w) $\leftarrow 1$, father (w) $\leftarrow v$, $v \leftarrow w$, turn (3)];

If the mark(w)=1, then for

[BACK \leftarrow BACK \cup $\{(v, w)\}$, transfer (3)];

5) If the father (v) $\neq 0$, then for

[$v \leftarrow$ father (v), turn (3)];

Otherwise, as,

[If $v \in V(G)$ always have mark(v)=1, then the algorithm ends; otherwise for $i \leftarrow i+1$, turn (2)].

4 Network segmentation algorithm based on DFS

Large-scale network segmentation is the Division of a graph, traversing through the nodes on the network, the network can be divided to obtain sufficient to control the spread of the worm node.

Definitions 4.1. Segmentation point. If a network-connected graph $G(V, E)$ nodes in v ($v \in v(G)$), and v all associated edges deleted from the G , increase the connectivity number of blocks, then v is the dividing point, also called the backbone node.

Definitions 4.2. Leaves. If v has one and only one side connected to the other vertex, v is said to be graph leaves. It is obvious that the personal computer is a leaf node in the network.

Definitions 4.3. Graph pruning. Due to the leaf node is not backbone nodes in the network, so before network segmentation, you can remove the leaves. If the parent node of leaf nodes in figure of leaf cutting, degenerate into leaves, you can also delete it until there are no leaves can be removed so far, this process is called pruning, referred to as pruning. As shown in Figure 3.

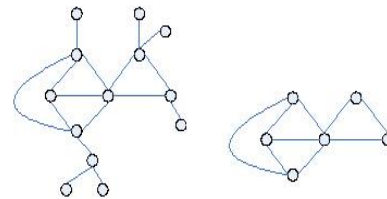


FIGURE 3 Pruning of diagram

Definition 4.4. T(v). T (v) is reached by the v start up the DFS tree T to v "seed" node u , up through a back edge (u, w) has reached the point where w collection. $v \in T(v)$.

Definition 4.5. Low(v). Low (v) is the minimum number of DFS T (v) in the set of vertices.

That is $low(v) = \min_{w \in T(v)} \{num(w)\}$.

The calculation steps of low (v) are as follows:

1) When you first visit v point, so low (v) \leftarrow num (v);

2) Through to the reverse side (v, w) , so low (v) \leftarrow min {low (v), num (w)};

3) The son node w of v search the exit from the stack, returning to the v -point, so low (v) \leftarrow min {low (v), low (w)}.

The basic idea for segmentation points using DFS is:

On the figure of $G(V, E)$ using DFS search method of all the vertices and edges of the inspection process, along information of the left low (v), when the search is over, the root node r is the dividing point, if and only if r has more than one son nodes; $v(\neq r)$ is the dividing point, when and only when any son node w of v does not exist in the "seed" node (including w) to the v 's "ancestors" nodes back edge.

From the foregoing, vertex v ($\neq r$) is the dividing point of G , if and only if v has child w , $low(w) \geq num(v)$. So, the algorithm steps of graph segmentation point by using DFS are as follows:

1) On the graph $G(V, E)$ by pruning;

2) $STACK \leftarrow \emptyset, i \leftarrow 1,$
 $v \in V(G)$ as
 $[father(v) \leftarrow 0, mark(v) \leftarrow 0];$
 3) Choose a point r satisfies $mark(r) = 0$, as
 $[v \leftarrow r, mark(v) \leftarrow 1, num(v) \leftarrow i, low(v) \leftarrow i];$
 4) If all v related sides have signs, then turn (6);
 otherwise, choose one of the edge (v, w) of no sign, add sign
 to the side (v, w) , and added the (v, w) to the stack top
 $STACK$, turn(5);
 5) If $mark(w) = 0$, then for
 $[i \leftarrow i+1, num(w) \leftarrow i, low(w) \leftarrow i, mark(w) \leftarrow 1,$
 $father(w) \leftarrow v, v \leftarrow w, turn(4)]$
 If $mark(w) = 1$, for
 $[low(v) \leftarrow \min \{ low(v), num(w) \}, turn(4)];$
 6) If $father(v) = 0$, then the algorithm ends; otherwise as
 If $low(v) \geq num(father(v))$, as
 $[from\ the\ STACK\ shift\ side\ (father(v), v)\ and\ its$
 elements and the stack to output, turn (7)];

7) $low(father(v)) \leftarrow \min$ { $low(v),$
 $low(father(v))\}, v \leftarrow father(v), turn(4).$

5 Summary

Results show that the segmentation method based on network detection method is a fast and effective method, the size of virus detection sub-graph is moderate and suitable for calculation algorithms applying in the flow path search algorithm, and classic graph algorithm. It is also advantageous for the mass virus transmission to network analysis. Through an analysis of the worm propagation behavior, found that there are certain constraints relationship of network size to the propagation speed of the worm. On this basis, network segmentation algorithm based on DFS is proposed to reduce the size of the network, in order to gain subnet boundaries, in order to further suppress the spread of worms provide a theoretical basis, provide reference and basis for the erection of a network worm isolation system.

References

- [1] Lin T Y 2004 Mining associations by linear inequalities *Proceedings of International Conference on Data Mining Washington: IEEE Computer Society* 154-61
- [2] Lin T Y 2009 Granular computing: Fuzzy logic and rough sets Zadeh I.A, Kacprzyk J *Computing with words in information intelligent systems PhysicaVerlag (A Springer-Verlag Company)* 183-200
- [3] Watts D J, Strogatz S H 2008 Collective dynamics of small world networks *Nature* **393**(4) 440-2
- [4] Barabdsi A, Albert R 2009 Emergence of scaling in random networks *Science* 286(5439) 509-12
- [5] Singh S, Estan C, Varghese G, et al. 2004 Automated Worm Fingerprinting *Proceedings of the 6th Symposium on Operating System Design and Implementation(OSDI) USENIX* 45-60
- [6] Moore D, Paxson V, Savage S, et al. 2003 Inside the slammer worm [J] *IEEE Magazine of Security and Privacy* **1**(4) 33-9
- [7] Zoua C, Towsleyb D, Gongc W 2006 On the performance of Internet worm scanning strategies *Performance Evaluation* 63
- [8] Hyang-Ah Kim, Brad Karp 2004 Autograph: Toward Automated, Distributed Worm Signature Detection *Proceedings of the 13th USENIX Security Symposium*

Selection method of wireless communication modes in internet of vehicles

Feng Liu, Jing Wang

¹ShiJiaZhuang University of Economics, He Bei Shi Jia Zhuang, 050000, China

Corresponding author's e-mail: luifeng8879@126.com

Received 1 December 2014, www.cmnt.lv

Abstract

Internet of Vehicles has great effect on improving the efficiency of the transportation system and driving safety. Communication process of Internet of Vehicles can be done adopting various wireless communication modes which include 3G, WLAN and WAVE. As each wireless communication mode has different traffic scene applicability and different communication effects, this paper proposed a selection method for wireless communication mode based on support vector machine. This method obtained learning samples which indicate the communication mode with best communication performance through simulation of various traffic scenes in OPENT Modeler. Through the study of support vector machine algorithm, this designed method can output the predicted result mode of wireless communication adaptively under unknown traffic scenes. The outstanding results show that the selection method based on support vector machine can accurately choose the optimal communication mode in Internet of vehicles.

Keywords: internet of vehicles, wireless communication mode, support vector machine, communication performance, OPENT modeller

1 Introduction

Internet of Vehicles is important means of green travel for a modern city to reduce traffic congestion. Internet of Vehicles is the typical application of Internet of things in the transportation industry. With the vigorous development of the Internet of things technology in China, as an application of the Internet, Internet of Vehicles gets vehicles running parameters and road transport infrastructure such as usage, perception of real-time road traffic conditions and provides abundant comprehensive intelligent transportation services. Internet of Vehicles has a very broad application prospects in the aspect of improving efficiency of traffic and transportation system safety driving. According to the network architecture of Internet of things and the content of the web services it should provide and the networking architecture of Internet of Vehicles is shown in Figure 1. It can be divided into perception layer, network layer and application layer.

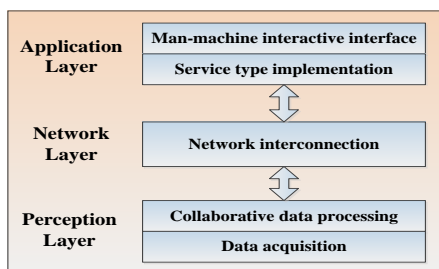


FIGURE 1 The networking architecture of Internet of Vehicles

Internet of Vehicles has similar characters with Vehicle Ad hoc Network (VANET) liking universality, movability and Intelligence. As its own constraints architecture of vehicle ad-hoc network, vehicle safety problems like lacking

of entire network data acquisition, insufficient information sharing and non-real time data interaction exist [1]. As topology structure of vehicles in Internet of Vehicles changes rapidly, the efficiency and security of wireless communication are confronted with great challenges and it may need a variety of communication modes to complete wireless communication tasks, such as 3G, Wireless Local Area Networks (WLAN) and Wireless Access in the Vehicular Environment (WAVE) which are described in Figure 2. In order to get better network performance, more appropriate should be adopted in specific traffic scene.

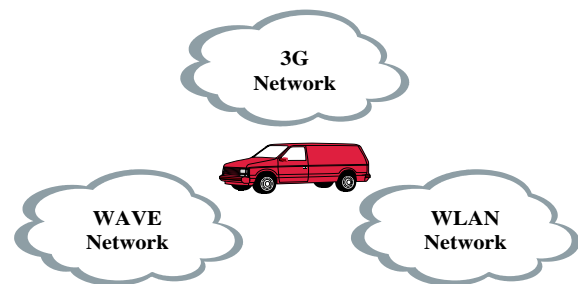


FIGURE 2 The structure of UMTS

Now many experts and scholars have constructed various communication modes and networking communication architecture in Internet of Vehicles. In [2], authors developed a simulation framework for holistic analysis of complex UMTS-based ITS. This framework couples simulation models with corresponding protocols of the UMTS link level, of higher network layers, and of road traffic. Based on our simulation framework and real-world 3G network coverage data, they evaluated a UMTS-based Traffic Information System (TIS) in a typical highway scenario, in

which information about traffic jams needed to be communicated to other cars for optimized route planning. The evaluation clearly outlines the capabilities of the simulation framework and evaluation results are consistent with all expectations. In [3], this paper designs and implements a multimode wireless gateway based on embedded system. The hardware uses ARM11 microprocessor, S3C6410, as controller and integrates 3G module, IEEE802.11g module and Bluetooth module. The software is based on Embedded Linux, develops drivers of integrated modules and user applications, and realizes the function of protocol conversion and routing. In [4], authors use GPS information to calculate the expected capacity using location, direction, velocity and RSSI information, in advance. Therefore, we suggest a handoff algorithm that uses the expected capacity to guarantee bandwidth. We implemented the suggested algorithm and experimentally verified the performance of the algorithm.

In [5], authors envision design VANET-UMTS integrated network architecture. In this architecture, vehicles are dynamically clustered according to different related metrics. From these clusters, a minimum number of vehicles, equipped with IEEE 802.11p and UTRAN interfaces, are selected as vehicular gateways to link VANET to UMTS and encouraging results are obtained in terms of high data packet delivery ratios and throughput, reduced control packet overhead, and minimized delay and packet drop rates. In [6], Seamless Internet 3G and Opportunistic WLAN Vehicular Internet Connectivity (SILVIO) is proposed, a solution for providing Internet connectivity in multi-hop vehicular ad hoc networks. Real traffic traces from the city of Madrid were used to feed the simulator which considers large vehicles as obstacles, as well. The obtained simulation results show that using SILVIO the cellular network can be offloaded by a factor up to 80%.

Neural network is also applied in the transportation system widely, but it has not been used for communication mode selection. Lee and Wai designed adaptive fuzzy neural network control model that applied magnetic levitation transportation system, and its online learning algorithm has solved the problem of the chattering phenomenon and stability of the system [7]. In this paper, the neural network is used for integrate wireless communication mode. In [8], various methodologies for traffic information prediction are investigated. Authors present a speed prediction algorithm.

NNTM-SP (Neural Network Traffic Modeling-Speed Prediction) that trained with the historical traffic data and is capable of predicting the vehicle speed profile with the current traffic information. Experimental results show that the proposed algorithm gave good prediction results on real traffic data and the predicted speed profile shows that NNTM-SP correctly predicts the dynamic traffic changes. In [9], aiming at limitation of the conventional network traffic time series prediction model and the problem that BP algorithms easily plunge into local solution, an optimization algorithm - PSO-QI which combine particle swarm optimization (PSO) and the quantum principle is proposed, and can alleviate the premature convergence validly. Then, the

parameters of BP neural network were optimized and the time series of network traffic data was modeled and forecasted based on BP neural network and PSO-QI.

The remainder of this paper is structured as follows. Section II gives a scope of wireless communication modes in Internet of Vehicles. Section III describes the proposed selection method for wireless communication mode based on support vector machine and verification for it is presented in Section IV. Section V finally concludes this paper.

2 Scope of wireless communication modes

2.1 3G COMMUNICATION MODE

UMTS (Universal Mobile Telecommunication Systems), as a 3G & beyond cellular network technology, operates with a frequency range of around 2 GHz [10]. UMTS make the WCDMA as the preferred air interface technology and achieve continuous improvement [11], but it also has introduced the TD-SCDMA and HSDPA technology. The structure of UMTS system mainly includes the wireless access network, CN (Core Network, the core network), UE (User Equipment) and UTRAN (UMTS Terrestrial Radio Access Network). UMTS support transmission rate with 1920 kbps and a peak downlink data rate of 2 Mbps. The structure of UMTS is described in Figure 3.

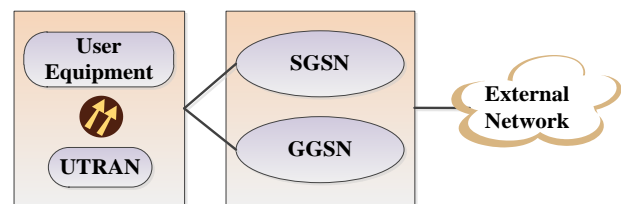


FIGURE 3 The structure of UMTS network

3G communication mode is suitable for communication scenarios with long distance and less traffic load. The advantage of 3G communication mode has less demand on the moving velocity of the node, and the disadvantage of 3G is the data transfer rate and limited capacity.

2.2 WLAN COMMUNICATION MODE

WLAN is a type of wireless communication system, with characters of flexibility, mobility, easy scalability, and low cost and used for providing wireless connectivity between moving vehicles [12]. Wi-Fi which is the widely application of WLAN is a brand of wireless communication technology, and its main communication protocol is the IEEE 802.11 series of protocol. Wi-Fi adopts the IEEE 802.11b protocol generally. There are many available routing protocols, including AODV, DSR, TORA routing protocol. Channel access protocols such as DCF (Distributed Coordination Function), PCF (Point Coordination Function) and HCF (Hybrid Coordination Function) are available. Other kinds of IEEE 802.11 series protocol for different application scenarios have different applicability. The typical routing protocol, channel access protocol and MAC protocol are listed in the following figure.

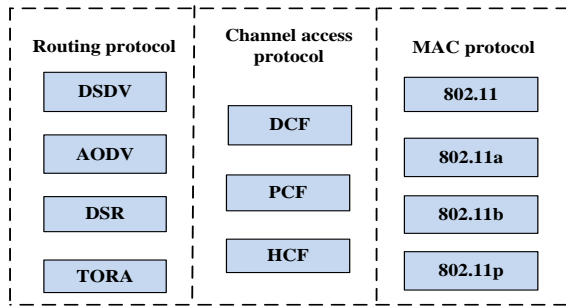


Figure 4 The networking architecture of Internet of Vehicles

WLAN communication mode is suitable for the communication scenario in which the number of vehicles, vehicle velocity, and communication distance are moderate. Overall, WLAN technology proved to work also at vehicular velocity [13].

2.3 WAVE COMMUNICATION MODE

WAVE technology is an efficient short-range wireless communication mechanism after the generation of cooperative vehicle infrastructure system in order to solve the vehicle-to-vehicle communication, vehicle-roadside communication problems. The advantage of WAVE is mainly reflected in the message transmission latency, node mobility, communication frequency of anti-interference. The applicability of the IEEE 802.11p for Internet of Vehicles, its comprehensive evaluation of network performance and cost of implementation and complexity aspects are superior to ordinary wireless communication technology.

The data Link layer includes LLC (Logical Link Control) and MAC, the IEEE 802.11p of MAC layer is the concentrated reflection of the performance advantages in the protocol architecture as shown in Figure 5. The IEEE 1609.4 standard sets rules on the multi-channel multiplexing technique and channels can be divided into SCH and CCH time slot by using the method of time slot, and the channel time is divided into synchronization intervals with a fixed length of 100ms [14, 15]. MAC layer provide services for data transmission channel and coordination control, and make more efficient exchange of data through reliable channel access protocol. The WAVE mode is more suitable for traffic scenarios with plenty of vehicles and high velocity.

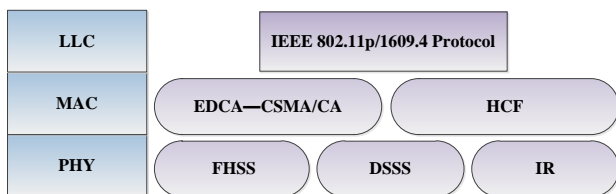


FIGURE 5 The protocol architecture of WAVE

3 Selection method for wireless communication modes based on support vector machine

The main function of proposed selection method for wireless communication modes is to select the most suitable wireless communication mode for the current traffic scene.

Support vector machine can learn the rule of optimal communication mode according the learn samples. As vehicle density and vehicle velocity are the regular characters of transportation system, so they regard as the input of the support vector machine network. Support vector machine (SVM) network model is adopted in selection method proposed in this paper.

3.1 SUPPORT VECTOR MACHINE MODEL

Support vector machine (SVM) method is built on the basis of statistical learning theory based on VC dimension theory and structure risk minimum principle and seek the best compromise between the limited sample information in the complexity of the model and learning ability to get the best generalization ability. The decision function of support vector machine (SVM) is similar to a support vector machine network, and the output is several linear combinations of the middle layer nodes. Each layer node corresponds to the inner product between input sample and a support vector, and then which is also called support vector networks. The structure of support vector machine network is shown as Figure 6. x_1 and x_2 represent vehicle density and vehicle velocity respectively. The essence of SVM is mapping the low-dimensional input space to a high-dimensional feature vector space. y is the output of support vector machine network model and its range of value is (0,1,2,3) which represent random mode, 3G mode, WLAN mode and WAVE mode respectively.

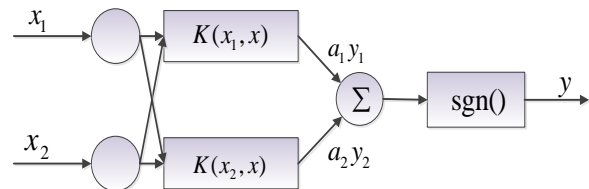


FIGURE 6 Structure of SVM network

$K(x_i, x_j)$ is the inner product function which satisfies condition of Mercer. $sgn()$ is the threshold function of this selection method.

$$K(x_i, x_j) = [(x_i \cdot x_j) + 1]^q, \quad q = 1, \tag{1}$$

$$sgn = \begin{cases} 1, & (0.5 \leq y < 1.5) \\ 2, & (1.5 \leq y < 2.5) \\ 3, & (2.5 \leq y < 3.5) \\ 0, & \text{other} \end{cases} \tag{2}$$

3.2 LEARNING SAMPLE

The learning samples consist of optimal simulation results of plenty of traffic scenes. Simulation scenarios with different vehicle densities and vehicle velocities are simulated using different communication modes in OPNET Modeler,

and then communication mode with the best communication performance is chose as the learning sample. The transmission delay and packet loss rate are the main communication performance evaluation indexes. The transmission delay means the time difference between the time of creating packet and the time of receiving packet. The packet loss rate means the proportion of lost packet in the whole packets. This paper puts forward a system evaluation factor C which integrates the transmission delay and packet loss rate as formula (3).

$$C = 0.5 \cdot \left(1 - \frac{D}{D_{\max}}\right) + 0.5 \cdot \left(1 - \frac{L}{L_{\max}}\right) \quad (3)$$

D and L are the average transmission delay and packet loss rate during current simulation scene. We think that the transmission delay and packet loss rate have the same importance for the performance of Internet of Vehicles nearly, so their scaling factor are 0.5 as well. D_{\max} and L_{\max} indicate the maximum value of them respectively. System evaluation factor C can reflect the performance of the network communication basically and $0 \leq C < 1$. The performance of communication change for the better as the value of C becomes larger.

System evaluation factor C regards as the reference standard which is put forward by the above paper. A number of different traffic simulation scenarios were finished and the communication mode with maximum of C was selected for learning samples. The whole learning samples of selection method based on SVM network model is described in Table 1.

TABLE 1 Learning samples of selection method

Input(veh, km/h)	Evaluation Factor	Optimal Mode
100,20	0.654	3G
100,40	0.702	3G
100,60	0.745	WAVE
200,20	0.723	WLAN
200,40	0.695	WLAN
200,60	0.821	WAVE
400,20	0.795	WLAN
400,40	0.765	WAVE
400,60	0.732	WAVE

3.3 LEARNING ALGORITHM

The process of learning algorithm for solving the problem of classification with support vector machine (SVM) is described in the following paper.

Step 1: One group of learning sample (x_1, x_2) and desired output (y_1, y_2) are given. There are 9 groups of learning samples in whole.

Step 2: Constraint condition are described in following Equation.

$$\sum_{i=1}^2 y_i a_i = 0, \quad a_i \geq 0 (i = 1, 2). \quad (4)$$

Then calculate the maximum value of $W(a)$ from the Equation (5) and obtain a_i^* .

$$W(a) = \sum_{i=1}^2 a_i - \frac{1}{2} \sum_{i,j=1}^2 a_i a_j y_i y_j (x_i \cdot x_j) \quad (5)$$

Step 3: Calculate the value of w^* and b^* as following Equation. x_s is a specific support vector.

$$w^* = \sum_{i=1}^2 a_i^* x_i y_i, \quad (6)$$

$$b^* = \frac{1}{y_s} - w^* \cdot x_s. \quad (7)$$

Step 4: For the vector x without classification, it can be calculated by $K(x_i, x_j)$ and $f(x)$.

$$f(x) = \text{sgn}\left\{\sum_{i=1}^2 y_i a_i^* K(x_i, x) + b^*\right\}. \quad (8)$$

Although the performance of the SVM algorithm is verified in the application in many actual problems, but there are some problems on the calculation of the algorithm, which include slow training algorithm, the complex algorithm that is difficult to implement and test phase with heavy computation. The memory size during training process is shown is Figure 7 and the memory size increase rapidly with the increase of sample size, and in the final it reaches 24M. When the above four steps are finished, the SVM network is constructed and it can be used for selection of communication mode.

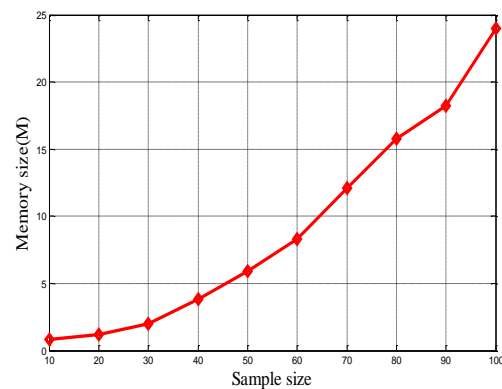


FIGURE 7 The relationship between memory size and sample size inSVM network

3.4 SIMULATION RESULTS OF SVM NETWORK

In order to verify the accuracy in the choice of communication mode in Internet of Vehicles by above designed support vector machine network model, the authors have designed more complex traffic simulation scenarios in which more elaboration of vehicle densities and vehicle velocities regard as the input of support vector machine

network. Through support vector machine learning algorithm, and the output of the communication mode by selection method is collected as follows Table 2.

TABLE 2 Result of support vector machine network model

Input(veh, km/h)	Output
150,20	3G
150,30	3G
150,40	3G
150,50	3G
150,60	WAVE
250,20	WLAN
250,30	WLAN
250,40	WLAN
250,50	WAVE
250,60	WAVE
300,20	WLAN
300,30	WLAN
300,40	WAVE
300,50	WAVE
300,60	WAVE

4 Performance evaluation

The purpose of evaluation of selection method for wireless communication mode based on support vector machine network is comparing the different choice results between the real optimal communication mode and the output of the selection method. At the same time, authors make research for the effect of performance with different communication mode in different traffic simulation environments.

4.1 ESTABLISHMENT OF SIMULATION SCENARIO

The simulation scenarios are constructed in OPNET Modeler. OPNET which is based on the time driving mechanism has good time management strategy. OPNET provide According to the particularity of communication process in Internet of Vehicles, the MANET model of OPNET Modeler model library is selected as vehicle equipment simulation experiments when WLAN and WAVE are selected as the communication modes. As the main information carrier, MANET node plays a decisive role to the entire network environment simulation.

Vehicle information is sent and received from the WLAN transceiver and in turn goes by the MAC layer, data link layer, IP, UDP, routing layer, application layer to complete the whole message communication process. The quantity of MANET model represents the vehicle density and the attitude of velocity represents the vehicle velocity. As the motion model is not essential for this selection method, so it is set as random mobility. Routing protocol, packet size and interval, channel access protocol parameters and other settings can be set by the user interface in OPNET Modeler. The number of MANET during simulation is placed according to the input of Table 2 and simulation process with WLAN mode is shown as Figure 8.

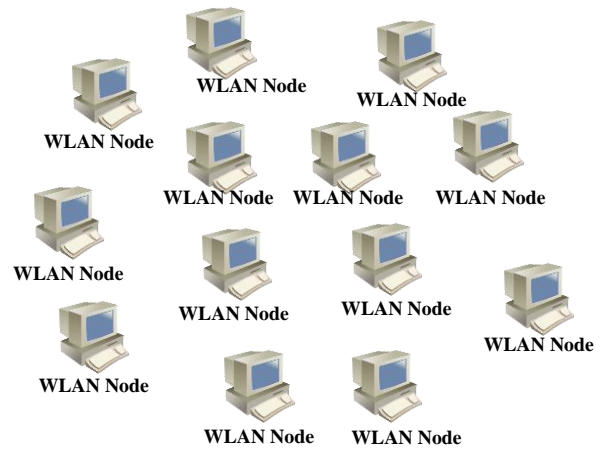


FIGURE 8 WLAN simulation process in OPNET Modeler

As the WAVE mode is based on 802.11p and OPNET Modeler don't provide its interface, so we need to modify the node internal code to simulate the communication process with WAVE communication mode. The focus of modification is the MAC layer and multi-channel operation.

The simulation process with WAVE mode is show as Figure 9.

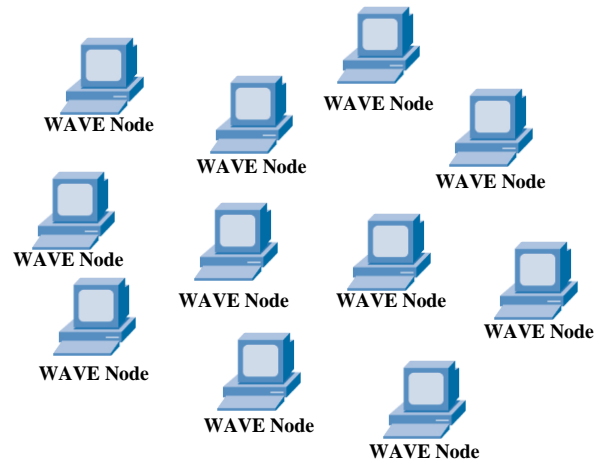


FIGURE 9 WAVE simulation process in OPNET Modeler

The simulation network topology of UMTS in OPNET Modeler is shown in Figure 10. UE represents the mobile user equipment, and Node_B represents the node B in UMTS. The RNC represents the radio network controller of UMTS, and CN represents the core network in UMTS. The quantity of UE is equal to the vehicle density. In order to generate UMTS data flow, an external network and the FTP server are built.

The simulation scenario needs to switch among different communication modes. The range of simulation scenario is one square kilometer. OPNET Modeler perform a variety of communication modes, which including 3G (UMTS), WLAN and WAVE.

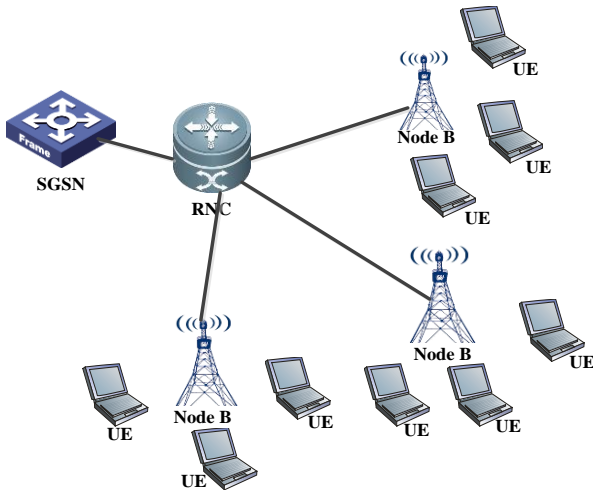


FIGURE 10 UMTS simulation process in OPNET Modeler

The attitudes of communication mode and above simulation scenario are set as the default settings which are described in Table 3. The simulation time lasts 10 minutes. The simulation results are managed by the statistics processing of OPNET Modeler during simulation and can export when simulation finished.

TABLE 3 The default settings of simulation

Settings	Value
Simulation range	1000m ²
Simulation time	10minutes
Packet size	1000 bytes
Packet interval	Exponential(1)
MAC protocol	802.11p/802.11b
Data rate	11M/s
Wireless transmission mode	TwoRay Ground
Network interface type	Wireless PhyExt
Interface queue model	PriQueue
Mobility model	Random
Channel access protocol	EDCA/DCF
Link layer	LL
Routing protocol	AODV

4.2 VERIFICATION OF SVM NETWORK

Through the simulation according to the input of support vector machine network and the system evaluation factor C , the optimal communication modes are obtained precisely. The verification results of support vector machine network model are described in Table 4. We can see from the results that only when the vehicle density and velocity are 150 and 50, the output of selection method and real optimal mode is different. This is because when 3G mode behaves well when the number of vehicles is small and WAVE mode behaves well when the vehicle velocity is high. Then the wrong judgment is made as the miscalculation of transport properties and different traffic applicability. The probability of correct is 93.3%. In order to get higher accuracy of selection of communication mode, the

failure output can be joined in the learning samples as the new condition, then the feedback loop is constructed.

TABLE 4 Verification result of support vector machine network model

Input(veh, km/h)	Output	Optimal Mode
150,20	3G	3G
150,30	3G	3G
150,40	3G	3G
150,50	3G	WAVE
150,60	WAVE	WAVE
250,20	WLAN	WLAN
250,30	WLAN	WLAN
250,40	WLAN	WLAN
250,50	WAVE	WAVE
250,60	WAVE	WAVE
300,20	WLAN	WLAN
300,30	WLAN	WLAN
300,40	WAVE	WAVE
300,50	WAVE	WAVE
300,60	WAVE	WAVE

4.3 VERIFICATION OF NETWORK PERFORMANCE

The system evaluation factor can reflect the wireless network performance. In order to show the different network performance of simulation scenario with various vehicle densities and velocities visually, we stat the transmission delay and packet loss rate during simulation time. In order to make a fair comment for network performance, we calculate the average parameter of transmission delay and packet loss rate in specific simulation environment. The unit of transmission delay is sec and the unit of packet loss rate is %. The simulation result of transmission delay and packet loss rate in different simulation scenarios are shown in Figure 11 and Figure 12.

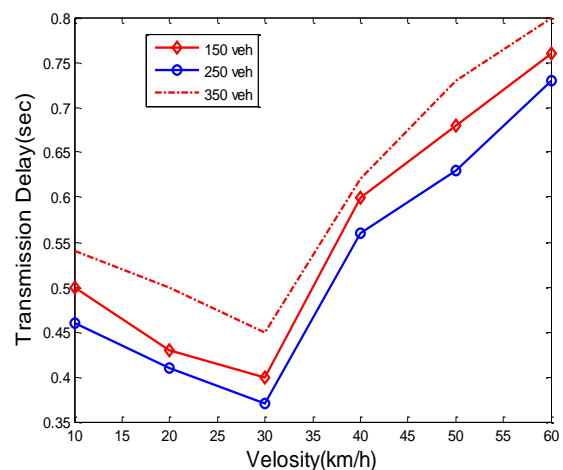


FIGURE 11 Results of transmission delay in different simulation scenarios

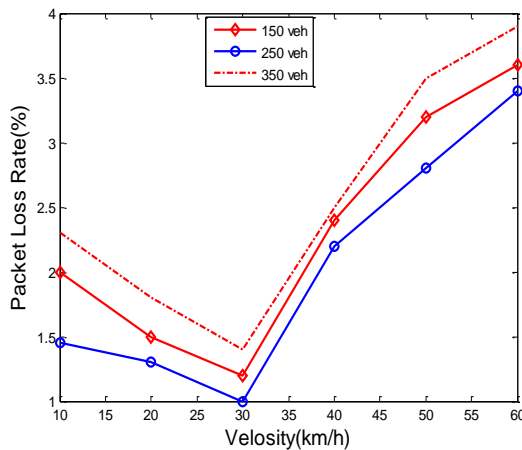


FIGURE 12 Results of packet loss rate in different simulation scenarios

It can be seen from the above result of transmission delay and packet loss rate that they have the similar variation tendency with the increase of velocity value. The velocity stands for average velocity of all the vehicles. When the velocity is low, vehicle nodes is equal to the fixed nodes and the miscellaneous function of movement has no show, so the network performance is not very good. When the velocity is high, network topology changes in frequent and the path of data packet transmission is unstable, then it leads to bad network performance. When the velocity is moderate, the communication performance is optimal relatively.

The effect of vehicle density on the performance of communication is also similar. When the vehicle density is small, the path that reaches the destination node is less and when the vehicle density is large, the possibility of traffic jams increase, so above conditions lead to the increase of transmission delay and packet loss rate. The system evaluation factor integrates the transmission delay and packet loss rate reasonably.

Figure 13 shows the system evaluation factor C in all simulation scenes. From it we can see that when the density is modest and velocity is low, the performance of network is better and the reason of it is that when the topological structure and routing of network is relatively stable, the path between source node and destination node is unblocked and the probability of sending failure is small relatively. As the selection method can choose the optimal communication mode, their network performances have little difference in the changing process of velocity.

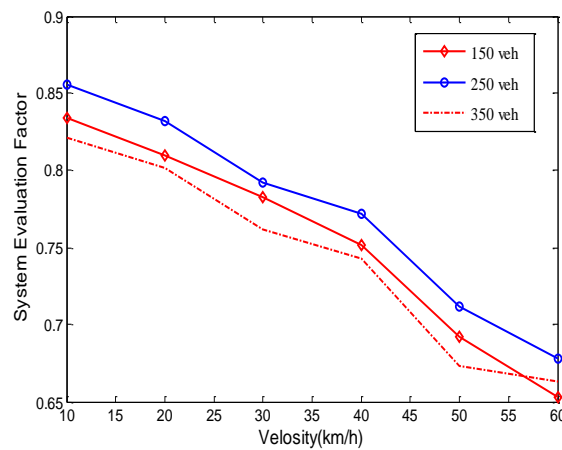


FIGURE 13 Results of system evaluation factor in different simulation scenarios

5 Conclusion

Through the study of the 3G, WLAN and WAVE communication mode applied in the Internet of Vehicles and analyzing the applicability of the communication mode, and then the selection method for wireless communication mode based on support vector machine network was proposed. The learning samples are created through plenty of simulation scenarios built in OPENT Modeler. After support vector machine learning algorithm, it forms a complete support vector machine network model to make choice of communication mode. More complex simulation scenes are built for the verification of selection method based on support vector machine network. The verification results show that the applicability of the selection method based on support vector machine network is great and basically can find out the optimal communication mode. The network performance factors which include transmission delay and packet loss rate reflect the variation tendency with different traffic simulation scene and the system evaluation factor integrate the transmission delay and packet loss rate reasonably.

This paper also has shortcoming, for example, the reasonability of support vector machine network has no strict mathematical reasoning; the learning samples have no integrity; the selection of evaluation parameters have no argument whether they are justice. In the future, we will search for more accurate selection methods of wireless communication mode in Internet of Vehicles.

References

- [1] Hossain E, Chow G, Leung V C M 2010 Vehicular telematics over heterogeneous wireless networks: A survey *Computer Communications* 33(7) 775-93
- [2] Sommer C, Schmidt A, Chen Y 2010 On the feasibility of UMTS-based Traffic Information Systems *Ad Hoc Networks* 8 506-17
- [3] Mao Y, Xia W, Wu Y 2012 Designing and Implementing of Multimode Wireless Gateway in VANET in *Proc 2012 International Conference on Wireless Communications & Signal Processing (WCSP 2012)* 978-83
- [4] Kim D H, Byun S K, Kim J D 2014 Expected Capacity Based Handoff Scheme for Multimedia Data in WLAN *In Proc International Conference on Information Networking* 358-89
- [5] Benslimane A, Taleb T, Sivaraj R 2011 Dynamic clustering-based adaptive mobile gateway management in integrated VANET-3G Heterogeneous Wireless Networks *IEEE Sel Areas Commun* 29(3) 559-70
- [6] Gramaglia M, Bernardos C J, Calderon M 2011 Seamless internet 3G and opportunistic WLAN vehicular connectivity *Eurasip Wirel Comm* 5 1-20

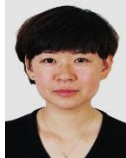
- [7] Wai R J, Lee J D 2008 Adaptive Fuzzy-Neural-Network Control for Maglev Transportation System *IEEE Trans Neural Net* 19(1) 54-70
- [8] Park J, Li D, Murphey Y L 2011 Real Time Vehicle Speed Prediction using a Neural Network Traffic Model in *Proc International Joint Conference on Neural Networks (IJCNN 2011 - San Jose)* 2991-6
- [9] Zhang K, Liang L, Huangin Y 2013 A Network Traffic Prediction Model Based on Quantum Inspired PSO and Neural Network in *Proc. Sixth International Symposium on Computational Intelligence and Design (ISCID)* 219-22
- [10] Taleb T, Benslimane A 2010 Design guidelines for a network architecture integrating vanet with 3g & beyond networks in *Proc IEEE GTC* 1-5
- [11] Dahlman E, Gudmundson B, Nilsson M, Skold A 1998 UMTS/IMT-2000 based on wideband CDMA *IEEE Commun Mag* 36(9) 70-80
- [12] Cuyu C, Yong X, Meilin S, Liang L 2009 Performance observations on mac protocols of vanets in intelligent transportation system in *Proc. IEEE CMC* 2 373-9
- [13] Wellens M, Westphal B, Mahonen P 2007 Performance evaluation of IEEE 802.11-based WLANs in vehicular scenarios in *Proc IEEE 65th Veh Technol Conf* 1167-71
- [14] Miao L, Djouani K, Van Wyk B J, Hamam Y 2013 Performance evaluation of IEEE 802.11p MAC protocol in VANETs safety applications in *Proc IEEE WCNC* 1663-8

Authors



Feng Liu, February 17, 1980, HeBei Province, China

Current position, grades: assistant professor.
University studies: HeBei Normal University.
Scientific interest: computer network.
Publications: 4 papers.



Jing Wang, June 27, 1979, HeBei Province, China

Current position, grades: assistant professor.
University studies: North China Electric Power University.
Scientific interest: computer network.
Publications: 4 papers.

Study on the task scheduling problem of complicated products' design

XiaoBo Cao*, ChengDong Xu, GuoChao Fan

Key Laboratory of Dynamics and Control of Flight Vehicle, Ministry of Education, Beijing

School of Aerospace Engineering, Beijing Institute of Technology, Beijing, China

**Corresponding author's e-mail: caoxiaobo198610@163.com*

Received 1 December 2014, www.cmnt.lv

Abstract

The process of complicated products design has the characters of high complexity, long period and various requirement of resource. So a reasonable resource scheduling scheme has great significance to the design of complicated product, so as to shortening product development cycles and reducing the cost of product. Firstly, design task collaboration and scheduling features in three complicate product design process modes are discussed in terms of research results of collaboration design and Integration Design Environment (IDE). Secondly, Virtual Design Unit (VDU) is adopted to be taken as the basic task execute unit, VDU design is a complex product design, Furthermore, Design Task Scheduling Approach based Design Ability (DTSADA) is detailed stated by combining ACO and GA.. Finally, a design task scheduling case is demonstrated to validate the proposed approach.

Keywords: complicated product, virtual design unit (VDU), IDE, task scheduling

1 Introduction

With the increase of structure complexity and function requirement, design process of complicate product involves in more and more disciplines and design resources. Customer-oriented product design with low cost and high efficiency has become a tendency. How to realize design resources share and optimization allocation in a high efficiency is the key to short the design time and cost. Aiming to the drawbacks of traditional design modes, some distributed network collaboration design technologies such as Concurrent Engineering (CE) [1], Cloud Computing (CC) [2] and Cloud Manufacturing (CMfg) [3] try to address above problems in design process by design resources virtualization, knowledge reuse, reasonable design process model and high efficiency design task scheduling. It has become a widely attention problem to facilitating product design by scheduling reasonable design resources to finish complicate product design task with low cost and short time.

In the design process of complicate product, design task scheduling problem mainly refers to design task modeling, design executor selection, design ability evaluation and task scheduling approach construction. 1) Design task model must be clearly abstracted from different types of design tasks. It is important to specifically describe task basic information, design constrains, design requirement, task interaction relation and design process association in the design task model. Only if design task targets are determined, can we select suitable design resources to finish it; 2) Design resources must be organized in certain form of high-efficiency executor unit to play full role in the design activity. There are so many kinds of design resources involved in the design process such as design people, equipment, tool,

software and network. Design people are the core in the design activity. So it is necessary to construct high-efficiency design unit by matching reasonable resources with designer so as to bring into play maximum initiative of designer; 3) Design abilities of design executor must be accurately evaluated by comprehensively considering design success ratio, design skilled degree and design robust. Design ability of executor will dynamically change following the change of design experience. A design ability evaluation model that can reflect the effect of success ratio, design skilled degree and design robust is indispensable; 4) Optimization mathematics function is supposed to be built, and it is as important as a high-efficiency scheduling approach of design task.

From what we discuss above, our research aims to develop a new design task scheduling approach with accurate design ability model, and it makes efficient utilization of distributed design resources in such a way as to minimize design cost. Remainder sections of this paper are organized as follows.

2 The algorithm of complex task scheduling problem

With the development of distributed network collaboration modes in the domain of computing, design and manufacturing, design task scheduling become an important frontier problem. Some heuristics intelligence algorithms are prevailed to solve the distributed task scheduling optimization problems such as Simulated Annealing (SA), Genetic Algorithm (GA), Ant Colony Optimization (ACO) and Particle Swarm Optimization (PSO). Based on the above methods, there are a lot of researches oriented to complicated product design task scheduling at home and board.

Yu, XB [4] puts forward a novel adaptive hybrid algorithm based on PSO and DE (HPSO-DE) by developing a balanced parameter between PSO and DE. Adaptive mutation is carried out on current population when the population clusters around local optima. The HPSO-DE enjoys the advantages of PSO and DE and maintains diversity of the population. S.J. Shyu [5] proposes an application of the ACO to a two-machine flow-shop scheduling problem. In the flow-shop, no intermediate storage is available between two machines and each operation demands a setup time on the machines. The transformation of the scheduling problem is translated into a graph-based model. The method seeks to compose a schedule that minimizes the total completion time. A.Y. Abdelaziz [6] introduces the Ant Colony Optimization algorithm (ACO) implemented in the Hyper-Cube (HC) framework to solve the distribution network minimum loss reconfiguration problem. The HC framework limits the pheromone values by introducing changes in the pheromone updating rules resulting in a more robust and easier to implement version of the ACO procedure. ZHANG Yu [7] brought up an algorithm combining Genetic algorithm (GA) and Ant Colony algorithm (ACO) for the programming framework of cloud computing. In the algorithm, the GA adopts task-worker coding method, every chromosome representing a specific scheduling scheme, and chooses the average completing time of all tasks as its fitness function. Timur Keskinurk [8] proposes Ant Colony Optimization (ACO) method outperforms heuristics and genetic algorithm, and it is used to solve the problem of minimizing average relative percentage of imbalance (ARPI) with sequence-dependent setup times in a parallel-machine environment. A mathematical model that minimizes ARPI is proposed. As papers limited, the other researches are not detailed stated.

Most academics place different emphasis on resources selection and task scheduling. But several items are neglected as follows:

1) Pay much attention to task scheduling in single design stage and ignore the relation between task and design process, interaction among design tasks. Design task in design process is not modeled from the angle of multi-granularity and multi-stage. Design task decomposition and combination are also not reasonable.

2) Design ability models are simple or partial. Average completing time and cost are used to calculate the design consumption of one design task while ignore or pay little attention to the effect of task success ratio, design skilled degree and design robust in the design ability quantity evaluation. Experience growth and ability dynamically promotion of manpower in design activity are not considered in the former models.

3) Design task executor is usually limited in single design resource. There are few reasonable design resources organization unit and resources selection mechanism.

4) Most of design task scheduling methods are limited to solve scheduling problem of same task type. In the former scheduling methods, a design executor is constrained to

execute one kind of task in the former methods, which cannot play full role of design resources.

Accordingly, in our work we seek to address above problems and contribute to the works towards design resources structure optimization, quantity design ability modeling and high-efficiency design task scheduling.

3 Design task collaboration and scheduling modes

Complicated product design is a complicated collaboration process refers to reasonable tasks decomposition and combination, resources organization, task scheduling and result assessment. And it involves in multiple stages, multiple design entities, multiple iteration processes, multiple disciplinary and multiple resources. From the macroscopic angle, the keys to optimization design cost of complicate product is to reduce the interconnection among design tasks, reduce the iteration times in process and increase the control of design flow. In the design process:

1) Data interaction and design tasks are closed coupled together. Data input and output are finished inner the design task. Data interaction is transparency outside of design module. Only setting the execution sequence of design executor, a design process will be done. The interfaces of design executors is only task driven interface, it is not associated with design behavior, and data interaction is independence with interface.

2) Data interaction and design tasks are loose coupled. Design task executors only take responsibility for the execution of task, and data interaction is independent from design tasks. It made a request that design parameters pattern must match with the interfaces of design task execution modules.

Traditional design systems have used a sequential model for design generation, which breaks the design task into subtasks that are serially executed in a predefined pattern. This type of design process model is easy to realize and modeling. But sequential design is not extensible. Any mistake of one design node will affect the overall design process. Downstream information flow of sequential design makes it difficult to iterative design and feedback from low-level design activity to high-level activity. In this paper, VDU is taken as the example of complicated product, and VDU design process mainly includes design task decomposition, task agglomeration, resources and task scheduling and result evaluation. Refer to complex product design processes of VDU, this paper summarizes design task collaboration modes in three typical VDU design process:

1) Subsystem Paralleled Collaboration Design Pattern.

Subsystem paralleled design pattern is mainly oriented to mature VDU products. In the mode, design process is relatively matured, so it generally does not need to undertake large-scale iterative design across the system. Design object structure is already decided, and subsystems design tasks are separated in the light of production structure. Each subsystem design node is independent designed. When each subsystem attains some periodic result, design results of the subsystem are comprehensively collected and evaluated.

Design confliction are checked out, and modify opinions are also put forward. Design data of the upstream subsystem are delivered to downstream subsystem. Consequently, when some design conflictions between two subsystem design nodes occur, local optimization of subsystem can solve the own existence conflictions. In the level of part design task, confliction between two tasks inside one subsystem is eliminated by iterative amendments of all part design tasks. Conflictions of two part design tasks do not affect the other subsystem design tasks. When mission conversion of two task nodes occurs, design result data, next design requirements and tolerance specifications information are delivered to the execution of downstream process unit.

2) Global Iterative Design Pattern.

Global iterative design pattern is mainly oriented to the study and development of new types of VDU. In the mode, each subsystem is associated design with other subsystems. When each subsystem reaches a stage of node, all subsystem of design result are put together to carry out comprehensive evaluation. Modify opinions is put forward to solve the conflicts by all participants. And modification schemes are used in the process of the next iteration of amendments to eliminate conflict. The synergy mode is called global iterative design pattern. Subsystem is taken as design and verification nodes. Firstly, local optimization design of subsystems is realized. And then overall design optimization is achieved according to optimize and combine the various subsystems index. When problems are founded in the subsystem, it is need to modify each subsystem to iteration to achieve. "Multiple input, multiple output" is the main input and output characteristics of task nodes relation.

3) Assisted Association Design Pattern.

Assisted association design pattern is oriented to component coordinated design, and design tasks are collaborated with several units. As shown in Figure 1.

	Subsystem Paralleled Collaboration Design Pattern	Global Iterative Collaboration Design Pattern	Assisted Association Collaboration Design Pattern
Application object	Mature type missile or component design	New type missile or component design	Component or subsystem design
Design entity/Design task	Multi-entity/Single object	Multi-entity/Multi-object	Multi-entity/Single object
Executor coupling degree			
Design process complexity			
Concurrent design degree			
Iterative Number			

NOTE: Low Weak Moderate Strong

FIGURE 1 Features of three collaboration design modes

Design changes of a subsystem design is closely subjected by the other subsystem. Every subsystem design node carry forward according to the overall design index. As a design collaborator, modifications of other subsystem design nodes will cause large-scale design to design tasks affiliated to assisted association design pattern. "Multiple input, multiple output" is also the input and output characteristics of task nodes relation.

With comparing features of three modes, in the reality, it is rare to purely use single collaboration mode to complete VDU design. Mostly, three collaboration patterns that we discussed above are appropriate combined on appropriate occasions to meet different types of VDU.

4 VDU model

VDU is defined as a collection of some virtual design resources. VDU is taken as the basic execute unit of design task in this paper. The model of VDU is described in the form of five-tuple. $VDU = \{BasicInfo, Resource, DesignActivity, DesignAbility, Constrain\}$. Moreover, each tuple is explicated as following:

$BasicInfo = \{ID, Name, BuidTime, VmuType, Position, Workshop, Status\}$ denotes the basic information of VDU such ID, name, construction time, type, position, affiliated unit and status.

$Resource = \{ResouceStructure, ResouceRelation\}$ denotes the design resource and resource structure in the VDU. $ResourceStructure = \{M, E, T\}$. $M = \{m1, m2, m3, \dots\}$. $Vm \in M$, m denotes man resource, $M \neq 0$; $E = \{C, Eq, S, \dots\}$ denote the equipment resources include computers, experiment apparatus ,simulation platform. $Vc \in C$, c denotes computer resource, $C \cap E \neq 0$;

$DesignActivity = \{Da1, Da2, \dots, Dam\}$ denotes the design activities that can be executed in the VDU. $Dam = \{DesignObject, DesignMethod, DesignActivity, DesignInput, DesignOuput\}$ denotes the design activities attributes set.

$DesignAbility = \{DA1, DA2, \dots, DAN\}$ denotes the design abilities that VDU takes engage in different tasks. $DAN = \{DesignActivityID, SuccessRatio, SkilledDegree, Robust, DesignQuality, DesignCost, DesignTime\}$ denotes the design ability attributes.

$Constrain = \{Con1, Con1, \dots, Conx\}$ denotes the constrains restrain the design activity of VDU.

As the basic design task execute unit, each VDU can engage in at least 1type of design task. In the design activity, designer, computer equipment, simulation apparatus, software, model, tool and knowledge are the mainly factors that can affect quality of design activity. Inside, all kinds of designers are the dominant body. Designers engage in design, management and maintenance by operating all kinds of hardware and software. So designer is the indispensable element in VDU. In addition, main design computer is as important as designer. Design resources in the VDU connect together by main design computer with network. In the level of atom-resources, main design computer is used to register resources virtual information, accept design task, communicate among atom-resources and collect task information. In the level of VDU, it takes charge the communication and collaboration among different VDUs. Structure diagram of VDU is shown as Figure 2.

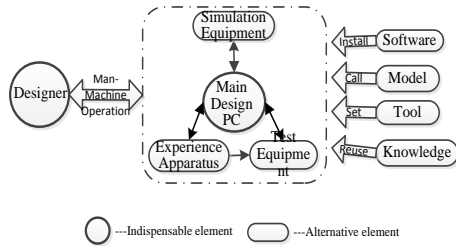


FIGURE 2 VDU structure diagram

5 Design task optimization model and its parameters

Building reasonable design task model is prerequisite of design task scheduling. According to the activity type in complicate product such as air-vehicle, design tasks are classified into product investigation, programming, design indicate determination, geometric modeling, mesh generation, mathematic formulation modeling, flight weight design, work flow design, structure design, aerodynamic analysis, intensity analysis, engine internal trajectory calculation, thermal simulation, control loop design ,control function analysis, warhead explosive simulation, flight kinetic simulation and result evaluation. Aim to abstract a general model for above design task types, design task model is built based on the study results, and it describes the basic information, design instance, design object, design activity, executor information and execution conditions as shown in Figure 3.

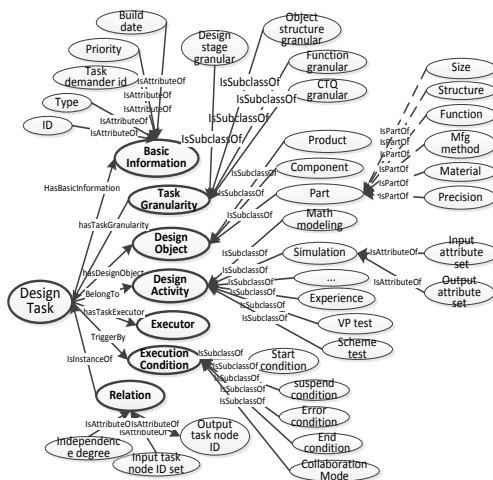


FIGURE 3 Design task optimization model

DT is used to denote design task model, and it is expressed with 7-tuple as follows: $DT=(B, G, O, A, E, C, R)$.

Among them, B denotes basic design information including task ID, task name, independence degree, priority and task demander ID.

G denotes granularity information of design task.

$G=(g_1, g_2, g_3, g_4)$. $g_1=(StageType, PhaseLevel)$ denotes stage granular dimension information.

$g_2=(Object-Type, Structure level)$ denotes design object structure granular dimension information.

$g_3=(Function Type, FunctionLevel)$ denote function granular dimension information.

$g_4=(TCQlevel, Time, Cost, Quality)$ denotes Time&Cost&Quality granular dimension information.

$O=(ObjID, ObjName, ObjClass, Size, Structure, Function, Mat, Mfgmethod)$ denotes object information of design task, it includes object Id, object name, object category, object size, object structure, function, material and Mfg method.

$A=(ActID, Name, Type, Method, InputIDSet, OutputIDSet)$ denotes design activity information of design task. It includes activity id, name, type, method, activity input attribute ID set and activity output attribute ID set.

$E=(ExecutorID, Name, Structurelevel, Function, Affiliation, DesignAbility)$ denotes design task executor information. It includes executor id, name, structure level, function, affiliation and design ability.

$C=(Execution, Transfer, Collaboration, Start, Suspend, ErrorDeal, End)$ denotes condition and constrain of design task in different status. It includes task execution condition, transfer condition, collaboration condition, start condition, suspend condition, error dealing condition and end condition.

$R=(Independence Degree, InputTaskIDSet, OutputTaskIDSet)$ denotes the interaction relation with other tasks. It includes task independence degree, Input task Id Set and Output task Id.

From the angle of design task [10], product design process can be defined as a sequential task set that executed with certain interaction and execution constrains. To realize high-efficiency product design, design process modeling must adhere to the following items.

a) Design process model should reflect the dependent degree among design tasks.

b) It is necessary to build input and output relation among different tasks.

c) It can contribute to improve design efficiency and short design cost.

In the design process of complicate product, each subsystem involves many components and parts. Design process of subsystem include design goal dissociation, design executor selection, tasks scheduling, cooperative decision, task execution, and schedule progress monitoring, etc. Thus, design process of complicate product can be described as a set with five elements: $DP=<P, E, S, C, M>$.

Moreover, each element is explicated as following:

$P=\{Subpro1, Subpro2, \dots, subpron\}$: goal dissociation.

The general project can be decomposed into n sub-process that demand interoperation with one another. Each sub-process is composed of many sequential tasks.

$E=\{E1, E2, \dots, Eq\}$: task executor selection.

Referring to the rules such as design priority, the lowest price and the shortest producing time, the process management server selects the candidate executors to participate in the cooperation team, and determines qualified total q executors to implement the total n subtasks together. Usually there is $q>n$.

$S=\{S1, S2, \dots, Sm\}$: tasks Schedule.

Each sub-process can be dissolved into several activities or tasks that can be carried out in terms of design cost,

design load and design time. Reasonable design task number must be allocate to the candidate executor to finish all the

$C=\{C1, C2, \dots, Co\}$: task coordination and negotiation between the different executors.

It devotes to the cooperation style by means of network dialogues and sharing information among all participants. Each Co is described as a set of three tuples $Co=\{Dinterdepend, Rel, Cor\}$. Design Task (DT) and Design Collaboration (Co) are the important links in design process. DT place emphasis on functional improvement and promotion, Co pay much attention to information interaction, nodes result check and scheme modification. Cost and time of design task are determined by design ability of executors. More design collaboration times can rectify design scheme, reduce iteration of wrong design error and add possibility to attain optimization design scheme. But more Co means more consumption of cost and time. Reasonable evaluation equation is needed to build So that it can determine rational number of Co.

$M = \{M1, M2, \dots, Mt\}$: schedule-progress monitor.

The dominant fractal-agent needs to monitor the schedule progress of the key subtasks. If necessary, the corresponding executive team may demand increased new partners.

6 Algorithm in Complex product development design process

Genetic algorithm (GA) and Ant Colony algorithm (ACO) are both efficient and powerful heuristics intelligence algorithms for solving optimization problems, which have been widely applied in many scientific and engineering fields. According to the comparison between GA and ACO, GA is less efficient than ACO, but it maintain the diversity of solutions. ACO is prevailed in convergence, but it can easily fly into local optima and lack the ability of jumping out of local optima. So it is a good idea to combine them together to realize the efficient researching of global solution. Refer to the hybrid methods combine GA and ACO.

7 Algorithm design

- 1) Decompose task and generate tasks list.
 - a) Dealing with multiple kinds of tasks, different design tasks are classified and agglomerated. Purpose of task allocation is to select reasonable number of every kind of task.
 - b) (2) Select a candidate VDU set according to the requirements of design task type and design characteristic.
 - c) Relevant degree between task and VDU is proposed to describe the matching degree between one task and one VDU. The value of relevance degree between task and VDU decides whether one VDU is suitable for executor the task. In general, there exists correlation between tasks and VDU. Let T be the correlation matrix of task and VDU, the element T_{ij} denotes the correlation factor between the i-th task and j-th VDU. $P=(p1, p2, \dots, pi)$ denotes the attributes set of task, and $Q=(q1, q2, \dots, qj)$ denotes ability attribute set of VDU. Euclidean distance is used to judge the relevance degree between task and VDU as follows

$$d_2(p, q) = \sqrt{\sum_{i=1}^m |p_i - q_i|^2} \tag{1}$$

As shown in Equation (1), if there is strong relevance between the i-th task and j-th VDU, $d2(pi,qj)=0$. If there is little or no relevance between the i-th task and j-th VDU, $d2(pi,qj)\neq 0$. According to the distance of design task and VDU, VDUs are selected as the candidate executors.

(2) Calculate and evaluate task's execution time and cost of VDU.

d) Execution time, design cost and shipping time of each working procedure are identified, when VDU carry out some design activities. Refer to paper [19], cost calculation Equation of VDU is showed as follows:

$$C_n = \frac{\sum_{k=1}^k (n_{ek} \cdot c_{ek}) + \sum_{s=1}^s (n_{ms} \cdot c_{ms}) + \sum_{t=1}^t (n_{tt} \cdot c_{tt}) + c_{aux}}{L_{ri}} \tag{2}$$

In the Equation (2), C_{ri} denotes the design activity cost when r-th VDU carry out the ith task. n_{ek} and c_{ek} denote the average work hour number and average hour cost of the k-th kind of equipment. n_{ms} and c_{ms} denote the number and hour cost of the s-th kind of man. n_{tt} and c_{tt} denote the number and hour cost of the t-th kind of auxiliary tools. c_{aux} denotes the sum of other affix cost. L_{ri} denotes the hourly workload of rth VDU when rthVDU take in ith design task. After calculating the average design time and design cost, DAC is used to evaluate design time and cost of next time design task followed Equation (2).

e) (4) Initialize Ant colony.

f) m is assumed as the number of ant. n denotes the number of ant iteration. Every design task type is task as the city node for ant visiting. When m-th ant visits the i-th type of design tasks, ant allocates task number of all design task types to execute by all VDUs. Every ant start randomly from one of i design types. And then, ant select visit sequence and design task number schem until all design task types are executed. All design tasks must be arranged when ant finish the whole journey. When ant completely visits all task types, design task number matrix in the path is generated as one solution. Minimum delivery time is used to judge whether one solution meet the charge time. If Equation (1) is not satisfied, it demonstrates that current task number schemes fail to meet the deliver time limitation. Under such situation, deliver time limitation or outsourcing processing is supposed to adjusted and executed.

g) (5) Initialize solution variable.

h) Candidate VDU could not execute all kind of task, so relevance correlation matrix is introduced as shown in Equation (3). If r-th VDU is suitable for i-th task, $eri=0$; else $eri=1$. x_{ri} denotes the number that rth VDU carry out i-th type design task. x_{ri} is taken as the solution variable. And then, initial value of x_{ri} is selected randomly from the value range $[0, Ni]$. Meanwhile x_{ri} value must meet the Equation (4). All the x_{ri} construct the design task number matrix of task allocation optimization as Equation (5).

$$E = \begin{bmatrix} e_{11} & e_{12} & \dots & e_{1i} \\ \dots & \dots & \dots & \dots \\ e_{r1} & e_{r2} & \dots & e_{ri} \end{bmatrix} \tag{3}$$

$$x_{ri} = N_i - \sum_{r=1}^{r-1} x_{ri} \cdot e_{ri} \tag{4}$$

$$X = \begin{bmatrix} x_{11} & x_{12} & \dots & x_{1i} \\ \dots & \dots & \dots & \dots \\ x_{r1} & x_{r2} & \dots & x_{ri} \end{bmatrix} \tag{5}$$

i) (6) Select next task type of mth ant at the t time.

j) When mth ant moves from j-th type of design task to k-th type of design task in t time. Taboo table is built to exclude task types that ant has visited. The line between j-th types and k-th types is denoted with (j, k), and pheromone is denoted with τ_{jk} . Initial value of τ_{jk} is set as $\tau_{jk}(0)=1$. Motion transition probability that ant select the j-th design types is formulated as Equation (6).

$$P_{jk}^m(t) = \frac{\tau_{jk}^\alpha \cdot (\eta_{jk})^\beta}{\sum_{l \in Tabu} [\tau_{jl}(t) \cdot (\eta_{jl})^\beta]} \tag{6}$$

k) (7) Update local pheromone. When ant moves from j-th type of design task to k-th type of design task, it leaves pheromone in the line(j,k).The more ants move from line(j, k),the more pheromone leave. When one ant move from line(j,k), local pheromone is updated by the Equation (7) and Equation (8).

$$\Delta \tau_{jk}^m = \begin{cases} Q, & \text{when ant m vist jk node} \\ 0, & \text{else} \end{cases} \tag{7}$$

$$\tau_{jk}(t+1) = \rho \cdot \tau_{jk}(t) + \Delta \tau_{jk}^m \tag{8}$$

When ant visits from start design task type to the current j-th design task type, j-1lines are visited. The total cost C_j and total time T_j of j-1 lines are calculated by path calculation Equation (9) and Equation (10). Walking path length of ant dall is calculated by weighted function Equation (11). To consider effect from both financial cost and time, weight factor δ is introduce to calculate the comprehensive overall cost of the path.

$$C_j = \sum_{j=1}^j (e_{ji} \cdot (\sum_{i=1}^i x_{ji} \cdot (C_{ji} + C_{ji \rightarrow i+1}))), \tag{9}$$

$$T_j = \sum_{j=1}^j \sum_{i=1}^i (e_{ji} \cdot (x_{ji} \cdot T_{ji} + T_{ji \rightarrow i+1})), \tag{10}$$

$$d_{all} = \delta \cdot C_j + (1 - \delta) \cdot T_j, (\delta \in [0,1]) \tag{11}$$

(8) Generate new solutions by adaptive crossover and mutation operation.

1) In order to avoid the local optimal, crossover and mutation operation have to be carried out to the components

of solution after pheromone updating to achieve the global optimal.

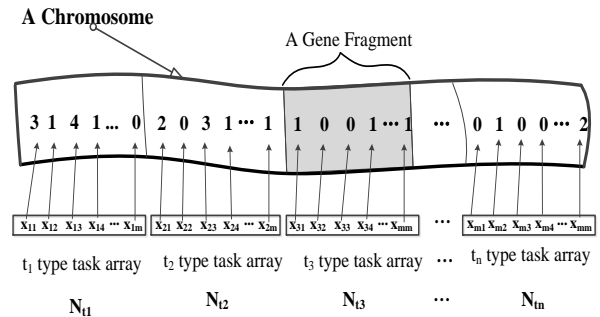


FIGURE 4 A chromosome model of task number

Every ant completely finishes path visiting, a design task number matrix is generated and it is taken as one solution. Each solution is taken as a chromosome of task number as shown in Figure 4. According to path length Equation (11), two solutions are selected to carry out crossover by certain probability. Suppose that m-th ant path length is denoted by $d_{over, m}$ and its probability of being chosen is formulated as Equation (12). In the traversal paths of m ants, the smaller the path length ant travel, the choose probability is smaller. Smaller choose probability means better solution.

$$P_m = d_{over, m} / \sum_{d=1}^m d_{over, d} \tag{12}$$

In the crossover operation, supposed $x(1)=(x11, x21, \dots, xr1)T$ and $x(2)=(x12, x22, \dots, xr2)T$ are 1th and 2th column elements set of selected solution(X). Crossover is executed between column elements set $x(1)$ and $x(2)$. Real crossover probability is calculated by Equation (13) and Equation (14).

$$P_{cross} = P_{system} \cdot P_c, \tag{13}$$

$$P_c = d_i / \sum_{h=1}^m d_h, \tag{14}$$

$$d_i = \sum_{r=0}^r [e_{ri} \cdot x_{ri} \cdot (C_{ri} + C_{ri \rightarrow i+1})]. \tag{15}$$

psystem is generated by system. Comparison probability $p \in [0,1]$ is also randomly generated. If $P > p_{system}$, crossover operation is executed. $\alpha \in [0,1]$ is generated randomly. $x(1)'$ and $xr(2)'$ are used to replace $x(1)$ and $x(2)$. $x(1)' = \alpha \cdot x(1) + (1 - \alpha) \cdot x(2)$; $x(1)' = \alpha \cdot x(2) + (1 - \alpha) \cdot x(1)$.

After executed crossover operation, mutation operation is randomly executed between two elements of column elements set $x(1)$ and $x(2)$ by certain system probability. Real mutation probability is calculated by Equation (16)

$$P_{mutation} = P_M \cdot P_m \tag{16}$$

PM is generated by system, and Comparison probability $p \in [0,1]$ is also randomly generated. If $p > p_M$, mutation operation is executed. $\epsilon \in [0,1]$ is generated randomly, $x11' = \epsilon \cdot x11 + (1 - \epsilon) \cdot x12$; $x12' = \epsilon \cdot x12 + (1 - \epsilon) \cdot x11$.

(9) Select best solution and carry on iterate.

m) After above crossover and mutation, two new solutions are generated and walking path length is calculated. Design task number matrix of the shortest walking path in m solutions is selected as the initial solution of next iteration.

(10) Update Global pheromone.

n) For the shortest line of path, pheromone is updated by Equation (17) and Equation (18).

$$\tau_{jk}^{new} = \alpha \cdot \tau_{jk}^{old} + \Delta \tau_{jk}^m \tag{17}$$

$$\Delta \tau_{jk}^m = \begin{cases} \frac{Q}{d_{shortest}} & \text{when (j,k) is the shortest line of path} \\ 0 & \text{else} \end{cases} \tag{18}$$

(11) Finish Iteration and output the best task allocation scheme.

The experimental results and the parameter analysis.

Task scheduling as discussed above is an assignment of the task type and task number to the suitable task executors [9]. Refer to the DAC model and DTSADA. To demonstrate the validation of DTSADA, traditional GA algorithm and ACO algorithm are also integrated into the prototype system. To compare the efficiency of GA, ACO and DTSADA, a design task schedule case is used to discuss the iteration efficiency and solution diversity. Design task attributes and task number of every task type are listed in Figure 5. There are 6 candidate VDUs that can execute the above design tasks. Each VDU has different design abilities to deal with different types of design tasks. Design ability attributes of 6 candidate VDUs are listed in Figure 6. Budget overall design cost is ¥42759, and budget overall design time is 2723 work hours. What the problem we should solve is try to figure out a design task scheduling scheme with lowest overall design cost by following constrains of budget design cost and budget design time.

Activity Type	Object	ID	Specification	t_{budget}	C_{budget}	N
Geometric Modeling	Part	1	10 ¹ features	5	52	20
		2	10 ² features	8	130	20
	Component	3	10 ² features	13	275	15
		4	10 ³ features	16	340	12
Mesh Modeling	Structure mesh	5	10 ⁴ features	9	120	25
		6	10 ⁵ features	10	160	22
	Non-structure mesh	7	10 ⁴ features	3	60	10
		8	10 ⁵ features	5	80	3
Aerodynamic Analysis	3 dimension	9	10 ³ mesh number	11	150	18
		10	10 ⁴ mesh number	16	210	25
		11	10 ⁵ mesh number	17	240	15
Structure Analysis	Statics	12	10 ³ mesh number	6	60	3
	Dynamics	13	10 ⁴ mesh number	10	150	32
Flight Dynamics Analysis	Dynamics	14	10 ⁵ mesh number	11	185	28
		15	6 Freedom degree	7	145	9
Internal trajectory Analysis	Dynamics	16	10 ¹ constrains	4	42	2
		17	10 ² constrains	8	115	2

t_{budget} is denotes the maximum average budget time to finish one single task.

C_{budget} is denotes the maximum average budget cost to finish one single task.

$$\star \left(\begin{array}{l} \text{Budget Overall Design Time} = (\text{h})2723 \\ \text{Budget Overall Design Cost} = (\text{¥})42759 \end{array} \right)$$

FIGURE 5 Design tasks attributes

Name	Activity Type	Object	Specification	\bar{t}_i	c_i	Coef	C_{avr}	C_{DAC}
Vdu1	Geometric Modeling	Part	10 ¹ features	2.5	20.5	0.95	51.3	54
			10 ² features	5.5	22	0.92	121	131
	Mesh Modeling	Component	10 ² features	13	18	0.95	234	246
			10 ³ features	15	20	0.96	300	312
			10 ⁴ mesh number	7	16	0.97	112	115.4
Vdu2	Geometric Modeling	Part	10 ¹ features	4	15	0.98	60	61.2
			10 ² features	9	15	0.97	135	139.1
	Mesh Modeling	Component	10 ² features	12.5	20	0.91	250	274.7
			10 ³ features	15.2	20	0.905	304	336
			10 ⁴ mesh number	8	14	0.97	112	115.4
Vdu3	Aerodynamic Analysis	3 dimension	10 ³ mesh number	10.5	13	0.95	136.5	143
			10 ⁴ mesh number	15.5	13	0.92	201.5	219
	Structure Analysis	Dynamics	10 ³ mesh number	15	15	0.92	225	239
			10 ⁴ mesh number	8	18	0.97	144	148
			10 ⁵ mesh number	10.5	16	0.92	168	182
Vdu4	Geometric Modeling	Part	10 ¹ features	3	18.5	0.96	55.5	58
			10 ² features	7	16	0.965	112	116
	Structure Analysis	Dynamics	10 ³ mesh number	4.5	12.5	0.95	56.5	59
			10 ⁴ mesh number	9	15	0.925	150	162.5
			10 ⁵ mesh number	7	18	0.91	126	138.6
Vdu5	Geometric Modeling	Part	10 ¹ features	3.5	18	0.98	63	64
			10 ² features	8	20	0.97	160	165
	Mesh Modeling	Non-structure mesh	10 ³ mesh number	5.5	18	0.95	121	127.4
			10 ⁴ mesh number	8	20	0.925	160	173
			10 ⁵ mesh number	3	18	0.91	54	59
Vdu6	Aerodynamic Analysis	3 dimension	10 ³ mesh number	4	18	0.905	72	80
			10 ⁴ mesh number	10	14	0.95	140	147
	Structure Analysis	Dynamics	10 ⁴ mesh number	12	16	0.95	192	202
			10 ⁵ mesh number	18	12	0.92	216	234
			10 ⁶ mesh number	9	15	0.95	135	142
Flight Dynamics Analysis	Dynamics	10 ³ mesh number	9	17	0.95	153	161	
		10 ⁴ mesh number	11	15	0.97	165	170	
		10 ⁵ mesh number	2.5	15.5	0.95	38.8	40.8	
Internal trajectory Analysis	Dynamics	10 ¹ constrains	5.8	18.5	0.95	107.3	113	
		10 ² constrains	6.5	20	0.905	130	143.6	

\bar{t}_i is average work hours number of complete a task, its unit is hour.
 c_i is design resources cost /h of complete a task, its unit is ¥/h.
 $C_{avr} = \bar{t}_i \cdot c_i$ is average cost of complete a task, its unit is Yuan.

FIGURE 6 Design ability attributes of candidate VDUs

Traditional GA algorithm and ACO algorithm are used to compare the iteration efficiency and result accuracy with DTSADA. According to the simulation result in Figure 6 and Figure 7, GA prevails in the global solution, but it needs more iteration than ACO when the solutions are equal. Convergence speed of ACO is faster than GA, but it is easy to fall into local optimization. DTSADA assimilates the advantages of GA's solution diversity and ACO's convergence efficiency. Simulation results show that DTSADA is valid. Simulation result curve of GA, ACO and DTSADA is illustrated in Figure 7.

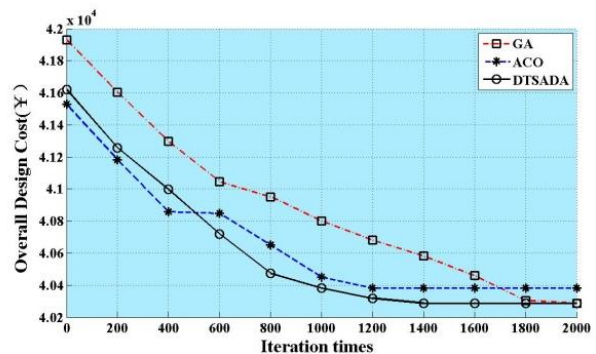


FIGURE 7 Simulation result curve of GA, ACO and DTSADA

TABLE 1 50 times simulation result of three methods

Section	Average value of 50 times simulation	Best Value	Variance
GA	40290	40288	0.386
ACO	40325	40288	1.716
DTSADA	40289.2	40288	0.341

Activity Type	Object	Specification	N	Vdu1	Vdu2	Vdu3	Vdu4	Vdu5	Vdu6
Geometric Modeling	Part	10 ¹ features	20	4	3	0	3	10	0
	Part	10 ² features	20	13	5	0	1	1	0
	Component	10 ² features	15	12	3	0	0	0	0
	Component	10 ² features	12	6	6	0	0	0	0
Mesh Modeling	Structure mesh	10 ² features	25	9	11	0	0	5	0
	Structure mesh	10 ² features	22	2	16	0	0	4	0
	Non-structure mesh	10 ² features	10	0	0	0	0	10	0
Aerodynamic Analysis	3 dimension	10 ³ mesh number	18	0	0	6	0	12	0
		10 ⁴ mesh number	25	0	0	5	0	20	0
		10 ⁵ mesh number	15	0	0	5	0	10	0
Structure Analysis	Statics	10 ³ mesh number	3	0	0	0	3	0	0
	Dynamics	10 ³ mesh number	32	0	0	26	0	4	2
		10 ³ mesh number	28	0	0	2	0	25	1
Flight Dynamics Analysis			9	0	0	0	1	0	9
Internal trajectory Analysis		10 ¹ constrains	2	0	0	0	0	0	2
		10 ² constrains	2	0	0	0	0	0	2

☆(Minimum Overall Design Cost = (¥)40288
 Overall Design Time = (h)2431.4
 Tasks execute sequence is (3 1 5 2 10 7 15 4 9 12 13 8 14 17 16 6 11)

FIGURE 8 Design task schedule result in minimum execute cost

8 Conclusions

Through the study of complex product development present situation at home and abroad and the present situation of the

References

[1] Gardoni M 2005 Concurrent Engineering in Research Projects to Support Information Content Management in a Collective Way *Concurrent Engineering* **13** 135-43 DOI: 10.1177/1063293X05053798

[2] National Institute of Science and Technology. The NIST definition of Cloud Computing [EB/OL] [2011-06-21] <http://csrc.nist.gov/publications/nistpubs/800-145/SP800-145.pdf>

[3] Li B, Zhang L, Wang S 2010 Cloud manufacturing: a new service-oriented networked manufacturing model *Computer Integrated Manufacturing Systems CIMS* **16** 1-7

[4] Kirkpatrick S, Gelatt C Jr, Vecchi M 1983 Optimization by simulated annealing *Science* (220) 671-80

[5] Goldberg D 1989 *Genetic Algorithms in Search, Optimization, and Machine Learning* Addison-Wesley Publishing Company Inc Reading MA

resource-constrained project scheduling, taking the VDU in the design of complex product development part of the process of design process for example. A hybrid design task scheduling approach combined GA and ACO-DTSADA is proposed. A prototype system of design task scheduling based DTSADA is constructed. Simulation demonstrated that DTSADA is valid. Solving the actual complex product development design process has important practical significance. Future research includes: (1) Multi-stage design task allocation method. (2) Multi-granularity design ability modeling.

Acknowledgment

This work is supported by the National High-Tech.R&D Program, China (No. 2011AA120505) and the National Natural Science Foundation, China (No. 61173077).

[6] Dorigo M, Gambardella L 1997 Ant colony system: a cooperative learning approach to the traveling salesman problem *IEEE Transaction on Evolutionary Computation* **1** 53-66

[7] Yu X B, Cao J, Shan H Y 2014 An Adaptive Hybrid Algorithm Based on Particle Swarm Optimization and Differential Evolution for Global Optimization *Scientific World Journal* DOI: 10.1155/2014/215472

[8] Shyu S J, Lin B M T, Yin P Y 2004 Application of ant colony optimization for no-wait flowshop scheduling problem to minimize the total completion time *Computers & Industrial Engineering* **47** 181-93

[9] Abdelaziz A Y, Osama R A, El-Khodary S M 2011 Distribution Systems Reconfiguration Using the Hyper-Cube Ant Colony Optimization Algorithm *SEMCCO Part II LNCS 7077* 257-66

[10] Zang Y, Li F, Zhou T 2012 Task scheduling algorithm based on Genetic Ant colony algorithm in Cloud Computing environment *Computer Engineering and Applications*

Diagnostics programs efficiency analysis in operation systems of radioelectronic equipment

Olexander Solomentsev*, Oleksiy Zuiev, Maksym Zaliskyi, Ivan Yashanov

Aviation radioelectronic complexes department, National Aviation University, Komarova Av. 1, 03680, Kyiv, Ukraine

*Corresponding author's e-mail: avsolomentsev@yandex.ru

Received 1 January 2015, www.cmmt.lv

Abstract

Two variants of diagnostics programs of radioelectronic equipment in exploitation systems are considered. Analytical formulas for calculation of efficiency indexes in the absence and presence of first and second kind errors are given.

Keywords: radioelectronic equipment, diagnostic programs, data processing; maintenance

1 Introduction

There are many processes in operation systems of Radioelectronic Equipment (REE): technical diagnostics, maintenance, running repair, metrological assurance, monitoring, etc.

The process of defining the diagnostics object (DO) technical state is technical diagnostics. The DO technical state changes in case of its elements failures. Therefore technical diagnostics is actually the process of searching a failed DO element [1–7].

The methods of REE technical state diagnostics can be conditionally divided into two groups: statistical and analytical.

Statistical methods are based on application of statistical data of failures and damages in REE units and elements REE, collected and analyzed be forehand.

Analytical methods of REE diagnostics technical state can be conditionally divided into two subgroups. The methods of the first subgroup set the method of REE serviceability checking. The methods of the second subgroup determine the sequence of control-measuring operations fulfillment.

The first subgroup of methods contains: method of the intermediate measuring (with application of voltages charts, voltages drafts, resistances charts etc.); external observation; method of unit replacement, board under checking on consciously operating unit, board; comparison of operating unit signals, board and diagnosed unit of equipment; simulation of input signals; supply on the input of special test sets (signals); signature analysis, etc.

The second subgroup contains such methods: probability/time; half partition; on the basis of informative criterion; branches and limits; on the basis of the dynamic programming; random search; engineering and others.

The methods of REE fault-detection differ in the level of material resources consumption (time, cost, necessary control equipment), as well as in qualification of service personnel, etc. [4].

2 The main objective

Diagnostics programs analysis and the best options choose can be performed on the basis of efficiency indexes set. In the field of technical diagnostics the following basic efficiency indexes are used: D – probability of correct diagnostics; $m_1(t_d)$ – mean duration of diagnostics; $m_1(C_d)$ – mean cost of diagnostics; $m_1(Z_d)$ – mean labour intensity of diagnostics.

In general case indexes t_d , C_d , Z_d are random variables.

It is known that the most complete characteristic of a random variable is a probability density function (PDF). So the article discusses the problem of t_d PDF finding.

3 Basic part

In scientific and technical literature the procedure of DP development is named DP synthesis. For DP synthesis the methods of diagnostics are used.

Let's consider the examples of DP creation. Let DO – radio station transmission section, which is composed of such functional units: frequency synthesizer (master oscillator), modulator, power amplifier, aerial device and power supply block. Depth of diagnostics – to the level of functional unit. Let's constitute DM taking into account control points at DO (Figure 1). Parameters X_5 characterize the up – state of DO elements taking into account connections of elements with each other.

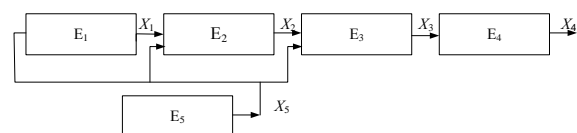


FIGURE 1 Diagnostic model of radiostation transmission section: element E₁ – frequency synthesizer (master oscillator); element E₂ – modulator; element E₃ – power amplifier; element E₄ – aerial device; element E₅ – power supply block

If in Figure 1 each DM element is considered separately, then parameters \vec{X}_5 will characterize the up-state of

corresponding DM elements only. If it is impossible to break the connection between DM elements, then values of parameters \bar{X}_5 are determined taking into account interconnection of elements $E_1 - E_5$. Let's consider the last case. Let in the process of DO analysis necessary information about parameters \bar{X}_5 be obtained from the corresponding table.

For DM in Figure 1 we'll develop DP according to engineering approach. We'll use the method of the \bar{X}_5 parameters intermediate measuring. The order of parameters checking is following: at first we control a parameter X_5 , then consequently – parameters X_1, X_2, X_3 . We'll consider that in the process of \bar{X}_5 parameters control there are no errors in estimation of these parameters to preset requirements correspondence. Corresponding DP is shown in Figure 2.

In Figure 2 operations which correspond to RRP are also shown. These are operations of failed elements replacement and the whole REE up-state checking.

Thus, for DP and RRP realization it is necessary to fulfill 5 STO, which allow to REE up-state restore.

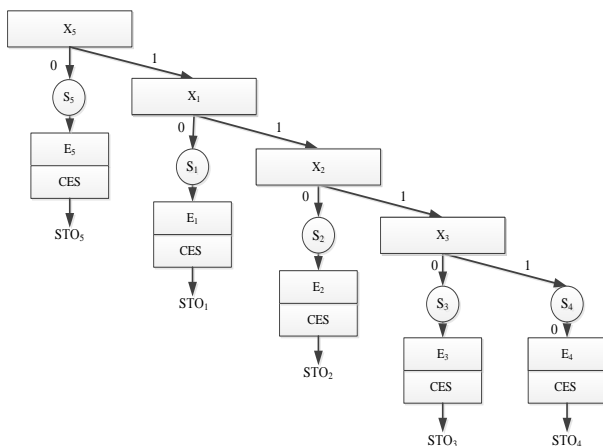


FIGURE 2 Diagnostic program and RRP with the use of engineering approach: RE – replacement of element; CPO – control of object up-state; STO – set of technological operations.

We will consider the example of DP development for DM (Figure 1), using simplified method on the basis of informative criterion. Following this criterion, for determination of \bar{X}_5 parameters control order it is necessary to calculate the preference function W at every step of control according to equation:

$$W_i = \min \left| \sum_{j=1}^N "0"_{ij} - \sum_{j=1}^N "1"_{ij} \right|,$$

where $\sum_{j=1}^N "0"_{ij}$ and $\sum_{j=1}^N "1"_{ij}$ – quantities of "0" and "1" in i -th row of table of DO states, N – quantities of DO states.

For this purpose we will conclude a table (matrix) of DO states. Rule of state table filling consists in following. If X_i

parameter of model i -th element is out of tolerances limits (or it is absent), i.e. DO is in S_i state, then on crossing of X_i -th row and S_i -th column zero is written down. The output parameters of other elements depending on their functional connections with failed element can be within the limits of tolerance and are signed by "1" or out of tolerance – by "0". In this case DO is characterized by such states: S_1 – failure of E_1 element; S_2 – failure of E_2 element, S_3 – failure of E_3 element; S_4 – failure of E_4 element; S_5 – failure of E_5 element. Then output state table will look as it is shown on the chart of RRO technical state tables' analysis (Figure 3). For determination of the first DP parameter row of output table (Figure 3) is chosen with the minimum module of zeros and units difference quantities. If quantity of such rows is more than one, the choice is done arbitrarily. For rows X_1 and X_2 of output table we have $W_{1,2}=1$, for rows X_3 and $X_5 - W_{3,5}=3$, and for $X_4 - W_4=5$.

For definiteness X_2 parameter is chosen first for the control, although it would be possible to choose X_1 parameter. The result of X_2 value control is binary: X_2 parameter can be within the limits of tolerance ($X_2=1$) or out of tolerance ($X_2=0$). In this case the state table is decomposed on two tables. If on the first step $X_2=1$, the quantity of the possible DO states reduces to two (S_3 or S_4). For rows X_1, X_4, X_5 of corresponding table we have $W_{1,4,5}=2$, for a row $X_3 - W_3=0$. Therefore on the second step it is necessary to control X_3 parameter. If $X_3=1$, decision is made, that DO is in S_4 state, i.e. E_4 element failed. If $X_3=0$, decision is made, that DO is in S_3 state, i.e. E_3 element failed.

If on the second step $X_2=0$, the quantity of the possible DO states reduces to three (S_1, S_2, S_5). For rows X_3, X_4 of corresponding table we get $W_{3,4}=3$, for rows $X_1, X_5 - W_1$ and $W_5=1$. For definiteness on the second step X_5 parameter is chosen. If $X_5=0$, decision is made, that DO is in S_5 state, i.e. E_5 element failed. If $X_5=1$, another table which has two states is created (S_1 or S_2). For rows X_3, X_4 of this table $W_{3,4}=2$, for X_1 row – $W_1=0$. Therefore on the third step it is necessary to control X_1 parameter. If $X_1=1$, decision is made, that DO is in S_3 state, i.e. E_3 element failed. If $X_1=0$, decision is made, that DO is in S_1 state, i.e. E_1 element failed. Then RRP is created on the basis of DP. Taking into account the chart of state table analysis (Figure 3) corresponding DP and RRP are shown in Figure 4. These programs look like this, if errors are not revealed during \bar{X}_5 parameters control. If such conditions are not fulfilled, then the process of running repair is complicated – there is a necessity of additional technological operations realization on the search for those elements which indeed failed in RRO.

For DP checking it is recommended to model the situations of DO elements failure consistently, and depending on distribution of DO measuring parameters values, to execute further operations according to DP. If conditions of modeling and results of diagnostics coincide, then DP is developed correctly.

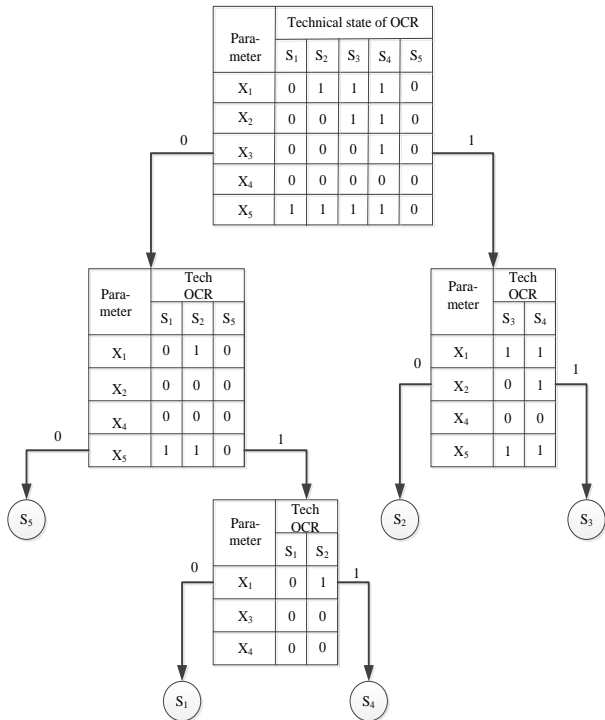


FIGURE 3 Chart of technical state analysis tables during RRO diagnostics according to informative criterion

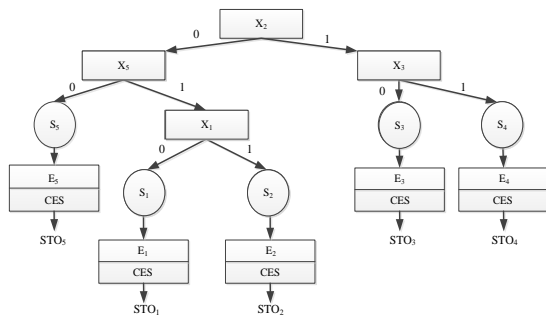


FIGURE 4 Diagnostic programs and RRP according to informative criterion

Every edge corresponds to conditional probabilities of transition from the initial state to a neighboring one, as well as other characteristics, for example, duration of technological operation, after which a change in DO technical state, material expenditures on technological operation etc. have taken place.

For drafting graphs it is possible to use corresponding DP or RRP, if they are supplemented with necessary data on resources consumption. In general case as many graphs are made, as there are elements in RRO. However, if there are no errors during DP control, then it is possible to apply one graph coinciding with DP or RRP image.

The graph of running repair process is built in accordance with the following general rules:

- after decision – making on the RRO functional element failure it is replaced with a serviceable one and the output control of the whole REE is executed;
- if the control testifies the REE up-state, the process of running repair is completed;

– if the RRO output control testifies the device faulty state, then regardless of whether there was replacement of RRO element, or not yet, successive replacement of RRO elements are done and obligatory output control of the whole RRO serviceability is fulfilled until RRO gets serviceable.

On the whole, application of these rules in case of control errors guarantees eventual duration of REE technical diagnostics and running repair process. Diagnostics or running repair graphs include sets of technological operations (STO).

This term determines a TO set, resulting in the search of the failed DM element or RRO serviceability restoration. To this set we refer the operations of DP control, replacement of failed RRO elements, and output control of RRO up-state after its repair. If there are no errors of DP control, the graph of RRO conditions, in the case of *i*-th REE element failure, will include one STO, stipulating restoration of REE serviceability after correct detection and replacement of the failed *i*-th element, by a serviceable one and positive control of the whole REE serviceability. Separate STO make a complete group of events.

Let's consider DP efficiency analysis. Each STO can be connected with corresponding material resources consumption – average aggregate time of *i*-th STO fulfillment, average aggregate labour intensity of *i*-th STO fulfillment, average aggregate costs of *i*-th STO fulfillment.

Conditional mean indexes of a certain DP efficiency during REE diagnostics, if there are no errors in the process of DP control, are determined as

$$m_1(t(STO_j / S_j)) = \sum_{i=1}^{l_j} t_{cij} ,$$

$$m_1(Z(STO_j / S_j)) = \sum_{i=1}^{l_j} Z_{cij} ,$$

$$m_1(C(STO_j / S_j)) = \sum_{i=1}^{l_j} C_{cij} ,$$

where $m_1(t(STO_j / S_j))$ – conditional mathematical expectation of total duration of *j*-th STO fulfillment in case of *j*-th DO element failure; $m_1(Z(STO_j / S_j))$ – conditional mathematical expectation of *j*-th STO set aggregate labour intensity in the case of *j*-th DO element failure; $m_1(C(STO_j / S_j))$ – conditional mathematical expectation of *j*-th STO set aggregate costs in the case of *j*-th DO element failure; t_{cij} – mathematical expectation of *i*-th DP control duration in the case of the *j*-th REE DM element failure; Z_{cij} – mathematical expectation of *i*-th DP control labour intensity in the case of *j*-th DM element failure; C_{cij} – mathematical expectation of *i*-th DP control cost in the case of *j*-th DM element failure; l_j – the quantity of the

control operations of detecting j -th DO failed element; S_j – DO condition in the case of j -th DO element failure.

To determine absolute efficiency indexes it is necessary to fulfill another averaging operation:

$$\begin{aligned}
 m_1(t_d) &= \sum_{j=1}^N m_1(t(STO_j / S_j))Q_j, \\
 m_1(Z_d) &= \sum_{j=1}^N m_1(Z(STO_j / S_j))Q_j, \\
 m_1(C_d) &= \sum_{j=1}^N m_1(C(STO_j / S_j))Q_j,
 \end{aligned}
 \tag{1}$$

where $m_1(t_d)$ – mathematical expectation of one DO diagnostics duration; $m_1(C_d)$ – mathematical expectation of one DO diagnostics cost; $m_1(Z_d)$ – mathematical expectation of one DO diagnostics labour intensity; N – total quantity of DO elements; Q_j – probability of j -th DO element failure.

Using efficiency indexes $m_1(t_d)$, $m_1(C_d)$, $m_1(Z_d)$, according to Equation (1), it is possible to perform a comparative analysis of different DPs efficiency.

If there are no statistical data about DO or RRO elements reliability, probabilities of elements failures Q_i can be calculated by the known technology [1]. For this purpose the specification to the REE principle electric chart is used, a list and quantity of ERC contained in each DO or RRO element are determined. Assuming, that in terms the reliability theory ERC are connected in series, failures rate of i -th DM or RRO element can be calculated according to the Equation

$$\lambda_i = \sum_{j=1}^{K_i} n_{ij} \lambda_{ij}, \tag{2}$$

where K_i – quantity of ERC groups, of which the electric chart of i -th element is built (to ERC groups we may refer resistors, capacitors, chips etc.); n_{ij} – quantity of j -th group ERC, included in the principle chart of i -th element; λ_{ij} – average failure rate of j -th group ERC, included in the i -th DO or RRO element.

Failure rates are taken from reference tables [5], considering operation conditions as normal.

Calculating value of λ_i according to formula (2), failure probabilities of DO or RRO elements are determined, assuming, that only one element of the equipment can fail and elements failures are independent of each other:

$$Q_i = \frac{\lambda_i}{\sum_{j=1}^N \lambda_j}.$$

In case errors in DP state classification, both the REE diagnostics and running repair procedures are sharply complicated. There may be the situations of erroneous decisions as to DO or RRO condition that may result in excessive consumption of resources during REE diagnostics or running repair.

As for the running repair let's note that in case of any element failure RRO state graph will contain as many STOs as there are elements in RRO. In this case only one of all possible STOs will provide faithful detection of the faulty element, others will be characterized with additional consumption of resources due to erroneous replacement of RRO elements as a result errors of DP condition control. Analyzing RRP efficiency, it is necessary to make as many RRO state graphs, as there are elements in RRO. These graphs will help to define probabilities of STO performance correctly taking into account which element is faulty, and the probability of the first and second kind errors. According to the probabilities theory certain STO make a complete group of events.

Every STO during RRP can be connected with corresponding conditional consumption of material resources, such as conditional mathematical expectation of i -th STO aggregate time during maintenance and in case of the j -th RRO element failure $m_1(t(STO_i / S_j))$.

Then conventional average efficiency criteria are calculated as follows:

$$m_1(t_r / S_j) = \sum_{i=1}^{M_j} P(STO_i / S_j) m_1(t(STO_i / S_j)),$$

where $m_1(t_r / S_j)$ – conditional mathematical expectation value of time – taking for current repair with RRO j -th element faulty; M_j – the number of STO during RRO running repair due to its j -th element failure. STO quantity is equal to the quantity of RRO elements; $m_1(t(STO_i / S_j))$ – conditional mathematical expectation of the i -th STO total time during maintenance and in case of the j -th RRO element failure; $P(STO_i / S_j)$ – conditional probability of the i -th STO resulting from RRO j -th element failure.

To determine the RRO efficiency index unconditional value it is necessary to perform one more averaging operation:

$$\begin{aligned}
 m_1(t_r) &= \sum_{j=1}^N m_1(t_r / S_j) P(S_j), \\
 \sigma(t_r) &= \left(\sum_{j=1}^N (m_1(t_r) - m_1(t_r / S_j))^2 P(S_j) \right)^{1/2},
 \end{aligned}$$

$$P(S_j) = Q_j,$$

where N – total RRO elements quantity; Q_j – RRO j -th element failure probability.

The Equation for determining correct diagnostics of DO average probability is the following:

$$m_1(D) = \sum_{j=1}^N D(S_j)Q_j,$$

where $D(S_j)$ – is conditional probability of DO correct diagnostics in the case of j -th element failure.

To determine $D(S_j)$ we may consider any of the RRO running repair graphs.

Consider the case, where $\alpha \neq 0, \beta \neq 0$. Diagnostics program of a given object is divided into n conditional subprograms, where n – number of elements in DO. Each i -th subprogram will be based on the condition that the i -th element is refused in object. So the branches of the graph can be marked by errors of the first and second kind value.

Consider the example of DO, which includes four elements (E_1, E_2, E_3, E_4) connected in series (Figure 5).

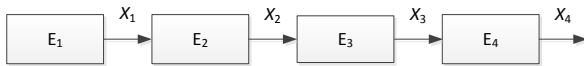


FIGURE 5 Example of DO

In Figure 5 X_i – information parameter (IP), which characterizes the work of corresponding of i -th DO element.

For this DO (Figure 5) will lead one of the four graphs for the case when first element failures (Figure 6).

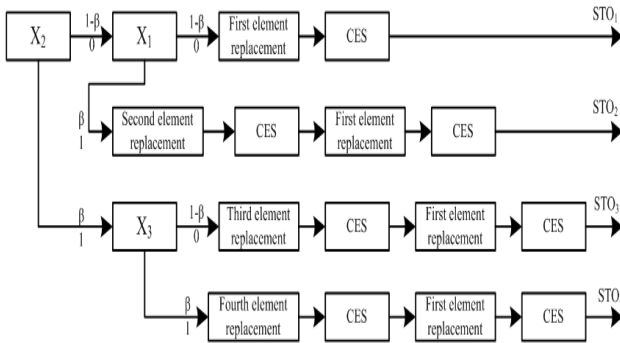


FIGURE 6 DO state graph in case of first element failure and the presence of control error

Each graph will contain three STO related to “false” element detection, and only one – with “true”. The number of operations, that are part of “false” element detection STO, will be determined by strategies, which are accepted in these cases. Among these strategies are: DR initially repetition, second signal control at output of elements with maximum failure probability.

Let’s use a strategy, in which during diagnostics the element with failure is replaced on objective functional. Then there is all DO control (this type of control hasn’t errors of the first and second kind). If as a result of final DO control is “failure”, the decision is taken about next fault DO

element, starting from the first. Then again there is all DO control.

Analysis of Figure 6 shows that in the presence of errors of the first and second kind consumption of resources for diagnosis are increasing.

Consider the determination problem of probability density function of the time required to PD implementation $f(t_d)$ (in case, where $\alpha \neq 0, \beta \neq 0$).

Consider the example, when DO first element objectively failures. Since the results of test operations are random, then certain STO will random too both in number and in duration. Probability of implementation certain operations $P(STO_i / S_1)$ are conditional and form a complete group of events:

$$\sum_{i=1}^4 P(STO_i / S_1) = 1,$$

where $P(STO_i / S_1)$ – probability of the i -th STO implementation, if first element objectively failures .

Let’s the probabilities of first and second kind errors for all elements are equal: $\alpha = \alpha_i, \beta = \beta_i$.

Then

$$P(STO_1 / S_1) = (1 - \beta)^2,$$

$$P(STO_2 / S_1) = \beta - \beta^2,$$

$$P(STO_3 / S_1) = \beta^2,$$

$$P(STO_4 / S_1) = \beta - \beta^2.$$

Suppose, that we know the conditional PDF of STO duration in the case of the first element failure $f(t_{STO_i} / S_1)$. These conditional PDF satisfy the normalization condition, so

$$\begin{aligned} f(t_d / S_1) = & P(STO_1 / S_1)f(t_{STO_1} / S_1) + \\ & + P(STO_2 / S_1)f(t_{STO_2} / S_1) + P(STO_3 / S_1)f(t_{STO_3} / S_1) + \\ & + P(STO_4 / S_1)f(t_{STO_4} / S_1). \end{aligned}$$

According to the normalization condition:

$$\begin{aligned} \int_0^\infty f(t_d / S_1) dt_d = & P(STO_1 / S_1) \int_0^\infty f(t_{STO_1} / S_1) dt_{STO_1} + \dots + \\ & + P(STO_4 / S_1) \int_0^\infty f(t_{STO_4} / S_1) dt_{STO_4} = P(STO_1 / S_1) + \\ & + P(STO_2 / S_1) + P(STO_3 / S_1) + P(STO_4 / S_1) = 1. \end{aligned}$$

After defining all conditional PDF $f(t_d / S_i)$, we can determine unconditional PDF of PD:

$$\begin{aligned} f(t_d) = & Q_1 f(t_d / S_1) + Q_2 f(t_d / S_2) + \\ & + Q_3 f(t_d / S_3) + Q_4 f(t_d / S_4). \end{aligned} \tag{3}$$

Unconditional PDF $f(t_d)$ will satisfy the normalization condition, i.e.:

$$\int_0^\infty f(t_d) dt_d = Q_1 \int_0^\infty f(t_d / S_1) dt_d + Q_2 \int_0^\infty f(t_d / S_2) dt_d + Q_3 \int_0^\infty f(t_d / S_3) dt_d + Q_4 \int_0^\infty f(t_d / S_4) dt_d = Q_1 + Q_2 + Q_3 + Q_4 = 1.$$

These Equations for conditional and unconditional PDF can be generalized to the case when the DO consists of n elements. Thus the expression for STO duration PDF will depend on the number of elements in the object and PD type.

Let's consider the determination of moments for PDF, that represented by Equation (3). The expression for mathematical expectation:

$$m_1(t_d) = \int_0^\infty t_d f(t_d) dt_d = Q_1 \int_0^\infty t_d f(t_d / S_1) dt_d + Q_2 \int_0^\infty t_d f(t_d / S_2) dt_d + Q_3 \int_0^\infty t_d f(t_d / S_3) dt_d + Q_4 \int_0^\infty t_d f(t_d / S_4) dt_d = Q_1 I_1 + Q_2 I_2 + Q_3 I_3 + Q_4 I_4. \tag{4}$$

In the Equation (4) the expression for I_i can be written as:

$$I_i = P(STO_1 / S_i) m_1(t_{STO_1} / S_i) + P(STO_2 / S_i) m_1(t_{STO_2} / S_i) + P(STO_3 / S_i) m_1(t_{STO_3} / S_i) + P(STO_4 / S_i) m_1(t_{STO_4} / S_i).$$

Equation (4) is a generalization of (2), when in the diagnostics errors of first and second kind are present.

The expression for the variance advisable to submit as follows:

$$\mu_2(t_d) = \int_0^\infty (t_d - m_1(t_d))^2 f(t_d) dt_d = m_2(t_d) - m_1^2(t_d).$$

In this case second initial moment $m_2(t_d)$ can be written as follows:

$$m_2(t_d) = \int_0^\infty t_d^2 f(t_d) dt_d = Q_1 \int_0^\infty t_d^2 f(t_d / S_1) dt_d + Q_2 \int_0^\infty t_d^2 f(t_d / S_2) dt_d + Q_3 \int_0^\infty t_d^2 f(t_d / S_3) dt_d + Q_4 \int_0^\infty t_d^2 f(t_d / S_4) dt_d = Q_1 J_1 + Q_2 J_2 + Q_3 J_3 + Q_4 J_4. \tag{6}$$

In the Equation (6) the expression for J_i can be written as:

$$J_i = P(STO_1 / S_i) m_2(t_{STO_1} / S_i) + P(STO_2 / S_i) m_2(t_{STO_2} / S_i) +$$

$$+ P(STO_3 / S_i) m_2(t_{STO_3} / S_i) + P(STO_4 / S_i) m_2(t_{STO_4} / S_i).$$

To assess the trustworthiness of that formulas statistical modeling was conducted using Monte-Carlo method for units, that shown in Figure 5.

Simulations carried out on condition that i -th STO duration PDF is Gaussian with following parameters: $m_1(t_{STO_i} / S_i)$, $\mu_2(t_{STO_i} / S_i)$, where $(i = \overline{1, 4})$. Numerical values of the parameters of general block of data are listed in Table 1.

In addition, we assume that (if $i \neq j$):

- 1) $m_1(t_{STO_i} / S_j) = m_1(t_{STO_i} / S_i) + 5$, if $i = 1$ or $i = j + 1$;
- 2) $m_1(t_{STO_i} / S_j) = m_1(t_{STO_i} / S_i) + 10$, if $i = j + 2$;
- 3) $m_1(t_{STO_i} / S_j) = m_1(t_{STO_i} / S_i) + 15$, if $i = j - 1$.

TABLE 1 Numerical values of the parameters of general block of data

Parameters of general block of data	Variant number				
	1	2	3	4	5
Q_1	0,4	0,25	0,1	0,2	0,1
Q_2	0,2	0,25	0,25	0,5	0,2
Q_3	0,1	0,25	0,4	0,15	0,3
Q_4	0,3	0,25	0,25	0,15	0,4
$m_1(t_{STO_1} / S_1)$	50	50	50	50	50
$m_1(t_{STO_2} / S_2)$	60	60	70	70	55
$m_1(t_{STO_3} / S_3)$	75	70	80	90	75
$m_1(t_{STO_4} / S_4)$	90	80	100	100	90
$\mu_2(t_{STO_1} / S_i)$	25	25	49	49	36
$\mu_2(t_{STO_2} / S_i)$	36	25	36	49	36
$\mu_2(t_{STO_3} / S_i)$	25	25	36	25	49
$\mu_2(t_{STO_4} / S_i)$	49	25	25	36	25
α	0,02	0,04	0,05	0,05	0,05
β	0,03	0,02	0,03	0,04	0,05

During the simulation was performed statistical estimation of mathematical expectation $m_1^*(t_d)$, variance $\mu_2^*(t_d)$, standard deviation $\sigma^*(t_d)$ and PDF of diagnostic duration $f^*(t_d)$. The simulation results in the form of point estimates of the parameters $m_1^*(t_d)$, $\mu_2^*(t_d)$, $\sigma^*(t_d)$, lower t_{dL} and upper t_{dU} limits of mathematical expectation $m_1^*(t_d)$ interval estimates and results of theoretical calculations of the parameters $m_1(t_d)$, $\mu_2(t_d)$, $\sigma(t_d)$ listed in Table 2. Interval estimates were calculated for a confidence probability $\gamma = 0,95$.

Graphics of diagnostics duration PDF for option number five of input data are shown in Figure 7. Comparison of theoretical calculations of diagnostics duration PDF in the absence ($f_1(t_d)$) and presence ($f_2(t_d)$) of first and second kind errors is shown in Figure 8.

TABLE 2 The simulation results

Variant number	Point estimates			Interval estimates	Calculation data		
	$m_1^*(t_d)$	$\mu_2^*(t_d)$	$\sigma^*(t_d)$	t_{dL} / t_{dU}	$m_1(t_d)$	$\mu_2(t_d)$	$\sigma(t_d)$
1	66,3	270	16,43	65,98/66,62	66,35	268,1	16,37
2	65	251	15,8	64,68/65,32	65	259	16,03
3	79,9	212,1	14,6	79,58/80,22	80,1	238,3	15,4
4	73	262,4	16,2	72,68/73,32	73,1	371	16,46
5	74,4	272	16,5	74,08/74,72	74,3	266,6	16,33

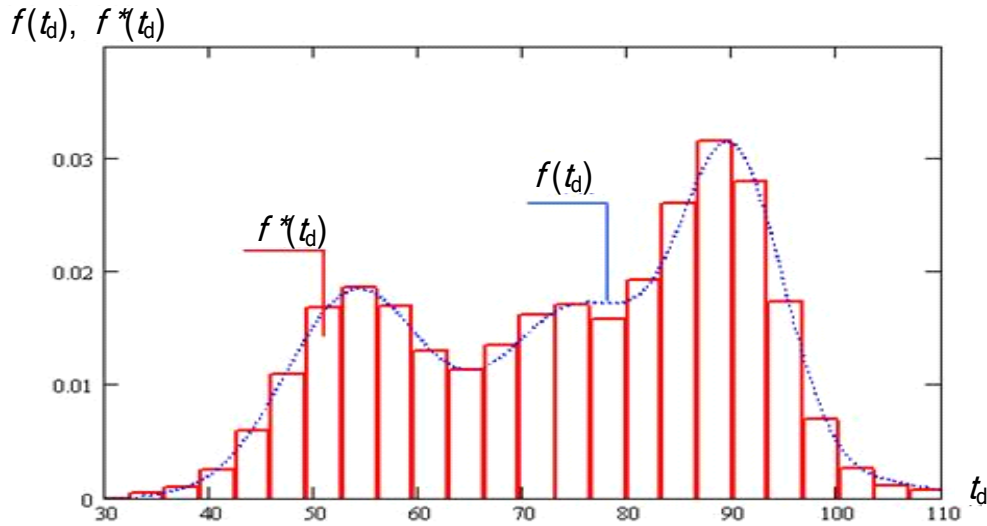


FIGURE 7 Results of theoretical calculations ($f(t_d)$) and statistical ($f^*(t_d)$) simulations to determine the diagnostics duration PDF (option input data – number 5)

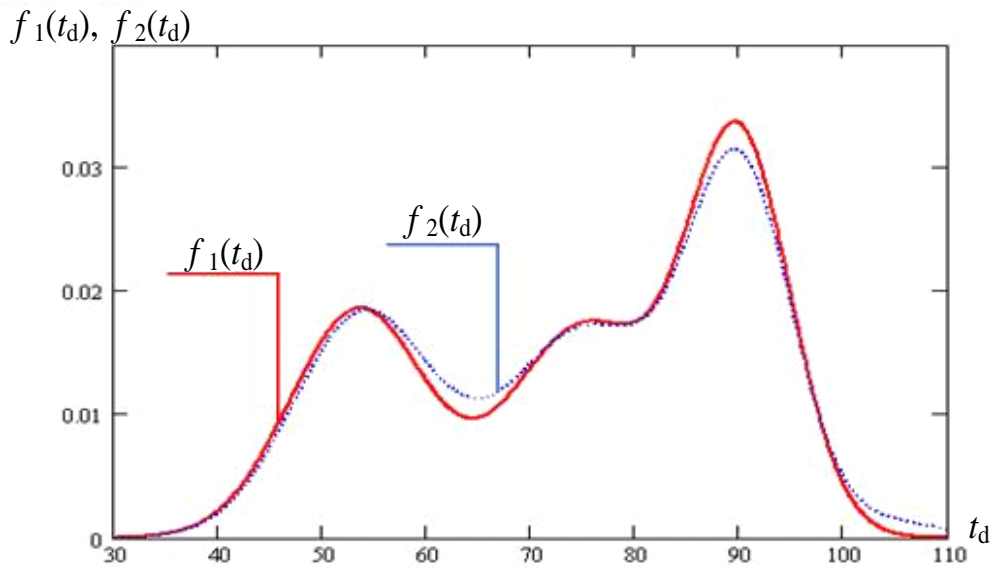


FIGURE 8 Comparison of theoretical calculations of diagnostics duration PDF in the absence ($f_1(t_d)$) and presence ($f_2(t_d)$) of first and second kind errors (option input data – number 5)

4 Conclusions

Problem of diagnostics duration PDF finding is considered in the article. This approach is adequate taking into account resources costs in the diagnostics process and running repairs.

Based on the comparison of the results of diagnostics process statistical modeling and theoretical calculations on the basis of the formulas can be concluded about the truthfulness of analytical formulas.

The results can be used for the design and modernization of Radioelectronic Equipment operation systems.

References

[1] Nakagawa T 2005 Maintenance theory of reliability *London: Springer-Verlag* 270

[2] Smith D J 2005 Reliability, Maintainability and Risk Practical methods for engineers *London: Elsevier* 365

[3] Dhillon B S 2006 Maintainability, maintenance, and reliability for engineers *New York: Taylor & Francis Group* 214

[4] Solomentsev O, Zaliskyi M, Zuiev O 2013 Radioelectronic equipment availability factor models *Jachranka Village, Poland: Signal Processing Symposium 2013 (SPS 2013) Proceedings*

[5] Solomentsev O, Zaliskyi M, Zuiev O 2013 Questions of radioelectronic equipment diagnostics programs efficiency analysis *Jachranka Village Poland: Signal Processing Symposium 2013 (SPS 2013) Proceedings*

[6] Solomentsev O V, Zaliskyi M U, Asanov M M, Zuiev O V 2013 Data Processing in Exploitation System of Unmanned Aerial Vehicles Radioelectronic Equipment *Kyiv Ukraine: IEEE 2nd International Conference on Actual Problems of Unmanned Air Vehicles Developments (APUAVD 2013) Proceedings* 77–80

[7] Barlow R E, Proschan F 1965 Mathematical Theory of Reliability *New York: John Wiley and Sons*

Authors	
	<p>Olexander Solomentsev, 20.08.1949, Simferopol, Ukraine.</p> <p>Current position, grades: professor at National Aviation University, Kyiv, Ukraine, D.Sc.</p> <p>University studies: National Aviation University, Kyiv, Ukraine.</p> <p>Scientific interest: operating systems and processes design, statistical data processing in radio engineering equipment operating systems.</p> <p>Publications: 101 papers.</p> <p>Experience: about 45 years.</p>
	<p>Oleksiy Zuiev, 08.01.1966, Kiev, Ukraine.</p> <p>Current position, grades: associate professor at National Aviation University, Kyiv, Ukraine, Ph.D., academician of Science Academy of Applied Radioelectronics.</p> <p>University studies: National Aviation University, Kyiv, Ukraine.</p> <p>Scientific interest: maintenance processes of radio engineering equipment optimization.</p> <p>Publications: 78 papers.</p> <p>Experience: about 30 years.</p>
	<p>Maksym Zaliskyi, 28.12.1984, Kiev, Ukraine.</p> <p>Current position, grades: associate professor at National Aviation University, Kyiv, Ukraine, PhD</p> <p>University studies: National Aviation University, Kyiv, Ukraine.</p> <p>Scientific interest: statistical data processing in radio engineering equipment operating systems.</p> <p>Publications: 46 papers.</p> <p>Experience: about 7 years.</p>
	<p>Ivan Yashanov, 05.07.1984, Lutsk, Ukraine.</p> <p>Current position, grades: PhD student at National Aviation University, Kyiv, Ukraine.</p> <p>University studies: National Aviation University, Kyiv, Ukraine.</p> <p>Scientific interest: diagnostics of radio engineering systems operating, security systems and Inspection technology.</p> <p>Publications: 19 papers.</p> <p>Experience: about 7 years.</p>

Time series neural network systems in stock index forecasting

Chaoyou Wang

School of Management, Harbin Institute of Technology, Harbin, China

Corresponding author's e-mail: wangchaoyou@gmail.com

Received 1 December 2014, www.cmmt.lv

Abstract

This paper adopts artificial neural network (ANN) and two varieties of time series neural network to forecast the stock index of Chinese market. Daily close prices between 1999 and 2011 are tested. The ANN works as a benchmark. Its inputs include delayed price and technical indicators. Time series neural network with external input (NARX) outperforms the Time series neural network (NAR), and it works best when the delay is 8. Moreover, NARX has the best ability of the three. This is mainly resulted from the fact that it contains external data and the technical indicators while NAR does not. As a whole, the ANN and NARX models achieved satisfying results. They can be employed by practitioners to assist trading and by regulators for monitoring. The NARX will be improved when more external data imported.

Keywords: forecasting, ANN, NAR, NARX

1 Introduction

China is the second biggest and the fastest growing economy in the world now. However Chinese financial markets are still under developed. There are two stock exchanges in Shanghai and Shenzhen respectively. And two distinct kinds of common stocks: A shares and B shares. In early times, Chinese investors could only trade A shares, and B shares are traded in U.S. dollars and H.K. dollars by foreign investors. The mechanism of the markets have many aspects need be improved, such as the lack of short trading and T+0 transactions is not supported. Moreover, inside information trade, financial fraud and the frequently changing policies cause fluctuations and jumps. The Chinese stock market is still not an ideal and stable investment channel, especially for the uninformed and retail investors. However, these characteristics of instability may provide a lot of researchable opportunities.

This paper is motivated by the fact that many investors in China make significant profits in predicting the stock markets. Generally, there are two types of practitioners who survive in the market: fundamental analysts and technical analysts. Fundamental analysts are more interested in the general policies, market information and companies' financial statements. However, technical analysis makes use of the historical data to build a model, which can predict the future price. Academic researchers are more interested in technical analysis for its easiness to be described by mathematical equations.

Many existing theories support the classical efficient market hypothesis (EMH) according to which the current price of the market already fully reflects the overall information. Any imbalance should be detected and diminished immediately [1]. Most developed markets prove the EMH theory holds [2-4]. However, there are still many technical analysts who make profit in the market. This paper also reported the Chinese market is analyzable which may challenge the weak form of the EHM.

Artificial Neural Networks is a mostly used classifier which can also be utilized for prediction. There exist vast literatures, which used ANN to predict the price return and the direction of its movement. ANN and its varieties have been demonstrated to provide promising outcome in the stock price prediction.

2 Literature review

In recent years, there have been a growing number of researches intending to capture the movements of various financial instruments. Tremendous efforts have been made to build models to describe and predict the price path. In the following section, we focus the review of the previous studies on ANN and its varieties' application in financial fields.

There exist vast literatures, which used ANN to predict the price return and the direction of its movement. ANN has been demonstrated to provide promising outcome in the stock price prediction. White [5] used Neural Networks to forecast the market first. He found the model were profitable for IBM common stock. Chiang [6] used ANN to forecast mutual funds. Some variations were later introduced. The probabilistic neural network is used to fit return directions. PNN is proved to outperform the GMM with random walk and Kalman filter [7]. Altay and Satman [8] tested the performances of ANN to predict the ISE-30 and ISE-All Indexes. The result shows that the ANN is better and OLS regression. Chinese market also draws some scholars' interest. Cao Leggio and Schniederjans [9] demonstrated the ANN outperformed the CAPM and Fama and French's 3-factor model in the empirical research about Shanghai Stock Exchange.

Many researchers tend to combine several pattern recognition techniques to improve the prediction model. Tsaih, Hus and Lai's [10] research indicate that the reasoning neural networks outperform the back propagation networks and perceptron.

However, ANN's application in stock prediction may has many flaws. Romahi Shen found ANN occasionally suffers from the over fitting problem.

3 Data description

Our data is collected from every trading day since the establishment of the exchange. The price used in the empirical study is the closing price of Shanghai Stock Exchange. Although there are two exchanges in China, Shanghai and Shenzhen, and no stock is allowed to be listed in both exchanges. However, Chinese policy makers show a strong inclination to develop Shanghai exchange as a main market and make Shenzhen exchange to be a growing enterprise market. Therefore the Shanghai exchange takes most part of the total market value, and Chinese investors and media always use Shanghai Composite Index as the main indicator. This paper also chooses Shanghai exchange's data by convention.

There are 5118 trading days from 1900 to 2011. Daily closing price is chose as the sample data. Figure 1 presents the whole data's pattern.

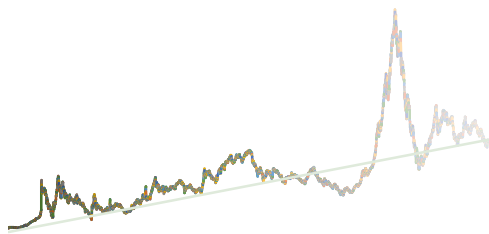


FIGURE 1 Shanghai composite index movement, 1990-2011

As shown in Figure 1, in the last twenty years, Chinese stock market did not grow as fast as its economy. The investors suffered a really long bear market in the first 15 years. Many scholars and practitioners put the blame on the imperfection of the institutional system. However, in 2007 the stock index tripled in less than a year. But the prosperity did not last long, it soon returned to 2006's level in 2008 due to the influence of American subprime mortgage crisis. Some experts claimed that the rapid up and down brought even greater damage to the market than the everlasting bear market before. In the post crisis period from 2008 to 2011, the stock market was not stable yet. Panics strike the market after rumors and news. In general, after more than twenty years development, the Chinese stock market is still fragile and instable.

The Figure 2 is the daily return of the Shanghai stock index, and many spikes are observed in the return plots, which means the market has a fat tail.

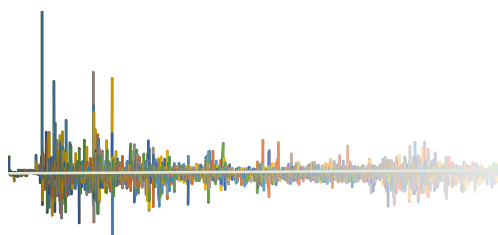


FIGURE 2 Daily return of the Shanghai composite index

Table 1 summarizes the common statistics of the daily return. The positive skewness of 5.37 indicates the data have a fat tail and high peak, which complies with the feature of most financial markets. The kurtosis is 140.55, which means the data is highly non-normally distributed. The Jarque-Bera normality test also rejects the hypothesis of normal distribution. The Arch test accepts that there is relation between the squared return and its one step lag. Finally, the L-B test shows autocorrelation of one, two and three steps all exist, which allow us to model the mean price movement with MA.

TABLE 1 Sample statistics of the Shanghai stock index daily return

Statistics	Estimate
Mean	0.0074
Maximum	0.312324
Minimum	-0.07776
Standard deviation	4.373974
Skewness	5.373978
Kurtosis	140.5569
Jarque-Bera normality test(lags=1)	p=0.001
ARCH test (lags=1)	p=0.1199
Ljung-Box autocorrelation test (lags=1,2,3)	p=0.001, 0.0295,0.0014

4 Prediction models

4.1 ARTIFICIAL NEURAL NETWORK

The ANN model is a two-layer BP network with single sigmoid hidden layer, which can be described by Equation (1) and Figure 3. The output neurons are linear. The network is feed-forward which can fit multi-dimensional mapping problems arbitrarily well, given consistent data and enough hidden neurons. The network is trained with Levenberg-Marquardt back propagation algorithm. The ANN are represented by Equations (2)-(7).

$$f(x) = \frac{1}{1 + e^{-x}} \tag{1}$$

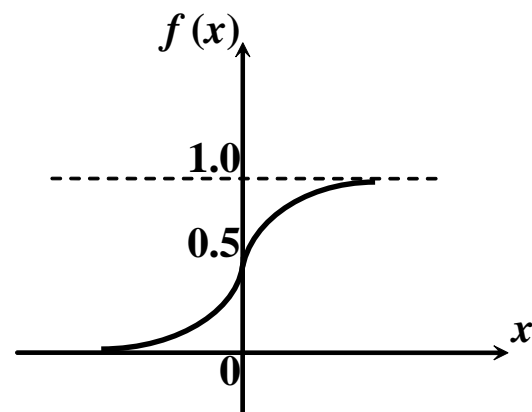


FIGURE 3 Sigmoid function

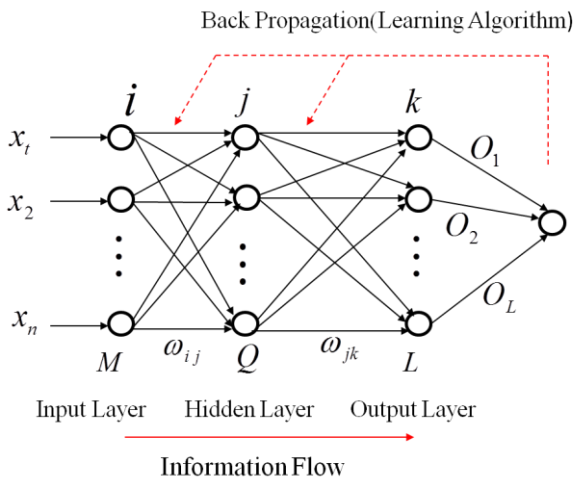


FIGURE 4 Network structure of ANN model

Hidden Layer:
Input:

$$net_j = \sum_{i=0}^n \omega_{ij} x_i \tag{2}$$

Output:

$$f(net_j) = \frac{1}{1 + e^{-net_j}} \tag{3}$$

Weight adjustment

$$\Delta \omega_{jk} = \eta \delta_k y_j = \eta (d_k - o_k) o_k (1 - o_k) y_j \tag{4}$$

Output Layer:
Input:

$$net_k = \sum_{j=0}^m w_{jk} y_j \tag{5}$$

Output:

$$o_k = f(net_k) \tag{6}$$

Weight adjustment

$$\Delta \omega_{ij} = \eta \delta_j x_i = \eta \left(\sum_{k=1}^L \delta_k w_{jk} \right) y_j (1 - y_j) x_i \tag{7}$$

How to select the input data is the key issue for the neural network. We use the present day and 3 earlier days' index as original data. We also use some technical indicators which are commonly used by practitioners. The indicators include Moving average convergence divergence (MACD), Price rate of change (PRC), Acceleration between times (ABT), Momentum between times (MBT), Relative strength index (RSI). There are 9 inputs for the network input in total.

TABLE 2 Technical indicators used in the ANN model

MACD	Moving averages of different time frames which indicate momentum changes and swings in the mood of the crowd, to give buying and selling signals that catches the big moves.
PRC	Percentage change between the most recent price and the price n periods in the past.
ABT	Difference of two momentums separated by some number of periods.
MBT	Difference between two prices (data points) separated by a number of times.
RSI	Recent performance of a security in relation to its own price history

4.2 TIME SERIES NEURAL NETWORK – NONLINEAR AUTOREGRESSIVE (NAR)

Prediction is a kind of dynamic filtering, in which past values of one or more time series are used to predict future values. Dynamic neural networks, which include tapped delay lines are used for nonlinear filtering and prediction.

There are many applications for prediction. For example, a financial analyst might want to predict the future value of a stock, bond or other financial instrument. An engineer might want to predict the impending failure of a jet engine.

Predictive models are also used for system identification (or dynamic modelling), in which you build dynamic models of physical systems. These dynamic models are important for analysis, simulation, monitoring and control of a variety of systems, including manufacturing systems, chemical processes, robotics and aerospace systems.

The time series neural network uses past prediction as input. Unlike the classic ARMA model, the time series neural network depicts the nonlinear autoregressive features of the series. And this model can rely on just the index data. No other technical indicators and information are needed.

$$y(t) = f(y(t-1), \dots, y(t-d), x(t)) \tag{8}$$

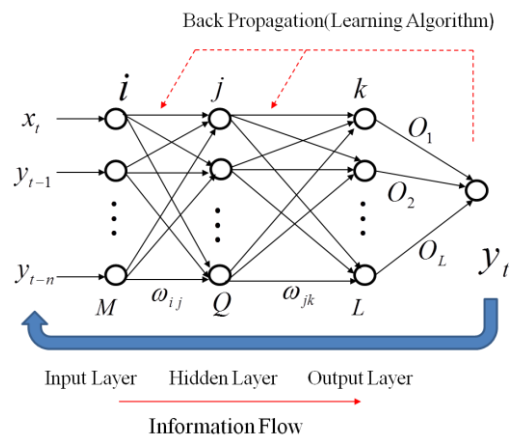


FIGURE 5 Network structure of NAR model

4.3 TIME SERIES NEURAL NETWORK WITH EXTERNAL INPUT-NARX

The NARX is an improved model of NAR. It can include information besides price to better the prediction. For example, in financial market some indicators like trade

volume can be introduced. However, unlike the single stock data, our stock index does not include these information. Therefore, we use the technical indicators as input data. We also import the same indicators, which are used in the ANN model before.

$$y(t) = f(x(t-1), \dots, x(t-d), y(t-1), \dots, y(t-d), x_{1,t}, x_{2,t}) \quad (9)$$

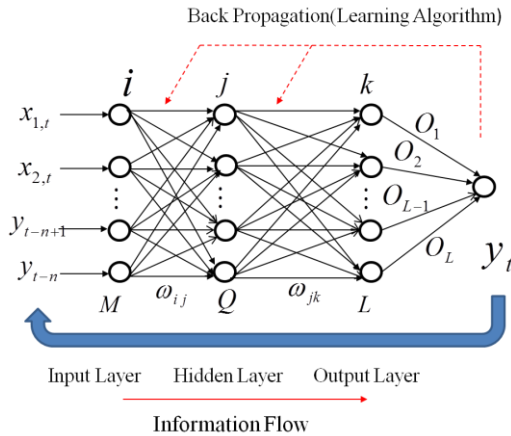


FIGURE 6 Network structure of NARX model

Both NAR and NARX networks will be trained with Levenberg-Marquardt back propagation algorithm.

5 Results and analysis

The 5118 trading days' close index are divided into three parts randomly. 70% are used to train the network, 15% are used to validate the training network, which could stop iteration when the validation result is convergence. The final 15% data are employed to test the predictive ability of the trained model. All the data are pre-treated to adapt for the sigmoid function. Therefore the inputs are standard normalized between 0 and 1.

TABLE 3 Prediction results of 3 neural network models

	MSE	R
ANN	1633	9.992616
NARX delay 1	1549	9.992736
NARX delay 2	1533	9.992814
NARX delay 3	1522	9.992920
NARX delay 5	1513	9.992883
NARX delay 7	1478	9.992896
NARX delay 8	1463	9.992905
NARX delay 9	1498	9.992891
NARX delay 14	1738	9.991821
NAR delay 1	1558	9.992778
NAR delay 2	1735	9.991892
NAR delay 3	1979	9.990803
NAR delay 5	4861	9.977734
NAR delay 7	5074	9.975614
NAR delay 14	6566	9.970092

As can be seen in the result table, NARX outperforms ANN and NAR. NARX performs best when delay is set 8. This means 8 earlier days' prediction is meaningful to future

prediction. When the delay is larger than 8, it will cause over fit issue which makes the trained network less adaptable. However, the NARX's performance indicates the external data is useful. This may result in the external data being mainly technical indicators, which are generated by the stock index and proved to be useful by practitioners. And when delay is longer, the NAR works worse.

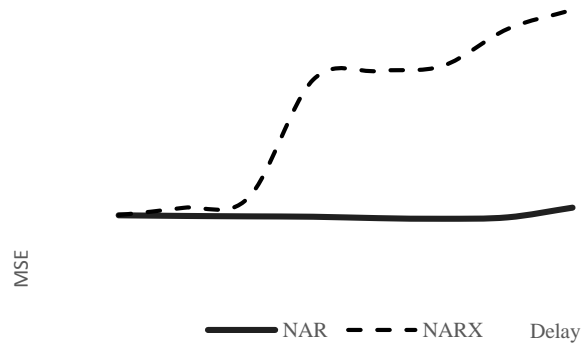


FIGURE 7 MSE of NAR and NARX with different delays

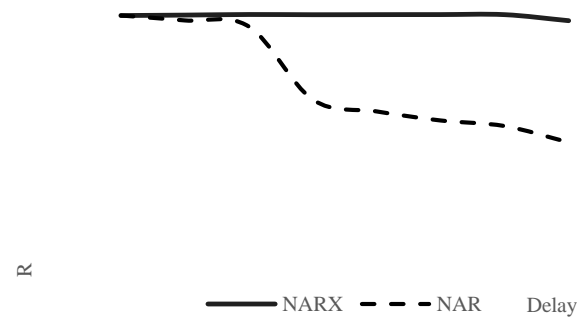


FIGURE 8 Prediction Relative Index of NAR and NARX with different delays

6 Conclusion

It is shown that the neural network models established in this research have several advantages such as high prediction accuracy and quick convergence speed. The basic ANN model works moderately, which is used as a benchmark in this paper. Two varieties of the time series neural network are introduced: Nonlinear Autoregressive (NAR) and Nonlinear Autoregressive with external data (NARX). NARX works much better than the ANN model, and it works best when the delay is set 8. NAR works less accurately than NARX and ANN since we use technical indicators as external data. The result shows that the model can be applied for analyzing the stock market, which is useful for practitioners and regulators. If more external data were imported, the NARX model will produce a better result.

References

- [1] Fama F 1970 Efficient capital markets: a review of the theory and empirical work *The Journal of Finance* **25**(2) 383-417
- [2] Lee C, Lee J 2010 Stock prices and the efficient market hypothesis: Evidence from a panel stationary test with structural breaks *Japan and the World Economy* **22**(1) 49-58
- [3] Borges M R 2010 Efficient Market Hypothesis in European Stock Markets *European Journal of Finance* **16**(7-8) 711-26
- [4] Lim T C, Lim X Y, Zhai R 2012 History of the Efficient Market Hypothesis *International Journal of Management Sciences and Business Research* **1**(11) 26
- [5] White H 1989 Neural-network learning and statistics *AI Expert* **4**(12) 48-52
- [6] Chiang W C, Urban T L, Baldrige G W 1996 A neural network approach to mutual fund net asset value forecasting *Omega* **24**(2) 205-15
- [7] Chen A, Leung M T, Daouk H 2003 Application of neural networks to an emerging financial market: forecasting and trading the Taiwan Stock Index *Computers & Operations Research* **30**(6) 901-23
- [8] Altay E, Satman M H 2005 Stock market forecasting: artificial neural network and linear regression comparison in an emerging market *Journal of Financial Management and Analysis* **18**
- [9] Cao Q, Leggio K B, Schniederjans M J 2005 A comparison between Fama and French's model and artificial neural networks in predicting the Chinese stock market *Computers & Operations Research* **32**(10) 2499-512
- [10] Tsaih R, Hsu Y, Lai C C 1998 Forecasting S&P 500 stock index futures with a hybrid AI system *Decision Support Systems* **23**(2) 161-74
- [11] Phua, Ming, D Lin July 2000 Neural Network with Genetic Algorithms for Stocks Prediction, Fifth Conference of the Association of Asian-Pacific Operations Research Societies 5th - 7th Singapore.
- [12] Yildiz B 2001 Use of Artificial Neural Networks in Prediction of Financial Failures *Journal of IMKB* **5**(17)
- [13] Gallant 1993 Neural network learning and expert systems *MIT Press*
- [14] Bollerslev T 1986 Generalized autoregressive conditional heteroscedasticity *Journal of Econometrics* **31** 307-27
- [15] Chang K H, Kim M J 2001 Jumps and time varying correlations in daily foreign exchange rates *Journal of International Money Finance* **20** 611-37

Author



Chaoyou Wang, born on Jan. 6, 1986, Chengdu, China

Current position: PhD candidate, School of Management, Harbin Institute of Technology.

University studies: Bachelor degree and master degree in Harbin Institute of Technology.

Scientific interest: financial engineering, mathematical modeling.

Study on the electrodeposited Au-Co alloy coating

Shanhong Zhu

¹Xinxiang University, Henan, China

²International School of Software, Wuhan University, Wuhan, China

Corresponding author's e-mail: 14878670@qq.com

Received 1 December 2014, www.cmnt.lv

Abstract

Au-Co alloy deposit was prepared by selecting the best component in the bath with citrate the deposit exhibited golden appearance and high percentage of coverage. Good hardness and improving anti-corrosion capability could be achieved by adding 3~4.5%Co element and little rare-earth element to the system, and micro-hardness could increase to 180~190Hv. Optimized bath has stable performance, good throwing power and good covering power. The Scanning Electron Microscope (SEM) illustrated that the deposit was smooth, compact and crystal was nice. It is suited for electrical production; decorative coating, advance electrodeposits and hard-gold deposit.

Keywords: Au electrodeposited, Au-Co alloy, citrate

1 Introduction

In recent years, gold plating on improving performance and technology research, and other new imitation gold gilded have made great progress [1-4]. Gold alloy coatings due to have good electrical conductivity and stable contact resistance; excellent chemical stability and magnificent golden sheen and is widely used in jewellery, handicrafts, electronics and printed circuit board and other fields [5, 6]. Gold alloy coatings due to have good electrical conductivity and stable contact resistance; excellent chemical stability and magnificent golden sheen is widely used in jewellery, handicrafts, electronics and printed circuit board and other fields [5, 6]. Au-Co alloy coating as a gold alloy coatings have high hardness, this process not only increases the wear resistance of the coating, but also saves the amount of gold. Selection of cobalt sulphate as the main salt of gold-plated can get a uniform appearance, light alloy coatings. Bath composition and process conditions affect the coating was tested on research and routine maintenance of the bath were analyzed and summarized.

2 Experimental study

2.1 GOLD PLATING PROCESS

Wax → degreasing ultrasonic cleaning → intermediate coating → pickling → cleaning → gilded → activation after treatment.

2.2 BATH PREPARATION AND OPEN CYLINDER

Gold salts: 1~3g/L; cobalt sulphate: 0.4~1.5g/L; potassium citrate: 10~20g/L; complexing agents Z1: 10~15g/L; additives Z2: 5~7ml/L; pH value: 3.5~4.5; T: 45~60°C; Jk: 0.15~0.30A/dm²; Time: 15~60sec; Time: 15~60sec; the cathode and anode area ratio: 1: 3; cathodic current density:

0.5~1.5A/dm²; mixing: cathode swing and bath circulation; filter: continuous filtration; anode: iridium, tantalum and titanium mesh coated electrodes.

Open cylinder: the first two-thirds of water were added into the plating tank, heating 45~50°C, then followed by adding gold salts, conductive salt and various additives and complexing agent. Adjust the pH of the bath with citric acid or potassium hydroxide. The proportion was adjusted to 12 degrees Baume, to plating.

1.3 TESTING INSTRUMENTS

- 1) Thickness testing: test using TT230 type coating thickness of coating thickness.
- 2) Appearance characterization: Japanese HITACHI's X-650 scanning electron microscope.
- 3) Coating of gold, Determination of cobalt content: U.S. PerkinElmer Instruments, Inc. Analyst 800 atomic absorption spectrometer.
- 4) PH value determination.

3 Results and discussion

3.1 THE EFFECT OF PLATING SOLUTION COMPOSITION AND QUANTITATIVE

3.1.1 Gold salts

Gold salts are the main bath salts exist in the form of complex ions into the bath. When gold content is low, the deposition rate is slow; taking a strong current plating, plating is red, not light. If the gold salt content is too low, there will be no coating and burning phenomenon. High gold content, allowing the cathodic current density range is wide, fast deposition rate, but cleaning with water phenomenon is relatively serious, thereby causing loss to the gold salts.

3.1.2 Cobalt sulfate and rare earth metals

Adding sulphuric acid cobalt and rare earth metals gloss coating can improve and enhance the hardness and corrosion resistance, improve the coating protection. Cobalt coating bath of sulphuric acid with increasing cobalt content increases, the hardness increases with increasing cobalt content while. As shown in Figure 1, In the case of cobalt was added, a significant increase in the hardness of the coating, the gold micro-hardness from 88 to 93 increased to between 160 to 190, when the cobalt content than 4wt% after micro hardness increase the speed decreases, the alloy color change. Under normal circumstances, the cobalt content of the alloy coating should desirably be controlled within 4wt%.

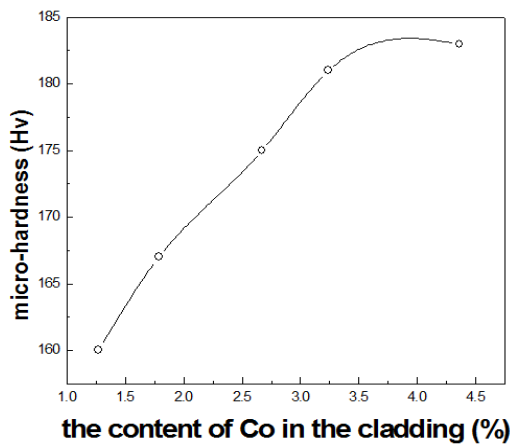


FIGURE 1 Co content with the coating micro-hardness change map

3.1.3 Citrate

Potassium citrate is gilded main conductive salt, but also can be used as an auxiliary complexing agent. Because of citric acid salt and complexing agent additive in Z1 and Z2, reduce the gold, cobalt element to balance the potential difference, in order to achieve total deposits. Maintain stability of the plating solution, improve the cathodic polarization, increased electrical conductivity, reduce energy consumption, promote cell voltage drop. At the same time is also a kind of buffer. Potassium citrate content is too high, affecting the movement of ions, cathodic polarization is too large, the current density decreases; potassium citrate content of less insufficient conductivity, impact adhesion of the gold layer and the underlying particle size of the coating. By the test optimization, potassium citrate concentration in 10~20g, L-1 ideal conductive, complexing properties can be obtained.

3.2 EFFECTS OF PROCESS CONDITIONS ON THE COATING QUALITY AND DEPOSITION RATE

3.2.1 PH value

As shown in Table 1, Figure 2, plating bath pH is too low, hydrogen evolution is serious, low plating efficiency, the

deposition rate is too fast, and easy matt coating surface pinholes and airway. If the pH between 0.5 ~ 4.0, coating deposition rate slows, gas precipitation amount is more, gloss coating apparent slant red; if pH > 6, the precipitation speed slowed sharply, because the Au + mass concentration in plating solution is very low, matt coating surface. Tests showed that pH was able to obtain satisfactory results from 4.0 to 4.5.

TABLE 1 The influence of pH value on the coating appearance

pH	>6	5.0~5.5	4.0~4.5	0.5~4.0	<0.35
Coating appearance	Matt	Golden dark	Bright golden	Shiny reddish	Matt

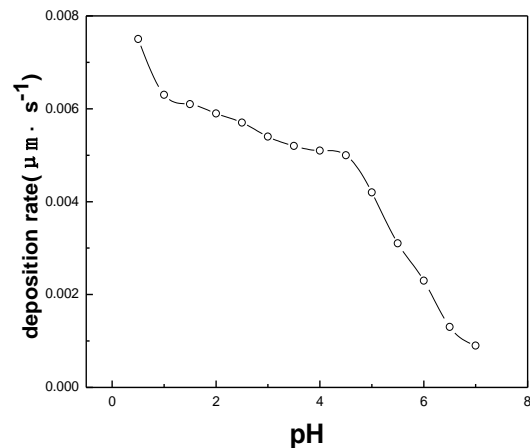


FIGURE 2 Effect of pH on the deposition rate

As shown in Figure 3, as the temperature increases, the coating deposition rate increased rapidly, reaching a high rate in 50~70°C. This is because the high temperature bath will help improve the diffusion of ions migration speed, lower activation energy, while reducing the degree of polarization of cathodic electrodeposition bath when the metal is conducive to improve the electrical ion deposition reaction rate, but the temperature too high as to cause the bath aging and instability. Low temperature, the deposition rate is slow, it is difficult once the quality of the electrodeposition coating, the coating is not bright; temperature is high, the electrodeposition speed is too fast, the coating adhesion is not good. So the control of temperature in 50~60°C can get good coating, high deposition rate [7].

3.2.3 The cathode current density

As shown in Figure 4, the deposition rate increases with increasing current density. When $J_k < 0.5A/dm^2$, the cathode current density, more conducive to more positive potential gold deposit, the mass fraction of gold plating up to 98%, failed to effectively render the alloy coating performance; when $J_k > 3A/dm^2$, the coating is uneven, rough, which may be the cathode current density is too high, cathodic hydrogen evolution seriously, thus affecting the appearance quality of the coating; when $J_k > 4A/dm^2$ time, due to the current is too large, the cobalt content is too high, crystallization will

become rough, dark coating, surface dull, too much current will be high potential burning phenomenon. The experimental results show that the cathode current density is generally controlled at 0.5~1A/dm² can get a better coating.

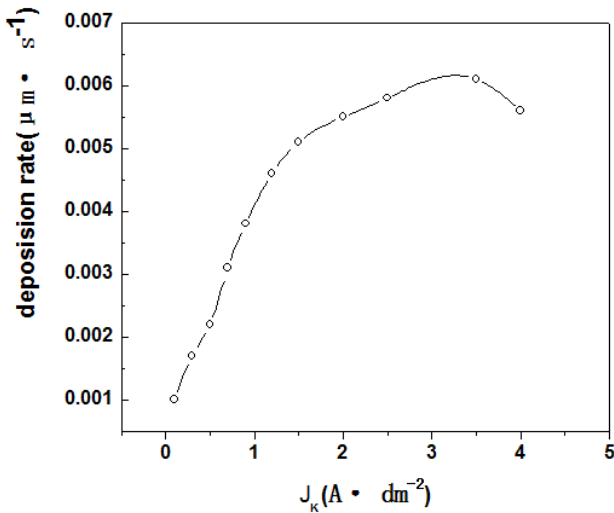


FIGURE 3 Effect of temperature on the deposition rate

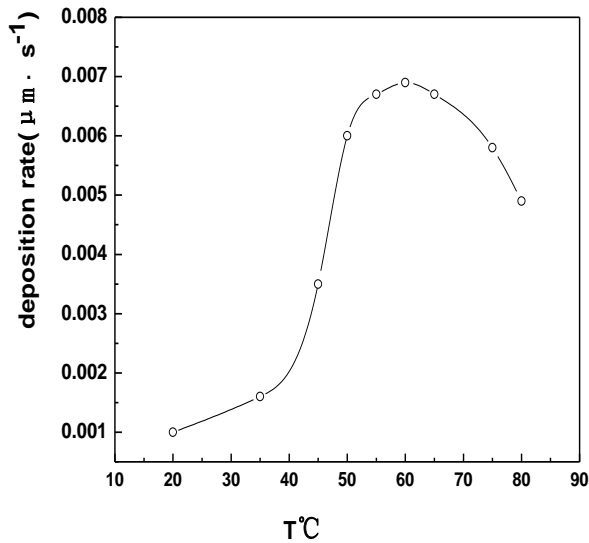


FIGURE 4 Effects of current density on the deposition rate

3.3 GOLD - CHARACTERIZATION OF COBALT ALLOY COATINGS

3.3.1 The appearance of the coating

Coating on the surface of the SEM photos shown in Figure 5 and Figure 6, as can be seen from figure crystalline coating fine, evenly distributed, smooth surface.

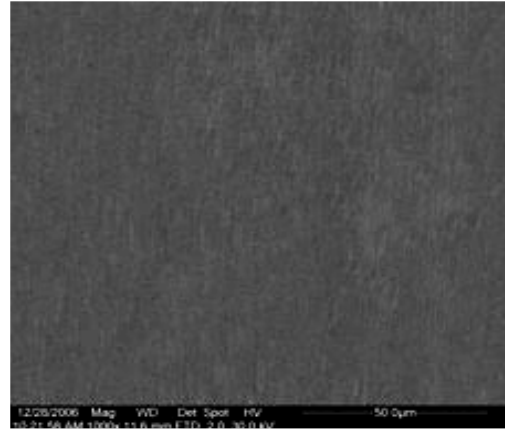


FIGURE 5 The 1000×11.6mm SEM picture of Au-Co Electrodepositing surface

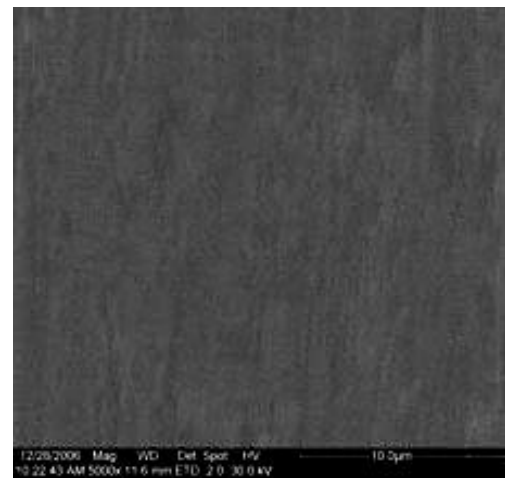


FIGURE 6 The 5000×11.6mm SEM picture of Au-Co Electrodepositing surface

3.3.2 Coating thickness

Using TT230 type coating thickness test coating thickness, coating thickness between 0.05~0.3μm. Because the coating is too thin, the coverage is not enough; coating is too thick, the high cost of electroplating. Coating deposition rate is 0.001~0.007μm · s⁻¹, under appropriate process conditions and bath formulations, depending on the length of time the bath, the plating 10~20s, can achieve the proper coating thickness.

4 Electroplating fault diagnosis and repair

In "Hull Cell" Based on experiments and experimental results on small groove, study concluded coating defects that may occur. It's a detailed analysis of the reasons, in a simple and intuitive form proposed repair methods and measures, as shown in Table 2.

TABLE 2 Electroplating fault repair

Electroplating failure	Fault diagnosis	Repair methods
No alloy plating or "off gold" phenomenon	1. In the process of electroplating power supply connection 2. Master of salt in the plating solution concentration is low 3. The base material surface with oil or wax excrement 4. Before plating workpiece passivation membrane 5. Improper treatment before plating or plating passivation 6. Contaminated with cyanide plating solution 7. In the plating solution mixed with chromic acid oxidation impurities, etc	Check the power supply circuit and a joint of Yin and Yang and corrected Replenish the gold content of the bath and add a certain amount of conductive salt Improve the oil removal to wax concentration and temperature, increasing trichloroethylene ultrasound degreasing Strengthen the activation treatment before plating, reducing plating pieces of residence time in the air Check gilded before plating process, strengthen pre-coating process Adjust pH value, heating, stirring to remove cyanide Adjust pH value, add ferrous salt precipitation reduction after high pH
Coating roughness	1 bath cloudy 2 gilt plating has been rough before 3 cathodic current density is too high	Filter bath added main salt Check gilded before plating process, strengthen pre-coating process Reduce the cathode current density and add a certain amount of conductive salt
Coating color bleak	1 gold content is too low 2 cathode current density is too low 3.pH not in the specified range 4 temperature is too low	Add gold salt bath and add a certain amount of conductive salt Based on results of the analysis appropriate to add gold and conductive salt bath Adjust the solution pH value To improve the bath temperature process specification
Coating redness	1 solution of copper impurities 2 gold content is too high 3 temperature is too high, 4 the cathode current density is too high	Add a certain amount of complexing agent to copper ions masking Fill gold-plated lower concentration of water, and the appropriate adding amount of conductive salt and complexing agent Add cold water to cool and adjust the electrolyte temperature to 50°C, and appropriate additional main salt Reducing the current density, adding gold and conductive salt bath
Coating hair green	1 the solution containing silver or other impurities	Added conductive salt and complexing agent mask interference ions.
Plating solution was muddy brown	1 complexing agent is too low 2 bath aging has a lot of impurities contaminated plot	Need to supplement the complexing agent and conductive salt Need to filter in removing impurity, clean up the amount of gold plating tank recovery solution

5 Conclusions

Gold - cobalt alloy plating optimum conditions are: pH value: 3.5 to 4.5; temperature: 45~60°C; cathodic current density: 0.5~1.5 A/dm²; gold plating the mass fraction of about 96.5%, the coating thickness is between 0.05~0.3µm.

Appropriate process conditions can be prepared gold - cobalt alloy plating, the coating hardness, surface bright and

compact, fine crystal, which was the golden color. Can effectively improve coating performance, cost savings, and has broad application prospects.

Coating and plating quality problems can be solved through appropriate technical methods to achieve safe and efficient production of gold plating.

References

[1] Cai J 2000 Sulfite gold-plated *Plating and environmental protection* **20**(6) 16217
 [2] Jin J 1998 Sulfite full bright gilt *Material Protection* **31**(2) 26227
 [3] Stuemke R Bath for the Galvanic Deposition of Gold and Gold Alloys and Uses Thereof: US **20** 040 065 225 [P] 2004204208
 [4] Buchtenirch Gold Colored Alloy Used for Dentistry and Jewelry: US 68 352 **52** 2004212228
 [5] Guo S, Zhou G, Chen Z 1999 Development of gold alloy plating *Precious metals* **20**(1) 53257
 [6] Cao R, Xiao S 2006 Studies of non-cyanide gold plating *Plating and environmental protection* **26**(1) 11
 [7] Xi Bing 2005 Non-cyanide gold plating on molybdenum *Plating and environmental protection* **25**(3) 35235

The micro-structure study on mechanical properties of Dredge fills

Yun Ma, Hua Si*

Xinxiang University, Henan, China

**Corresponding author's e-mail: 2477574601@qq.com*

Received 1 December 2014, www.cmmt.lv

Abstract

Mechanical tests and electron microscopy scanning tests were done and micro-structural parameters were quantitatively analyzed in order to study the essence of structural characteristics of Dredge Fills. After comparing the mechanical test results with the statistical results of microstructure parameters, it can be found that the transition stage of the stress-strain curve of dredge fill compression test is also the mutation stage of the curve of micro-structural parameters, and at the same time, the micro-structural parameters of shear test soil samples under different axial strain were not linear variation with the axial strain increases and mutated in 10% to 15% axial strain. The analysis result shows that the structural mechanical properties of the dredge fill are subject to its microstructure, and mutation of mechanical test curve is a macroscopic manifestation of microscopic structure damage. The experimental results indicate that dredge fill has the basic mechanical properties of structural soil.

Keywords: Dredge Fills, structural constitution, microstructure, mechanical properties

1 Introduction

Currently, reclamation forms an effective way to develop land resources, dredge channels, and clean the coastal water environment. China has a coastline of 18,000km with rich tidal-flat resources amounting to some 22,000km² in area. Reclamation using hydraulic filled silty soil in the Shadow Sea is one of the main approaches used to explore land resources in the coastal areas of China. However, dredge fill, as a special type of artificial soil, is characterized by its strong structural properties. Due to its special engineering properties, a series of problems are usually encountered. Current research is mainly focused on the methods of treating dredge fill. However, more systematic studies [1], aimed at the relationships between the factors influencing structural properties, the structural strength of dredge fill, and its microstructure, are few in number.

Dredge fill from Zhengzhou, China is taken as the object of the current study. By means of mechanical and micro-structure testing in the laboratory, the variation of stress-strain and the microstructure of the dredge fill during consolidation and shearing processes is investigated. We also give a quantitative discussion of the mechanical properties of the structural dredge fill at the microscopic level.

2 The mechanical properties of structural dredge fill

The soil sample used in this study was taken 3m under the ground at a dredge-filled site in Zhengzhou, China. The Hydraulic fill ground opened in the early 1980s and was improved by vacuum preloading. The soil sample is mainly composed of clay particles and 78–99% of the total weight is made up of particles smaller than 75µm. The clay content

of the mineral components is high; illite accounts for 30–37%, kaolinite for 9–10%, chlorite for 11–12%, and illite mixed layers for 42–45% of the total clay content.

To study the structural properties of the dredge fill, undisturbed and disturbed dredge soil samples are subjected to consolidation testing using a triaxial shear test and uniaxial compression test, respectively. Figure 1 shows the e-LgP correlation curves of the undisturbed and disturbed samples obtained from these tests. From the figure, it can be seen that there is a distinctive structural yield stress in the dredge fill consolidation test. When the consolidation stress is about 112.5 kPa, a notable deflection is found in the test curve from the undisturbed sample. When the consolidation stress is less than 112.5 kPa, the compression test curve has the form expected from a strain softening type of soil. On the other hand, when the consolidation stress is greater than 112.5 kPa, the compression curve shows a variation characteristic of a strain hardening type. As the curve obtained in this test is characterized by typical properties of structural soil compression [1–3], Zhengzhou dredge fill is demonstrated to be a kind of structural soil.

The shear strength of the dredge fill is measured using a triaxial shear test. To evaluate the structural properties of the dredge fill, the undisturbed dredge fill sample and the reconstructed one are subjected to a consolidated, undrained triaxial test. The figure shows that the shear strength parameter of the undisturbed dredge fill sample is much greater than that of the reconstructed one. Also, the shear strength envelope of the undisturbed dredge soil sample is broken and a deflection occurs when the confining pressure exceeds 300 kPa. In contrast, the envelope of the reconstructed dredge fill is straight. All of these properties correspond to shear strength properties characteristic of

structural soil [2, 3], which is indicative of the strong structural properties of the dredge fill.

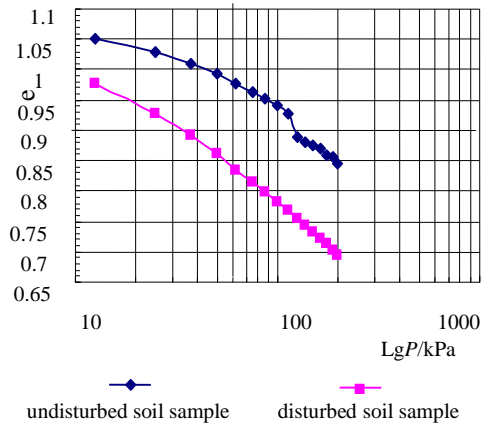


FIGURE 1 Contrast curve of hydraulic fill compression test between undisturbed soil sample and disturbed soil sample

3 The microstructure responses of the mechanical properties of structural dredge fill

Soil is a kind of porous continuum. The cause, size and appearance of pores at all levels directly influence the deformation and failure of the soil mass. A soil mass with an abundance of macropores is extremely unstable and is one of the root causes of soil deformation. Ceteris paribus, soils with a higher porosity are more liable to compressive deformation and shear failure, and thus lead to the destruction of upper buildings. Therefore, some emphasis on the pore characteristics [4] is necessary in the study of the microstructure of the dredge fill.

3.1 MICROSCOPIC TESTING AND METHODS OF STUDYING THE DREDGE FILL

3.1.1 Preparation of the soil sample

A set of compression tests was designed to investigate the rules governing the changes in the microstructure caused by the process of dredge fill compression. Soil samples are taken when the compression tests are stable. Then, vertical cross-sections of the soil sample are analysed using a scanning electron microscope (SEM). Figure 2 illustrates the method of making the soil sample via compression under different stresses. The shaded region in the figure is the scanning area.

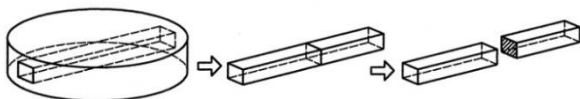


FIGURE 2 Soil samples for micro-structural testing after consolidation test

To investigate the rules governing the changes in the microstructure during shear failure of the dredge fill, a triaxial shear test sample is made from the same soil sample.

A consolidated, undrained triaxial shear test with a confining pressure of 40 kPa is performed. The test ends when the axial strain reaches 5, 10, 15, and 20%, respectively. As shown in Figure 3, the tested soil sample is processed to be the soil sample of microstructure test during the shearing of the dredge fill.

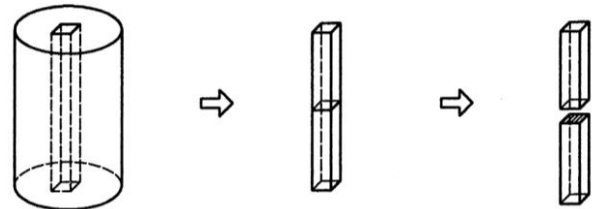


FIGURE 3 Soil samples for micro-structural testing after shear test

To observe the rules governing the changes in the microstructure in different positions after shear failure of the dredge fill, a triaxial shear test under a confining pressure of 300 kPa was performed. Then, a sample was taken after shear failure for microscopic analysis using SEM. A cross-section in parallel with the shear failure surface is of particular interest. The method used for making the soil sample is shown in Figure 4, where a shaded cylinder denotes the shear failure surface, and a shaded cuboid refers to the scanned cross-section.

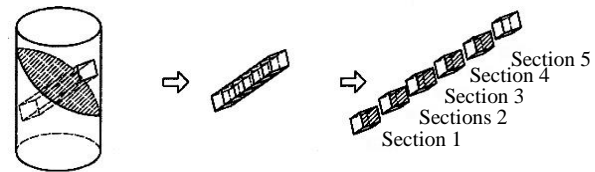


FIGURE 4 Soil samples for near shear failure surface

The dry soil sample is processed using a freeze-drying method. The vacuum freezing sampling instrument for investigating soil microstructure developed by the Guangzhou Institute of Geochemistry, Chinese Academy of Sciences and the Tianjin Institute of Urban Construction was used for this purpose. The operating procedure is as follows. First, the undisturbed soil is sawn to produce a soil slice measuring 4mm×4mm×10mm using a thin steel wire. This is then put into isopentane (boiling point 140°C) and the isopentane vessel equipped with sample is placed into liquid nitrogen (boiling point 190°C). This causes the sample to be frozen so that the liquid in the soil is turned into non-crystallized ice without expansion. Finally, the soil sample is vacuum pumped at 50°C for over 15 hours to sublime out the non-crystallized ice in the soil directly. The procedure used thereby achieves the objective [6] that the soil sample is dried without deformation.

3.1.2 Microstructure imaging

Scanning electron microscopy is one of the most important tools currently used to investigate clay soil microstructure. This is because it is capable of producing excellent images at various levels of magnification, has wide view, high

resolution and images may be stereoscopic. In addition, they can be used to directly image rough surfaces with large fluctuations. SEM is regarded as the only method of microstructure testing that can directly observe the distribution and contact relationship between particles.

SEM's working principal involves secondary electron imaging. That is, the image is produced point by point in a temporal and spatial sequence and displayed on the kinescope of an external microscope. Due to the porosity and desiccation of the soil sample and its poor electrical conductivity, the sample is treated with gold spray before imaging by the SEM. This prevents generation of a discharge by the bombardment from the electron beam used in the scanning process. To ensure high image definition, the typical structure cell can first be found using high magnification. Then, the magnification is gradually reduced [7, 8] until the SEM magnification of $\times 2000$ is selected. In this way, a more ideal statistical law could be invoked for use in this research.

3.1.3 *Microstructure parameter selection and their physical meaning*

Considering that moisture content has a great effect on the mechanical properties of the dredge fill, the space taken up by moisture needs some emphasis. This is illustrated by the distribution of pores in the microscopic images. Therefore, the pores are chosen to be the object of a quantitative study of the soil microstructure. Based on the above experimental conditions, dredge fill samples are scanned using SEM and quantitative statistical analysis is carried out on the pores in the sample. Five pore microstructure parameters [9, 10] are selected for consideration.

1) *Equivalent diameter*: Defined as the diameter of a circle with area equivalent to the pore area, which is an important parameter to illustrate the size and properties of the pores. All pores are statistically included and averaged.

2) *Pore number*: The number of pores in a microscopic image can directly illustrate the pore size, the distribution, and contact relationship of the soil particles.

3) *Pore perimeter*: This is equal to the sum of the boundary lengths of all the pores. It shows the contact area between pores and particles, and indirectly indicates the size, appearance, and regularity of the pores.

4) *Pore morphology ratio*: This is the ratio of the major and minor axes of the pore. The higher the ratio, the more 'strip-like' is the pore. If the ratio is close to 1, the pore is more likely to be a square or circle.

5) *Pore roundness*: This is another parameter representing pore morphology. The further its value is from 1, the more irregular the pore is. The closer its value is to 1, the more like a circle the pore becomes (when its value is 1, the pore turns into a standard circle).

3.1.4 *Acquisition of the microstructure parameters*

The above microstructure parameters are mainly obtained for dredge fill samples by analyzing the pores in the SEM images using the 'Field and Feature' measuring tool modules in Leica Qwin. The parameters express the morphology and distribution features of the pores during the deformation of the dredge fill from different aspects.

3.2 MICROSTRUCTURE RESPONSE TO THE COMPRESSIVE PROPERTIES OF STRUCTURAL DREDGE FILL

3.2.1 *The response to compression*

Figure 6 displays vertical cross-section SEM images of soil samples used in compression tests at different consolidation pressures. In general, all the images show a plate stack structure. When the consolidation stress is less than 100 kPa, the arrangement of the particles is relatively loose with a line-area contact relationship. The pore directionality is indistinct. When the consolidation stress is in the 100-125 kPa range, the particle arrangement is much looser with line-area and area-area contact. The whole structure is presented as a plate frame structure or a laminated bracket structure. When the consolidation stress exceeds 125 kPa, fine particles are arranged gradually closer with smaller pores, poorer pore directionality, and a main line-area contact relationship. The change in the microstructure demonstrates that the dredge fill has experienced structure failure and the formation of new structures during the consolidation process. The result is in good agreement with the compression test curve.

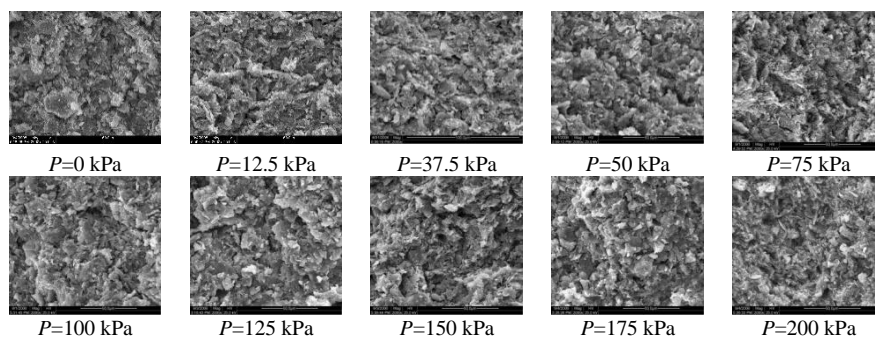


FIGURE 6 The SEM images of compressed soil samples under different consolidation stress

3.2.2 Microstructure parameter variation during compressive deformation and its meaning

Figure 7 shows microstructure parameter variation curves accompanying dredge fill consolidation.

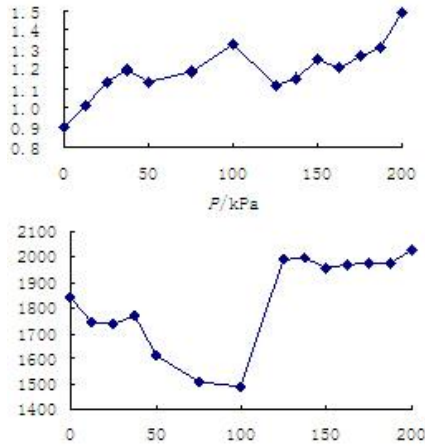


FIGURE 7 The micro-structure parameter curve of compressed soil samples under different consolidation stress

It can be seen that when the consolidation stress is less than 100 kPa, an increase in consolidation stress causes an increase in pore equivalent diameter, pore morphology ratio and pore roundness. At the same time, pore number and pore perimeter decrease. Further, when the consolidation stress exceeds 100 kPa, all the pore structure parameters change abruptly. When the consolidation stress exceeds 125 kPa, a further increase in consolidation stress causes an increase in pore equivalent diameter, pore morphology ratio and pore roundness. Also, the pore number and pore perimeter decrease.

Comparing the pore microstructure curves with the consolidation test curves, it is readily found that the turn phase

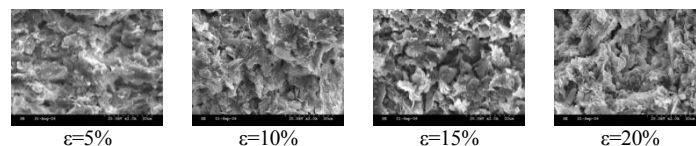


FIGURE 8 The SEM picture of soil sample after the shear test under the different strain

3.3.2 Parameter variation during the shear process and interpretation

Figure 9 displays curves showing the variation in the microstructure parameters of the dredge fill in the shear tests. In the figure, as axial strain increases the variation in the parameters is not always linear; it changes abruptly when the axial strain is 10–15%. This shows that the structural properties of the dredge fill change during the shear failure process. When the axial strain is less than 10%, the shear process is manifested as 3D compression, gas compression and moisture migration into the pores. Moisture is gradually taken up in the pores and approaches saturation. This moisture migration enables the connection of different parts of the pores, and some particles concentrate on aggregates

of the stress-strain curve coincides with the mutation phase of the microstructure variation curve. This illustrates that the change in mechanical properties of the soil is essentially caused by the variation in the microstructure [11, 12].

3.3 THE MICROSTRUCTURE RESPONSES TO THE SHEAR RESISTANCE PROPERTIES OF STRUCTURAL DREDGE FILL

3.3.1 The response to shear processes in the microstructure images

Figure 8 shows SEM images of shear tested soil samples when the axial strain is set to 5, 10, 15, and 20%. Comparing the 5% and 10% axial strain images, the compactness of the particle arrangement of the soil sample when the axial strain is 10% is seen to be higher than that when the axial strain is 5%. Furthermore, both images show little difference in their structure as a whole, which indicates that the dredge fill structure is not damaged during shear deformation when the axial strain is less than 10%. Next, the 10% and 15% axial strain images are compared. The resulting comparison shows that each present notable variations in the structure as a whole. The soil sample has a flocculated microstructure when the axial strain is 10%, while at 15% axial strain there is a plate frame structure. Moreover, with an increase in axial strain, the arrangement of particles and aggregates becomes closer, and trellis pores partially occur. This shows that the whole structure of the soil sample has been damaged through a process of structural failure, and shear dilatation occurs. When the axial strain is 20%, the whole structure turns into a flocculated structure again, which a new structure is resulting from shear failure.

or the skeleton. This results in the single pore volume increasing and reduced pore regularity. Also, variation in the microstructure parameters include: reduction in pore number and an increase in equivalent area, pore morphology ratio and pore roundness. When the axial strain is 10–15%, shear stress exceeds the structural strength of the dredge fill and shear failure occurs in parts of the aggregates. This leads to an increase in pore number and pore perimeter and a decrease in equivalent area. However, the segmentation of pores improves the pore regularity in the microscopic images and thus the morphology ratio and roundness are reduced. When the axial strain is greater than 15%, the shearing process is characterized by triaxial compression, along with an increase in pore perimeter and equivalent area.

Under the shearing effect, pores are more irregular and their roundness and morphology ratio increase.

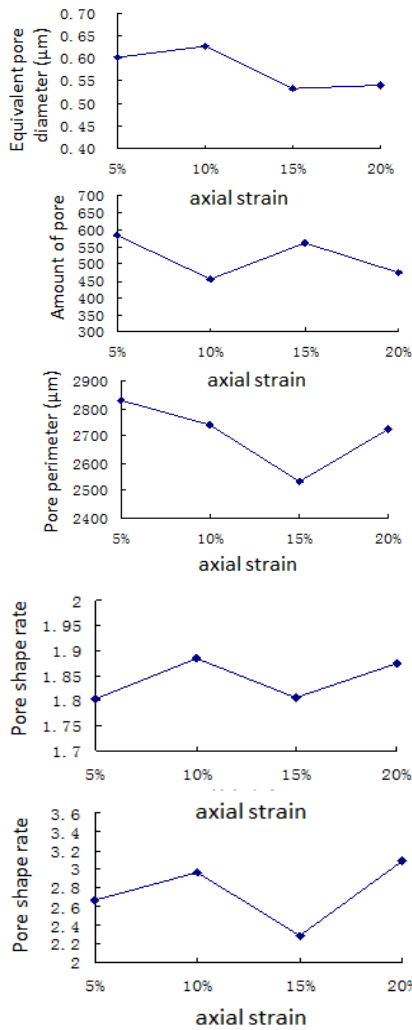


FIGURE 9 The micro-structure parameter curve of shear test soil samples of different axial strain

3.4 MICROSTRUCTURE RESPONSE FOR THE SHEAR FAILURE OF STRUCTURAL DREDGE FILL

3.4.1 The response to shear failure in microstructure images

Comparing the five images, it is seen that the morphology of sections 1 and 5 are similar. Likewise, the morphology of sections 2 and 4 are similar. Furthermore, analysis of the morphology indicates that sections 1 and 5 display macropore development and a flocculated structure as a whole. Also, the particles' contact relationship is generally line-area. The pore development in sections 2 and 4 is inferior to those in sections 1 and 5. Furthermore, their particle arrangement is closer with visible signs of shear cracking; the particle contact relationship represents a coexistence of line-area and area-area contacts. Section 3 is completely different in microstructure morphology from the other four sections. It shows a laminated support structure on the whole

and there is an extremely notable directional alignment of flaky minerals. This indicates that section 3 has a position which is just on the shear failure surface. Due to the shear slipping failure, the structure of the dredge fill is completely damaged, resulting in the rearrangement of mineral particles. As sections 2 and 4 are closer to the shear failure surface, partial shear cracking is apparent, but the whole structure has not been damaged irrevocably. Sections 1 and 5 show macropore developments and flocculated structures as a whole, mainly due to the dilatation during shear testing.

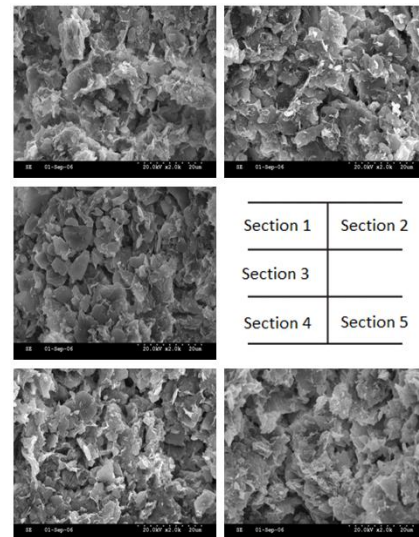


Figure 10 The SEM picture of soil sample at different distances to shear failure surface

3.4.2 Microstructure parameter variation at different distances from the shear failure surface and interpretation

To investigate the range of influence of the shear failure in soil, five sections are taken parallel to the shear failure surface and their microstructure parameters is obtained. This allows one to analyze the microstructure properties of the soil mass at different distances from the shear failure surface.

Figure 11 shows the microstructure parameter curves on the shear failure surface and its pores on both sides. As can be seen from the figure, the equivalent diameter, morphology ratio, and roundness of the third soil sample are the smallest compared to the other samples. Meanwhile, its pore number and perimeter are the largest. These changes may be explained by the fact that the third sample is much closer to the shear failure surface. The reason for this is that aggregates of the dredge fill are crushed when the shear stress exceeds the shear structure strength of the dredge fill. However, shear dilatation is not distinct when the shear failure of the soil sample occurs under a confining pressure of 300 kPa and the microscopic sample lies in the middle of the shear sample. Therefore, compared to both sides of the shear failure surface, the average pore diameter, pore morphology ratio, and pore roundness at the shear failure surface are smaller, while its pore number and perimeter are larger. These results are mainly due to the increase in pore

number and irregularity of the morphology driven by the slipping and crushing of aggregates [13].

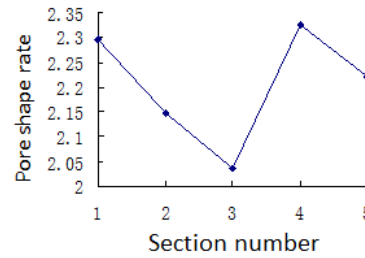
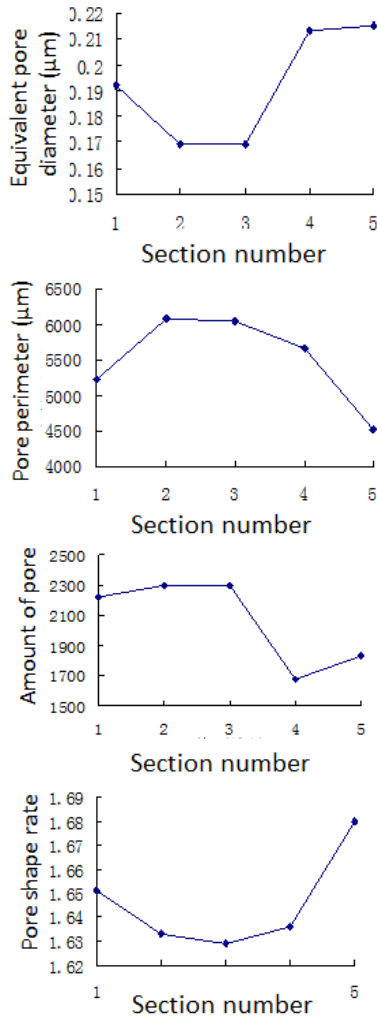


FIGURE 11 The micro-structure parameter curve of soil sample at different distances to shear failure surface

4 Conclusions

1) This is specifically illustrated by the existence of a yield stress in the compression process. When the stress is smaller than the yield stress, the compression test curve shows a strain softening type of behaviour and when the stress is larger than the yield stress, it presents a strain hardening type. Meanwhile, the shear strength envelop has a broken line form.

2) Based on a quantitative analysis of the microstructure of the dredge fill during consolidation, the turn stage of the stress-strain curve of the dredge fill coincides with the mutation phase of the microstructure parameter variation curves. This is explained by the fact that the variation in the mechanical properties of the soil is basically caused by the changes in microstructure.

3) The quantitative microstructure analysis of the effect of shear testing on the dredge fill show that the microstructure parameters mutate when the axial strain is 10–15% (instead of varying linearly with an increase in axial strain). This demonstrates that the structural properties of the dredge fill change during shear failure in a macroscopic way.

References

[1] Liu E-l, Shen Z-j, Fan W 2005 Advance in researches on structured clay *Rock and Soil Mechanics* 26 (Supp) 2-8

[2] Gong X-n, Xiong C-x, Xiang K-x 2000 The formation of clay structure and its influence on mechanical characteristics of clay *Journal of Hydraulic Engineering* (10) 43-7

[3] Chen T-l, Zhou C, Shen Z-j 2004 Compression and shear test of structured clay *Chinese Journal of Geotechnical Engineering* 26(1) 31-5

[4] Qi J-l, Xie D-y, Shi Y-c 2001 Status quo and method of quantitative study on soil structure *Northwestern seismological Journal* 23(1) 99-103

[5] Wang B-j, Shi B, Cai Y, et al 2008 3D visualization and porosity computation of clay soil SEM image by GIS *Rock and Soil Mechanics* 29(1) 251-5

[6] Li Z-l 2007 Research on the micro-structure and engineering properties of hydraulic fill in Tianjin Binhai New Area *Xi'an: Chang'an University*

[7] Chen J-o, Ye B, Guo S-j 2000 Primary exploration on engineering properties of soft ground microstructure in Zhejiang Delta *Chinese Journal of Rock Mechanics and Engineering* 19(5) 674-8

[8] Cheng Y-x 2008 Research on the formation mechanism of structural strength of seashore dredger fill and the key technique of vacuum preload method *Xi'an: Chang'an University*

[9] Lei H-y 2002 Micro-structural effect of consolidation deformation in saturated soft clay *Journal of Hydraulic Engineering* (4) 91-100

[10] Zhou Y-q, Hong B-n 2005 Experimental research on microstructure changes of clayey soil in process of compression *Rock and Soil Mechanics* 26(5) 82-6

[11] Li J-h, Shen Z-j 2007 Study on mechanism of micro-failure of structured soils *Rock and Soil Mechanics* 28(8) 1525-32 1550

Method of calculating forest land surface area based on automatic boundary extraction

Jiahzu Zheng, Yehemin Gao

Jiangsu Nanjing Forestry University, 210037, China

Corresponding author's e-mail: zhengjiahzu@126.com

Received 1 December 2014, www.cmnt.lv

Abstract

Calculation of the forest land parcel surface area is vital to the confirmation, segmentation and assignment of forest ownership. Therefore, the method calculating irregular forest land parcel surface area, which is based on the principle of space triangle area calculation, establishes automatic extraction of irregular forest parcel boundary and structures Triangulated Irregular Network (TIN) model by interpolating feature points based on Thin Plate Spline (TPS) function. This paper expounds the feasibility of this method and complete calculation process. By experimental comparison, this method can reduce about four-fifths of field data collection effort in the case of no accuracy loss in calculating results. Simultaneously, this method extracts boundary automatically without manual drawing boundary lined, improves degree of automation in computing within the industry greatly.

Keywords: forest land parcel, surface area, boundary extraction, thin plate spline (TPS)

1 Introduction

Forest ownership is an important part of real estate registration and forest land parcel area is a vital element in forest ownership. Horizontal projection area of forest land parcel is generally considered as surface area of the land parcel. However, horizontal projection area of mountain forest cannot reflect the characteristic of forest land parcel accurately, which is not conducive to the confirmation, segmentation and assignment of forest ownership. Using the land parcel surface area to indicate the size of forest land can solve this problem. Currently, the most common method of calculating irregular land parcel surface area is to build TIN model and calculate space area of every triangle. A series of interconnected space triangles are composed by many ground feature points, which are, measured [1]. These triangular facets compose the entire land parcel surface and its area can be obtained by the sum of the area of each triangle. Describing the surface morphology by TIN model is related to distribution location and density of ground feature points. The accuracy of surface area calculated by this model and the number of measured feature points are closely related, that is, the more the feature points are, the more accurate results are. But in the actual field data acquisition, it is difficult to obtain a large number of feature points due to the influence of various unfavorable factors. So it generally uses Spline interpolation, Kriging and Inverse Distance Weighted interpolation to interpolate [2-4], and constitute a TIN based on interpolation points. This paper studies the TPS interpolation function, and validates the result in order to reduce the workload of field data collection. At the same time, it extracts boundary of area automatically by convex hull forming principle and improves the degree of automation in the industry calculation.

2 Surface area calculation principle

2.1 SPACE TRIANGLE AREA CALCULATION

As shown in Figure 1, point A, point B, point C are three vertices of the space triangle and point O is the origin of the coordinate system. If the spatial coordinates of point A, point B, point C in this space coordinate are known, the space vectors \overline{OA} , \overline{OB} , \overline{OC} will be obtained. The length of three sides of triangle ABC (a , b , c) can be obtained by the three vectors module operation. The triangle area can be obtained according to Heron formula.

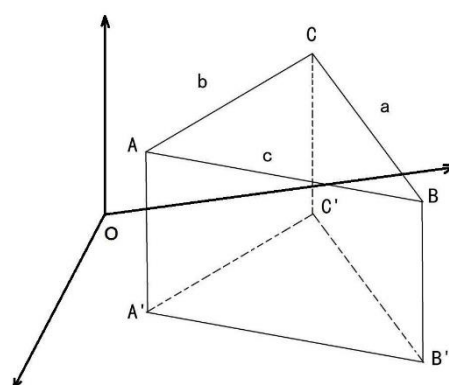


FIGURE 1 Space triangle schematic diagram

$$p = \frac{a+b+c}{2}, \quad (1)$$

$$S = \sqrt{p(p-a)(p-b)(p-c)} \quad (2)$$

Wherein, p is half of the perimeter of the triangle, S is the area of triangle.

2.2 THIN PLATE SPLINE FUNCTION

Thin Plate Spline function is a cubic polynomial interpolation function defined on a two-dimensional area. Construct a function $S(x, y)$ on the set of points composed by field sampling points, making

$$S(x_i, y_i) = z_i (i = 1, 2, \dots, n) \tag{3}$$

Here, (x, y) is plane coordinating of sampling point and z is elevation of the point. According to the coordinates and elevations of the ground feature points collected outside industry, specific form of $S(x, y)$ can be calculated and corresponding elevations can be calculated by Equation (3). The TIN model can be built in accordance with the provisions of the plane coordinate grid points.

Define functions

$$\eta(r) = \begin{cases} \frac{1}{16\pi} r^2 \log r & r > 0 \\ 0 & r = 0 \end{cases} \tag{4}$$

Presume (x, y) are the coordinates of the ground points $t = [x, y]^T$, and define three functions:

$$\Phi_1(x, y) = 1 \quad \Phi_2(x, y) = x \quad \Phi_3(x, y) = y \tag{5}$$

Then any linear function of the space area can be expressed as linear combination of $\Phi_j (j=1, 2, 3)$. Suppose there is a matrix T in three rows and n columns, whose elements are $T_{jk} = \Phi_j(t_k)$. That is,

$$T = \begin{bmatrix} 1 & 1 & \dots & 1 \\ t_1 & t_2 & \dots & t_n \end{bmatrix} = \begin{bmatrix} 1 & 1 & \dots & 1 \\ x_1 & x_2 & \dots & x_n \\ y_1 & y_2 & \dots & y_n \end{bmatrix} \tag{6}$$

$\|\bullet\|$ represents a European form in two-dimensional space, scilicet $\|t\|^2 = t^T t$. If we find a suitable constant $\delta = [\delta_1, \delta_2, \dots, \delta_n]^T$ and $\alpha = [\alpha_1, \alpha_2, \alpha_3]^T$ that make

$$S(x, y) = S(t) = \sum_{i=1}^n \delta_i \eta(\|t - t_i\|) + \sum_{j=1}^3 \alpha_j \Phi_j(t) \tag{7}$$

Satisfy the interpolation condition (3), the Equation (7) is the TPS function of point set (t_1, t_2, \dots, t_n) . If there is

$$T\delta = 0 \tag{8}$$

Then the Equation (7) is called natural TPS function.

Define a matrix E whose elements are

$$E_{ij} = \eta(\|t_i - t_j\|) = \frac{1}{16\pi} \|t_i - t_j\|^2 \log \|t_i - t_j\| \tag{9}$$

In order to calculate constants $\delta = [\delta_1, \delta_2, \dots, \delta_n]^T$ and $\alpha = [\alpha_1, \alpha_2, \alpha_3]^T$ in Equation (7). And the solution of following linear equation is the desired.

$$\begin{bmatrix} E & T^T \\ T & 0 \end{bmatrix} \begin{bmatrix} \delta \\ \alpha \end{bmatrix} = \begin{bmatrix} z \\ 0 \end{bmatrix} \tag{10}$$

Among the Equation, $z = [z_1, z_2, \dots, z_n]^T$.

2.3 CONVEX HULL FORMING PRINCIPLE

Convex hull is the boundary of the target area which is a minimum polygon containing all points in point set. Find the upper half of the convex hull in counterclockwise order from the starting point. Then find the under half of the convex hull in same order from the terminal point. As shown in Figure 2.

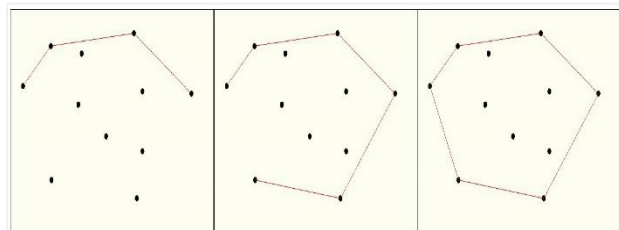


FIGURE 2 Convex hull forming principle

3 Realization of algorithm to calculate the surface area

3.1 THE BASIC PROCESSES

The basic process of forest land parcel irregular surface area calculation based on automatic boundary extraction is to extract the boundary of target area automatically and use the interpolation function to form a TIN model to calculate surface area. The specific processes are:

- 1) A number of ground feature points obtained by field measurements;
- 2) Draw scatter-plots in MATLAB, and extract the irregular forest land parcel boundary in accordance with convex hull forming principle;
- 3) Using the measured ground feature points to calculate the coefficients of TPS function and interpolate this region;
- 4) Construct TIN model by interpolation points and calculate surface area by Heron formula.

3.2 METHOD OF EXTRACTING BOUNDARY AUTOMATICALLY BASED ON MATLAB

Boundary of the target area need to be obtained when we calculate the irregular land parcel area. Software used in the calculation need operator to connect the target area boundary line manually and this will reduce the automatic degree of software. This paper presents an automatic method for extraction of boundary in MATLAB, which can extract

quickly the target area boundary without human intervention. This method improves the automatic degree of calculation. Specific codes are omitted. Result of the process is shown in Figure 3.

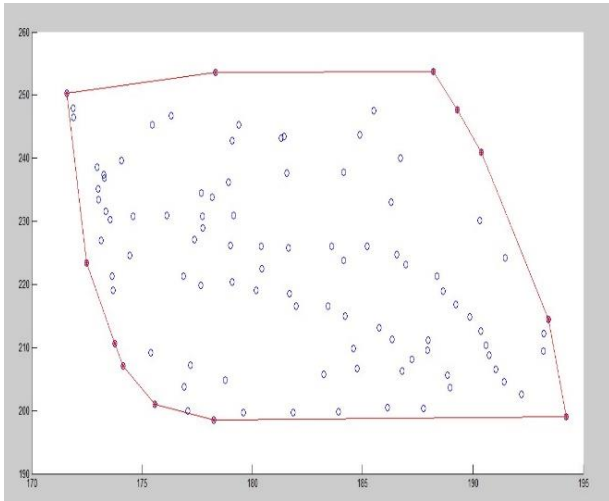


FIGURE 3 Automatically-extracted boundary

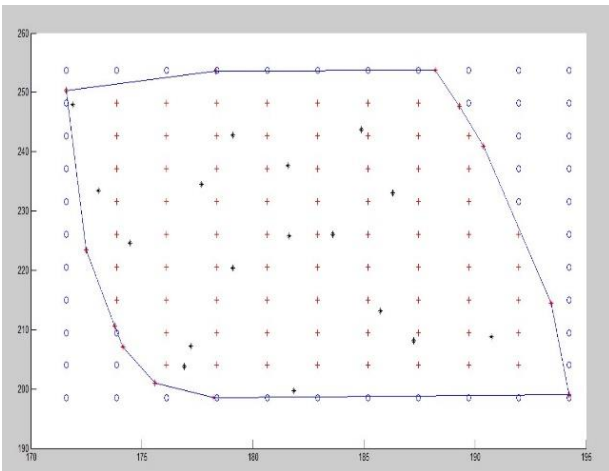


FIGURE 4 Interpolated points obtaining

3.3 INTERPOLATION ALGORITHM BASED ON TPS FUNCTION

1) *Interpolate on the set of points.* Select vertical and horizontal coordinates of the interpolation intervals

according to the measured ground feature points. Then calculate the coefficient of interpolation function according to Equation (10) and obtain plane coordinates of interpolation points. Interpolation algorithm codes for point set are omitted. The result is shown in Figure 4.

2) *Calculation of interpolated point elevations.* Calculate the elevations of interpolation points in accordance with Equation (7). The program codes are omitted.

3) *Generation of TIN.* Generate TIN using interpolation points and collection points. Delaunay triangulation is usually used. The codes are omitted and result is shown in Figure 5.

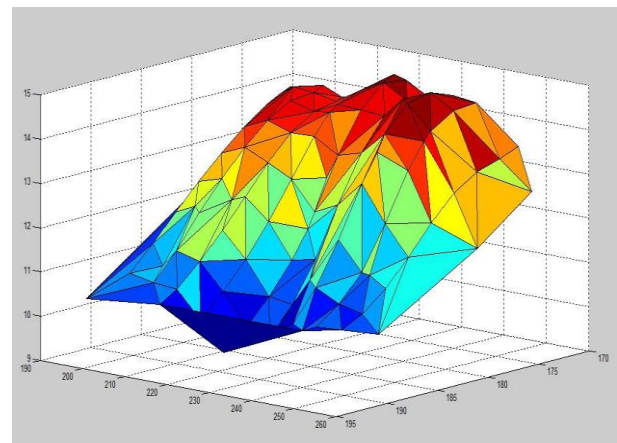


FIGURE 5 Generated TIN

(4) *Surface area calculation.* Calculate the area of each triangle according to Equation (2) and sum to obtain the surface area of irregular forest land parcel. The codes are omitted.

4 Experimental validation analysis

This paper selected irregular forest land parcel whose horizontal projection area is 1031.179m². Ninety-nine feature points, which can reflect a detailed ground feature, are obtained through field measurement. Scatter plots are shown in Figure 6. Then select twenty-nine points, which can reflect roughly. These points are shown in Figure 7. Extract the boundaries automatically of point sets in Figure 6 and Figure 7 and build TIN models based on the measured feature points (Figure 8 and Figure 9). Then calculate surface area. The results are shown in Table 1.

TABLE 1 Comparison of surface area

	Direct Method		Interpolated Method	Absolute Error	Relative Error
	99 Feature Points	29 Feature Points			
Surface Area (m ²)	1090.898	1076.085	1090.657	0.241	0.22%

Exegesis: Absolute error and relative error are based on comparison between the result of direct method and 99 feature points.

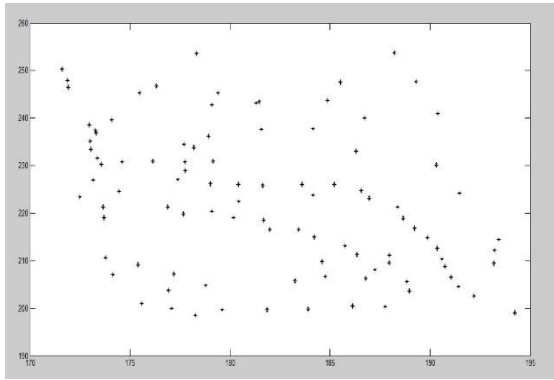


FIGURE 6 Dense points

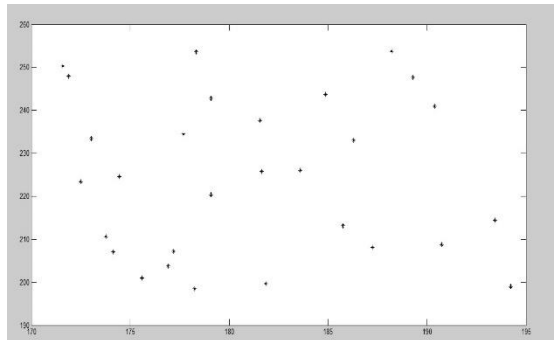


FIGURE 7 Sparse points

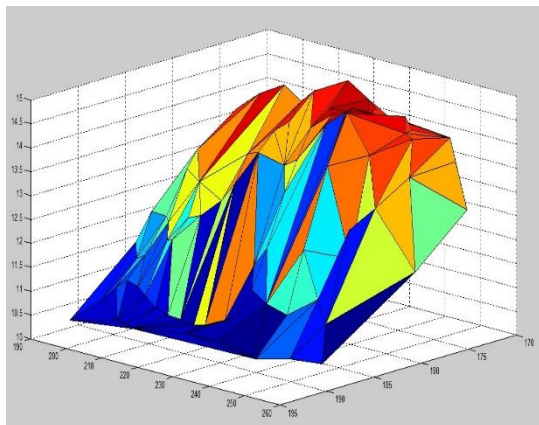


FIGURE 8 TIN of dense points

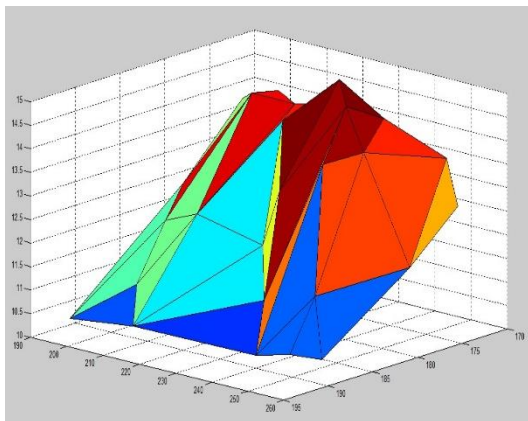


FIGURE 9 TIN of sparse points

The twenty-nine points which can reflect ground feature roughly was interpolated by TPS and the number of interpolation points is one hundred and twenty-one. As shown in Figure 10. This number made the number of small triangle in TIN model after interpolating close to the number of small triangle in dense points' TIN model uninterpolated. The new TIN model was built on the one hundred and twenty-one interpolation points and twenty-nine feature points(as shown in Figure 11).The surface area was calculated and shown in Table 1.

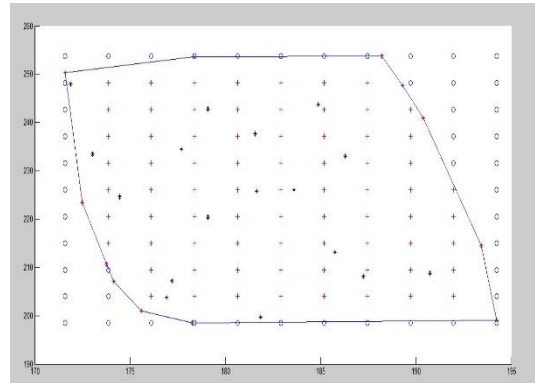


FIGURE 10 Scatter plot

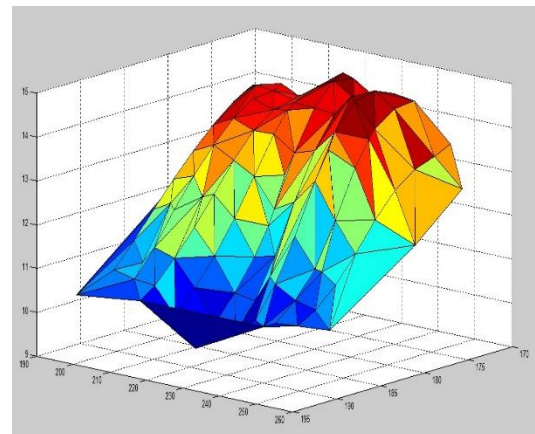


FIGURE 11 The new TIN

As can be seen from Table 1, the area based on less points is a lot less than the area based on more points. This is consistent with the feature of surface area calculation based on TIN. However, the number of feature points may not be large in actual measurement. So, the sparse points should be interpolated by TPS function. The difference between interpolated method and direct method using dense points just is 0.241m². It shows that the interpolation algorithm is feasible and it can reduce the workload of field data collection.

5 Conclusions

1) The method of irregular surface area calculation based on MATLAB is to use MATLAB to extract boundary of irregular land parcel surface and interpolate the sampling points by TPS function, then generate TIN model, finally

calculate area of irregular land parcel. This method has a comprehensive theoretical foundation and it is proved feasible by experiments. It can solve area-calculating problem in forest right confirmation better.

2) The irregular surface area-calculating method based on MATLAB just need to enter the measured feature points file and select the appropriate number of interpolation points. It's easy to use and has high degree of automation in the industry.

3) In the case measured featured points can reflect the basic topography of target area, calculation accuracy can

meet the requirement of practical work when the number of interpolation points is about 4 times as the number of measured feature points. This decreases about four-fifths of the workload outside the industry, greatly improved work efficiency.

Acknowledgements

The work was supported by the fund of the Priority Academic Program Development of Jiangsu Higher Education Institutions (PADP).

References

[1] Jiang F, Lv X-h, Wang Z-l 2005 The Analysis of DEM Surface Area Based on Composed Calculus Algorithms *Journal of Institute of Surveying and Mapping* 22(4) 263-5

[2] Yu J, Lv P, Zheng C 2010 A Comparative Research on Methods of Delaunay Triangulation *Journal of Image and Graphics* 15(8) 1158-67

[3] Li M, Zhang X-l 2010 Research on the Algorithm of TIN Building and its Application *Geomatics & Spatial Information Technology* 33(2) 44-5

[4] Li L-s, Zhang Y 2012 Spatial Interpolation Method of the Meteorological Factor In Northeast China Based on GIS *Meteorological and Environmental Research* 3(3-4) 23-5, 33

[5] Sun H-y, Ding D 2005 Thin plate spline and mathematic description of complicated surface *Engineering Of Surveying And Mapping* 15(2) 7-8

[6] Zhang Z-y 2010 MATLAB Tutorial: R2010a *Beijing university of aeronautics and astronautics press*

Authors	
	<p>Jiahzu Zheng, born in 1971, Jiangsu Province of China</p> <p>Current position, grades: associate professor.</p> <p>University studies: PhD degree was earned in major of surveying and mapping, Nanjing Forestry University in 2012.</p> <p>Scientific interest: GPS principle and its application in forestry engineering, the application of civil engineering, precise engineering survey.</p>
	<p>Yehemin Gao, born in 1992, Anhui Province of China</p> <p>Current position, grades: student.</p> <p>University studies: postgraduate studies in major of surveying and mapping engineering, Nanjing Forestry University.</p> <p>Scientific interest: GPS principle and its application in forestry engineering, the application of civil engineering, precise engineering survey.</p>

Application of computer virtual reality technology in ship equipment assembly

Ying Wang

Jiangsu Maritime Institute, Jiangsu, 211107, China

Corresponding author's e-mail: wyyingw@163.com

Received 12 September 2014, www.cmmt.lv

Abstract

It is known to us all that in factors of determining shipbuilding cycle, ship assembly occupies an important position in shipbuilding. In traditional shipbuilding model, front-line workers conduct assembly according to the two-dimensional drawing of marine designer. They will make mistakes inattentively, which results in the waste of manpower and material resources. At the same time, the abstraction of drawing will tend to generate deviation in the communication system between designer and ship-owner because of no concrete model object. This paper adopted a kind of technology that could use three-dimensional entity form to express ship model and assembling process-ship virtual assembly technology. The combination of virtual reality technology and ship assembly technology revealed the insufficient and defect in design, which avoided the waste of manpower and material resources during practical assembly. Through the selection and comparison of virtual assembly, we could optimize assembly technology, thus to convenient for the learning and execution of front-liner workers, enhance shipbuilding efficiency and shorten shipbuilding cycle.

Keywords: Virtual technology; Ship assembly; Digitalized shipbuilding; Three-dimensional model

1 Introduction

With the development of economy, land resources are increasingly shortening, thus varies countries in the world have converted their orientation to the ocean of rich resources. In order to occupy a place in the future resource competition, shipbuilding industry has become the basic industry that must increase development by each country. Since the modern times, the shipbuilding technology in our country makes progress year by year. However, compared with shipbuilding powerful countries, there still exist large gaps. Such kind of technology in China not only has long shipbuilding cycle, but also causes the ship-owner with less professional knowledge cannot reach a consensus with shipping firm because of the professionalization of drawing [1]. In the face of the existing problem of traditional shipbuilding industry, our specialists have constantly thrown themselves into the researches in these years. In the article Virtual Verification of Fishing Boat Total Design Scheme [2], Wang Ning from Dalian University of Technology conducted scientific research on special project "research on fishery energy conservation key technology and development of important equipment" relied on national public welfare industry. With the platform of CATIA, he studied the current situation and achievement about virtual simulation technology at home and abroad. Combined with the theory of man-machine engineering and took a fiberglass fishing boat for prototype, he conducted research and technological development on some subject matters in virtual verification process of total fishing boat design, which was benefit for promoting constant development and progress of ship design level. In the article Ship Equipment Information Management for Ship Design and Construction

[3], Wang Xuhui and Jiang Yiping conducted introduction on ship equipment in the process of total ship design and building. In addition, on this basis, they introduced the main content of informatization management of ship equipment information. Their research contents have certain referential significance on the promotion of ship enterprise competitiveness. In the article Construction and Implementing of Ship Equipment RCM Maintenance Architecture, Dai Daoqi broke through the traditional ship maintenance mode, and brought Reliability-Centered Maintenance (RCM) in Ship equipment maintenance [4]. Through continuous or periodic condition monitoring on the operation status of ship equipment, we drew a judgment on the running status of mechanical equipment and forecasted its developmental trend, thus to effectively guide maintenance activity. The innovation of its maintenance model avoided the limitation of ship planning periodical repair, which has greatly enhanced the efficiency and effectiveness of equipment maintenance, improved the reliability and usability of equipment and saved the cost ship equipment maintenance.

This paper proposed to conduct digitalized shipbuilding using virtual reality technology, and to display the assembly process of three-dimensional ship model in simulation platform. It has made up the inconvenient brought about by the two-dimensional drawing of traditional ship industry, and avoided the potential assembly conflict and defect in practical assembly. The solution on the shortage of the professional quality of front-line workers and the non-professional background of ship has provided new research orientation for shortening shipbuilding cycle and enhancing shipbuilding technology.

2 Virtual reality technology and its application status

2.1 DEFINITION OF VIRTUAL REALITY

Virtual reality technology is firstly put forward by American VPL Research Inc., which is the outcome of the combination of multiple advanced technologies, like computer, micro-electronics, simulation and sensor measurement. It

can constructs an environment that is same or extremely similar to real world by using calculator on computer, thus to have people communicate in virtual environment through virtual device [5, 6]. Virtual reality system is mainly made up of five parts: virtual engine, input/output device, software and database, user and task, of which virtual engine and I/O device are the core parts. They finish virtual task through the following composition relationship, as shown in Figure 1:

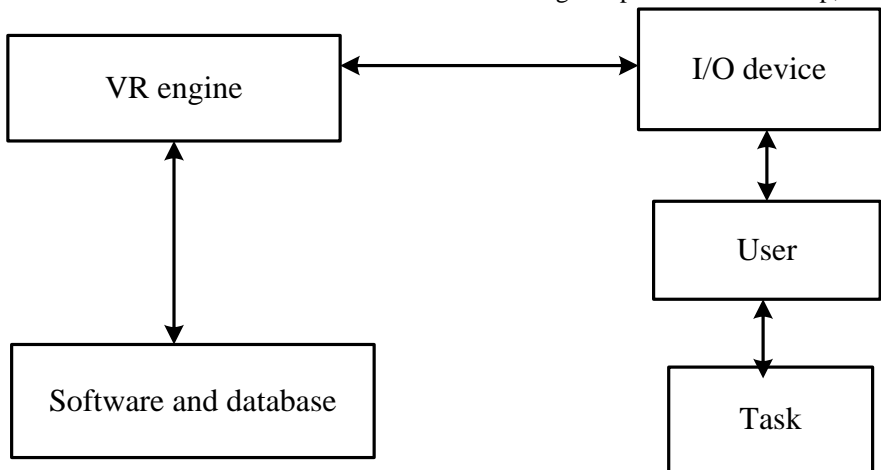


FIGURE 1 Constituent part of virtual reality system

2.2 THE APPLICATION OF VIRTUAL REALITY TECHNOLOGY IN ENGINEERING FIELD

The application of virtual reality technology in engineering industry mainly reflects in two aspects: product appearance structural design, and determination of the optimization of products assembly. The design of product appearance structure is also divided into three aspects: virtual manufacturing technology centered on design, virtual manufacturing technology centered on production and virtual manufacturing technology centered on control.

3 Ship assembly technology and digitalized shipbuilding technology

3.1 SHIP ASSEMBLY TECHNOLOGY

The hull is a complex structural body. In the process of ship building, assembly technology almost occupies half of the whole shipbuilding process, thus it is the key link of determining shipbuilding cycle. Traditional ship assembly is generally divided into preassembly, general assembly and shipway assembly. Each stage will appear some problems of rework caused by unqualified production design, wrong assembly sequence, etc, thus prolongs the whole shipbuilding cycle and cause severe waste of manpower and material resources. It is the vital disadvantage of the development of shipbuilding industry in today of resource shortage and competition intensification [7, 8].

In order to shorten shipbuilding cycle and reduce shipbuilding cost, shipbuilding industry strives to make a breakthrough in assembly technology. Based on foreign advanced shipbuilding technology and combined with practical status of China’s shipbuilding industry, we conducted practical analysis, experience summary, etc, and

conducted constant technology improvement on shipbuilding. According to the differences of shipbuilding model in each stage, China’s shipbuilding model is roughly divided into traditional shipbuilding model, modern shipbuilding model and future shipbuilding model.

3.2 DIGITALIZED SHIPBUILDING TECHNOLOGY

Digitalized shipbuilding technology refers to comprehensively applied informatization technology, advanced digitalized manufacturing technology, advanced shipbuilding technology and modern shipbuilding model to each stage and aspect of whole life cycle, like ship design, manufacture, test, experiment and management and maintenance, under the premise of integrated various of knowledge during shipbuilding and with digitalized modeling and simulation for light spot.

It can be said that, in recent years, no matter the civil ship or military ship, digitalized shipbuilding technology has played an important role in method and tool of ship design. It plays powerful effect, especially in improving quality, lowering cost and shortening delivery time. The future shipbuilding industry belongs to digitalized shipbuilding technology, which determines the success or failure of shipbuilding enterprise reform in a certain extent.

4 Establishment of three-dimensional model of marine engine room subsection

4.1 APPROACHES AND TOOLS OF THREE-DIMENSIONAL MODELING OF MARINE ENGINE ROOM SUBSECTION

Among world shipbuilding field, the earliest ship drawings were all hand painted, which were not only of heavy workload and low efficiency, but also consumed a mass of

manpower and material resources for amending when error appeared. To a large extent, it prolonged the cycle of shipbuilding and hand drawing was not benefit for technology. Shipbuilding industry began to get rid of the era of hand painted drawings until the appearance of CAD/CAM system software.

The reasons why CAD is widely applied to shipbuilding industry are that, on the one hand, with the rapid development of science and technology, many new technologies have integrated into various software systems. A series of design software like CAD has made ship design more simple and convenient and ship design ideas wider. On the

other hand, compared with traditional design approaches, CAD software is more intelligent, efficient and environmentally friendly.

SB3DS ship body design software independently researched and developed by Shanghai technical study based on CAD/CAM system was adopted in this paper for modeling. This software has added many new functions based on the intrinsic function of CAD. Especially on the design of ship piping system, the behavior of Sb3ds was extremely outstanding, which has basically solved the problem of difficult piping system design. The specific module function of Sb3ds is shown in Figure 2:

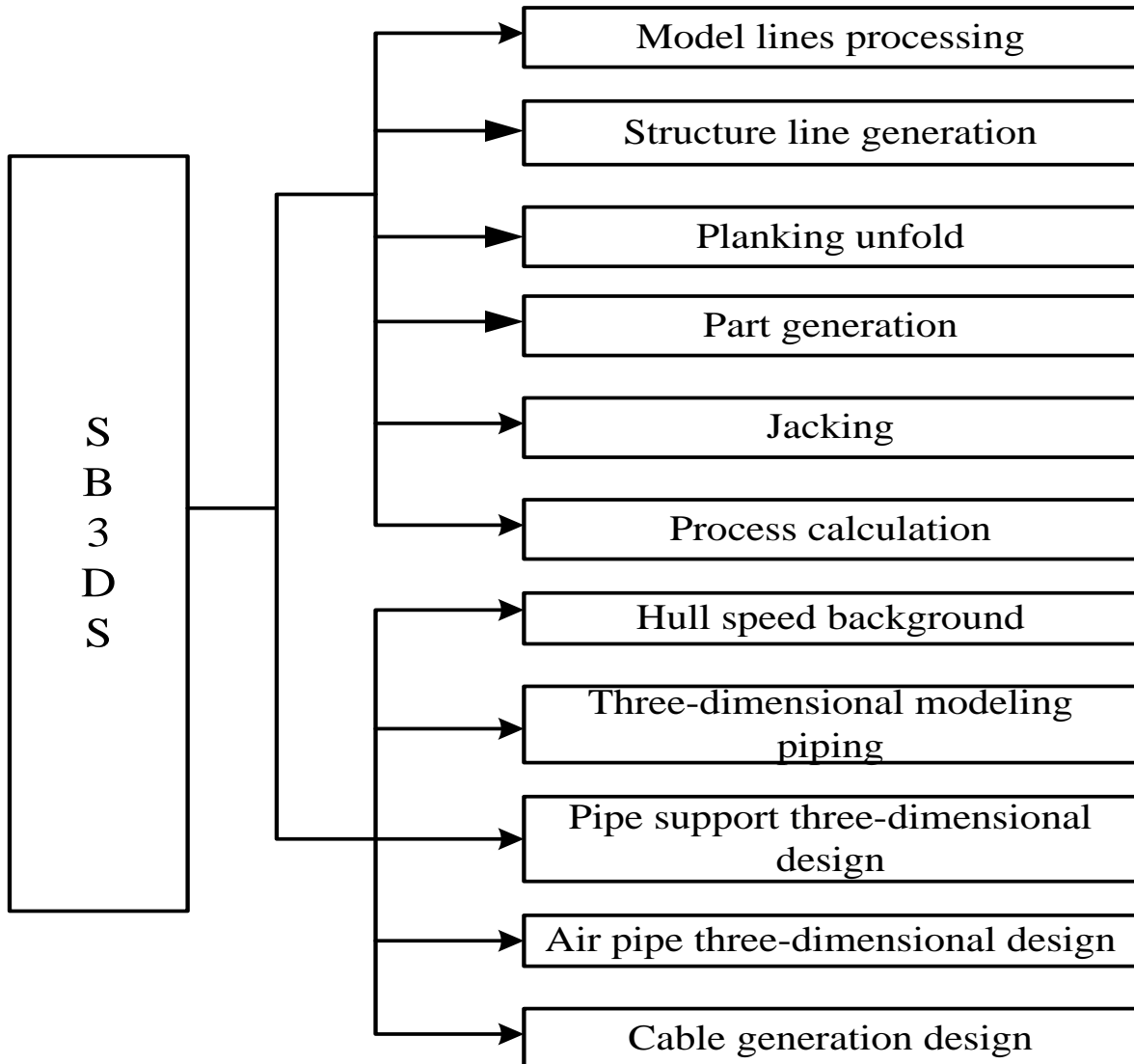


FIGURE 2 Sb3ds system module structure

4.2 MODELING PROCEDURE

In the initial stage of modeling, according to the marine engine room structure and operating principle of ship design drawing, and the relation of their mutual position, we did a full understanding on the cohesive relation among equipment parts and preliminarily planned modeling approach.

Then we obtained the chartlet of hull, equipment and piping system by photographing or other methods. In addition, we established model in3dsmax and conducted animation. At last, we imported the established model and animation to VRP for further optimizing process, thus to make it more vivid. The modeling process is shown in Figure 3:

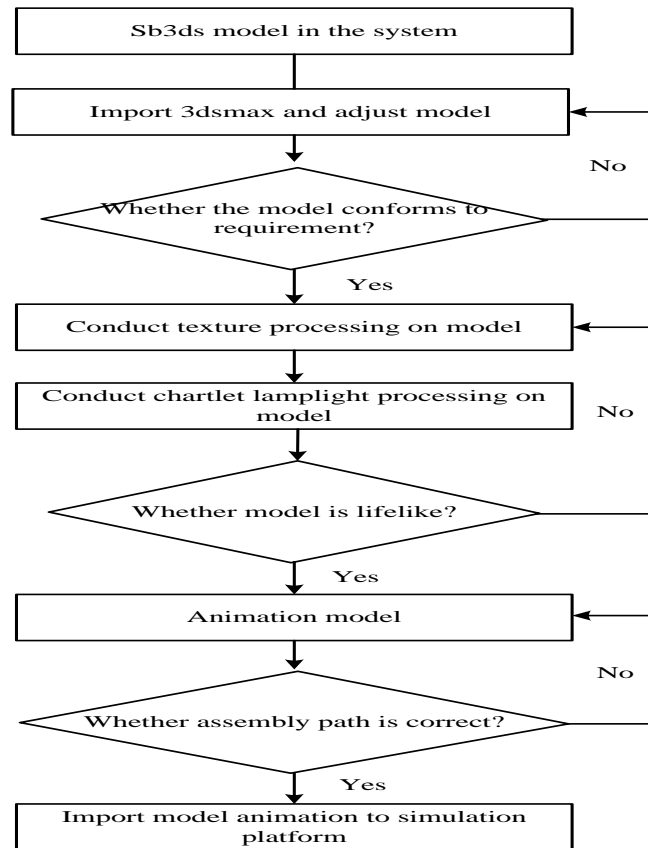


FIGURE 3 Flow chart of modeling

5 Conclusion

With the development of ocean industry economy, and in order to take the lead in the future ocean resource development, countries compete against each other and put lots of research and development technologies into shipbuilding industry. Though China has made great progress in this aspect, but compared with world shipbuilding power, the gap is still large. In order to keep up with or even surpass world shipbuilding power, we must increase the application of informatization technology and realize digitalized shipbuilding. The powerful effect of virtual reality technology

also appears in other fields [9]. Therefore, the adoption of virtual reality technology is imperative. Through the analysis on the existing problems of digitalized shipbuilding technology and traditional ship assembly technology, this paper put forward the necessity of the application of virtual assembly technology in shipbuilding industry, designed the technical lines and implementation procedure in virtual assembly simulation process. To a large extent, they have provided referential experience and practice reference for China’s shipbuilding enterprises, and played powerful impelling action on the booming of China’s shipbuilding industry.

References

[1] Xu Y C, Li M M, Feng Y 2010 Status Analysis of China’s Shipbuilding Industry *Internet Fortune* (5) 62-63
 [2] Wang N (2013); Virtual Verification of Fishing Boat Total Design Scheme *Dalian University of Technology* 5 1
 [3] Wang X H, Jiang Y P 2012 Ship Equipment Information Management for Ship Design and Construction *Ship & Boat* 23(6) 78-82
 [4] Dai D Q 2014 Construction and Implementing of Ship Equipment RCM Maintenance Architecture *Ship Standardization Engineer* 3(2)
 [5] Harrison G W, Haruvy E, Rutstrom E 2011 Remarks on Virtual World and Virtual Reality Experiments *Southern Economic Journal* 78(1) 87
 [6] Falloon G 2010 Using Avatars and Virtual Environments in Learning: What Do They Have to Offer? *British Journal of Educational Technology* 41(1) 108
 [7] Liang Z Y 2011 Gorgeous turns of Korean Shipbuilding Industry, *China Ship Survey* (4) 54-58
 [8] Kong P 2011 Study on the Virtual Simulation of Ship Controllable Pitch Propeller Manipulation *Xiamen: Jimei University*
 [9] Ying X D 2010 Implementation of Computer Virtual Reality Technology in Conceptual Design *Wireless Internet Technology* (1) 29-50

Author



Ying Wang, born 1982, Hubei Province of China

Current position, grades: lecturer

University studies: Master’s degree was earned in major of marine engineering, Jiangsu University of Science and Technology in 2007.

Scientific interest: ship engineering

Ecological architecture system based on landscape ecology

Fengquan Ji, Yuanyuan Jia

College of Architecture & Urban Planning, Anhui Jianzhu University, Anhui, 230022, China

Corresponding author's e-mail: jfqxdp@163.com

Received 10 October 2014, www.cmnt.lv

Abstract

This paper briefly summarized the concept of landscape ecology and ecological architecture and the current research status of ecological architecture both at home and abroad. It also analyzed ecological architecture system based on landscape ecology, and studied the construction of ecological architecture from the aspects of the construction of ecological architecture system and space structure. In addition, this paper reviewed with the green building demonstration in University of Logistics for instance.

Keywords: landscape ecology, ecological architecture

1 Introduction

Ecological environment crisis has become a worldwide problem, especially in developing countries. Due to the weak ideology on sustainable development, the pursuit of economic and social benefits at the cost of wasting ecological environment resource, and the ignorance of the natural environment and resources protection, it is increasingly threatening the survival and development of human society.

The principle of landscape ecology is adopted to bring natural ecosystem and landscape planning into architectural planning, thus to change the traditional planning and design mode and build ecological architecture. In ecological architecture, ecological corridor serves as a link and connects with relatively independent landscape patch, thus continuous and perfect ecological network is embedded on the basis of ecological architecture and the natural skeleton of architecture is formed. Ecological architecture with functions like natural ecological service, reasonable development of ecospace, etc has become one of the trends of current architecture development.

2 An overview of landscape ecology and ecological architecture

International association for landscape ecology defines landscape ecology as: landscape ecology is the researches on the change of landscape space of different scales, which include analysis of biology, geography and social cause of landscape heterogeneity. It mainly studies the relation among landscape spatial pattern, landscape pattern and ecological process, the influence of human activity on pattern, process and change, the function of scale and interference on landscape. Landscape ecology refers to bring landscape into ecology, and to combine the “horizontal” analytical method for representing space adopted by geographer and “vertical” analytical method for representing function used by ecologist, thus to study the influence of landscape space structure and morphological characteristics on biological activity and human activity [1]. The main research objects of landscape ecology are shown in Figure 1.

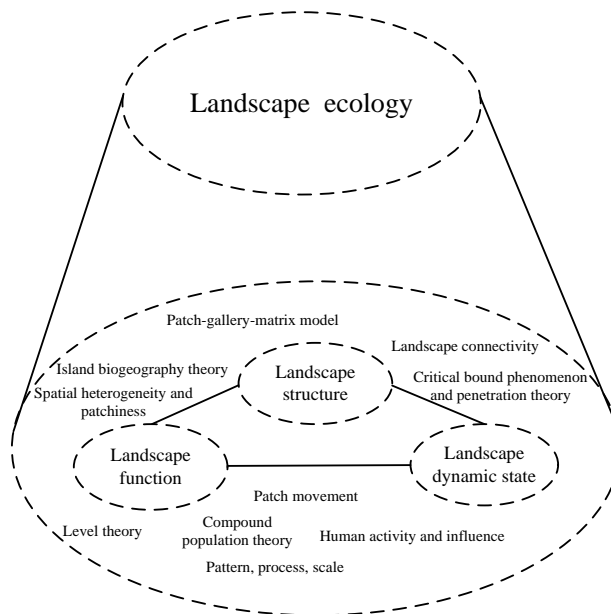


FIGURE 1 Main research subject of landscape ecology

Ecological architecture refers to use the basic thought and technological means of ecology and architectural technology science based on the basic principle of harmonious development of man and nature, thus to coordinate the relationships among human, architecture and natural environment and to make them become an organic coalition. Ecological architecture is the combination of artificial beauty and natural beauty [2].

Principle of landscape ecology is brought into the planning and design of ecological architecture. By means of improving the landscape structure of architecture and reasonably setting the number of landscape elements like patches, gallery, matrix, etc and their spatial distribution, principle and method of architectural material is integrated with ecological architecture for research. Stress on the rationality of spatial structure and environmental protection property of architecture material can more effectively enhance green structure function and environmental quality of residence zone.

3 Overseas and domestic research status

3.1 APPLICATION PRINCIPAL IF WIRELESS SENSOR IN MIDI PRODUCTION

Ecological architecture is the option and response of architecture to positively meet the challenges of sustainable development and to cope with energy crisis and ecological crisis. Compared with China, foreign countries have experienced

long time of theoretical researches and practical explorations on ecological architecture, and they have obtained plenteous achievements. However, the development degrees of researches in various countries are different. Theoretical research and time exploration of ecological research in China is later than developed countries for at least 10 to 20 years. Research statuses of ecological architecture at home and abroad are shown in Table 1.

TABLE 1 Research statuses of ecological architecture at home and abroad

Country	Research status
Germany	In the 1970s, architecture, college scientific institution and ecological protection organization carried out effective cooperation on theoretical research and practical exploration of ecological architecture. In architecture design, recently various of developed energy-saving technologies and equipments have been extensively used; progress of many researches and experiments have become the frontier in this field, like water-saving architecture, solar energy utilization, treatment of domestic sewage, etc; in addition, for the formulation of laws and regulations in aspects like the application of architecture materials, architecture heat insulation, energy-saving technology, Germany has become the leading country in aspects like ecological architecture research, design, development of energy-saving technology, formulation of laws and regulations, etc.
Japan	Japan is the country that comparatively earlier adopting recycle water technology. It is always engaged in researches of architecture research system of maximize space and extremely reliable that are obtained with minimum energy consumption.
America	Silent Spring (1962): initially awakened human strong awareness of earth ecosystem and environment; Design with Nature (1969): first put forward the application of ecology and ecological design method in research of urban planning and environmental evaluation; in 1995, green architecture committee put forward a set of Questa Vanguard Program of energy and environment design, and its version of 2.0 was released in 2000; in 1999, architects association selected ten blocks of local architectures as examples of ecological architecture creation at present stage for popularizing ecological architecture. Energy and environment design guideline is put forward in the evaluation of ecological architecture, a set of self evaluation system, which is used for the construction of commerce of newly built and built, public buildings or high-rise residence, including six items of evaluation. Namely sustainable development scene, energy and atmosphere, water efficiency, indoor environmental quality, material and resource, innovation and design.
France	A kind of brand new idea of ecological residence will be published recently.
Canada	“green architecture challenge” is put forward in ecological architecture evaluation: total process is divided into two stages in four years, users regulate indicator weight and metewand according to local status, and develop GBTOO1 with features of regionalization, then input the feature and performance data of for evaluate architectures to GBTOO1, and then get the evaluation result of software automatic calculation. At present, at least 19 countries have involved in GBC process.
Britain	“Building research organization environmental assessment mode” is put forward in ecological architecture evaluation: then environmental mark provided by the system is suitable for marketable development project. At present, 15% to20% of Britain newly built office building market accept and participate the evaluation mode.
China	In the 1980s, the idea of ecological architecture burgeons in China; researches on architecture energy saving were mainly focus on energy-saving design, development and application of energy-saving product, green construction, etc; in recent ten years, our specialists have carried out studies on ecological urban planning, building energy conservation in hot in summer and cold in winter region, earth-sheltered buildings, solar house, etc, and held some ecological city construction forums.

4 Researches of the construction and spatial structure of ecological architecture system based on landscape ecology

Patch, gallery and matrix are the basic elements of landscape. Numerous green galleries intertwine and form network, so landscape ecology names this objective exist natural landscape phenomenon as ecology network. Ecological construction can make full use of natural resources, and construct a kind of healthy architecture that is suitable for living under the condition without destroying ecological balance. Within life cycle of whole architecture, ecological architecture also focuses on the production, transportation, design, construction, operation, maintenance and recycle of materials after demolition, etc of material equipment, thus to reduce its consumption and influence on environment [3].

4.1 ECOLOGICAL DESIGN OF ECOLOGICAL ARCHITECTURE

The basic principles of ecology include entirety and orderliness, cyclic regeneration, mutually reinforcement and neutralization of each other, self-regulation and layer

transfer, and promotion. Ecology has provided theoretical basis for ecological architecture, generated new mode of thinking and research method, which mainly reflected in the following aspects: intention of coordinating relationship between human and nature; ecological architecture and its existing environment is an organic whole; it is a segment of whole ecological environment; ecosystem of the architecture has certain abilities of self regulation; ecological architecture should make the whole ecological ecosystem in balanced status of virtuous cycle. Therefore, ecological architecture has the characteristics of strong system idea and whole awareness, high energy usage efficiency, no pollution and flexible adaptation.

4.2 RESEARCH ON LANDSCAPE PATCH OF ECOLOGICAL ARCHITECTURE

The location, size, shape and amount of patch have influence on the network distribution of patches in ecological architecture. Fu Man divides the most common landscape type into four types: residue patch, interference patch, resource type patch and artificial patch.

The network node of ecological architecture is generally

made up of artificial and natural patches together. Combined with the classification method of ecological patch in ecology and according to the distributed location of ecological element, the network node of ecological architecture is divided into three types: cross type, affiliate type and independent type. In addition, due to its different performances, node also can be divided into native type, symbiotic type and regenerative type [1]. Cross type node is the ecological patch node that locates in ecological venation

overlapping areas; affiliate type ecological node refers to node that adhere to the ecological gallery context in ecological network system, and the most common type is the greenbelt or woodlot beside the road; independent type ecological network node refers to the natural ecological patch that is not in ecological venation overlapping area, nor adhere to ecological venation. According to the different node performances, the corresponding planning proposals are shown in Table 2:

TABLE 2 Planning proposal under different ecological network node

Types of ecological network node	Planning proposals
Cross type	Native type: increase ability to withstand interference, properly enlarge scope of patch node, and set relief area for protecting the living condition of original inhabit species within landscape patch nodes. Symbiotic type: center on maintaining the stability of original species living condition within nodes, and to have certain degree of integration with its staying venation under the premise of guarantee the heterogeneity. Regeneration type: mainly consider the temporary habitat features of migration species in venation.
Affiliate type	Native type: select venation that is similar or not conflict to ecological situation to adhere to, and not bring into competitive species and interference species. Symbiotic type: increase the variety and heterogeneity of species at the same time of considering the original ecological stability of node patch. Regenerative type: establish brand new environment that fit in with the type and attribution of venation
Independent type	Pay attention to the reasonable combination arrangements of native, symbiotic and regenerative type, to keep proper distance with other ecological components.

4.3 RESEARCH ON THE GALLERY VENATION OF ECOLOGICAL ARCHITECTURE

Gallery is differing from the linear or strip landscape elements of the surrounding landscape matrix. In ecological architecture, gallery not only has the ecological service functions of protecting biological diversity, species habitat, species

distribution and species filter, but also should have the function of resident’s leisure, recreation, regulation, etc. It is mainly made up of ecological elements like vegetation, water body, etc. Landscape ecological gallery can be divided into linear gallery, strip gallery and riverway gallery. Its planning construction proposals [1] are shown in Table 3.

TABLE 3 Construction proposals under different gallery venation types

Gallery venation types	Proposals of gallery venation construction
Water body venation	Graphic design of water body: first, not to destroy natural conditions; second, to keep the natural curve of waterway as much as possible; in addition, to keep the bottom of waterway maintaining natural status as much as possible; final, as far as possible to promote the intercommunication of water body ecological venation. Section design of water body: under the basis of not destroy the natural distribution of river, to recover the integrity of cross section of river.
Vegetation venation	Road ecological gallery: to pay attention to lower the side effects on ecological system division. Through the construction of green gallery on both sides if traffic line, to improve the functions like transportation, zoology, service, etc of road gallery. Strip greenbelt gallery: first choice for regional vegetation, and consider the elements of strip greenbelt of different level, size, function, etc; pavement design should select flooring of good differential permeability so as to guarantee the continuity of venation.

4.4 RESEARCH ON THE SPATIAL STRUCTURE OF ECOLOGICAL ARCHITECTURE

The planning and construction of ecological architecture are considered from multiple aspects, levels and dimensions and studied from spatial structure. According to planning structure and planning of green spaces system of ecological architecture, its spatial structure is divided into core type,

axis type and complex type of ecological network structure. These three types of ecological network structures are divided respectively centered on the ecological matrix dot form and group form ecological elements, linear and strip form ecological elements and dot, linear and strip form compound ecological elements. The corresponding construction proposals are shown in Table 4.

TABLE 4 Construction proposals under different ecological network structures

Types of ecological network structure	Construction proposals
Core type	Location: construct according to the angle of city and region. Scale: reasonably allocate core type landscape patch and scattered small scale landscape patch. Shape: partially present many tentacle shape, but on the whole present structured and closeness shape Number: if conditions permit, we can construct multi-core landscape patches
Axis type	Location: plan as a whole and consider the construction of landscape ecological gallery in city and region, and galleries must be continuous. Scale: under the basis of meeting minimum width, it would be better if the scale is wider. Shape: it is not proper for excessive straight or curve, and to shape according to the double need of ecology and landscape shape. Number: under the basis of meeting the basic function requirement, it would be better if the number is larger.
Complex type	Location: combine with the layout of region and city ecological network, to reflect the construction of strategic point and city gallery. Scale: to level “point” and “axis”, and meet the dual factors of ecological effect and social effect. Shape: start from the double perspectives of landscape ecology and urban design, set “point” as to maintain partially present many tentacle shape and totally present structured and closeness shape, set “axis” as to avoid straight type, and mainly in curve type. Number: to set as much as possible.

5 Cases

The green building demonstration in University of Logistics is located in the southwest of new campus in University of Logistics of university town in Chongqing. It is leaning against Jinyun Mountain. The original ecology vegetation around the site is better. It is the building complex that integrates teaching, work, reception, etc together. The total area is 11609 m², five storeys aboveground and one storey underground. Figure 2, 3, 4 and 5 are respectively the surrounding mountain slope protection greening, slope greening that meet the basement lighting requirement, roof garden and south side outer wall vertical greening [4, 5]:



FIGURE 2 Massif slope protection greening around demonstration building



FIGURE 4 Roof garden



FIGURE 5 South side outer wall vertical greening



FIGURE 3 Slope greening that meet basement lighting requirement

This green demonstration building is belonging to one part of campus ecosphere. Greening pattern is coincident with the whole campus. In massif slope protection planning, slope greening is used to combine with roof greening, thus to create spatial level and good landscape effect. In the basement lighting, the application of slope greening not only obtains good atmospheric conditions of lighting, but also transfers flat greening into vertical greening. The setting of roof garden will integrate with the surrounding massif greening. Warm in winter and cool in summer fully embodies the role of heat preservation and heat insulation of roof greening. South side outer wall vertical greening makes an integration design of architecture maintaining structure,

sunshade component and vertical greening. At the same time of meeting shaded effects, it has fully considered model of construction elevation and requirement of picture composition [6].

6 Conclusion

Besides bringing us wealth and employment, the rapid growth of economy is also bringing us tremendous ecological environmental crisis. This paper took ecological architecture as research subject, and also applied landscape ecology. Through the organic combination of man and nature, sustainable development architecture with characteristics like energy saving and emission reduction, environment beautification and enhancement of people’s living comfort will come true. Started from green ecology, aimed at livability, and supported by effective engineering technology, the

new healthy architecture with advantages of maximizing environmental benefit, economical benefit and social benefit is the main development tendency of current ecological architecture. Based on the discussion of the ecological architecture of landscape ecology, this paper has provided certain theoretical bases and technical support for ecological architecture [7].

Acknowledgement

Key Project for Natural Science Fund of Anhui University (KJ2013A070).

Science and Technology Plan Project of Construction Industry of Anhui (2012YF-11).

Key Project of Teaching Research of Anhui (2012jyxm373).

References

[1] Li Guangyao 2009 Research of Community Ecological Network Construction and Spatial Structure Based on Landscape Ecology. *Liaoning: Northeastern University*.

[2] Tian Na, Li Yaguang, Tian Ying 2010 A Brief Study of the Development of Domestic and International Eco-architecture. *Journal of Central South University of Forestry & Technology (Social Sciences)*, 4(5) p.99-102.



[3] Liu Miaomiao 2013 Research on the Life Cycle Cost and Benefit of Ecological Architecture. *Shanxi: Xi'an University of Architecture and Technology*.

[4] Li Yuan, Hu Wangdu, Li Meng, Wang Jianqi 2013 Exploration on Integrated Design of Building Vertical Planting—Take the Green Building Demonstration in University of Logistics for Instance. *Chongqing Architecture*, 12(8) p.19-21.

[5] Sun Changhui. The Primary Investigation on the Combining Way of Vertical Planting and Building Integrated Design. *Huazhong Architecture*, 2012, (9) p.28-30.

[6] Hu Wangshe, Jiang Liyong, Xue Ming, Yuan Nan 2010 Practices of Campus Sustainable Building—Take the Green Building Demonstration in University of Logistics for Instance. *Journal of Logistical Engineering University*, 26(1) p.1-5.

[7] Huang Qiao 2013 Urban Green System Planning Overseas Based on Landscape Ecology—Take Kia County of Chongqing as Example. *Chongqing: Chongqing University*.

Authors	
	<p>Fengquan Ji, born 1976, Anhui Province of China</p> <p>Current position, grades: associate professor University studies: Master’s degree was earned in major of Landscape Architecture, Huazhong Agricultural University in 2004. Scientific interest: landscape ecological planning, city greening quality and quantity, urban green space system planning, water landscape, rural landscape</p>
	<p>Yuanyuan Ji, born 1989, Anhui Province of China</p> <p>Current position, grades: master student University studies: Bachelor’s degree was earned in major of urban planning, Anhui JianzhuUniversity in 2010. Scientific interest: city grass land planning</p>

Modelling and simulation of relationship between internal cell temperature and apparent resistivity for lithium-ion battery

X B Hong*, N Z Li, W W Yin, J H Feng, G X Liu

College of mechanical and automotive engineering, South China University of Technology, Guangzhou, 510640 China

Corresponding author's e-mail: mexbhong@scut.edu.cn

Received 22 August 2014, www.cmnt.lv

Abstract

Safety problems caused by thermal runaway have been restricting the popularization and application of power lithium-ion battery (LIB). As Electrical Resistance Tomography (ERT) method can potentially detect the variations of internal cell apparent resistivity influenced by temperature, the simulation of the relationship between the internal cell temperature and apparent resistivity is presented to monitor the thermal circumstance inside LIB cell. Using the linear interpolation functions, the LIB model is built and meshed. The appropriate boundary conditions are imposed to simulate the cell virtual heating process and ERT process. During the simulations, the distributions of the apparent resistivity at different temperatures are given. It is found that the correlation of apparent resistivity and temperature is well fitted by quintic function. Meanwhile, the evaluation of quintic fit under cell discharge reveals a deviation of 6.2K between the cell core temperature and the surface temperatures. The presented method cannot only be applied in thermal balance management, life prediction and load control, but also afford a possible way for monitoring the health of separator structure of LIB.

Keywords: lithium-ion battery model, thermal simulation, internal cell temperature, apparent resistivity

1 Introduction

The lithium-ion battery (LIB) cells with the advantages of high energy density and long cycle life have been the research hotspot of the new energy automotive technology [1]. With the rapid development of new energy vehicle, an increasing number of problems on the LIB cells are frequently occurring. As a result, the related cell performance test is highly valued. As the irregular change of internal cell temperature is the roots of many security problems, such as leakage, fire, explosion, and so on, the thermal security problems of LIB cells are urgent to be resolved.

There are many researches focusing on LIB cells temperature measurements, which mainly concentrate on developing numerical models of LIB cells to estimate the core temperature. Kim et al. [2] developed a model of LIB considering the possible internal thermal reaction, which was used in the temperature field simulation of small cylindrical LIB. Then the researchers investigated mutual effect between a battery cell of thermal runaway and another normal cell [3]. It is particularly gratifying that some novel advanced techniques have been generating in recent years. Srinivasan et al. [4] (2011) proposed an Electrochemical Impedance Spectrum (EIS) method to explore the correlation between the internal cell temperature and the phase angle of electrochemical impedance at a certain frequency. The method increases the accuracy of the temperature measurement without setting up additional external sensors and wires. Subsequently, Schmidt et al. [5] (2013) investigated the sensitivity of the method on temperature and state of charge (SOC). However, these current methods can only measure or estimate the overall internal cell temperature, but cannot effectively detect the local cell temperature, which is the essence of thermal safety problems of LIB.

Electrical Resistance Tomography (ERT) method is used to assess the internal structure conditions of objects,

and has been widely applied in many fields such as concrete structure investigation, two-phase flow detection and medical inspection. For example, Paulo et al. [6] performed three dimensional detection analysis of massive concrete in different conditions using the relative excitation. Rodgers et al. [7] studied the regional network model of fluid distribution of turbulent pipeline using the adjacent excitation. Though the ERT technique has been used widely in many fields, there is little research for condition assessment of LIB cells.

The feasibility of ERT method to investigate the distribution of internal cell apparent resistivity has been validated by the authors [8]. This study aims to explore the relationship between the internal cell temperature and apparent resistivity by simulating the cell virtual heating process and ERT process. For this purpose, a steel shell LIB cell model was built and the appropriate boundary conditions were applied. Then the distribution of the cell internal temperature distribution was achieved, as well as the apparent resistivity. Finally, the correlation of the temperature and the apparent resistivity was fitted and evaluated under cell discharge in experiments.

2 Modelling

2.1 HEAT GENERATION MODEL FOR LIB CELL

Sato et al. [9] have obtained the total heat Q generated from the LIB cell and Ni-MH cell in experiments. The results show that the heat from battery mainly contains four aspects, joule heat Q_j from ohmic resistance, side reaction heat Q_s from internal waste gas, heat Q_p from electrodes polarization, and heat Q_r from chemical reaction. Generally, heat release and heat absorption occur in charge and discharge. Under a certain temperature and pressure, a constant thermodynamic relation would exist in LIB cell, and the heat energy of chemical reaction equals to the change of standard

Gibbs free energy change ΔG of current described as follow,

$$\Delta G = \Delta H - T\Delta S, \tag{1}$$

where ΔH and ΔS respectively denote the enthalpy and entropy changes of chemical reaction, and T is the absolute temperature. As the processes of charge and discharge are reversible and the term $T\Delta S$ just represents the reaction heat Q_r , which can be further expressed as,

$$Q_r = T\Delta S = T\left(-\frac{\delta\Delta G}{\delta\Delta T}\right), \tag{2}$$

where

$$\Delta G = -nFE_e, \tag{3}$$

where n denote the charge number of chemical reaction, F indicates the Faraday constant and E_e is the electromotive force of reversible cells. Furthermore, Q_r can be deduced as,

$$Q_r = nFT\left(\frac{\delta E_e}{\delta T}\right). \tag{4}$$

In normal circumstances, side reaction of waste gas would not happen, namely $Q_s=0J$. Therefore, the total heat Q generated from charge and discharge can be expressed as,

$$Q = Q_r + Q_j + Q_p + Q_s = nFT\left(\frac{\delta E_e}{\delta T}\right) + I^2(R_e + R_p), \tag{5}$$

where R_e and R_p are cell ohmic resistance and polarization resistance. In practical, the heat generation rate q is used for evaluating the cell thermal performance as follow,

$$q = Q / V_b, \tag{6}$$

here, V_b is the volume of battery cell. It can be seen that Q and q both correlate with reaction heat, charge and discharge current and internal resistance. In order to accurately estimate the heat generation rate and total heat produced in cell operation, these three parameters just mentioned above should be known in advance.

2.2 TWO DIMENSIONAL FEM MODEL OF LIB CELL

The rationale of ERT technique can be explained by electromagnetism, and a two dimensional Finite Element Method (FEM) model in electromagnetic is used to solve some engineering matters. The main concept of the FEM is based on subdividing the geometrical domain of a boundary-value problem into smaller sub-domains, called the finite elements, and expressing the governing differential equation along with the associated boundary conditions as a set of linear equations that can be solved computationally using linear algebra techniques [10]. The nodal FEM will be applied to a generic 2-dimensional (2-D) Boundary Value Problem (BVP) in electromagnetic for LIB model. Specifically, a proper application of the FEM for the solution of 2-D BVPs must involve the following major steps:

- (a) Discretization of the 2-D domain.
- (b) Derivation of the weak formulation of the governing differential equation.
- (c) Proper choice of interpolation functions.
- (d) Derivation of the element matrices and vectors.
- (e) Assembly of the global matrix system.
- (f) Imposition of boundary conditions.

(g) Solution of the global matrix system.

(h) Post-processing of the results.

Here, three of the most important steps below are considered before the modeling.

Problem definition: A BVP characterized by a generic form of a second-order partial differential equation will be considered to illustrate the major steps involved in a 2-D nodal,

$$\frac{\partial}{\partial x}\left(\alpha_x \frac{\partial u}{\partial x}\right) + \frac{\partial}{\partial y}\left(\alpha_y \frac{\partial u}{\partial y}\right) + \beta u = g, \tag{7}$$

where α_x , α_y , β , and g are constants to be defined by the specific application and u is the primary unknown quantity. Poisson's equation, for a linear and isotropic medium, is given by

$$\nabla(\epsilon\nabla V) = -\rho_v, \tag{8}$$

where ϵ presents the dielectric constant, V denotes the fixed potential and ρ_v is the uniform electron volume charge density. In a 2-D space, Equation (8) is often written as

$$\frac{\partial}{\partial x}\left(\epsilon \frac{\partial V}{\partial x}\right) + \frac{\partial}{\partial y}\left(\epsilon \frac{\partial V}{\partial y}\right) = -\rho_v. \tag{9}$$

Equation (9) is a special case of the generic form given by Equation (7). Comparing these two partial differential equations would be identical if $u=V$, $\alpha_x=\alpha_y=\epsilon$, $\beta=0$ and $g=-\rho_v$. Consequently, the 2-D Poisson's equation, which is widely used to solve electrostatic problems, is a special case of Equation (7). The set of boundary conditions could be either of Dirichlet type

$$u = u_0 \quad \text{on } \Gamma_1, \tag{10}$$

or mixed type

$$\left(\alpha_x \frac{\partial u}{\partial x} \hat{a}_x + \alpha_y \frac{\partial u}{\partial y} \hat{a}_y\right) \cdot \hat{a}_n + \gamma u = q \quad \text{on } \Gamma_2, \tag{11}$$

where \hat{a}_n is the unit vector normal to the boundary Γ_2 and γ , q are constant to be defined.

Domain discretization: The domain of a 2-D BVP usually has an irregular shape. Using the FEM, the first step is to accurately represent the physical domain of the LIB model by a set of basic shapes. In general, a triangle is used instead of a rectangle as the basic element for the meshing of the 2-D domain, the discretization error would be effectively much smaller. A linear triangular element in the xy -plane is illustrated in Fig. 1(a). The triangle consists of three vertices which correspond to the three nodes of the element.

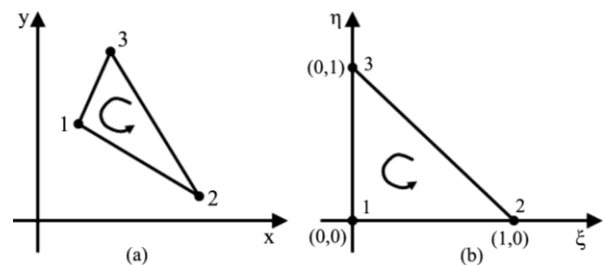


FIGURE 1 Linear triangular element respectively in the xy -plane (a) and (b) in the $\zeta\eta$ -plane.

Interpolation functions: The nodes are locally numbered in a counter-clockwise direction to avoid having a negative area using the Jacobian definition. This element has coordinate (x_i^e, y_i^e) , which correspond to local nodes $i = 1, 2$ and 3, respectively. A linear interpolation function spanning a triangle must be linear in two orthogonal directions. These could be the orthogonal axes defined by the natural coordinates ζ and η in Fig. 1(b). For isoparametric elements, the functions used to interpolate the space coordinates x and y can be described as

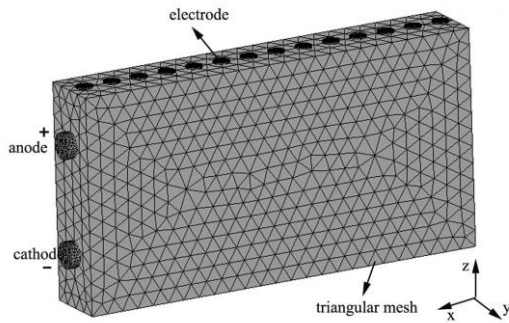
$$\begin{aligned} x &= x_1^e + \bar{x}_{21}\zeta + \bar{x}_{31}\eta \\ y &= y_1^e + \bar{y}_{21}\zeta + \bar{y}_{31}\eta \end{aligned} \tag{12}$$

where $\bar{x}_{21} = x_2^e - x_1^e$, $\bar{x}_{31} = x_3^e - x_1^e$, $\bar{y}_{21} = y_2^e - y_1^e$, $\bar{y}_{31} = y_3^e - y_1^e$.

2.2 STEEL SHELL LIB MODEL



(a) Physical photo of steel shell LIB



(b) LIB model

FIGURE 2 Investigated steel shell LIB with 14 electrodes arrayed on one sides

TABLE 1 Thermal performance parameters for mainly material models

Battery component	Material	Density[kg/m ³]	Specific heat[J/(kg·°C)]	Heat conductivity[W/(m·°C)]	Resistivity[ohm.m]
electrolyte	PC/DEC	2335	300	$\lambda_x=1.2, \lambda_y=1.5, \lambda_z=1.0$	10×10^{-3}
case	steel	7850	460	80	9.78×10^{-8}
electrode	Red copper	8800	381	386.4	1.8×10^{-8}

TABLE 2 Heat generation rates of LIB cells under different discharge rates and currents

Discharge rate [C]	Current[A]	Heat generation rate [W/m ³]
1.0	11	6335
2.0	22	19800
3.0	33	43345
4.0	44	75344
5.0	55	117725

The LIB cell with steel shell was investigated as shown in Fig. 2(a), which has a capacity of 10Ah, the maximum allowed discharge current of 40A and the internal resistance of 10mΩ. The cell size is 130*65*16.5mm³ and the weight is 0.4Kg. Discharge cut-off voltage is 2.7V at least and the maximum charge voltage is 4.2V at most. In the right one of the Fig. 2(a), 14 electrodes have been placed on one side of the battery. The electrode is made up of red copper, which size is 10*5*0.2mm³ and the distance between two adjacent electrodes is 9mm.

In order to synchronously produce the thermal field and the electric field, a two-dimensional hybrid model of the LIB cell is built using the ANSYS software and the mesh is divided by the linear interpolation function as discussed in Section 2. Fig.2 (b) shows the LIB cell model, which will be used in simulations below. In total, there are 14679 triangular meshes with 26132 nodes. Corresponding to Fig. 2(a), there are also 14 electrodes model placed on the cell model. The thickness of steel shell model is 0.6mm. In order to simulate the real conditions, red copper with higher conductivity than that of steel, is chosen as the cell electrode material.

3 Simulation and Analysis

3.1 THERMAL SIMULATION

The component of the LIB cell mainly consists of electrode (anode, cathode), electrolyte (mainly consists of Polycarbonate (PC) and Diethyl carbonate (DEC)), separator and cell case. Just as mentioned in Section 2, the cell internal heat mainly generates from four aspects, namely the joule heat of ohmic resistance, the side reaction of internal waste gas, the electrodes polarization and heat of chemical reaction. So the distribution of internal cell temperature can be determined by simulating with thermal specific parameters according to Table 1.

To comprehensively understand the change rule of the thermal field of the LIBs, the thermal simulation was performed to obtain the internal temperature distributions. During the process, the condition inside the LIB cell is considered as a homogeneous medium. The mass and specific heat capacity of the cell are constant and the thermal conductivity in x-y-z directions d keeps the same irrespective of the temperature and the cell capacity. The heat generation rate is consistent with a constant current in Table 2.

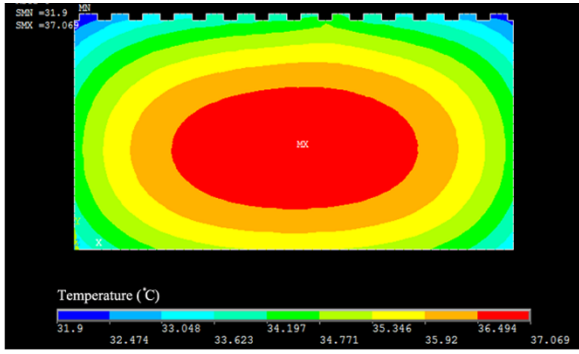


FIGURE 3 Internal cell temperature distribution in thermal simulation during discharge

In simulation, the environment temperature was set at 20°C, the battery model was discharged with the current of 1.0C discharge rate. The temperatures were recorded as the core temperature rising up 3°C. Due to the heat diffusion and convection on cell surface, the internal cell temperatures tend to be a gradient distribution. Fig.3 shows the distribution simulating at 15minutes. During the period, the internal cell temperature rises up rapidly, and the heat diffusion and convection are prominent. The internal temperatures apparently and gradiently distribute with the depth. The red area represents the highest temperature of 37°C, and the blue region represents the lowest temperature of 32°C. It is obvious that the temperatures in central place are higher than that in the verge of the cell.

3.2 ERT SIMULATION

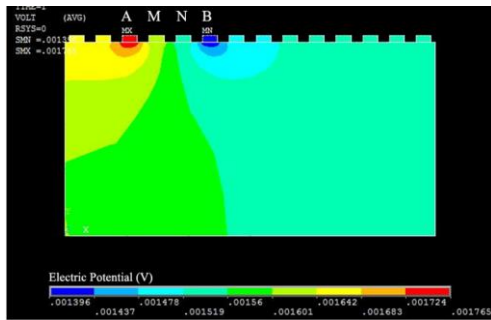


FIGURE 4 Transient of ERT simulation with four electrodes

It's important to note that the ERT simulation was performed simultaneously with the thermal simulation. The model parameters of the material resistivity were set in terms of Table 1. The boundary condition of excitation current I was set at 0.5mA. Before the simulations, the Wenner configuration

was chosen to excite the model. Four electrode models with a spacing of 9mm were selected to excite and measure respectively. Just as described in Fig. 4, four electrodes from the third to the sixth in the left were chosen to work, in which the bipolar pulse currents at a certain frequency were imposed on electrodes A and B. As a result, a stable electric filed is gradually produced, which is described with a variety of color ribbons in the figure. Then, the electric potential of electrodes M and N was recorded. After one set of measurements finishes, another four electrodes would be selected to repeat in the same way. The recorded electric potential difference ΔU between the electrodes M and N can be transferred into resistivity data as

$$\rho = K \frac{\Delta U}{I}, \tag{13}$$

where K is the geometrical factor.

In total, four layers including twenty six data points can be obtained, which have a gradient distribution with the depth. Fig.5 shows the distribution of the apparent resistivity. It seems that the ERT method divides the internal complex structure of a battery cell into four independent levels. Each level, depending on the number of electrodes, can be further subdivided into many simple model blocks with the total number of thirty eight. The effective blocks determined by datum points would be constructed into images of apparent resistivity distribution.

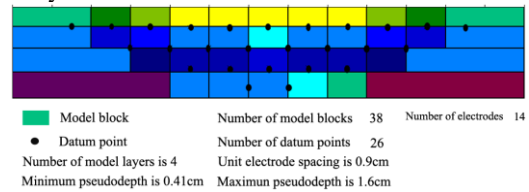


FIGURE 5 Arrangement of model blocks and datum points

Then, the distribution of the apparent resistivity at different temperatures can be achieved by the least square algorithm, which is used to reconstruct the inversion image of complex structure conditions of the objects. Fig.6 describes the apparent resistivity distribution respectively at 25°C and 30°C for LIB cell model. The two images reflect the changes of the apparent resistivity with the temperatures. It can be found that the apparent resistivity significantly distributes with the depth, more importantly, the color ribbons of same region exist obvious discrepancy with temperature. It is suggested that the relationship between the apparent resistivity and temperature can be inferred by the difference. The further analysis of fit results will be demonstrated.

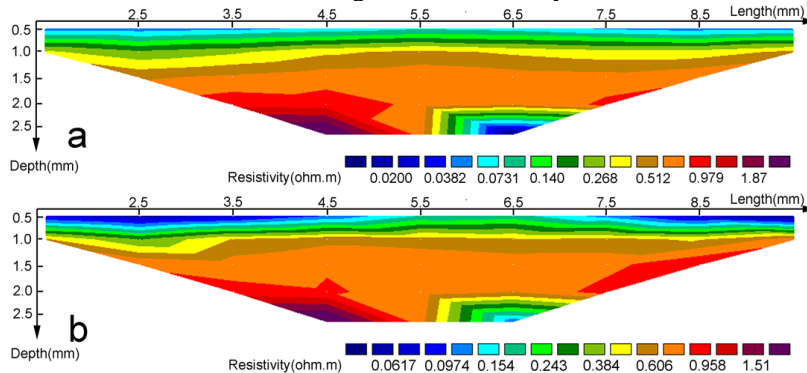


FIGURE 6 Apparent resistivity distribution of LIB cell at respectively at 25°C (a) and 30°C (b)

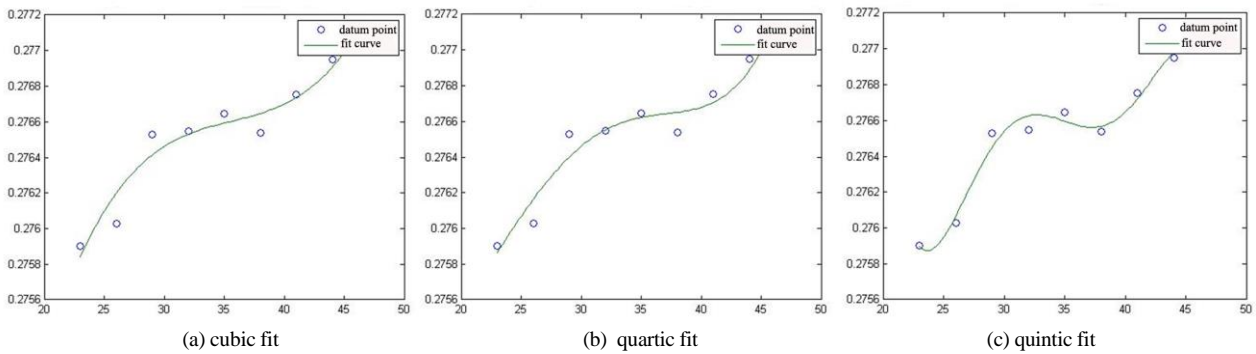


FIGURE 7 Fitted results with three different fitting methods

3.3 FITTING ANALYSIS

At the end of the simulations, the internal cell temperatures approached to 45 °C, and a set of data of the apparent resistivity and temperature has been obtained. Due to the attenuation of current density in cell deeper region, the apparent resistivity value would tend to increase up with the depth. However, the apparent resistivity value of the same depth would remain in a smaller range. Therefore, one set of the data in the first layer was chosen to analyze at first. In order to seek the relationship between the apparent resistivity and internal cell temperature, the data was fitted respectively by polynomial functions.

Here, the scatter plots of the data are presented in Fig. 7. Each data in the graphs is the average value of ten independent simulations. It can be inferred that the apparent resistivity substantially increases with the temperature rises up. This law also can be found in other data at different depth. Furthermore, it suggests that the internal cell temperature can be determined by the apparent resistivity via a certain function.

Therefore, the correlation of internal cell temperature and apparent resistivity is fitted by three different fitting functions, which are cubic fit, quartic fit and quintic fit. It can be seen that the fitting effect of the quintic fit, which has a lower mean square error of 3.06e-04, gets better than that of other two fits, 3.38e-04 for (a) cubic fit and 3.37e-04 for (b) quartic fit. As a result, this quintic function can be considered as a preliminary principle for the correlation under simulation conditions,

$$\rho = a_0T^5 + b_0T^4 + c_0T^3 + d_0T^2 + e_0T + f_0 \tag{14}$$

Herein, a_0 , b_0 , c_0 , d_0 , e_0 and f_0 are the fitted coefficients.

4 Evaluation under cell discharge

Usually, the core temperature would get higher than other regions in LIB cell. Evaluating the core temperature makes sense for thermal management of LIB cell. Meanwhile, in order to evaluate the quintic fit results, apparent resistivity measurements were performed under cell discharge. The experimental set-up can be seen in the Fig.8. Using the quintic function, the cell core temperature T_{core} can be determined. As there is no effective method of internal cell temperature measurements as a reference for ERT results, the calculated results will be compared with cell surface

temperatures, namely T_{top} and T_{bottom} .

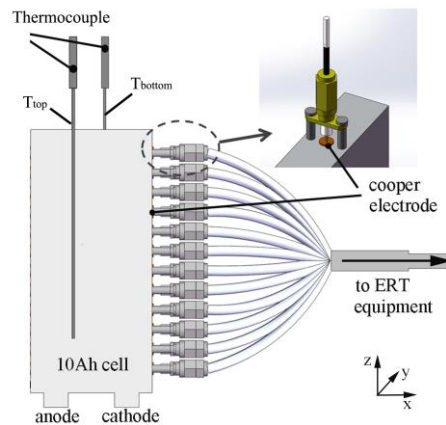


FIGURE 8 Diagram of experimental set-up

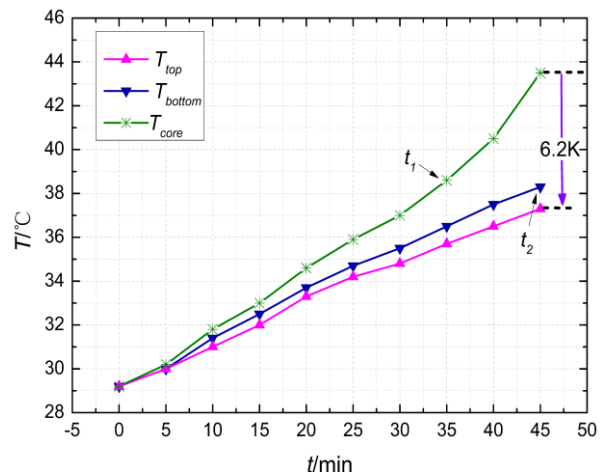


FIGURE 9 Comparison between core temperature and measured surface temperatures during LIB cells discharge (right). The initial ambient temperature was set at 30°C. Surface temperatures on top and bottom of the cell were measured with thermocouples type K

As can be observed in Fig.9, the core temperature T_{core} determined by apparent resistivity rises un normally, and do not coincide with the measured surface temperatures T_{top} and T_{bottom} especially as times goes on. After cells discharge, the core temperature reaches the highest of 43.5°C, which is 6.2K higher than T_{top} . In some degree, this is approximate to the results from a similar experiment conducted by Schmidt [5]. Meanwhile, the two surface temperatures are also not equal with each other. The temperature of top surface with 37.3°C would be almost 1k lower than that of

bottom surface. In some case, an inhomogeneous distribution of internal cell temperature is the root of the surface temperature difference. In detail, the great temperature difference could result in a great delay for heat transfer. For example, there is a delay of almost 10 minutes when T_{core} reaches to $T_{surface}$ at t_1 . This underlines the importance of local cell temperature, as already described in the Introduction.

5 Conclusions

This article first put forward the ERT method as a potential solution to measure the internal cell temperature for LIBs, which can be realized by the determination of the apparent resistivity on temperature. The correlation of apparent resistivity and temperature was effectively investigated by FEM simulation on steel shell LIB model.

The distribution images of the apparent resistivity indicate that the internal cell temperature significantly affects the apparent resistivity. This effect can be described by quintic fitting curve, which has been evaluated under cell

discharge. The results also reveal that the core cell temperatures significantly deviate about 6.2K from the surface temperature measured by external sensors in this experimental study. But further improvements of accuracy of this method in experimental circumstance are challenging and will have to be the subject of future works. In general, the presented method cannot only be applied in thermal balance management, life prediction and load control, but also afford a possible way for monitoring the health of separator structure of LIB cell.

Acknowledgments

The authors thank for the support from the National Natural Science Foundation of China (NSFC) under grant No.51305141 and Guangdong-Hongkong Technology Cooperation Funding under grant No.2012A090200005 and Fundamental Research Funds Program for the Central Universities under grant No.2014ZG0016.

References

- [1] Khare, Neeta, Rekha 2008 Modeling automotive battery diagnostics *Power Electronics Technology* **34**(3) 36-41
- [2] Kim G H, Pesaran A, Spotnitz R 2007 A three-dimensional thermal abuse model for lithium-ion cells *J. Power Sources* **170** 476-89
- [3] Kim G H, Pesaran A 2007 Analysis of heat dissipation in Li-ion cells & modules for modeling of thermal runaway *The 3rd International Symposium on Large Lithium Ion Battery Technology and Application* Long Beach, California
- [4] Srinivasan R, Carkhuff B G, Butler M H, et al. 2011 Instantaneous measurement of the internal temperature in lithium-ion rechargeable cells. *Electrochimica Acta* **56** 6198-204
- [5] Schmidt J P, Arnold S, Loges A, et al. 2013 Measurement of the internal cell temperature via impedance: Evaluation and application of a new method *J. Power Sources* **243** 110-7
- [6] Kinmomo K, Paulo J, Monteiro M 2010 Electrical Resistance Tomography imaging of concrete. *Cement and Concrete Research* **40** 137-45
- [7] Rodgers T L, Siperstein F R, Mann R, et al. 2011 Comparison of a networks-of-zones fluid mixing model for a baffled stirred vessel with three-dimensional electrical resistance tomography *Measurement Science and Technology* **22**(10) 1-12
- [8] Hong X B, Li N Z, Yin W W, et al. 2014 A novel monitoring method for internal temperature of vehicle power battery based on electrical resistance tomography *Optics and Precision Engineering* **22**(1) 193-203 (In Chinese)
- [9] Hong X B, Liu G X 2010 Double-layer compression method based on PLSR-SBR for IP mode measurement and control system. *Optics and Precision Engineering* **18**(10) 2280-87 (In Chinese)
- [10] Sato N, Yagi K 2001 Thermal Behavior Analysis of Lithium-ion Batteries for Electric and Hybrid Vehicles *J. Power Sources* **99**(1) 70-7

Authors	
	<p>Xiaobin Hong, born in 1979, Guangdong province, China</p> <p>Current position, grades: associate professor, postgraduate tutor University studies: South China University of Technology in China Scientific interest: network measuring technology & instruments and non-destructive detection technology Publications: totally 28 publications, main publications as follow, 1. 2014 <i>Optics and Precision Engineering</i> 22(1), 193-203. 2. 2013 <i>Smart Materials and Structure</i> 22(4),1-13 3. 2010 <i>Optics and Precision Engineering</i> 18(10), 2280-87. Experience: He received bachelor's degree at Wuhan University of technology in 2002, and doctorate at South China University of Technology in 2007, then worked in South China University of Technology. He spent one year as a visiting scholar at University of Houston in 2012.</p>
	<p>Nianzhi Li, born in 1989, Hubei province, China</p> <p>Current position, grades: postgraduate students in second grade University studies: South China University of Technology in China Scientific interest: measurement techniques & measuring instruments Publications: one publication as follow, 1.2014 <i>Optics and Precision Engineering</i> 22(1), 193-203. Experience: He received bachelor's degree from Wuhan University of Technology in 2012.</p>
	<p>Wenwei Yin, born in 1983, Guangxi province, China</p> <p>Current position, grades: postgraduate students in third grade University studies: South China University of Technology in China Scientific interest: instrument and apparatus Publications: one publication as follow, 1.2014 <i>Optics and Precision Engineering</i> 22(1), 193-203. Experience: He received bachelor's degree from National University of Defense Technology in 2006.</p>



Jinheng Feng, born in 1990, Guangdong province, China

Current position, grades: postgraduate students in first grade

University studies: South China University of Technology in China

Scientific interest: measurement techniques & measuring instruments

Experience: He received bachelor's degree from Zhongkai University of Agriculture and Engineering in 2013.



Guixiong Liu, born in 1968, Guangdong province, China

Current position, grades: professor, doctoral tutor

University studies: South China University of Technology in China

Scientific interest: Intelligent sensing technology, network measuring technology, Manufacturing process quality inspection, Modeling and control.

Publications: 65 publications, main publications as follow,

1. 2009 *Acta Phys. Sin.* 58(3), 2005-10.

2. 2008 *Acta Phys. Sin.* 57(4), 2500-04.

3. 2008 *Optics and Precision Engineering* 16(5), 965-971.

Experience: He received bachelor's degree and doctorate at Chongqing University respectively in 1990 and 1995, now worked as a professor in South China University of Technology.

Authors' index	
Cao XiaoBo	41
Fan GuoChao	41
Feng J H	97
Gao Yehemin	72
Hong X B	97
Ji Fengquan	80
Jia Yuanyuan	80
Kang Fan	23
Karatun N	15
Khatjatouski S	15
Li N Z	97
Lin Haitao	7
Liu Feng	33
Liu G X	97
Liu Wei	23
Ma Yun	66
Si Hua	66
Solomentsev O	49
Statsenko A	15
Tang Cunchen	23
Wang Chaoyou	57
Wang Jing	7
Wang Jing	33
Wang Xiaodong	18
Wang Ying	77
Wang Zhiyong	7
Xu ChengDong	41
Xu Fang	7
Xu Ning	7
Yang Jianhui	18
Yashanov I	49
Yin W W	97
Yu Peng	7
Zaliskyi M	49
Zhang Huyin	7
Zheng Jiahzu	72
Zhou Xuejun	7
Zhou Yuanyuan	7
Zhu Shanhong	29
Zhu Shanhong	62
Zuiev O	49

Operation Research: Modelling and Simulation

An improved adaptive weighted clustering algorithm based on time interval grade in Mobile Ad Hoc networks

Zhang Huyin, Wang Jing, Xu Fang, Xu Ning, Wang Zhiyong, Zhou Xuejun, Lin Haitao, Yu Peng, Zhou Yuanyuan
Computer Modelling & New Technologies 2015 19(1B) 7-14

Mobile Ad Hoc Networks (MANETs) are self-configuring dynamic networks of mobile devices connected by wireless links without any fixed infrastructure or centralized administration. In order to achieve stable clusters, the cluster-heads (CHs) maintaining the cluster should be stable with minimum re-affiliation times and number of changes on CHs, with maximal throughput of the clustering formation and maintenance. An improved adaptive weighted clustering algorithm based on time interval grade (IATIGWCA) in MANETs is proposed. Each node can be assigned an adaptive role and set its status value through their Hello messages in the formation procedure of clusters, and an appropriate CH of a cluster is elected by the calculation the total weight which comprising four factors: degree difference, average Euclidean distance, average relative speed and consumed battery power. In the maintenance procedure of clusters, the duration of clustering maintenance is set to 2 grades which are Little Time Slot and Big Time Slot in order to improve the efficiency of clustering and decrease the times of computation of the total weight of every node. The simulation results show that the selection of numbers of CHs and numbers of clusters in the stage of the formation of clusters is an optimal solution which brings higher throughput, less re-affiliation times, less number of changes on CHs and longer residence time of cluster in IATIGWCA than LID and WCA.

Keywords: clustering, cluster-head (CH), time interval grade, clustering maintenance

Calculation modelling of static constructions

Karatun N, Khatjatouski S, Statsenko A
Computer Modelling & New Technologies 2015 19(1B) 15-17

The mathematic model of force loads calculations of static constructions in the framework of Theoretical Mechanics course is presented. The software to visualize and analyse force loads of static constructions is created.

Keywords: theoretical mechanics, informative systems of engineering analysis, visualization and analysis of static constructions, visualization of the force loading

Application of the fiber image detection algorithm based on the Grey system theory and Directed graph

Wang Xiaodong, Yang Jianhui
Computer Modelling & New Technologies 2015 19(1B) 18-22

After doing research on fiber image with low quality and the Grey prediction model, the Grey correlation degree, directed graph and existing edge detection algorithm, this article proposed a new edge detection algorithm to obtain complete and continuous edge and to improve the defects in traditional operators profiled fiber contour extraction, such as the discontinuous edge, the false edge. This article obtains the fiber outline firstly, and then the edge detection algorithm is applied to the adhesive fibers. Thus, filling algorithm and contour tracking algorithm are used to get the fibers' outer contour. After that applying the directed graph algorithm to edge detection and the complete edge is gained after the burr is eliminated. Proven by the experimental results, the proposed edge detection algorithm can overcome the defects of the conventional edge detection algorithm, such fracture as edge, false edge, etc.

Keywords: grey correlation degree, directed graph, edge detection algorithm, directed graph

Research in search engine user behaviour based on cloud computing

Liu Wei, Tang Cunchen, Kang Fan
Computer Modelling & New Technologies 2015 19(1B) 23-28

User behavior analysis is important for both Web information retrieval technologies and commercial search engine algorithms. With the expansion of information data, the current search engine is facing some serious problems, such as limited storage space and computing power. The paper discussed the shortcomings and technical bottlenecks of the current traditional search engine. Then, in the understanding of search engine features and technical requirement, it improved the system by means of the cloud computing architecture. With the combination of the static analysis of user behaviour and real-time monitoring, real-time acquisition of Web log and user to access the context information of the page, the paper tested the whole system performance in the laboratory environment, demonstrated the superiority of the system by analysis of experimental data.

Keywords: user behavior analysis, search engine, cloud computing, system performance

Worm detection and prevention based on network segmentation algorithm

Zhu Shan hong
Computer Modelling & New Technologies 2015 19(1B) 29-32

Due to large space demanding and time-consuming, as the Internet is large and complex, the detection and prevention of the worm has many engineering constraints factors, the classic graph theory algorithms cannot suitable for solving some problems

in the large-scale network. Sub-graphs of vertices have a higher density of edges within them while a lower density of edges between sub-graphs. To solve large-scale network analysis, the method of using DFS network segmentation algorithm based on network topology was proposed by analyzing the study of graph depth-first search (Depth First Search, referred to as DFS) segmentation algorithm, and thus obtain a description of the network connectivity of undirected connected graph $G(V, E)$. This provides a strong theoretical support for fast access network backbone node. The result of experiments shows that the proposed method is effective.

Keywords: worm detection, sub-graphs, DFS, network segmentation algorithm

Selection method of wireless communication modes in internet of vehicles

Liu Feng, Wang Jing

Computer Modelling & New Technologies 2015 19(1B) 33-40

Internet of Vehicles has great effect on improving the efficiency of the transportation system and driving safety. Communication process of Internet of Vehicles can be done adopting various wireless communication modes which include 3G, WLAN and WAVE. As each wireless communication mode has different traffic scene applicability and different communication effects, this paper proposed a selection method for wireless communication mode based on support vector machine. This method obtained learning samples which indicate the communication mode with best communication performance through simulation of various traffic scenes in OPENT Modeler. Through the study of support vector machine algorithm, this designed method can output the predicted result mode of wireless communication adaptively under unknown traffic scenes. The outstanding results show that the selection method based on support vector machine can accurately choose the optimal communication mode in Internet of vehicles.

Keywords: internet of vehicles, wireless communication mode, support vector machine, communication performance, OPENT modeller

Study on the task scheduling problem of complicated products' design

Cao XiaoBo, Xu ChengDong, Fan GuoChao

Computer Modelling & New Technologies 2015 19(1B) 41-48

The process of complicated products design has the characters of high complexity, long period and various requirement of resource. So a reasonable resource scheduling scheme has great significance to the design of complicated product, so as to shortening product development cycles and reducing the cost of product. Firstly, design task collaboration and scheduling features in three complicate product design process modes are discussed in terms of research results of collaboration design and Integration Design Environment (IDE). Secondly, Virtual Design Unit (VDU) is adopted to be taken as the basic task execute unit, VDU design is a complex product design, Furthermore, Design Task Scheduling Approach based Design Ability (DTSADA) is detailed stated by combining ACO and GA. Finally, a design task scheduling case is demonstrated to validate the proposed approach.

Keywords: complicated product, virtual design unit (VDU), IDE, task scheduling

Diagnostics programs efficiency analysis in operation systems of radioelectronic equipment

Solomentsev O, Zuiev O, Zaliskyi M, Yashanov I

Computer Modelling & New Technologies 2015 19(1B) 49-56

Two variants of diagnostics programs of radioelectronic equipment in exploitation systems are considered. Analytical formulas for calculation of efficiency indexes in the absence and presence of first and second kind errors are given.

Keywords: radioelectronic equipment, diagnostic programs, data processing; maintenance

Time series neural network systems in stock index forecasting

Wang Chaoyou

Computer Modelling & New Technologies 2015 19(1B) 57-61

This paper adopts artificial neural network (ANN) and two varieties of time series neural network to forecast the stock index of Chinese market. Daily close prices between 1999 and 2011 are tested. The ANN works as a benchmark. Its inputs include delayed price and technical indicators. Time series neural network with external input (NARX) outperforms the Time series neural network (NAR), and it works best when the delay is 8. Moreover, NARX has the best ability of the three. This is mainly resulted from the fact that it contains external data and the technical indicators while NAR does not. As a whole, the ANN and NARX models achieved satisfying results. They can be employed by practitioners to assist trading and by regulators for monitoring. The NARX will be improved when more external data imported.

Keywords: forecasting, ANN, NAR, NARX

Study on the electrodeposited Au-Co alloy coating

Zhu ShanHong

Computer Modelling & New Technologies 2015 19(1B) 62-65

Au-Co alloy deposit was prepared by selecting the best component in the bath with citrate the deposit exhibited golden appearance and high percentage of coverage. Good hardness and improving anti-corrosion capability could be achieved by

adding 3~4.5%Co element and little rare-earth element to the system, and micro-hardness could increase to 180~190Hv. Optimized bath has stable performance, good throwing power and good covering power. The Scanning Electron Microscope (SEM) illustrated that the deposit was smooth, compact and crystal was nice. It is suited for electrical production; decorative coating, advance electrodeposits and hard-gold deposite.

Keywords: Au electrodeposited, Au-Co alloy, citrate

The micro-structure study on mechanical properties of Dredge fills

Ma Yun, Si Hua

Computer Modelling & New Technologies 2015 19(1B) 66-71

Mechanical tests and electron microscopy scanning tests were done and micro-structural parameters were quantitatively analyzed in order to study the essence of structural characteristics of Dredge Fills. After comparing the mechanical test results with the statistical results of microstructure parameters, it can be find that the transition stage of the stress-strain curve of dredge fill compression test is also the mutation stage of the curve of micro-structural parameters, and the same time, the micro-structural parameters of shear test soil samples under different axial strain were not linear variation with the axial strain increases and mutated in 10% to 15% axial strain. The analysis result shows that the structural mechanical properties of the dredge fill are subject to its microstructure, and mutation of mechanical test curve is a macroscopic manifestation of microscopic structure damage. The experimental results indicate that dredge fill has the basic mechanical properties of structural soil.

Keywords: Dredge Fills, structural constitution, microstructure, mechanical properties

Method of calculating forest land surface area based on automatic boundary extraction

Zheng Jiahzu, Gao Yehemin

Computer Modelling & New Technologies 2015 19(1B) 72-76

Calculation of the forest land parcel surface area is vital to the confirmation, segmentation and assignment of forest ownership. Therefore, the method calculating irregular forest land parcel surface area, which is based on the principle of space triangle area calculation, establishes automatic extraction of irregular forest parcel boundary and structures Triangulated Irregular Network (TIN) model by interpolating feature points based on Thin Plate Spline (TPS) function. This paper expounds the feasibility of this method and complete calculation process. By experimental comparison, this method can reduce about four-fifths of field data collection effort in the case of no accuracy loss in calculating results. Simultaneously, this method extracts boundary automatically without manual drawing boundary lined, improves degree of automation in computing within the industry greatly.

Keywords: forest land parcel, surface area, boundary extraction, thin plate spline (TPS)

Application of computer virtual reality technology in ship equipment assembly

Wang Ying

Computer Modelling & New Technologies 2014 19(1B) 77-79

It is known to us all that in factors of determining shipbuilding cycle, ship assembly occupies an important position in shipbuilding. In traditional shipbuilding model, front-line workers conduct assembly according to the two-dimensional drawing of marine designer. They will make mistakes inattentively, which results in the waste of manpower and material resources. At the same time, the abstraction of drawing will tend to generate deviation in the communication system between designer and ship-owner because of no concrete model object. This paper adopted a kind of technology that could use three-dimensional entity form to express ship model and assembling process-ship virtual assembly technology. The combination of virtual reality technology and ship assembly technology revealed the insufficient and defect in design, which avoided the waste of manpower and material resources during practical assembly. Through the selection and comparison of virtual assembly, we could optimize assembly technology, thus to convenient for the learning and execution of front-liner workers, enhance shipbuilding efficiency and shorten shipbuilding cycle.

Keywords: Virtual technology; Ship assembly; Digitalized shipbuilding; Three-dimensional model

Ecological architecture system based on landscape ecology

Ji Fengquan, Jia Yuanyuan

Computer Modelling & New Technologies 2014 19(1B) 80-84

This paper briefly summarized the concept of landscape ecology and ecological architecture and the current research status of ecological architecture both at home and abroad. It also analyzed ecological architecture system based on landscape ecology, and studied the construction of ecological architecture from the aspects of the construction of ecological architecture system and space structure. In addition, this paper reviewed with the green building demonstration in University of Logistics for instance.

Keywords: landscape ecology, ecological architecture

Modelling and simulation of relationship between internal cell temperature and apparent resistivity for lithium-ion battery

X B Hong, N Z Li, W W Yin, J H Feng, G X Liu

Computer Modelling & New Technologies 2015 19(1B) 85-91

Safety problems caused by thermal runaway have been restricting the popularization and application of power lithium-ion battery (LIB). As Electrical Resistance Tomography (ERT) method can potentially detect the variations of internal cell apparent resistivity influenced by temperature, the simulation of the relationship between the internal cell temperature and apparent resistivity is presented to monitor the thermal circumstance inside LIB cell. Using the linear interpolation functions, the LIB model is built and meshed. The appropriate boundary conditions are imposed to simulate the cell virtual heating process and ERT process. During the simulations, the distributions of the apparent resistivity at different temperatures are given. It is found that the correlation of apparent resistivity and temperature is well fitted by quintic function. Meanwhile, the evaluation of quintic fit under cell discharge reveals a deviation of 6.2K between the cell core temperature and the surface temperatures. The presented method cannot only be applied in thermal balance management, life prediction and load control, but also afford a possible way for monitoring the health of separator structure of LIB.

Keywords: lithium-ion battery model, thermal simulation, internal cell temperature, apparent resistivity